Forschungszentrum Karlsruhe
in der Helmholtz-Gemeinschaft
Wissenschaftliche Berichte
FZKA 6958

Investigation of Atmospheric Effevts on the Development of Extensive Air Showers and their Detection with the Pierre Auger Observatory

B. G. Keilhauer

Institut für Kernphysik

Februar 2004

Forschungszentrum Karlsruhe
in der Helmholtz-Gemeinschaft

Wissenschaftliche Berichte
FZKA 6958

Investigation of Atmospheric Effects on the Development of Extensive Air Showers and their Detection with the Pierre Auger Observatory

Bianca Gerlinde Keilhauer
Institut für Kernphysik

Zur Erlangung des akademischen Grades eines Doktors der Naturwissenschaften von der Fakultät für Physik der Universität Karlsruhe (TH) genehmigte Dissertation

Forschungszentrum Karlsruhe GmbH, Karlsruhe
2004

Impressum der Print-Ausgabe:

Als Manuskript gedruckt
Forschungszentrum Karlsruhe GmbH
Postfach 3640, 76021 Karlsruhe

Mitglied der Hermann von Helmholtz-Gemeinschaft
Deutscher Forschungszentren (HGF)

ISSN 0947-8620

Untersuchung von atmosphärischen Einflüssen auf die Entwicklung von ausgedehnten Luftschauern und auf deren Beobachtung mit dem Pierre Auger Observatorium

Für die Entwicklung ausgedehnter Luftschauer, die von der kosmischen Strahlung induziert werden, spielt die Atmosphäre eine entscheidende Rolle. Zudem werden beim Pierre Auger Observatorium die Observablen von den atmosphärischen Bedingungen beeinflußt. Die Untersuchung dieser Effekte wird durchgeführt einerseits auf der Basis von generellen Atmosphärenmodellen und andererseits anhand von argentinischen Atmosphärenmodellen, die aus Daten von Radiosondierungen gewonnen werden. Die Atmosphärenprofile wurden in fünf Messkampagnen in allen vier Jahreszeiten gemessen. Bei der Luftschauersimulation wird die longitudinale Entwicklung mittels der atmosphärischen Tiefe beschrieben, und auch für die Rekonstruktion der Energie und Art des Primärteilchens ist dies die entscheidende Größe. Die Fluoreszenz-Teleskope des Auger Experimentes detektieren die Luftschauer jedoch in einem festen geometrischen Blickfeld. Somit ist die Transformation der atmosphärischen Tiefe zu geometrischer Höhe ein wichtiger Schritt, der sehr stark von dem Profil der Luftdichte abhängt. In Bezug auf die Beobachtungsgrößen der Teleskope werden die atmosphärischen Abhängigkeiten der Fluoreszenz-Ausbeute und der Lichttransmission untersucht. Das Elektron- zu Myon-Verhältnis der Sekundärteilchen am Erdboden ist eine wichtige Eigenschaft, die von den Wasser-Cherenkov-Detektoren vermessen wird. Der atmosphärische Einfluß auf die Elektronzahl ist leicht unterschiedlich zu dem auf die Myonzahl, was zu variierenden Verhältnissen bei verschiedenen atmosphärischen Bedingungen führt. Schließlich werden einige Aspekte der Kurz- und Langzeitvariabilität der Daten der argentinischen Atmosphäre diskutiert, sowie mögliche Alternativen für die Bestimmung der atmosphärischen Bedingungen in Argentinien.

Investigation of Atmospheric Effects on the Development of Extensive Air Showers and their Detection with the Pierre Auger Observatory

For the development of extensive air showers induced by cosmic rays, the atmosphere plays a major role. Additionally at the Pierre Auger Observatory, the atmospheric conditions influence the observables. The investigation of the effects is based on the one hand on more general atmospheric models and on the other hand on Argentine atmospheric models derived from radio sounding data. These measurements of atmospheric profiles were performed in five campaigns in all four seasons. Within air shower simulations, the longitudinal development is described by the atmospheric depth and also for the reconstruction of the energy and type of the primary particle, this quantity is decisive. However, the fluorescence telescopes of the Auger experiment detect extensive air showers in a fixed geometrical field of view. Thus, the correct transformation of the atmospheric depth profiles to geometrical altitudes is an important step which is strongly dependent on the atmospheric density profile. With respect to the observables of the fluorescence telescopes, the atmospheric dependences of the fluorescence yield and of the light transmission are studied. The electron-to-muon ratio of the secondary particles at ground is an important quantity which is measured by the water Cherenkov detectors. The atmospheric influence on the electron number is slightly different from that on the muon number and therefore small variations of this ratio are expected for different atmospheric conditions. Finally, several aspects of the short- and long-term variability of the Argentine atmospheric data are investigated as well as possible alternatives for the determination of atmospheric conditions in Argentina.

Contents

Deutschsprachige Zusammenfassung

Die Beobachtung von ausgedehnten Luftschauern (EAS) beschäftigt die Physiker seit nunmehr vielen Jahrzehnten. Anhand der Observablen können Informationen über Teilchenreaktionen gewonnen werden, die teilweise in Energiebereichen ablaufen, die weit oberhalb der Energien sind, die an von Menschen gebauten Teilchenbeschleunigern erzeugt werden können. Die Rekonstruktion der Eigenschaften des Primärteilchens, der eigentlichen kosmischen Strahlung, ermöglicht zudem auch Aussagen über kosmologische Quellen der Strahlung, eventuelle Beschleunigungsmechanismen und Wechselwirkungen in den Feldern im inter- und intragalaktischen Raum. Da die Ereignisrate der höchstenergetischen kosmischen Strahlung, bei der die Primärenergie $E_0 > 10^{18}$ eV ist, hier auf der Erde sehr gering ist, ist eine direkte Beobachtung kaum realisierbar. Deshalb werden die Sekundärteilchen der kosmischen Strahlung, die ausgedehnten Luftschauer, detektiert. Die Teilchenkaskade entwickelt sich in der Erdatmosphäre, sendet dabei Licht aus und ein gewisser Teil der Sekundärteilchen erreicht die Erdoberfläche. Dies eröffnet zwei verschiedene Nachweismethoden, die im Pierre Auger Observatorium kombiniert werden.

Wie bereits angedeutet, übernimmt die Atmosphäre bei diesem Experiment eine wesentliche Rolle. Der Luftschauer entwickelt sich in der Atmosphäre, womit diese als Kalorimeter dient. Durch Ionisationsprozesse wird vom Luftschauer Fluoreszenzlicht emittiert. Die Atmosphäre stellt somit ein Szintillator-Medium dar. Letztendlich treten weitere Abhängigkeiten von den atmosphärischen Bedingungen bei der Transmission des Lichtes vom Emissionsort hin zum Detektor auf. Die atmosphärischen Einflüsse auf die Entwicklung der ausgedehnten Luftschauer und auf die Schauer-Beobachtungsgrößen, so wie sie vom Pierre Auger Observatorium gemessen werden, sollten in dieser vorliegenden Arbeit untersucht und wenn möglich quantifiziert werden. Besondere Schwerpunkte waren dabei sowohl die jahreszeitliche Variabilität der Atmosphäre, als auch die höhenabängigen Veränderungen der einzelnen Zustandsgrößen der Atmosphäre.

Zur ersten quantitativen Abschätzung der zu erwartenden jahreszeitlichen Effekte wurden die üblicherweise in der Analyse verwandte US Standard Atmosphäre 1976 (US-StdA) und zwei extreme Atmosphärenmodelle für Sommer und Winter in Süddeutschland zugrunde gelegt. Die höhenabhängigen Profile dieser Modelle zeigen große Variationen untereinander auf, die, wie in der vorliegenden Arbeit gezeigt wurde, sich auch in der Entwicklung und Beobachtung der Luftschauer niederschlagen. Die Ergebnisse dieser theoretischen Untersuchungen legen die Notwendigkeit von Messungen der atmosphärischen Profile am Ort des Experimentes nahe. Es wurden daraufhin zunächst an verschiedenen Orten im Gebiet des Pierre Auger Observatoriums in Argentinien meteorologische Radiosondierungen durchgeführt. Die erste Meßkampagne war im Winter und vier weitere Kampagnen in allen weiteren Jahreszeiten folgten, wobei die letzte Kampagne im darauf folgenden Winter stattfand. Ab der zweiten Meßreihe wurde die Empfangsstation für die Radiosondierung fest am Fluoreszenzdetektor-Gebäude *Coihueco* installiert. Automatische Radiosonden wurden mit Helium-gefüllten Ballonen auf Höhen von 20 - 25 km üNN gebracht, wobei beim Aufstieg etwa alle 20 m Daten aufgezeichnet wurden. Es wurden insgesamt 52 Aufstiege erfolgreich durchgeführt, so dass die markanten Eigenschaften der einzelnen Jahreszeiten und auch die Variationen innerhalb der Jahreszeiten erfaßt werden konnten. Fünf jahreszeitlich gemittelte Atmosphärenmodelle wurden erstellt, wobei extrem unterschiedliche Winterbedingungen zwei Wintermodelle erforderten.

Im Rahmen dieser Arbeit wurden mittels Simulationsstudien hauptsächlich drei Einflüsse der Atmosphäre untersucht. Diese sind die Transformation der vertikalen atmosphärischen Tiefe in geometrische Höhen, die Erzeugung des Fluoreszenzlichtes und die Transmission des Lichtes hin zum Teleskop, welche nun detailliert zusammengefaßt werden. Vom physikalischen Standpunkt aus ist das Maß der durchquerten Materie, die sogenannte atmosphärische Tiefe, für die Luftschauerentwicklung die ausschlaggebende Größe. Daher werden EAS in Simulationsprogrammen und Rekonstruktionsprozeduren mittels dieser Variable beschrieben. Die Fluoreszenz-Teleskope beobachten die longitudinale Schauerentwicklung in dunklen Nächten in einem geometrisch festgelegten Blickfeld. Daher kann in diesem Zusammenhang die Beschreibung der Luftschauer nicht über die atmosphärische Tiefe erfolgen, sondern es muß die geometrische Höhe herangezogen werden. Die Transformation dieser beiden Größen ineinander unterliegt dem funktionalen Zusammenhang zwischen der Luftdichte und der Höhe. Da die Luftdichte von der Lufttemperatur und dem Luftdruck abhängt, ist eine jahreszeitliche Schwankung offensichtlich. Im Vergleich zur US-StdA treten die größten Unterschiede in der atmosphärischen Tiefe zwischen Sommer und Winter in der Höhe von 4 bis 10 km üNN auf. Die optische Beobachtung der EAS erfolgt über die Messung des Fluoreszenzlichtes mit Teleskopen. Die Sekundärteilchen im Luftschauer regen die Stickstoff-Moleküle der Luft durch Ionisation an, und ein Teil der Abregung erfolgt über die Emission von Fluoreszenzlicht. Die Fluoreszenz-Effizienz hängt von der Lufttemperatur und dem Luftdruck ab, folglich weist die Effizienz ein höhenabhängiges, zeitlich variierendes Profil auf. Die abgeleitete Fluoreszenz-Ausbeute ist proportional zum lokalen Energiedeposit des Luftschauers und zum Luftdichteprofil. Damit weicht das im Fluoreszenzlicht meßbare Luftschauerprofil etwas vom EAS Profil der geladenen Teilchen oder des Energiedeposits ab. Eine weitere Quelle für atmosphärischen Einflüsse resultiert daher, dass die Atmosphäre auch als Transportmedium für das Licht dient. Auf seinem Weg von der Emission hin zum Teleskop wird das Licht teilweise absorbiert und gestreut. Die Streuung kann in zwei Aspekte unterschieden werden. Der erste bezieht sich auf Streuung an Gasmolekülen, die sogenannte Rayleigh-Streuung, und der zweite Teil auf die Streuung an Aerosolen, die Mie-Streuung. Die Rayleigh-Streuung ist exakt berechenbar, wohingegen die Mie-Streuung je nach Größe und Form der Aerosole stark fluktuiert. Um den Einfluß der Mie-Streuung berücksichtigen zu können, wird die Konzentration und Natur der Aerosole im Rahmen des Pierre Auger Projektes mehrere Male pro Nacht gemessen. Die Rayleigh-Streuung hängt von der Lufttemperatur, dem Luftdruck und der Luftdichte ab, was abermals eine Abhängigkeit von der Höhe und eine jahreszeitliche Variation induziert. Der Aspekt der Lichtabsorption ist vernachlässigbar für den beobachteten Wellenlängenbereich von 300 bis 400 nm, da die infrage kommenden Absorber wie Ozon und NO_2 nur in niedrigen Konzentrationen in der unteren Atmosphäre vorkommen und einen nicht ausreichend großen Wirkungsquerschnitt in diesem Wellenlängenbereich haben.

Für Luftschauer, die von der ultrahochenergetischen kosmischen Strahlung mit einem Einfallswinkel von $> 30°$ ausgelöst werden, stimmt der Höhenbereich der möglichen Position des Schauermaximums mit dem Höhenintervall der größten saisonalen Variation der atmosphärischen Tiefe überein. Da die Natur des Primärteilchens des EAS von der Position des Schauermaximums abgeleitet werden kann, ist dies für die Analyse von EAS Daten der wesentliche Bereich, wenn die Fluoreszenz-Technik Anwendung findet. Die gesamte, sichtbare Verschiebung des Schauermaxiums, die durch Sommer- gegenüber Winterbedingungen hervorgerufen wird, ist etwa genauso groß wie die Verschiebung, die z. B. durch einen Proton-induzierten statt eines Eisen-induzierten Schauers hervorgerufen wird.

Im Folgenden werden die Ergebnisse der Messungen in Argentinien zusammengefaßt und die argentinischen Daten auf die Berechnungen der Luftschauerentwicklung und deren Beobachtung mit den Auger Detektoren angewandt. Legt man die Profile der atmosphärischen Tiefe zugrunde, kann festgehalten werden, dass die größten Unterschiede zwischen dem mittleren Sommer und Winter in Argentinien ebenfalls im Bereich zwischen 5 und 10 km üNN auftreten. Es treten im Bereich der Positionen der Schauermaxima Schwankungen von 20 bis 30 g/cm^2 auf. Allerdings sind diese Unterschiede nicht so stark ausgeprägt wie für die gewählten deutschen Bedingungen. Der kältere Wintertyp ist sehr ähnlich zu der US-StdA, während der argentinische Sommer die Abweichungen des deutschen Sommers von der US-StdA übersteigt. Auch der argentinische Herbst ist sehr unterschiedlich zur US-StdA, was zu einer starken Verzerrung der Luftschauerprofile in der unteren Atmosphäre (0 - 7 km üNN) führt. Dies hat großen Einfluß auf die Energierekonstruktion der EAS. Die atmosphärenabhängige Fluoreszenz-Ausbeute variiert die sichtbaren EAS Profile nur leicht im Vergleich zu den Profilen des Energiedeposits. Höhere Lufttemperaturen bewirken eine Reduktion der Fluoreszenz-Ausbeute, ein Anstieg der Lufttemperatur um +5°C verursacht 1% weniger Fluoreszenz-Photonen. Somit wird, in Kombination mit dem Defizit des Energiedeposits in der unteren Atmosphäre im Sommer und Herbst, die Energie des Luftschauers systematisch unterschätzt, wenn die US-StdA in den Rekonstruktionsprozeduren angewandt wird. Die Verschiebung der Position des Schauermaximums könnte eine schwerere Komposition der einfallenden kosmischen Strahlung im Sommer vortäuschen. Die Variation der Rayleigh-Transmission aufgrund der Jahreszeiten ist recht klein. Die atmosphärischen Effekte auf die Beobachtungsgrößen der Bodendetektoren des Auger Observatoriums wurden nur angerissen. Die Triggereffizienz sollte über den Bodenluftdruck korrigiert werden können. Der Einfluß auf das Verhältnis der Elektronen zu Myonen kann jedoch nicht so einfach korrigiert werden. Die Myonzahl wird durch die gesamte longitudinale Entwicklung beeinflußt. Daher wird ein Unterschied in dem Verhältnis der Elektronen zu Myonen in der Größenordnung einiger Prozent erwartet.

Führt man nun jahreszeitlich gemittelte argentinische Atmosphärenprofile ein, so können die Schwankungen und die damit verbundenen Unsicherheiten in der Simulation und Rekonstruktion reduziert werden, insbesondere im Hinblick auf die atmosphärische Tiefe. Innerhalb der einzelnen Jahreszeiten treten im Bereich der Position der Schauermaxima Unterschiede in der atmosphärischen Tiefe von bis zu 10 g/cm^2. Dies ist eine deutliche Verbesserung gegenüber der Anwendung der US-StdA, zeigt aber zugleich die verbleibenden Unsicherheiten. Somit wird es auch in Zukunft unumgänglich sein, Radiosondierungen durchzuführen. Die jahreszeitlich gemittelten Atmosphärenparamater, die aus den argentinischen Daten abgeleitet werden konnten, sind ab jetzt in dem Luftschauer-Simulationsprogramm CORSIKA anwendbar.

Die kontinuierliche Messung von atmosphärischen Profilen stellt jedoch einen hohen finanziellen und personellen Aufwand dar. Deshalb wurden einige Möglichkeiten untersucht, die zu einer Reduktion der notwendigen Radiosondierungen führen sollen. Hierfür wurden weitere Atmosphärenmodelle getestet. Das vielversprechendste war ein Modell, welches atmosphärische Profile für alle 5° geographischer Breite und für jeden Monat liefert. Ein Vergleich mit den Meßdaten führt zu dem Schluß, dass die generellen Eigenschaften der Atmosphäre in Argentininen mit diesem Modell erheblich besser beschrieben werden können als mit der US-StdA. Ein Vergleich der einzelnen Monate zeigte jedoch einige Ungereimtheiten. Eine weitere Möglichkeit ist die Nutzung von bodengebundenen Wetterstationen, die kontinuierlich Daten erfassen. Dies könnte eine sinnvolle Ergänzung zu Radiosondierungen sein, die nur noch an drei bis vier Nächten pro Dunkelperiode im Monat durchgeführt werden. Allerdings sind die Daten der Bodenwetterstationen nur dann aufschlußreich, wenn zwei Stationen in unterschiedlichen Höhen (z.B. 1750 und 2500 m üNN) errichtet werden. Erste Indikator-Variablen wurden bereits erarbeitet, weitere detaillierte Untersuchungen müssen jedoch noch durchgeführt werden. Besonders in diesem Zusammenhang deuteten sich mögliche Effekte durch die *El Niño Southern Oscillation* (ENSO) an. Dieses Thema könnte aber auch hilfreich sein, denn es hat derzeit hohe Priorität im Bereich der Klimatologie und daher werden detaillierte Atmosphären-Informationen auf großflächiger Skala angeboten. Langzeit-Untersuchungen müssen zeigen, ob die hier erarbeiteten Atmosphärenmodelle für Argentinien allgemein gültig sind und wie groß die Schwankungen durch ENSO Ereignisse sind.

Introduction

The fascination of the cosmic rays captivates the physicists since almost 100 years. In 1911, Victor Hess was one of the pioneers exploring these highly energetic particles from outer space. Years later, in 1938, Pierre Auger and his colleagues figured out that the energy of cosmic rays is so high that they may initiate a large cascade of secondary particles in Earth's atmosphere. First assumptions lead to reconstructed energies of the primary particles of several 10^{13} eV. This was far beyond every man-made energy concentrated in an elementary particle. The challenge of discovering new, possibly theoretically predicted, particles was accepted.

Nowadays, the energy of measured cosmic ray events has risen up to 10^{20} eV being still high above the energies achieved in modern particle accelerators despite huge efforts in that field. Thus, also the probability of discovering new particles firstly in cosmic ray events and their extensive air showers is still valid. However, the large energy of cosmic rays is not the only fascinating fact. Cosmic rays are massive particles from outer space, not only a glow of the visible universe. The particles are able to teach us details about the composition of space and the fields between the massive objects like solar systems or galaxies. Their odyssey has began millions of years ago when they were produced and accelerated or were born as daughter particles of much heavier or elder relict particles of the Big Bang.

The cosmic rays and their extensive air showers combine the exploration of the smallest structures in the Universe, the elementary particles, and the largest and farthest objects as the structure of the Universe itself. This growing field in physics, named Astroparticle Physics, was already insinuated by Werner Heisenberg: *"Die kosmische Strahlung erweckt heutzutage vor allem aus zwei Gründen Interesse. Sie erlaubt, mit Elementarteilchen höchster Energie zu experimentieren und bringt Kunde von Vorgängen auf den Sternen und im interstellaren Raum. ..." (W. Heisenberg, 1953, Vorträge über kosmische Strahlung)* With the **Pierre Auger Observatory**, we want to study cosmic rays at the upper end of the known energy spectrum, events with $E_0 > 10^{18}$ eV. Theoretical predictions however, postulate a strong decrease in flux above $\approx 5 \times 10^{19}$ eV which might reflect the upper limit of the observable spectrum. Cosmic rays with energies above this cutoff lose part of their energy while interacting with the cosmic microwave background, thus reaching the Earth with strongly reduced energy. In recent years, two experiments using two different techniques have been trying to measure the cosmic ray spectrum around this so called *Greisen Zatsepin Kuz'min* cutoff. One experiment is based on the measurement of the fluorescence emission of extensive air showers while the other detects the secondary particles at ground. Their results diverge in the confirmation of the cutoff's existence, but both experiments have only low statistics at these energies. The Pierre Auger Observatory is expected to measure the energy range of interest accurately enough to resolve the enigmas of cosmic rays. One of the main advantages of this experiment is its hybrid technique, combining the observation of the fluorescence emission and the secondary particles at ground. Furthermore, the setup in size and sensitivity gives the opportunity to detect cosmic rays at highest energies and at highly inclined incidence angles with high statistics.

In contrast to particle accelerator experiments, the cosmic ray experiments take place in the Earth's atmosphere and not in vacuum. On the one hand, this enables us to detect the cosmic rays via their secondary particles. The primary particle of the cosmic ray could hardly be observed since its incoming path is not known. The indirect measurement via the extensive air shower makes it easier to "find" the event. On the other hand, this also represents a difficulty while simulating and reconstructing the events. It is not possible to simulate all secondary particle reactions and the experimental "laboratory" conditions change from event to event and even during one event while crossing large spatial areas. Therefore, the influence of atmospheric conditions on the development of extensive air showers and on their detection with the Pierre Auger Observatory has to be investigated. A check has to be done how realistic the usually applied US standard atmosphere is, strictly speaking, how large the induced errors on the observables are while using that model. For this study, the Monte Carlo code CORSIKA is applied for simulating the cosmic ray induced extensive air showers and meteorological techniques are applied for recording the atmospheric conditions in Argentina, the location of the first part of the Pierre Auger Observatory. Mainly, the molecular aspects of the atmosphere are examined like temperature, pressure and density profiles. These conditions directly influence the development of air showers and their emission of fluorescence light. The aerosol conditions of the atmosphere are not detected by the used methods within this work and are recorded by other groups of the collaboration.

A general description of the cosmic ray phenomenon and the Pierre Auger observatory is given in Chapter 1. The structure of the atmosphere and physical processes of air molecules are introduced in Chapter 2. Some atmospheric models used in this work are presented as well as the conditions in Argentina, the place of the first part of the Auger experiment. In Chapter 3, the atmospheric influences on the development of extensive air showers and on their detection with the observatory are studied on the basis of the previously introduced atmospheric models. After revealing the main variables, the appropriate measurements performed in Argentina are presented in Chapter 4. Profiles of atmospheric variables are measured by launching radiosondes. The data obtained are applied to shower development simulations and the consequences for the observables of the Auger fluorescence detector are discussed in detail in Chapter 5.1 and more briefly for the data of the Auger surface detector in Chapter 5.2. For deducing more general descriptions of the Argentine atmospheric conditions, the atmospheric data measured are compared with other atmospheric models in Chapter 6.1. In Chapter 6.2, possibilities for avoiding too frequent radio soundings by operating ground-based weather stations are outlined.

Chapter 1

Cosmic Rays and the Pierre Auger Observatory

The Earth's atmosphere is permanently exposed to relativistic particles from outer space, the cosmic rays. These particles carry information about far regions and objects of the universe as well as particle physics processes (rec.[1] [Nagano & Watson 2000]). Using cosmic rays as probes, we try to elicit these information by measuring particle energy, type of particle, and arrival direction. One of the most advanced instruments for this purpose is the Pierre Auger Observatory. This detector, currently under construction, is based on two different techniques observing the secondary products of the collisions of cosmic rays in the Earth's atmosphere.

1.1 Cosmic Rays

The cosmic rays are mainly nuclei of large kinetic energy which covers a range of ten magnitudes (Fig. 1.1). With increasing energy E of particles the differential intensity observed at Earth decreases which can be approximated by a power law (rec. [Sokolsky 1989]):

$$dN/dE \propto E^{-\gamma}. \tag{1.1}$$

Apart from the steeply falling shape of the overall energy spectrum of primary cosmic rays, three remarkable regions indicated by a changing spectral index γ can be claimed.

The low energetic part of the spectrum reaches up to the "knee" being at $\approx 3 \times 10^{15}$ eV. The flux at the lower end amounts to roughly 1 particle per m^2 and second, thus these cosmic rays can be observed directly by satellite or balloon borne experiments. Partly, the particles are associated with solar flares [Hagiwara et al. 2002]. Towards higher energies, the cosmic rays mainly originate from outside the solar system. The acceleration of the particles may be described by the first order Fermi mechanism[2] at strong shocks caused by supernova remnants (rec. [Gaisser 1997]). This happens in the disk of the galaxy. However, not all particles accel-

---

[1] rec. = recensuit (lat.) = reviewed from

[2] The average fractional energy gain of a particle per cycle is of first order in the relative velocity between the shock front and the isotropic cosmic ray frame. A cycle is defined as one crossing and the re-crossing of the shock after the particle is turned back by the magnetic field (rec. [Bhattacharjee & Sigl 2000]).

erated reach the Earth, some of them are escaping from the galaxy with an energy dependent rate. This explanation of the cosmic ray acceleration with energy $< 10^{15}$ eV fits quite well: the power law spectrum is induced by the Fermi mechanism and the power available in kinetic energy of supernova ejecta matches well with the requirements to maintain the observed flux.

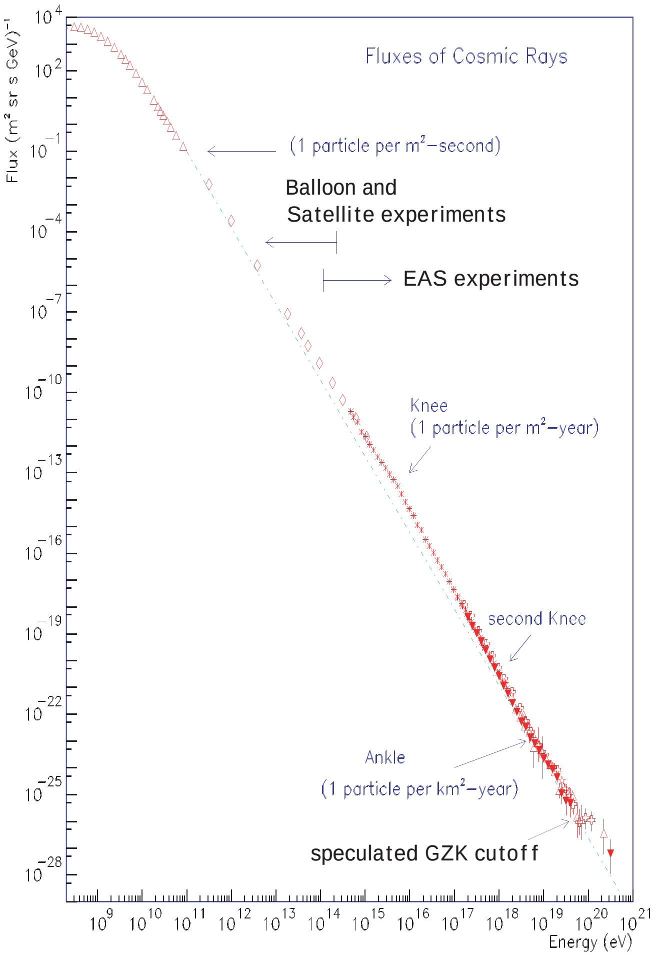

Figure 1.1: Observed energy spectrum of primary cosmic rays (rec. [Nagano & Watson 2000], [Bertou et al. 2000]).

The second region in the cosmic ray spectrum ranges from the knee up to the "ankle" at several 10^{18} eV to 10^{19} eV. The spectral index γ has changed from 2.7 to 3.0 which most likely reflects the upper energy limit of some accelerators. Despite a less clear situation in this region, the ankle is sometimes interpreted as a crossover from a galactic to an extragalactic component [Hillas 1984], rec. [Bhattacharjee & Sigl 2000]. Experimental results, e.g. from the KASCADE[3] experiment, give evidence for a composition becoming heavier above the knee [Antoni et al. 2002]. This would coincide with a re-acceleration process during the cosmic ray propagation by interacting with multiple supernova remnants in the interstellar medium (rec. [Nagano & Watson 2000]). The re-acceleration is less efficient because the particles undergo the second order Fermi mechanism[4] originally introduced by Fermi (rec. [Gaisser 1997]). This extended acceleration may take particles up to $\approx 10^{18}$ eV, the second knee. Another possibility is also given by supernovae. The different types of supernovae may lead to different accelerated spectra which provide a composition becoming heavier, too.

The region of interest for the Pierre Auger observatory is the spectrum above the ankle. Mainly two experiments have measured cosmic rays with an energy $> 10^{19}$ eV so far,

---

[3] **KA**rlsruhe **S**hower **C**ore and **A**rray **DE**tector

[4] The average fractional energy gain is proportional to $(u/c)^2$, where u is the relative velocity of the magnetised plasma with respect to the frame in which the cosmic ray ensemble is isotropic, and c is the velocity of light [Bhattacharjee & Sigl 2000].

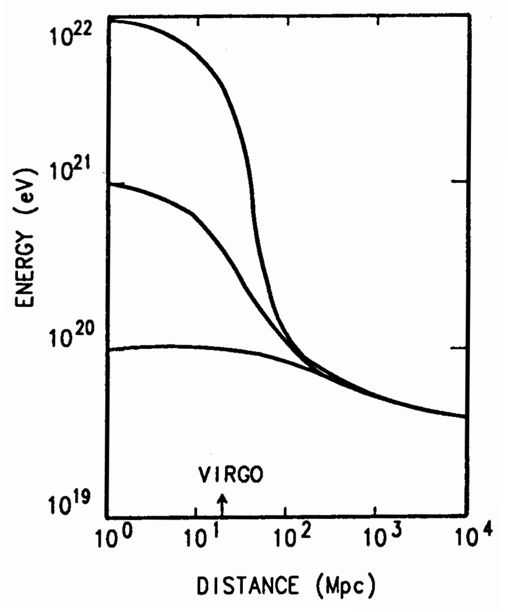

Figure 1.2: Calculation of the mean energy of protons due to the interaction with the 2.7 K radiation as a function of distance for various initial energies [Cronin 1992].

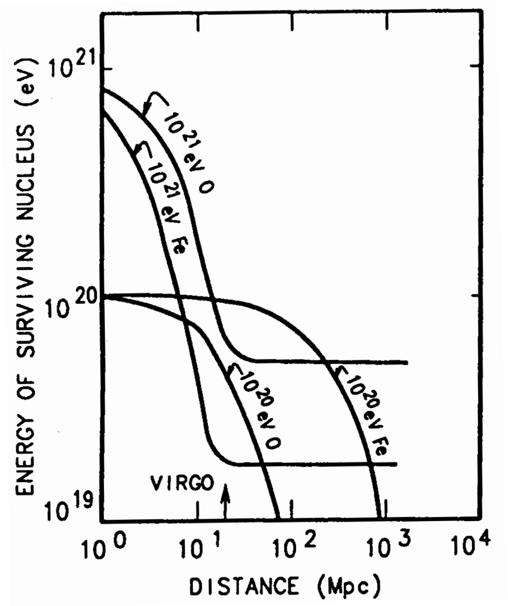

Figure 1.3: Calculation of the energy of the heaviest fragment of initial iron and oxygen nuclei as a function of distance due to photodisintegration by the 2.7 K background radiation [Cronin 1992].

these are AGASA[5] and HiRes[6] (rec. [Sommers 2001]). The spectrum becomes again more flat and the arrival distribution seems to be isotropic. The most important feature in this spectral region is the predicted Greisen-Zatsepin-Kuz'min cutoff (GZK cutoff) [Greisen 1966], [Zatsepin & Kuz'min 1966]. Protons with energy above 6×10^{19} eV interact with the cosmic microwave background (CMB), mainly via photo-pion production with subsequent Bethe-Heitler pair-production (rec. [Nagano & Watson 2000]):

$$
\begin{aligned}
p + \gamma_{2.7K} &\rightarrow n + \pi^{+} \\
&\rightarrow p + \pi^{0} \\
&\rightarrow p + e^{+} + e^{-} .
\end{aligned}
\tag{1.2}
$$

Heavy nuclei of mass A suffer photodisintegration and pair-production processes:

$$
\begin{aligned}
A + \gamma_{2.7K} &\rightarrow (A-1) + N \\
&\rightarrow (A-2) + 2N \\
&\rightarrow A + e^{+} + e^{-} ,
\end{aligned}
\tag{1.3}
$$

where N is a nucleon. The resulting effects of these processes can be seen in Figs. 1.2 and 1.3. The probability of particles arriving at Earth with an energy above 6×10^{19} eV and sources farther away than 50 to 100 Mpc is strongly suppressed. However, in particular the

---

[5] **A**keno **G**iant **A**ir **S**hower **A**rray

[6] High Resolution Fly's Eye, advanced successor of Fly's Eye

AGASA experiment has observed several events with energy above the GZK cutoff which even nowadays stresses the validity of the old question: *"On what can we now place our hopes of solving the many riddles which still exist as to the origin and composition of cosmic rays?" (V. F. Hess, Nobel Lecture 1936 "for his discovery of cosmic radiation" in 1911).* One way to explain the existence of such high energetic cosmic rays is to continue the ideas of accelerating particles within astrophysical objects like for energies below 10^{18} eV. The different models are summarised as "Bottom-Up" theories. Particles are accelerated in a region of a size comparable to their Lamor radius in a magnetic field. This magnetic field must be weak enough so that the synchrotron losses are smaller than the energy gain. The acceleration process is believed to be diffusive shock acceleration [Greisen 1965], [Hillas 1984]. The maximum energy a particle of charge $Z \cdot e$ can obtain is approximately

$$E \propto \beta ZeBR, \tag{1.4}$$

where β is the shock speed, B the magnetic field strength, and R the size of the shock region (rec. [Nagano & Watson 2000]). The relevant known astrophysical sources can be seen in Fig. 1.4. Galaxies with active nuclei and the Virgo cluster are the most probable extragalactic sources for ultra high energy cosmic rays. Also interacting galaxies and Gamma Ray Bursts were suggested [Ptuskin 2001]. In order to arrive at Earth, the accelerated particles

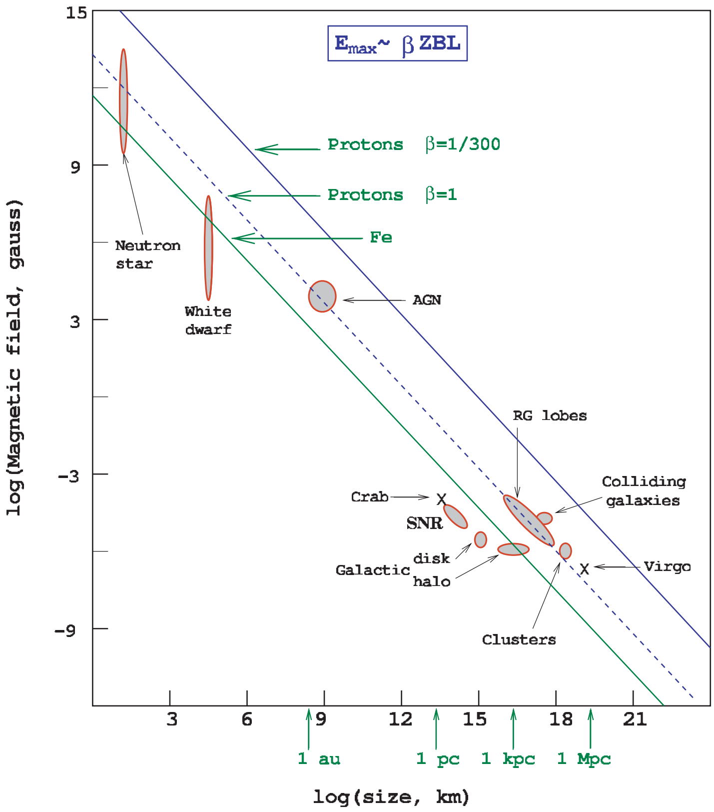

Figure 1.4: Size and magnetic field strength of possible acceleration sites. Objects below the diagonal lines cannot accelerate the corresponding elements (Iron with $\beta = 1$ or protons $\beta = 1$ and $\beta = 1/300$) above 10^{20} eV [Hillas 1984], rec. [Bertou et al. 2000].

have to traverse the intergalactic and galactic space. Interactions may cause deflection and energy loss. However at the highest energies above 10^{19} eV, the trajectories of particles are not affected significantly neither by galactic nor intergalactic magnetic fields [Olinto 1999]. Therefore, protons should reveal a strong anisotropy and also arrival directions of heavier nuclei up to iron should be anisotropically distributed assuming a magnetic field in the galactic halo of a thickness of ≤ 2 kpc [Cronin 1992]. Thus, the pure existence of events with energy above the GZK cutoff demands sources of distances less than 50 Mpc. This subsequently includes anisotropic arrival distributions, meaning point sources related to astrophysical objects. However, these objects have not been found up to now.

Motivated by the difficulties to explain at the same time the energy spectrum and the isotropy of the arrival distribution, many exotic physics scenarios have been proposed. These models are called “Top-Down” theories. Most of them introduce a new unstable supermassive “X-particle” with energies exceeding 10^{21} eV. The sources of the X-particles could be topological defects, like magnetic monopoles or cosmic strings, that could be produced in the early Universe during symmetry-breaking phase transitions envisaged in Grand Unified Theories (rec. [Bhattacharjee & Sigl 2000]). Its decay products include quarks and leptons. The quarks hadronise and form the known cosmic rays (rec. [Bertou et al. 2000]). Other candidates are superheavy metastable relic particles from the post-inflation era. Also ideas of stable supersymmetric hadrons as primary cosmic rays and a suppression of the GZK cutoff due to breaking of the Lorentz invariance are considered (rec. [Nagano & Watson 2000]).

1.2 Extensive Air Showers

Cosmic rays that enter the Earth's atmosphere interact with air nuclei. The collision results in secondary particles and these themselves may interact again with air nuclei or decay. For high energy primaries, the shower of secondary particles is called an Extensive Air Shower (EAS). A scheme of an EAS is illustrated in Fig. 1.5, right part.

As the density of air is quite low at higher altitudes, the height of first interaction is strongly fluctuating. The incoming particles represent the projectiles and the resting air nuclei are the target similar to the setup in fixed-target accelerator experiments. In the case of nuclei, not all nucleons of the projectile interact with the target, most of them are only spectators. In high energy hadronic interactions, mostly nucleons, charged and neutral pions ($\pi^{\pm}, \pi^0$), and kaons ($K^{\pm}, K^0_{L,S}$) are produced (rec. [Knapp 1997]). In general, the description of EAS can be divided into three particle components: the electromagnetic, muonic and hadronic (Fig. 1.5, left). The $\pi^{\pm}$ and K mesons have relatively long lifetimes of 10^{-8} s, thus they can interact with air nuclei or decay depending on their energy [Khristiansen et al. 1980]. If the $\pi^{\pm}$ decay before interacting, they fill up the muonic component accompanied by neutrinos: $\pi^{\pm} \rightarrow \mu^{\pm} + \nu$. Many of the muons reach the Earth's surface due to the relativistic time dilatation of their lifetime of 2.2 $\times 10^{-6}$ s and small energy loss. Those which decay, produce parts of the electromagnetic component: $\mu^{\pm} \rightarrow e^{\pm} + \nu + \bar{\nu}$. The neutral pions are the dominant source of the electromagnetic shower component. Their lifetime is much shorter than that of the charged pions, about 10^{-16} s. The main decay channel (98.8%) produces two photons. γ rays with energy exceeding 1.022 MeV undergo pair-production ($\gamma \rightarrow e^+ + e^-$). The resulting $e^{\pm}$ suffer bremsstrahlung, emitting again γ rays. The particle multiplication is large and the electromagnetic component is the most numerous part in the EAS (rec. [Allkofer 1975]).

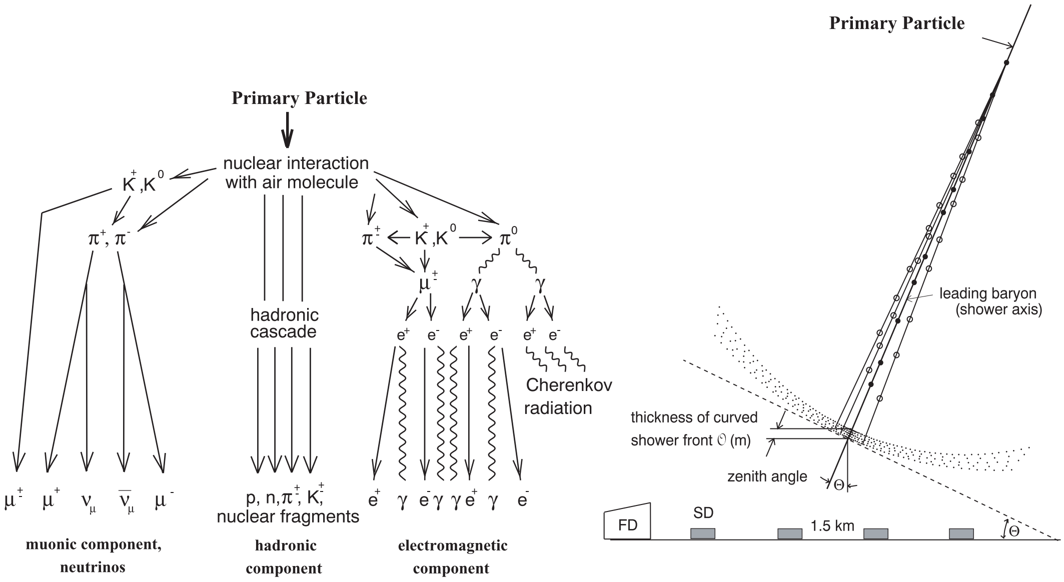

Figure 1.5: Schematic EAS development. In the left part, the three components created by the particle production are outlined. The lateral distribution is strongly elongated. In the right part, the curvature of the shower front can be seen, which moves through the atmosphere with almost speed of light. The Auger Observatory is schematically indicated.

The longitudinal shower development is therefore formed by particle production and energy losses. All these processes are steered by the amount of matter traversed, which is in the case of EAS the atmosphere. Therefore the unit *length* is replaced by *atmospheric depth* representing the amount of traversed air defined as (rec. [Knapp 1997]):

$$X(h_0) = \int_{h_0}^{\infty} \rho(h)\ dh, \tag{1.5}$$

with h = geometrical height[7].

The number of particles ($N(X)$) increases in the upper part of the EAS. After reaching a maximum (N_{max}), it decreases. An analytical function describing the shower size was given by *Gaisser* and *Hillas* [Gaisser & Hillas 1977]. Nowadays it is refined by simulation studies to the form [Knapp & Heck]:

$$N(X) = N_{max} \cdot \left(\frac{X - X_0}{X_{max} - X_0} \right)^{\frac{X_{max}-X_0}{a+bX+cX^2}} \cdot e^{\frac{X_{max}-X}{a+bX+cX^2}} . \tag{1.6}$$

The depth of shower maximum is indicated by X_{max} related to X as the slant depth along the shower axis. Already a simple toy model can demonstrate the relation between the basic features of an EAS [Gaisser 1990]. The energy of the primary cosmic rays E_0 is the total energy the EAS distributes. Thus, at a given depth X the energy per particle is $E(X) = E_0/N(X)$. This holds up to $E(X) = E_c$, the particle reaches a critical energy below which

---

[7] Here written for a vertical particle trajectory.

the energy loss dominates over particle production. Therefore, the number of particles and the atmospheric depth of shower maximum is correlated to the primary energy:

$$\begin{aligned} N(X_{max}) &= E_0/E_c & (1.7) \\ X_{max} &= X_\lambda \cdot \frac{\ln(E_0/E_c)}{\ln 2}, & (1.8) \end{aligned}$$

where X_λ is one interaction length. The energy loss of charged particles is due to ionisation. The atmosphere represents the matter traversed and the Bethe-Bloch formula can be applied [Heck et al. 1998].

For simulating EAS with all particle and energy developments Monte Carlo codes are used. A common program which is applied to this study is CORSIKA[8], [Knapp & Heck]. Within this simulation code, the longitudinal and lateral distribution of particles and their energy development is calculated. Additionally, the energy deposited in air via ionisation and excitation of air molecules is stored [Risse & Heck 2002]. Optionally, the Cherenkov photons produced by the charged particles in the EAS can be written out.

1.3 The Pierre Auger Observatory

As indicated previously (see Chap. 1.1), cosmic rays with energy $> 10^{14}$ eV are quite rare. Thus, a direct detection can hardly be performed but their induced EAS can be observed. One technique is to measure secondary particles arriving at the Earth's surface. These surface detectors mainly record the lateral distribution, the energy, and the type of particles. Another technique is to observe the fluorescence light induced by the EAS. The energy deposit in air excites the nitrogen molecules and part of the de-excitation proceeds via luminescence (for details see Chap. 3.3). The fluorescence detectors are telescopes viewing the clear night sky and supply direct information on the energy deposit and the longitudinal shower development.

The Auger Observatory is the first experiment which combines these two detection methods, and therefore it is called a hybrid detector. It provides shower information to a greater degree than either technique alone [Auger-DR 1997]. Both components measure the shower energy, direction and primary particle type in independent, complementary ways. A subsample of the observed EAS is detected by both detectors and can be used for cross checks. Furthermore, the Auger Observatory consists of two parts: the first system is currently installed in the southern hemisphere in Argentina and the second will be built in a couple of years in the northern hemisphere. Each part is located at around 35° - 40° latitude guaranteeing together a full sky exposure. The southern system is described in the following.

The particle detectors are placed on an area of about 3000 km^2 spaced out by 1.5 km on a triangular grid. The atmosphere above the array will be viewed by four fluorescence detector stations each covering 180° × 30° field of view (see Fig. 1.6). The necessity of a large almost flat area lead to the choice of a plain 1400 m a.s.l. with sparse human settlement, but with some infrastructure nearby the array. The visibility for the telescopes is good: no significant sources of light pollution and a cloud cover of less than 15%. The data communication system consists of two integrated radio networks. The high capacity *backbone network* supports the

---

[8] **CO**smic **R**ay **SI**mulations for **K**ascade and **A**uger

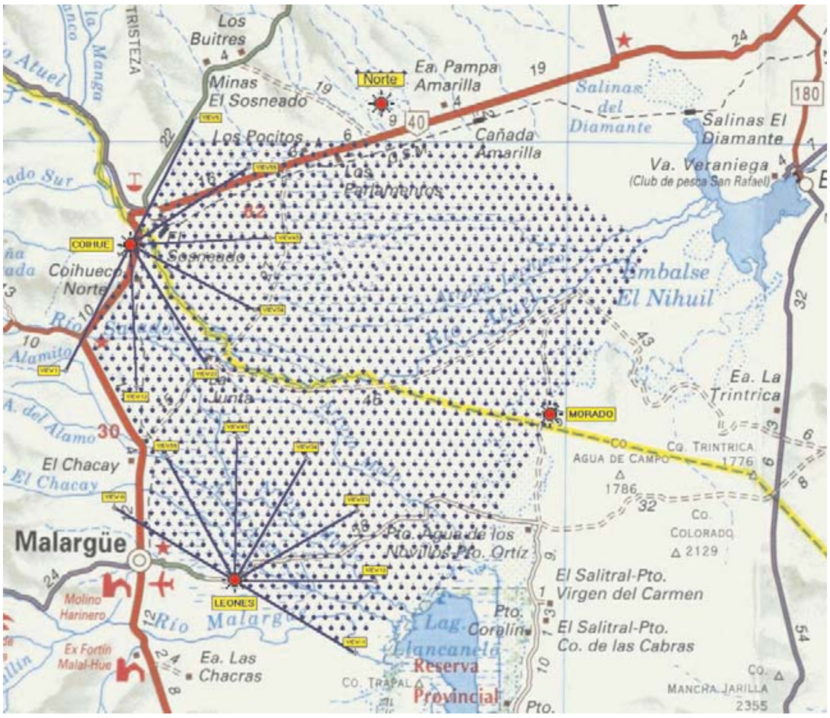

Figure 1.6: Auger Observatory array in Argentina near Malargüe, Mendoza. Each dot represents one of the 1600 water Cherenkov tanks. At the boundaries of the array are 4 telescope stations.

fluorescence detector stations and also the distributed collection points of the *surface detector wireless LAN network*. It is based on a commercial 34 Mbps telecommunication architecture. The *surface detector wireless LAN network* uses custom radio hardware operating in the 902 - 928 MHz ISM radio band supporting each of the 1600 water Cherenkov tanks. The whole data are collected at five telecommunication towers and from there transmitted to the central observatory buildings. Via TCP/IP the data are passed from the network to the Central Data Acquisition System [Auger-TDR 2002].

The experimental setup is designed for measuring EAS induced by cosmic rays of $E_0 > 10^{18}$ eV. The limiting factors at the lower end of the detectable energy spectrum are for the fluorescence detector the fluorescence rate and the absorption of the light on the path from the shower towards the telescope. The surface detector sensitivity is given by the distance between the water Cherenkov tanks. At the upper end of the detectable energy spectrum, the only limiting factor is the low flux of cosmic rays with very high energies.

1.3.1 Fluorescence Detector

The fluorescence detector consists of four telescope stations each built up of six separate optical systems each with a field of view of 30° × 30°, starting 2° above the horizon. A construction drawing of one building is shown in Figure 1.7.

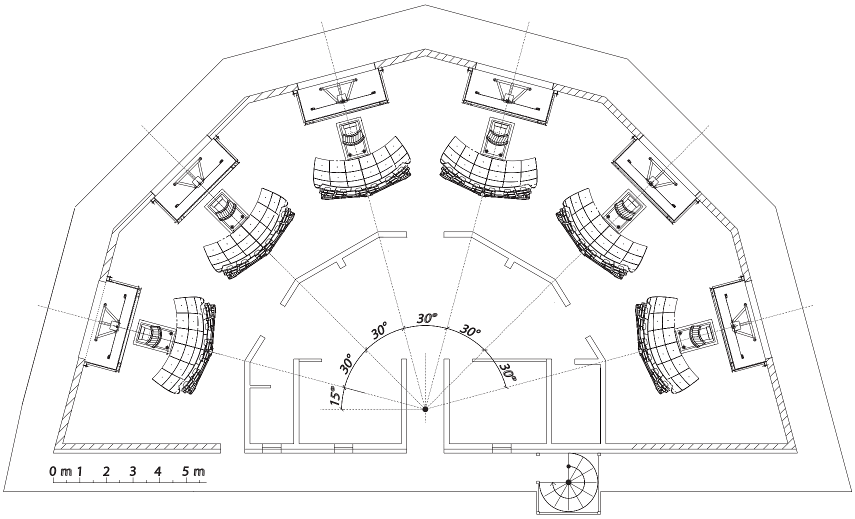

Figure 1.7: Fluorescence detector building with 6 telescope bays and computing rooms (Courtesy of H. Hucker).

The telescopes use a *Schmidt* optics comprising a segmented spherical mirror with 3.4 m radius of curvature, a corrector ring at the aperture, a UV filter, and a camera of 440 photomultipiers (PMT) placed in the focal plane [Waldenmaier 2001], see Figure 1.8. The surface of the mirror amounts to ≈ 12 m^2 , the radius of the aperture is 1.1 m. Since the fluorescence light emitted by the EAS is mainly in the ultraviolet wavelength region (λ = 300 - 400 nm), the UV filter has its main transmission window between 290 nm and 410 nm. The reflectivity of the mirrors reaches ≈ 90%. The PMT have a circular photocathode with 1.5° field of view [Blümer 2003]. For collecting all photons falling on the matrix of hexagonal pixels, light collectors in the form of a “Mercedes” star are put at the spaces between the PMT. Each camera inside a fluorescence detector building is read out separately, see Figure 1.9. The data taking of the PMT is done with a 10 MHz cycle. The whole system in each building is guarded by a *slow control* unit. The status of the electronics, the environmental conditions and other relevant data are monitored and in case of an emergency the shutters in front of the telescopes are closed and the system is shut down.

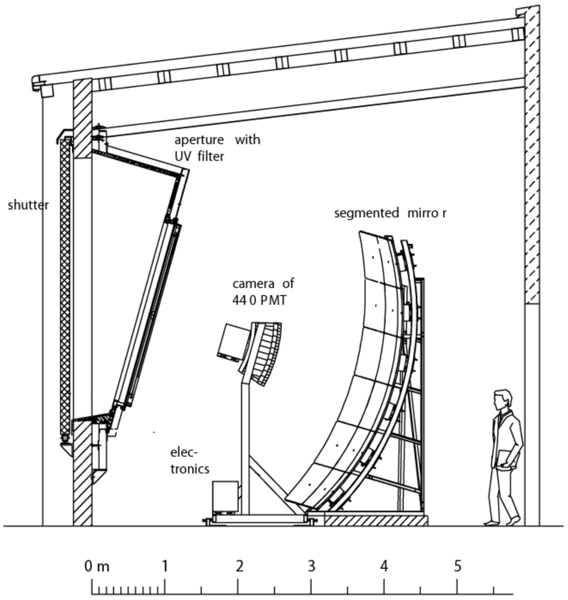

Figure 1.8: Schematic drawing of one fluorescence telescope system (Courtesy of H. Hucker).

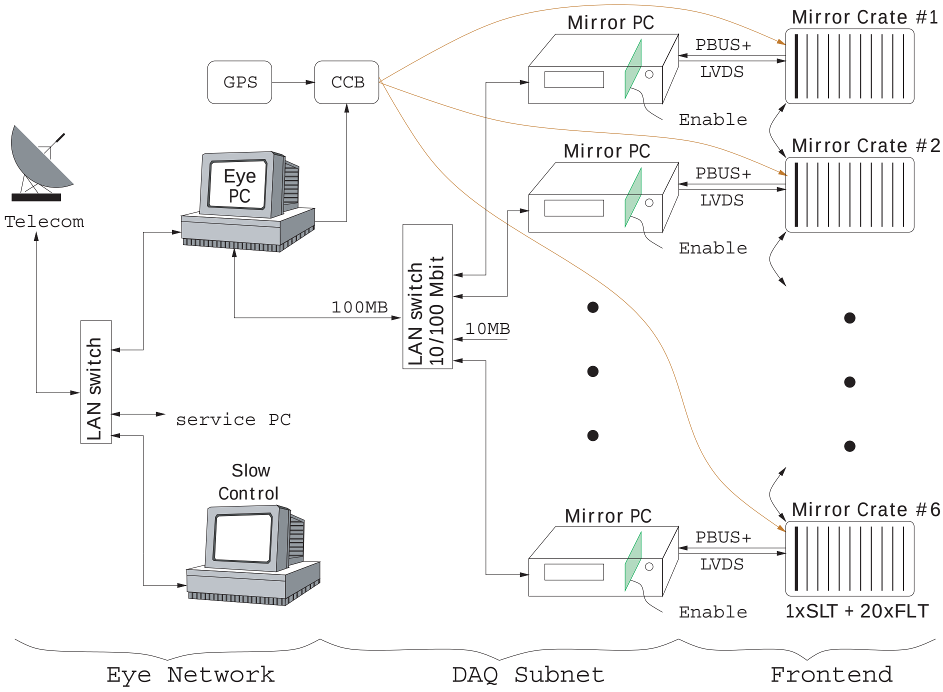

Figure 1.9: Readout scheme for the fluorescence detector electronics. Each camera is controlled by a Mirror PC, transferring all data to the Eye PC. The Eye PC supervises the equipment of one fluorescence detector building [Auger-TDR 2002].

Since the amount of emitted fluorescence light is quite small, measurements are only possible in clear nights with illuminated moon less than 50%. This induces a duty cycle of 10 - 15%. Using the fluorescence detector, one method to identify the primary particle is the determination of the position of shower maximum (see Chap. 1.2). The visible energy will be calculated as the integral of a fit function to the longitudinal energy deposit development. The desired resolution is ± 10 g/cm^2 in the depth and 10% in the energy depending on signal-to-noise requirements [Auger-DR 1997].

1.3.2 Surface Detector

The surface detector is a cluster of water Cherenkov tanks. Secondary particles of an EAS that hit a tank will emit Cherenkov light if their energy is above the Cherenkov threshold in water. This light is detected by three PMT (see Fig. 1.10). The height of the sensitive volume, 1.2 m water, provides a much better acceptance of very inclined showers than thin scintillation counters. Each tank is filled with 12 m^3 ultrapure water. The high water quality is necessary as the absorption of light must be minimised and a lifetime of 20 years must be ensured [Escobar et al. 2001]. The surface detectors measure time and shape of the PMT signals in 25 ns time intervals. It is possible to distinguish between the muonic and the electromagnetic component of the EAS. In general, muons produce a small number of early, large pulses whereas the particles of the electromagnetic component induce a large number of relatively small pulses with later arrival times.

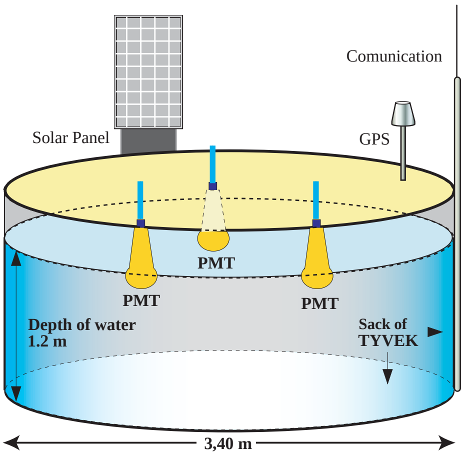

Figure 1.10: Schematic drawing of one water Cherenkov tank. It is filled with ultrapure water.

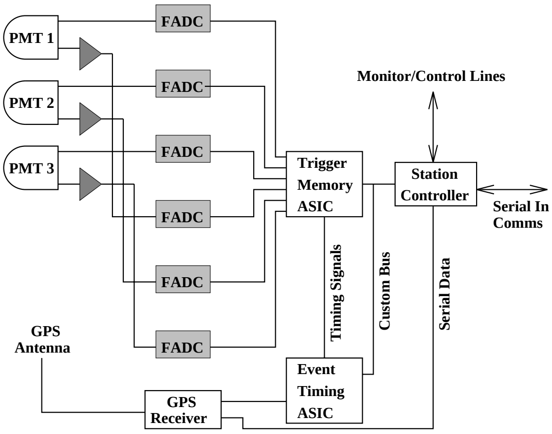

Figure 1.11: Block diagram of the tank electronics [Auger-TDR 2002].

The duty cycle of the surface detector will be 100%. The angular direction resolution is expected to be better than 1.1° depending on the EAS energy, type of primary particle and inclination angle. The energy resolution has been estimated to be in the order of 10% [Ave et al. 2001].

Chapter 2

The Atmosphere

The importance of meteorological influences on EAS was already discussed in the early years of this field of research. The variations of the EAS intensity with changing atmospheric conditions in particular and qualitative details of interaction processes in the shower were pointed out [Biermann & Schlüter 1953]. Higher temperatures at the production height of pions cause lower densities and thus higher intensities of muons at ground because of increasing decay rates for $\pi^{\pm}$ into μ (*positive temperature effect*). The *negative pressure effect* describes the chance of survival of a created μ while losing energy via ionisation which depends on pressure and by this on atmospheric depth. Nowadays, all these processes can be simulated and quantified with Monte Carlo codes like CORSIKA requiring a well established knowledge of the atmosphere. More over, using the fluorescence technique for detecting EAS, the atmosphere affects the measured signal as it serves as calorimeter and light propagation medium.

2.1 Physics of the Atmosphere

The Earth's atmosphere is a gaseous envelope. Its upper boundary is not well defined as it passes into the outer space. Below $\approx$ 18 km a.s.l. 90% of the mass of the atmosphere is accumulated and only 1% is left above 32 km a.s.l. (rec. [Roedel 1992]). The composition of the atmosphere is given in Table 2.1. The most important contributions relevant to EAS development are nitrogen and oxygen, but for the climatological classification of the Earth the small fraction of water vapour is a decisive factor. However, most of the physical processes in the atmosphere are due to the solar radiation and its spatial and temporal variations caused by the cycling of the Earth around the Sun and the rotation around its axis. These two movements of the Earth lead to changes in the input of solar radiation which can be recognised by the seasons, daily and zonal variations (rec. [Weischet 1977]).

State Variables

The atmosphere can be described by several state variables. The most perceived is the **temperature** T which is a measure of the average kinetic energy of the molecules. The unit is given in °C or K, where $T/°\mathrm{C} = T/\mathrm{K}$ - 273.15. The temperature is influenced by factors like [DWD 1987]

Table 2.1: Composition of the atmosphere near the Earth's surface [Ahrens 1994].

Gas	**Symbol**	**Percent** (by Volume) **Dry Air**	**Gas**	**Symbol**	**Percent** (by Volume)
nitrogen	N_2	78.08	water vapour	H_2O	0 to 4
oxygen	O_2	20.95	carbon dioxide	CO_2	0.036
argon	Ar	0.93	methane	CH_4	$1.7{\cdot}10^{-4}$
neon	Ne	0.0018	nitrous oxide	N_2O	$3{\cdot}10^{-5}$
helium	He	$5{\cdot}10^{-4}$	ozone	O_3	$4{\cdot}10^{-6}$
hydrogen	H_2	$6{\cdot}10^{-5}$	particles (dust, soot, etc.)		$1{\cdot}10^{-6}$
xenon	Xe	$9{\cdot}10^{-6}$	chlorofluorocarbons		$1{\cdot}10^{-8}$

- heat budget, dependent on the position of the sun and cloud cover;
- vertical exchange of sensible[1] and latent[2] heat between Earth's surface and atmosphere;
- horizontal transport of heat by air flow;
- kind of Earth's surface (snow, water, forest, desert, etc.) which determines the radiation and energy budget of a location according to the albedo[3], thermal conductivity and capacity, and evaporation;
- altitude of the location;
- wind conditions;
- topography.

Going up higher in the atmosphere, the temperature decreases. This can be understood in terms of the adiabatic expansion of a rising air 'parcel'.

The atmospheric **pressure** p is defined as the force per unit area acting perpendicular to the surface. It is caused by the weight of the air above the surface due to the gravitational force. The **humidity** specifies the content of water vapour in air. Assuming atmospheric air to be a mixture of two gases, namely dry air and water vapour, the latter can be expressed as the vapour pressure e. The maximal vapour pressure of air is called saturation pressure E_s depending on temperature (Magnus formula):

$$\begin{aligned} T &\geq 0.0^{\circ}C \quad : \\ E_s &= 6.1078 \cdot \exp\left(\frac{17.08085 \cdot T(^{\circ}\mathrm{C})}{234.175 + T(^{\circ}\mathrm{C})}\right) \qquad (2.1) \\ T &< 0.0^{\circ}C \quad : \\ E_s &= 6.10714 \cdot \exp\left(\frac{22.44294 \cdot T(^{\circ}\mathrm{C})}{272.44 + T(^{\circ}\mathrm{C})}\right). \qquad (2.2) \end{aligned}$$

---

[1] Sensed by humans; portion of total heat associated with temperature change (rec. [Stull 1995]).

[2] Hidden heat, stored or released in phase transitions (rec. [Stull 1995]).

[3] Ratio of total reflected to total incoming solar radiation (rec. [Stull 1995]).

The relative humidity u (%) is the ratio of the pressure of actually contained water vapour and the saturation pressure for a given temperature [DWD 1987].

The **density** ρ of air is a derived quantity. For dry air we use the ideal gas law, thus the density can be written as

$$\rho(h) = \frac{p(h) \cdot M_m}{R \cdot T(h)}, \tag{2.3}$$

where R is the universal gas constant = 8.31451 J/(K·mol) and M_m the molar mass of air in g/mol. Taking into account the humidity, either the virtual temperature[4] or a molar mass including the water vapour contributions can be used. In this work, the molar mass of air is parameterised by [Bodhaine et al. 1999]:

$$M_m = \frac{28.95949\frac{\mathrm{g}}{\mathrm{mol}} \cdot vol\%(air)}{100} + \frac{44.01\frac{\mathrm{g}}{\mathrm{mol}} \cdot vol\%(CO_2)}{100} + \frac{18.016\frac{\mathrm{g}}{\mathrm{mol}} \cdot vol\%(vapor)}{100}. \tag{2.4}$$

The first term gives the contribution of dry air without CO_2, the second the CO_2 contribution, and the third is an additional term for water vapour in which measured values of u are put in the expression $vol\%(vapor) = (E_s \cdot u)/p$. The resulting $vol\%(air)$ is 100% $-$ $(vol\%(CO_2) + vol\%(vapor))$.

An application of equation (2.3) is the calculation of the altitude dependence of p. A good approximation for the atmosphere is the hydrostatic equilibrium model (rec. [Visconti 2001]):

$$\frac{dp}{dh} = -\rho(h)g(h) = -g(h) \cdot \frac{p(h) \cdot M_m}{R \cdot T(h)}. \tag{2.5}$$

Often the simplification of the acceleration due to gravity $g(h) \approx g$ is done and also the height dependence of T is neglected:

$$\Rightarrow p(h) = p_0 \cdot \exp\left(-\frac{M_m \cdot g}{R \cdot T} \cdot h\right). \tag{2.6}$$

For estimating the atmospheric depth, the following approximation can be found:

$$\begin{aligned} p(h_0) &\approx g \cdot \int_{h_0}^{\infty} \rho(h)dh && (2.7) \\ \xrightarrow{(1.5)} p(h_0) &= g \cdot X(h_0). && (2.8) \end{aligned}$$

Performing a fully height-dependent calculation including the latitude dependence, the expression for g can be written as (rec. [Bodhaine et al. 1999]):

$$\begin{aligned} g(\Phi, h) = g_0 &- (3.085462 \cdot 10^{-4} + 2.27 \cdot 10^{-7} \cdot \cos(2\Phi)) \cdot h \\ &+ (7.254 \cdot 10^{-11} + 1.0 \cdot 10^{-13} \cdot \cos(2\Phi)) \cdot h^2 \\ &- (1.517 \cdot 10^{-17} + 6.0 \cdot 10^{-20} \cdot \cos(2\Phi)) \cdot h^3, \end{aligned} \tag{2.9}$$

with Φ = geographical latitude, g in cm/s^2, h in m, and g_0 at sea level:

$$g_0 = 980.616 \cdot (1.0 - 0.0026373 \cdot \cos(2\Phi) + 0.0000059 \cdot \cos^2(2\Phi)). \tag{2.10}$$

---

[4] Theoretical variable for compensating the overestimation of the density while using dry air conditions instead of humid air [DWD 1987].

Based on this knowledge, the corresponding lapse rate[5] for an air parcel can be calculated. Starting point is the First Law of Thermodynamics (rec. [Boeker & van Grondelle 1997]):

$$\delta Q = c_V dT + p dV, \tag{2.11}$$

where c_V is the specific heat in a volume V and δQ is the added heat. For a rising air parcel, the mass will be constant. Regarding a unit mass, the volume written as $V = 1/\rho$ changes:

$$\begin{aligned} \Rightarrow \delta Q &= c_V dT + p d\left(\frac{1}{\rho}\right) = c_V dT + d\left(\frac{p}{\rho}\right) - \frac{1}{\rho} dp \\ &= c_V dT + R dT - \frac{1}{\rho} dp = c_p dT - \frac{1}{\rho} dp, \end{aligned} \tag{2.12}$$

using $c_p = c_V + R$ being the specific heat for constant pressure. If the ascent and descent of the air parcel is adiabatic, δQ is Zero. Still we have to distinguish two cases: dry adiabatic (no water vapour in air) and moist adiabatic air (air that contains water vapour). For the dry adiabatic case we find:

$$c_p dT = \frac{1}{\rho} \Leftrightarrow \frac{dT}{dp} = \frac{R \cdot T}{c_p \cdot p} \tag{2.13}$$

$$\overset{(2.5)}{\Longrightarrow} \quad \frac{\partial T}{\partial h} = \frac{\partial T}{\partial p} \cdot \frac{\partial p}{\partial h} = -\frac{g}{c_p}. \tag{2.14}$$

Near the Earth's surface this value amounts to 10 K/km. For the moist adiabatic case, equation (2.14) can be extended by:

$$c_p = \frac{100 - u}{100} \cdot c_{p(air)} + \frac{u}{100} \cdot c_{p(vapor)}. \tag{2.15}$$

The cooling of the air parcel while rising entails partly condensation of the water vapour. The positive evaporation heat is designated as ΔH_ν leading to:

$$\delta Q = \frac{\Delta H_\nu}{-d\omega} \Rightarrow \frac{\partial T}{\partial h} = -\frac{g}{c_p} - \frac{\Delta H_\nu}{c_p} \cdot \frac{\partial \omega}{\partial h}. \tag{2.16}$$

Thus, the moist adiabatic lapse rate is smaller than the dry adiabatic.

Vertical Structure

In addition to the zonal variation of the atmosphere, there is a vertical structure (see Fig. 2.1). A large scale separation is based on the composition of air. Up to 80 km the mean molecular mass of dry air is constant, therefore it is called *homosphere*. This region is well-mixed by permanent convection in horizontal and vertical direction. Above, in the *heterosphere*, decomposition appears as heavier atoms and molecules tend to settle at the bottom of the layer, while lighter gases float to the top. Within the homosphere, a finer distinction can be carried out. It is mainly indicated by the temperature gradient. In the *troposphere*, short-time variations occur and most weather phenomena take place. The lowest part of this layer is called *boundary layer* or *peplosphere* because it is strongly influenced by the orography[6].

---

[5] Decreasing rate of air temperature with height [Ahrens 1994].

[6] Description of the relief of a landscape.

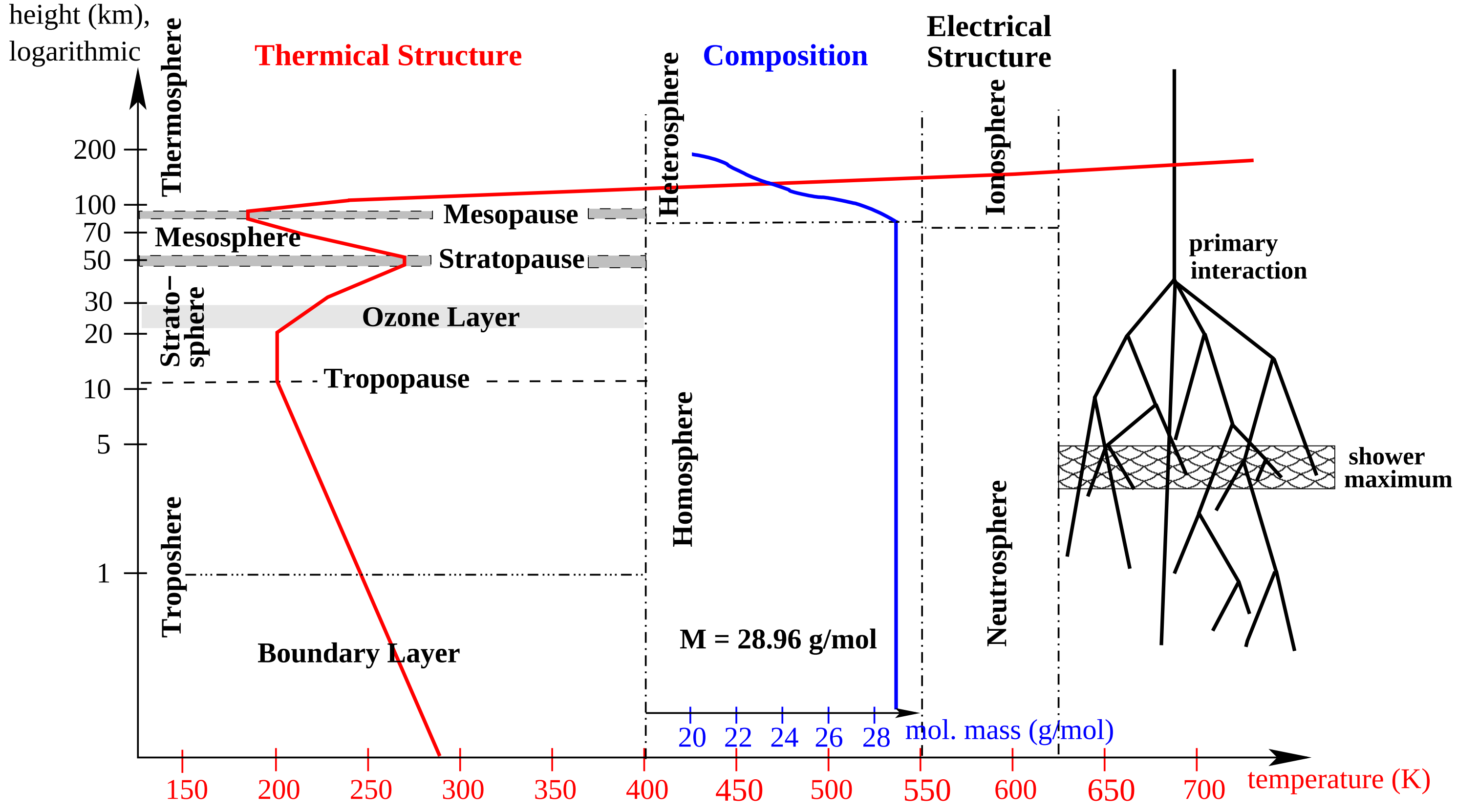

Figure 2.1: Layers of the atmosphere. The values are given for the US-StdA, nevertheless the principle devision is valid for every atmospheric condition. Rightmost, an EAS is adumbrated. Further explanations are given in the text.

The troposphere is characterised by a continuous lapse rate, which amounts to 6.5 K/km for the US Standard Atmosphere (US-StdA) [US-StdA 1976], (rec. [Kraus 2000]). A detailed description of the US-StdA will be given in 2.2. The boundary separating the troposphere from the *stratosphere* is called *tropopause*. Within this region, the temperature stays roughly constant, although the lower altitude for the tropopause varies depending on the latitude. Around the equator, the lower limit is highest (16 - 17 km) and goes down towards the poles to 8 - 9 km. Consequently, the temperature in the tropopause also depends on latitude. It is only -45°C at the poles but ≈ -75°C around the equator (rec. [Weischet 1977]). The temperature increases slowly in the stratosphere due to chemical processes activated by solar UV light:

$$\mathrm{O}_2 + h\nu(\lambda < 240\ \mathrm{nm}) \rightarrow \mathrm{O} + \mathrm{O} \tag{2.17}$$

$$\mathrm{O} + \mathrm{O}_2 + Y \rightarrow \mathrm{O}_3 + Y. \tag{2.18}$$

The Y represents a further molecule, e.g. N_2, which is necessary for the energy and momentum conservation (rec. [Roedel 1992]). The produced O_3 is a strong absorber for radiation between 200 and 300 nm protecting us from dangerous solar radiation. The main production region for O_3 is indicated in Fig. 2.1 as the ozone layer. The stratosphere reaches up to nearly 50 km and continues to the *stratopause* where the remaining pressure is only about 1 hPa. In the adjacent *mesosphere*, the temperature decreases similarly to the troposphere and the absolute temperature minimum of the atmosphere is at 90 - 100 km (*mesopause*). In the *thermosphere*, solar ultraviolet radiation is strongly absorbed, particularly by molecular and atomic oxygen, warming the air rapidly. Thus, the achieved temperature is strongly affected by the solar activity cycles [Ahrens 1994].

Variations of the State Variables

The temperature is the most important variable showing a daily and annually periodic cycle. It is strongly correlated with the relative humidity assuming a constant value for the absolute humidity (rec. [Malberg 2002]). Firstly, the course during the day is discussed. The lowest temperature of a day is reached early in the morning shortly after sunrise. During the morning, the temperature increases quite fast. The rate becomes lower around noon and the maximum temperature is ≈ 2 h after the sun has reached its highest point (rec. [Ahrens 1994]). Then the temperature decrease is again fast until evening, slow down during night. This daily specific variation is often distorted by local wind systems or moving fronts[7]. The course of the relative humidity is inverse to the temperature because warm air is able to contain more water vapour than cold air. The daily variation of the relative humidity is therefore only affected by the temperature dependence of the saturation pressure E_s. The air pressure shows almost no daily variation. It is characterised by high (anticyclones) and low pressure areas (cyclones). On very calm days with high pressure conditions, a double wave with an amplitude of only 2 hPa can be measured. All these courses are valid in each season, however being most pronounced on clear summer days.

For discussing annual variations, the data of each day are averaged and afterwards again averaged to monthly mean values. The consequences are the known seasons, not reviewed here in detail. Some effects are pointed out for Argentina in Chapter 2.3.

---

[7] Transition zone between two air masses of different densities most often caused by temperature differences (rec. [Ahrens 1994]).

2.2 Atmospheric Models

As discussed above, the atmosphere is a complex system suffering several changes with time. Therefore, general parameters and values are needed for comparable calculations including atmospheric effects. The World Meteorological Organization has derived a definition of a standard atmosphere:

> *"... A hypothetical vertical distribution of atmospheric temperature, pressure and density which, by international agreement, is roughly representative of year-round, mid-latitude conditions. Typical usages are as a basis for pressure altimeter, calibrations, aircraft performance calculations, aircraft and rocket design, ballistic tables, and mete(o)rological diagrams. The air is assumed to obey the perfect gas law and hydrostatic equation which, taken together, relate temperature, pressure and density with geopotential. ..."* [US-StdA 1976]

Underlying these words, the U.S. Committee on Extension to the Standard Atmosphere (COESA) established the *U.S. Standard Atmosphere, 1976* (US-StdA), with tables and graphs extending to 1000 km in altitude. It is a revision of the U.S. Standard Atmosphere, 1962, also inaugurated by COESA. The portion of these two atmospheric models are, up to 32 km, identical with the International Civil Aviation Organization (ICAO) 1964 "Manual of the ICAO Standard Atmosphere" and the International Standards Organization (ISO) Standard Atmosphere 1973. COESA has been established in 1953 and consists nowadays of 30 U.S. organisations representing government, industry, research institutions, and universities [NSSDC].

For studying the effects of annual variations on the EAS development and their detection, two further atmospheric models are chosen. They represent quite extreme mid-latitude (European) summer and winter constellations, as measured by the Deutscher Wetterdienst [DWD]. A comparison of the temperature and pressure profiles for the three, further on nominated as "standard", atmospheres within the troposphere are given in Figs. 2.2 and 2.3. The formulas used to obtain these numbers and also for the density are given in Appendix A. Some values of the different models are summarised in Table 2.2. The chosen summer atmosphere

Table 2.2: Comparison of the three standard atmospheric models.

	US Standard (US-StdA)		
	Pressure (hPa)	**Temperature** (K)	**Atmos. Depth** (g/cm^2)
0 km	1013.3	288.2	1036.1
1.4 km	856.0	279.0	875.5
	Summer (AT822)		
	Pressure (hPa)	**Temperature** (K)	**Atmos. Depth** (g/cm^2)
0 km	1011.7	302.0	1025.5
1.4 km	861.4	292.0	871.6
	Winter (AT223)		
	Pressure (hPa)	**Temperature** (K)	**Atmos. Depth** (g/cm^2)
0 km	1022.9	269.6	1044.6
1.4 km	854.5	258.8	871.9

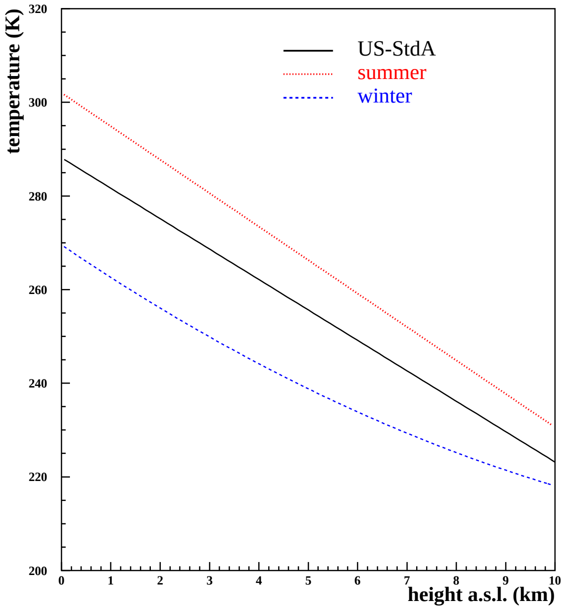

Figure 2.2: Temperature profiles for the standard atmospheres up to 10 km a.s.l.

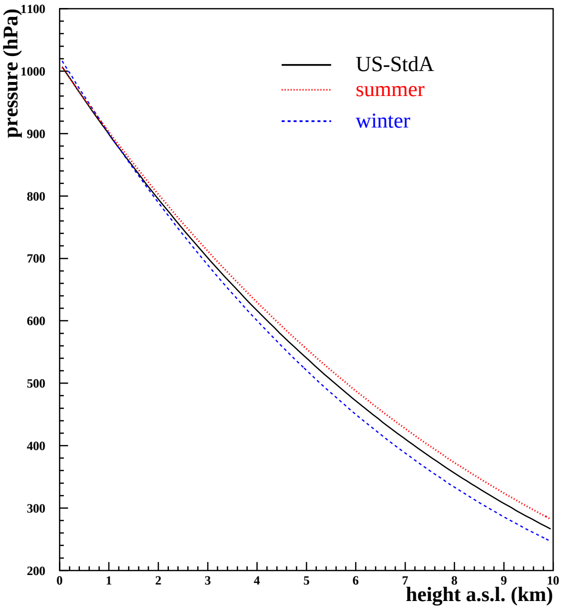

Figure 2.3: Pressure profiles for the standard atmospheres up to 10 km a.s.l.

(AT822) was measured on August 22nd, 1993, and the winter atmosphere (AT223) on February 23rd, 1993, in Stuttgart, Germany. Since the Auger Observatory is situated on a plain around 1.4 km a.s.l., the most important observables are also itemised for that height. At sea level, the relative pressure difference for summer to the US-StdA is -0.2% and for winter +1%. At 1.4 km height the differences are inverse, here the summer value exceeds by +0.6% and the winter value by -0.2% the US-StdA. Calculating the atmospheric depth using equations (2.3) and (1.5), a height dependence visualised in Fig. 2.4 is obtained. For emphasising the annual variations of this quantity, the differences according to the US-StdA are plotted in Fig. 2.5. The largest discrepancy between summer and winter occurs at heights from 4 to 10 km a.s.l. reaching a ΔX of ap-

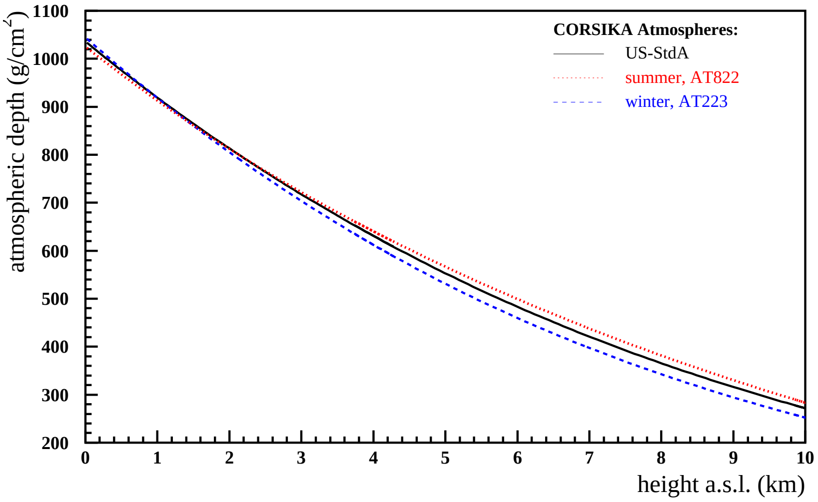

Figure 2.4: Atmospheric depth profiles for the standard atmospheres up to 10 km a.s.l.

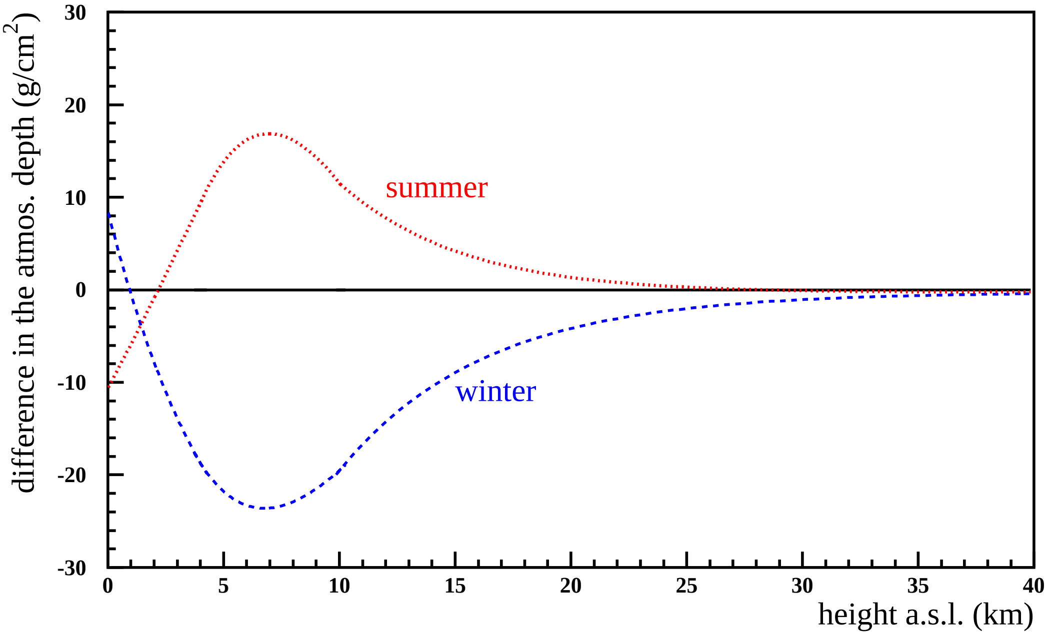

Figure 2.5: Difference in the atmospheric depth in g/cm^2 from the summer / winter atmosphere to the US-StdA.

proximately 40 g/cm^2. At heights around 8 km a.s.l., a 10^{19} eV EAS with 60° inclination reaches its maximum. The smaller the inclination angle of an EAS is, the deeper it penetrates in the atmosphere. At around 3 km a.s.l., the position of the shower maximum is situated for the vertical case. The simulation of the EAS is done with CORSIKA where the atmosphere is represented by the atmospheric depth profile. The atmospheric depth is fitted up to 112.8 km a.s.l. taken here as the upper limit of the atmosphere [Heck et al. 1998]. Up to 100 km a.s.l., the profile is divided into four layers parameterised by

$$X(h) = a_i + b_i \mathrm{e}^{-h/c_i} \tag{2.19}$$

and in the fifth layer the atmospheric depth decreases linearly with height

$$X(h) = a_5 - b_5 \frac{h}{c_5}. \tag{2.20}$$

The US-StdA is parameterised according to *J. Linsley* and also the European standard atmosphere can be chosen within the simulation code [Ulrich et al. 1997]. The values for the parameterisations are listed in Appendix B.

2.3 Conditions in Argentina

Argentina is the second largest country in South America covering an area of 2.78 Mio. km^2. Its expansions range from 22°S to 55°S and from 57°W to 74°W. Therefore, several climate zones can be found within this country. The Auger Observatory is being built in the province Mendoza, near the city Malargüe around 100 km east of the Andes Cordilleras. The *Köppen* climate classification for that landscape is given by **BS** and **BW**. The **B** stands for dry climates, subdivided into **BS** - semi-arid or steppe and **BW** - arid desert. For each region, the dry/humid boundary is calculated based on the mean annual temperature. If the mean annual precipitation in a region is below that boundary value, it belongs to **B**. The corresponding formulas, which *Köppen* found empirically, are [Müller 1987]:

$$N = 2 \cdot (T + 14), \text{ using for dry winter - most rain falls during summer} \tag{2.21}$$

$$N = 2 \cdot T, \text{ using for dry summer - most rain falls during winter} \tag{2.22}$$

$$N = 2 \cdot (T + 7), \text{ using for rain falls regularly during the year.} \tag{2.23}$$

Here, T is the mean annual temperature in °C and N the mean annual precipitation in cm. The subdivision between **BS** and **BW** is fixed at one-half of the dry/humid boundary. Figure 2.6 shows the corresponding climatologic diagram. The data have been obtained at the airport of Malargüe and are mean values of the years 1971 - 1980. The annual variations of the temperature are comparable with mid-latitude conditions even though the province Mendoza belongs to the subtropics or warm temperate zone. Maps of isotherms for summer and winter of a part of South America are given in Figs. 2.7 and 2.8. The complicate structures of the isotherms near the Andes are due to the *mountain mass effect* or *mass elevation effect*. Large mountain systems create their own surrounding climate. They serve as elevated heat islands where solar radiation is absorbed and transformed into long-wave heat energy, resulting in much higher temperatures than those found at similar latitudes in the free air.

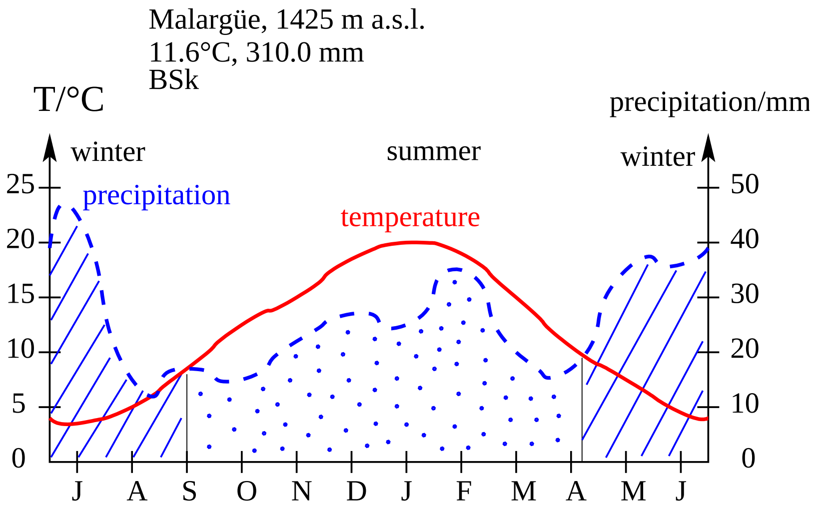

Figure 2.6: Walther Lieth Diagram for Malargüe. The data are taken at the airport, 35.3°S, 69.35°W, 1425 m a.s.l. (Courtesy of W. Endlicher).

More interesting concerning cosmic ray experiments are the pressure conditions (compare equation (2.8)). This annual variation for South America can be seen in Figs. 2.9 and 2.10.

Despite this typical annual variations of the atmospheric conditions in Argentina or more generally in South America mentioned above, the region is affected by the spacious

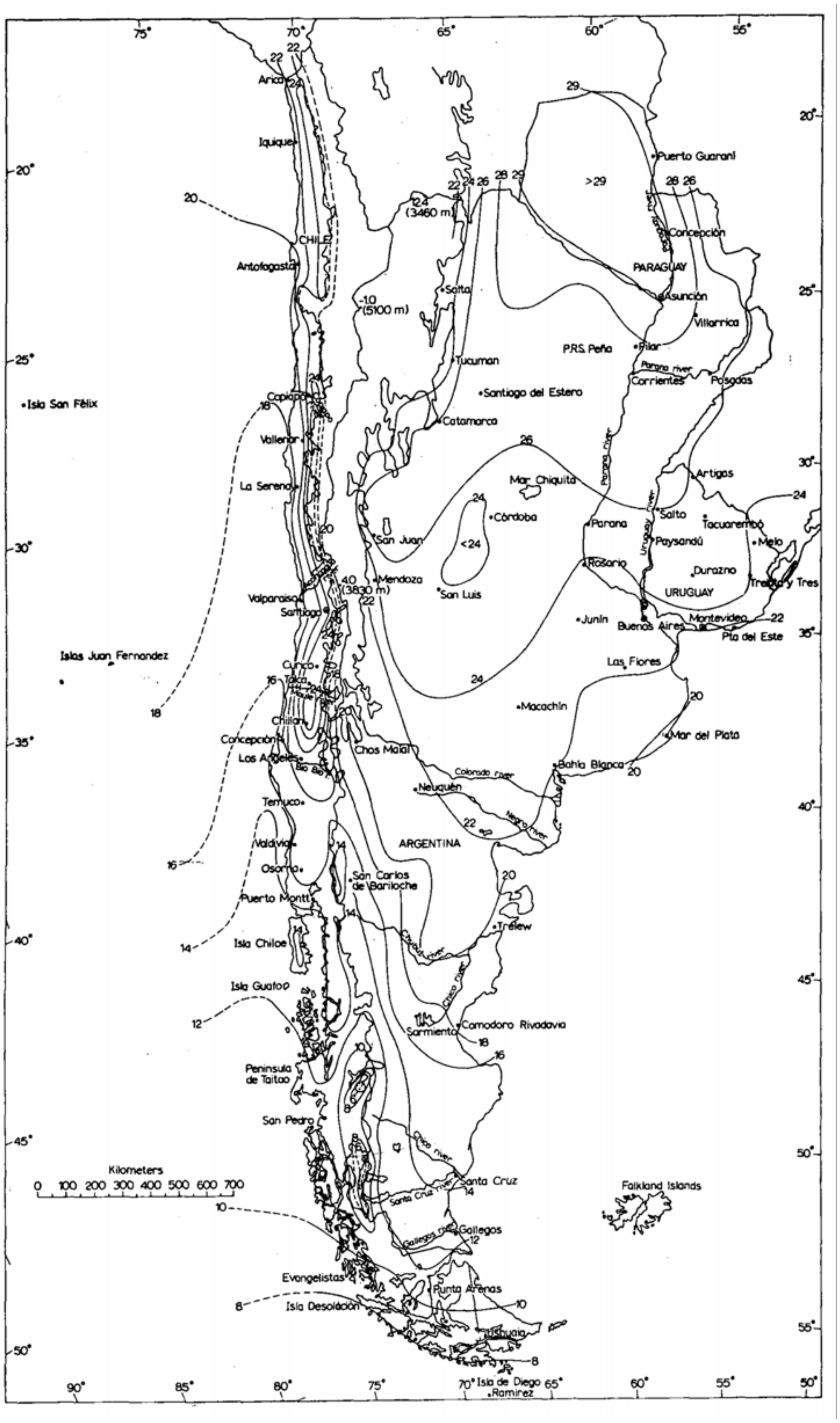

Figure 2.7: January isotherms in °C for South America [Schwerdtfeger 1976].

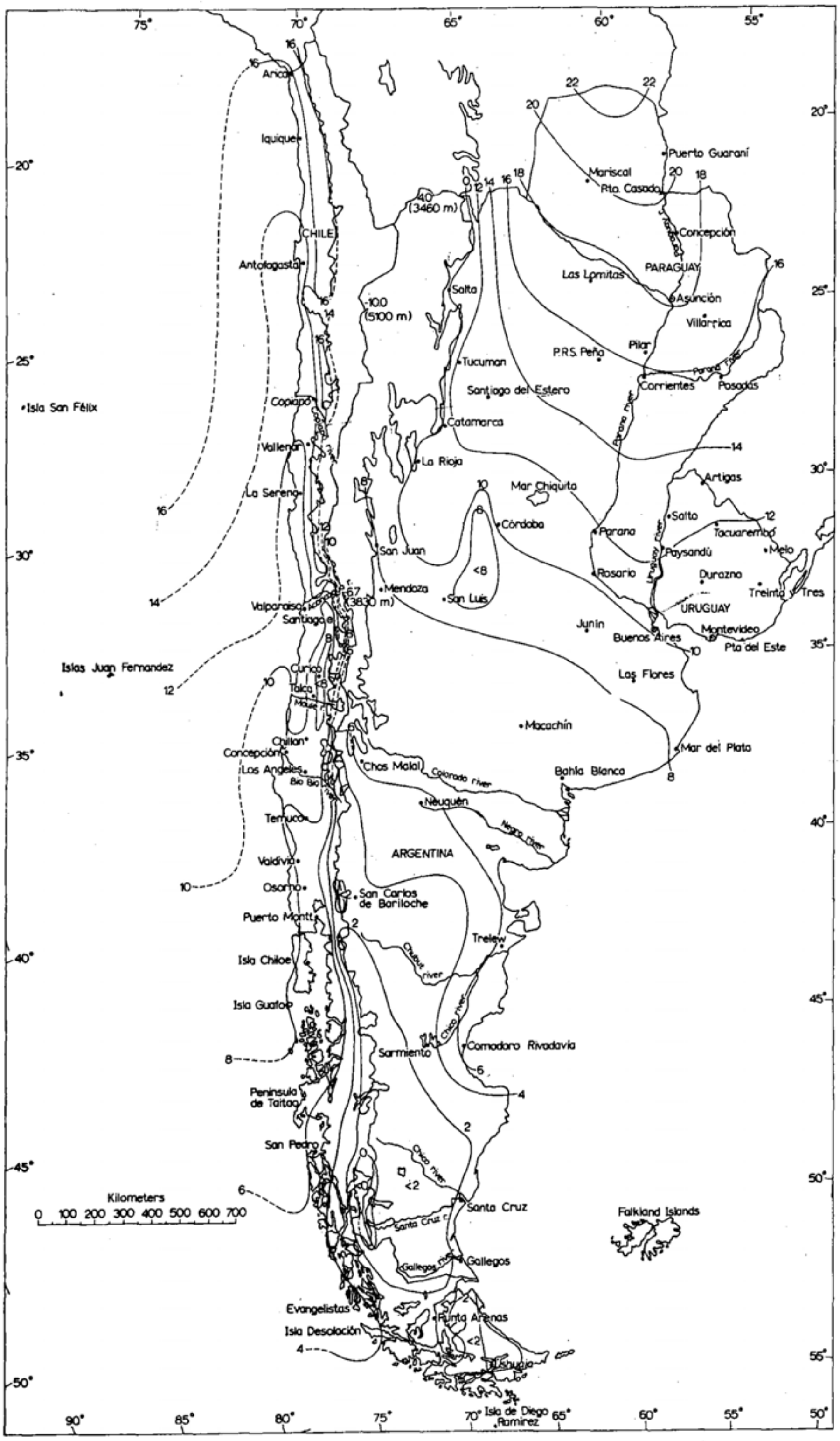

Figure 2.8: July isotherms in °C for South America [Schwerdtfeger 1976].

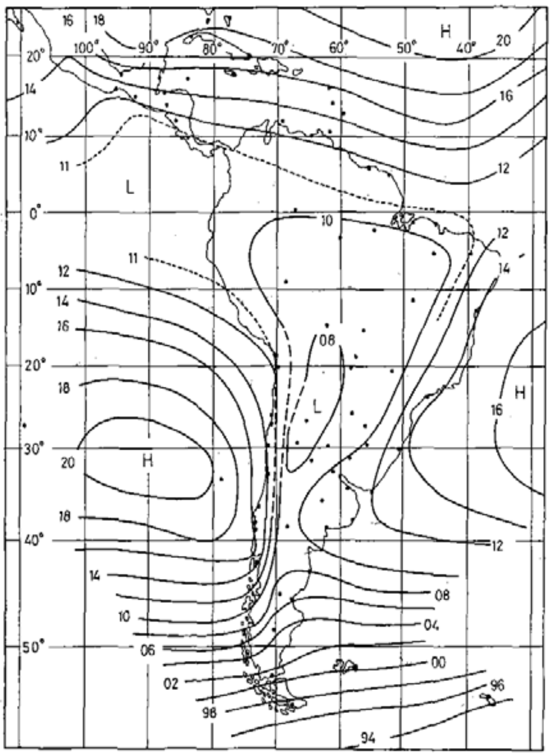

Figure 2.9: Summer isobars for South America. The values are reduced to sea level and average of the three months December - February. 20 = 1,020 hPa [Schwerdtfeger 1976].

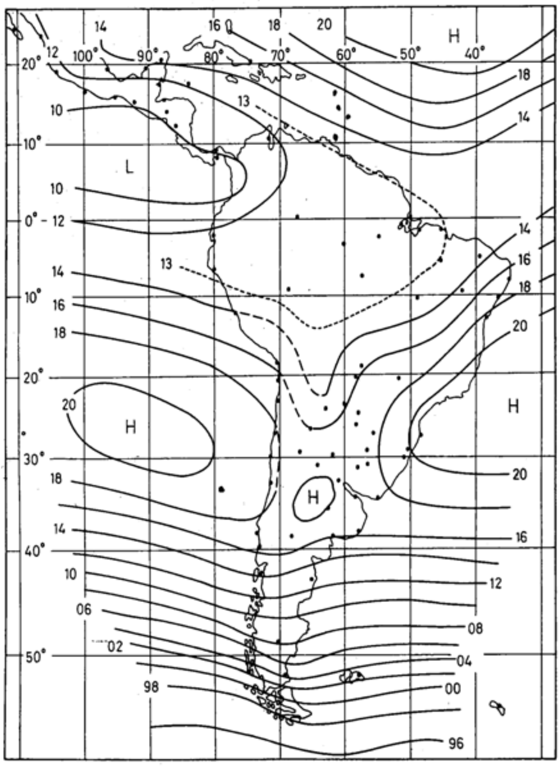

Figure 2.10: Winter isobars for South America. The values are reduced to sea level and average of the three months June - August. 96 = 996 hPa [Schwerdtfeger 1976].

ENSO phenomenon. ENSO is standing for *El Niño-Southern Oscillation* describing the sustainable breakdown of the *Walker circulation* and the sea currents in the Pacific ocean [Endlicher et al. 1988/89]. The oceanic and atmospheric components are sketched in Figure 2.11 for a "normal" year in the upper plot and for an El Niño episode in the lower. In intervals of about 3 up to 8 years, the air pressure above southeast Asia and west Pacific ocean increases for unknown reasons while it decreases above the east Pacific ocean. Thus, the southeast *trade winds* abate nearly entirely which normally "push" the surface water of the *Humboldt current* from South America towards Indonesia [Baldenhofer 2001]. The system of ocean and atmosphere gets into a positive feedback. The weakening of the trade winds leads to higher sea surface temperatures and also to an increased sea level in the east Pacific ocean and vice versa while the sea surface temperature and the sea level decrease in the west Pacific ocean. The intensity may vary however the symptoms exceed those of the annual weakening of the trade winds during southern summer above the southeast Pacific ocean. Such an El Niño episode may continue for several months.

The counterpart of the El Niño is the La Niña effect. It may appear directly after an El Niño but not necessarily. La Niña has a periodic appearance every 3 to 5 years and continues for 9 - 12 months, sometimes even 2 years. During this episode, the sea surface temperatures in east and central Pacific ocean are even lower than during the normal situation. In the

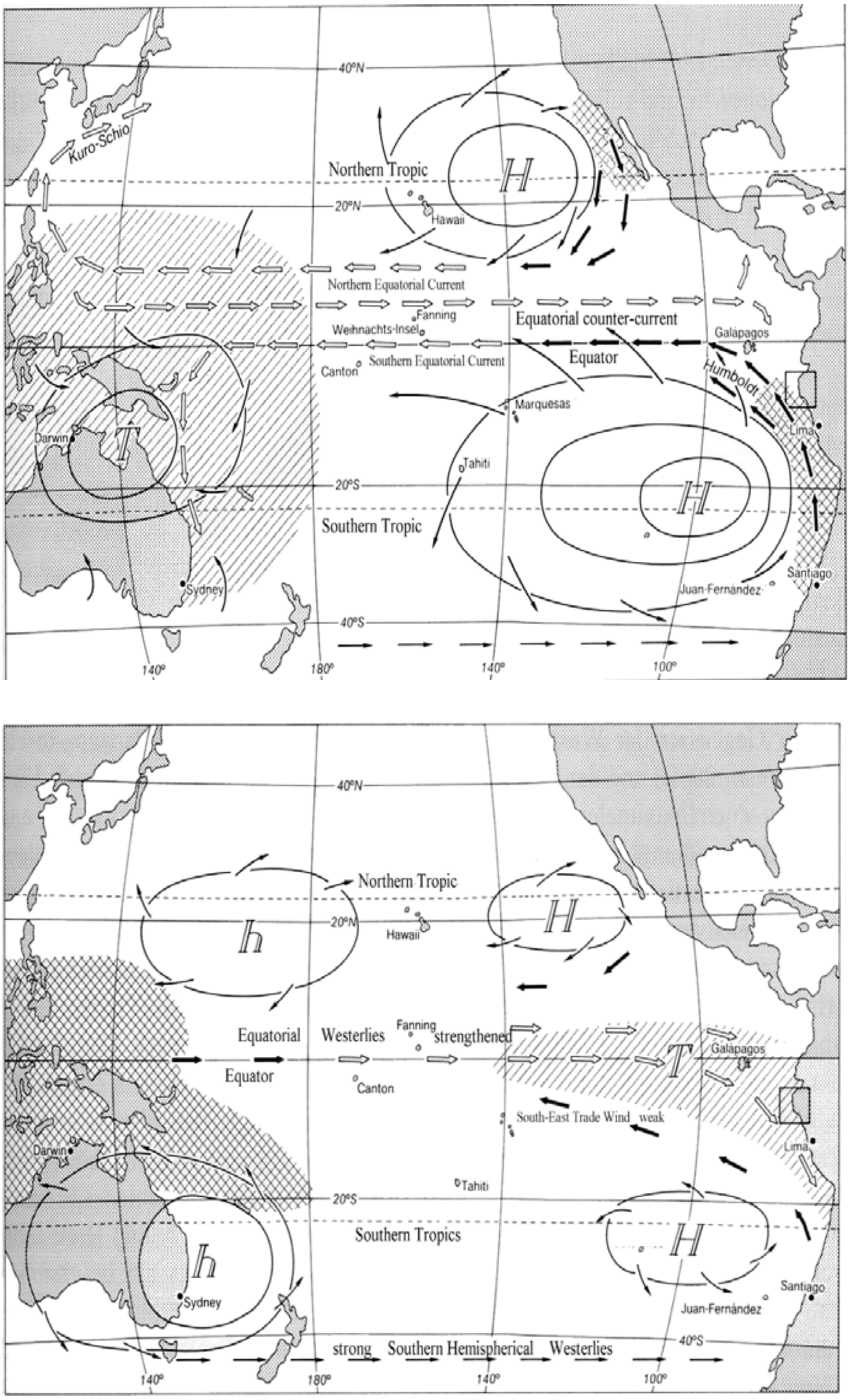

Figure 2.11: Oceanic and atmospheric circulation in and above the Pacific ocean in "normal" years (upper part) and during a ENSO episode (lower part). After [Endlicher et al. 1988/89].

tropic west Pacific ocean, the sea surface temperatures tend to higher values than usually. At the same time, the air pressure above Indonesia and North America is lower while it is increased above the east Pacific ocean.

For quantifying the intensities of the effects, a *Southern Oscillation Index* (SOI) has been introduced. The air pressure is measured at least above the Eastern Islands and Darwin (north Australia). The deviation of its difference (east minus west) from the many years mean values reflects the index. In Figure 2.12, the data of the last three years are shown. A positive SOI indicates low pressure in West (north Australia and Indonesia) and higher values in East (South America). Thus, large positive amplitudes are correlated to the La Niña episode and large negative amplitudes to El Niño. It can be seen that the amplitudes during these years are not very pronounced inducing only small ENSO effects. For a real El Niño or La Niña, the absolute value of SOI exceeds 20. Thus for Argentina, east of the Andes, the effects in terms of changed pressure conditions should be quite small. However, a significant chance of the conditions between August 2002 and July / August 2003, the dates of our first and fifth measurement campaign (see Chapter 4), has been observed.

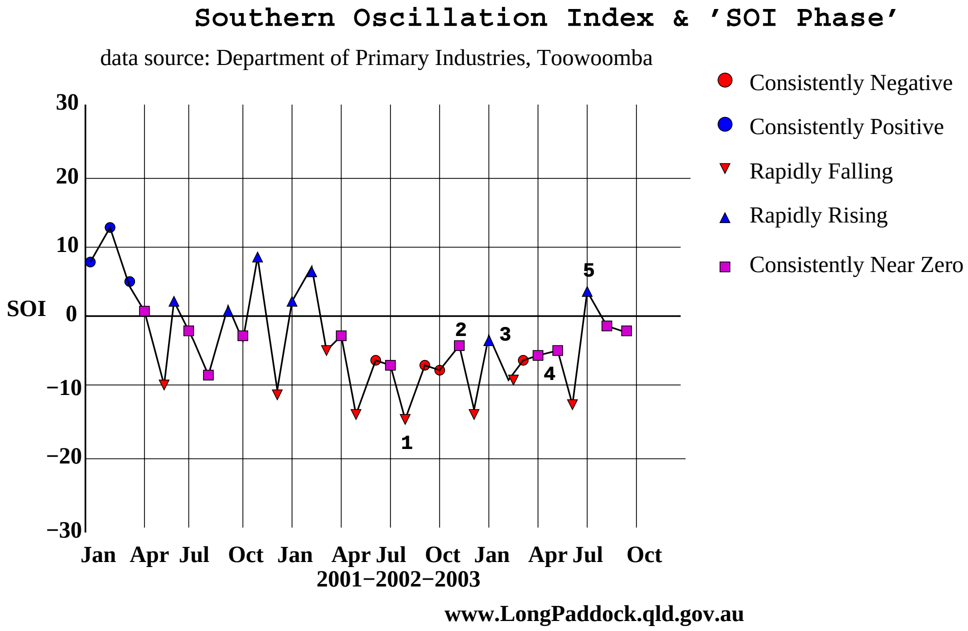

Figure 2.12: Southern Oscillation Index and Phase of the years 2001 - 2003. The numbers given next to the graph represent the radio soundings campaigns performed in Argentina, see Chapter 4. After [Queensland 2003].

Chapter 3

Atmospheric Influences on the EAS Development and Detection

The atmospheric conditions can mainly be described by temperature, pressure, and density profiles. These variables alter the development and detection of EAS.

The first concern is the interaction of the particles within the EAS and the atmosphere. According to the amount of traversed matter, the processes of collision and decay in the EAS cascade counteract. This behaviour can be described by the atmospheric depth being the integral of the air density profile (Chap. 1.2). However, the use of fluorescence telescopes for observing EAS stresses the geometrical aspects. The transformation from atmospheric depth to geometrical height is given by equation (1.5). The third point is the emission of fluorescence light. It is also density dependent but furthermore the temperature influences the amount of emitted photons. The last part deals with the transmission of the fluorescence photons towards the telescopes. On this way, the photons suffer absorption and scattering by the atmospheric molecules and aerosols.

The four aspects of the role of the atmosphere for EAS development and detection are now discussed in detail.

3.1 Shower Simulation and Longitudinal Development

A powerful tool for simulating EAS is the Monte Carlo code CORSIKA [Heck et al. 1998]. It generates shower cascades in the Earth's atmosphere initiated by photons, hadrons, or nuclei. The program is able to treat 50 different elementary particle types like γ, $e^{\pm}$, $\mu^{\pm}$, π^0, $\pi^{\pm}$, $K^{\pm}$, $K^0_{S/L}$, η, baryons with the corresponding anti-baryons, some resonance states, and the corresponding anti-baryonic resonances. Each particle above an adjustable energy (cut-off energy) is tracked individually. For this study the hadronic interaction model QGSJET01[1] [Kalmykov et al. 1997] and the electromagnetic interaction model EGS4[2] [Nelson et al. 1985]

---

[1] **Q**uark **G**luon **S**tring model with **JET**s version of the year 20**01**, based on exchanging supercritical Pomerons.

[2] **E**lectron **G**amma **S**hower version **4**, provides detailed information on momentum, space coordinates, and propagation time for all electromagnetic particles.

is used. CORSIKA delivers not only average numbers of the observables, it also describes the intrinsic shower-to-shower fluctuations. The mean free path of a particle is determined based on the cross section for a hadronic reaction, the atmospheric density along the flight path, and the decay probability. The decay length and the interaction length for each particle are calculated independently at random. The shorter one is taken as the actual path length, which includes the decision whether a particle decays or interacts. For stable particles, only the interaction length is acquired. In addition to the atmospheric density, also the atmospheric composition is defined in CORSIKA. The gas mixture is set to 78.1% N_2, 21.0% O_2, and 0.9% Ar of volume.

However, Monte Carlo codes like CORSIKA imply a number of systematic uncertainties. The first problem is the limited knowledge of the hadronic interactions. The parameters, e.g. cross sections, are derived from accelerator experiments. Compared to EAS, energies reached at man-made accelerators are small. Thus, the simulation programs have to extrapolate the measured information to higher energies, without knowing the exact dependences. Furthermore, existing collider experiments cannot detect particles in extreme forward direction. These are lost in the beam pipe, but carry the largest fraction of energy and thus represent the most important particles in the EAS development. This leads to uncertainties in the shower prediction. Another problem in Monte Carlo codes is the large number of secondary particles produced, especially for showers with $E_0 > 10^{16}$ eV. The computing time becomes excessive and one has to use *thin sampling*. The idea is to adopt the same technique used by the EAS detection (rec. [Knapp 1997]). The large amount of secondary particles at ground are spread over wide areas. The real detector area is comparatively small and only a statistical sample of the shower particles is registered. Applying thin sampling for simulating the showers, also a statistical sample is produced which is sufficient to conclude to the entirety. The procedure can be steered by a thinning level $\varepsilon_{th} = E/E_0$, adjusting the fraction of the primary energies below which not all particles are tracked separately anymore. After an interaction, only one secondary particle is followed if the energy sum of all j secondary particles in an interaction falls below the thinning energy

$$\varepsilon_{th} E_0 > \sum_j E_j. \tag{3.1}$$

The selection probability is

$$p_i = E_i / \sum_j E_j \tag{3.2}$$

while all other particles are discarded. For conserving the particle number and energy, the chosen particle is weighted with $w_i = 1/p_i$. The values can be set independently for electromagnetic and hadronic interactions. A further steering option is a weight limit. Particles exceeding this value are no longer subjected to the thinning algorithm. For the following simulated EAS an $\varepsilon_{th} = 10^{-4}$ is selected being an optimised value for achieving reasonable computing times and artifical fluctuation in the EAS development [Risse & Heck 2002]. The weight factor is also limited following the concept of “optimal thinning” [Kobal 2001].

The output of the simulation are detailed tables of particle numbers and their energy as well as the amount of energy deposited in the atmosphere. These data are available for a selectable step size, in this work a step size of 5 g/cm^2 is chosen. In the particle tables γ, $e^\pm$, $\mu^\pm$, hadrons, $\sum$(*all charged*), $\sum$(*nuclei*), and optional Cherenkov-photons are listed

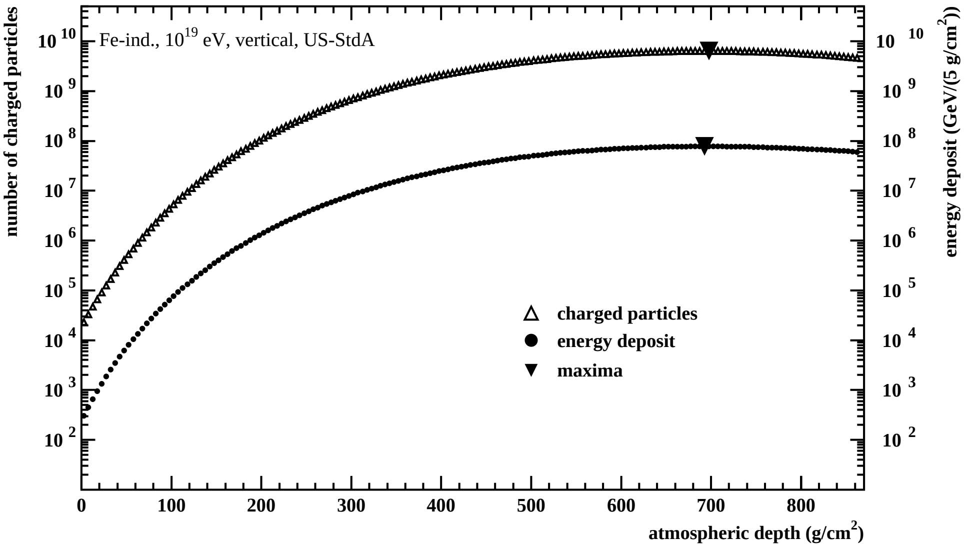

Figure 3.1: Average of the longitudinal shower development for 100 iron induced showers. The upper line represents the number of charged particles, the lower the energy deposit.

separately. For the energy deposit, several types of energy losses are distinguished. γ, $e^{\pm}$, $\mu^{\pm}$, and hadrons falling below the cut-off energy are not totally lost. Their energy is tabulated, just as the energy of those particles rejected by angular cuts (only particles with zenith angles $\lesssim 90^\circ$ are tracked). The losses due to ionisation are calculated by the Bethe-Bloch formula. In Fig. 3.1, the average of the longitudinal development of 100 iron induced, 10^{19} eV showers with vertical inclination is shown. The upper curve represents the number of charged particles in the shower. Nearly 10^{10} particles are created at the shower maximum which is reached at about 700 g/cm^2. After the shower maximum, the shower size decreases slowly and $\approx 5\times10^9$ particles arrive at the Auger level at around 840 g/cm^2. The lower curve reflects the energy deposit given in GeV/(5 g/cm^2). This development is very similar to the particle number and the maximum according to the energy deposit is reached at nearly the same height. In the following, the shower characteristics are discussed based on the energy deposit. Assuming a proportionality between energy deposit and fluorescence yield, the former one is the simulation quantity being of interest to the observable of the fluorescence telescopes of the Pierre Auger Observatory.

The ionisation losses of $e^{\pm}$ and the energy of those falling below the cut-off contribute with $\approx$ 99% to the energy deposit, see Fig. 3.2. Muons and hadrons play a minor role.

The shower-to-shower fluctuations are mainly caused by the height of first interaction of the cosmic ray with the atmospheric nuclei. The deeper a cosmic ray penetrates into the atmosphere before interacting, the later the shower develops and also the maximum is reached deeper in the atmosphere. The other extreme case are cosmic rays which interact very high up in the atmosphere. These showers develop earlier and especially the contributing electromagnetic part of the shower has diminished out at ground. The range of fluctuations can be illustrated by the behaviour of the position of the shower maximum, Fig. 3.3. The maximal variation of the shower maximum position of p-induced showers is larger than for Fe-induced ones and amounts to 130 g/cm^2 compared to 40 g/cm^2 for $E_0 = 10^{19}$ eV. This

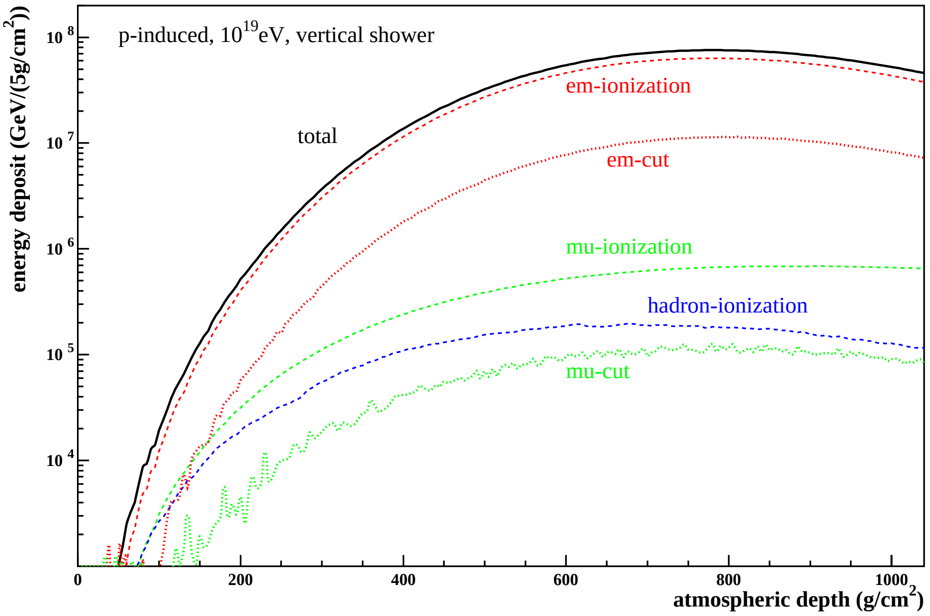

Figure 3.2: Contributions to the total energy deposit, shown for the average of 100 proton induced showers at 10^{19} eV with vertical incidence.

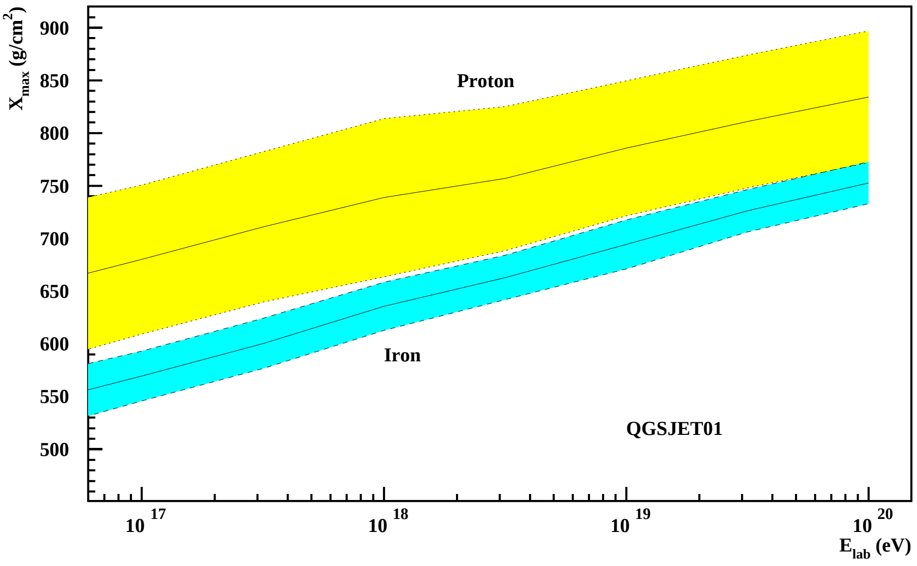

Figure 3.3: Shower-to-shower fluctuations described by the position of the shower maximum for increasing E_0. For the p-induced showers 500 simulations are performed and for the Fe-induced 200. The bands are correlated to one standard deviation (Courtesy of J. Knapp).

number decreases slowly with increasing primary energy of an EAS. However, for the investigation of atmospheric effects, the consideration of the average energy deposit is sufficient. As mentioned in Chap. 1.2, the longitudinal development of the shower size can be calculated by the Gaisser-Hillas formula, equation (1.6). This formula can also be applied to the energy deposit [Knapp & Heck]:

$$\frac{dE}{dX}(X) = \left.\frac{dE}{dX}\right|_{max} \cdot \left(\frac{X - X_0}{X_{max} - X_0}\right)^{\frac{X_{max}-X_0}{a+bX+cX^2}} \cdot e^{\frac{X_{max}-X}{a+bX+cX^2}}. \tag{3.3}$$

For the following analyses, 100 iron induced showers with $E_0 = 10^{19}$ eV have been simulated. The average shower development by the energy deposit can be compared for different atmospheres, in doing so the energy deposit is obtained by equation (3.3). In Fig. 3.4, examples of vertical showers and $\Theta = 60°$ inclined showers are presented for the three chosen standard atmospheres. For the inclined showers, also the vertical atmospheric depth is given at the abscissa and not the slant depth, which is defined as $X/\cos\Theta$. The variations caused by the atmospheres are hardly visible. In Figure 3.5, the US-StdA is chosen for performing a comparison between 60° inclined showers vs. slant depth and vertical showers vs. vertical depth. However, it should be mentioned that for vertical showers the slant depth is the same as the vertical depth. The variations caused by changed incidence of the EAS are also quite small.

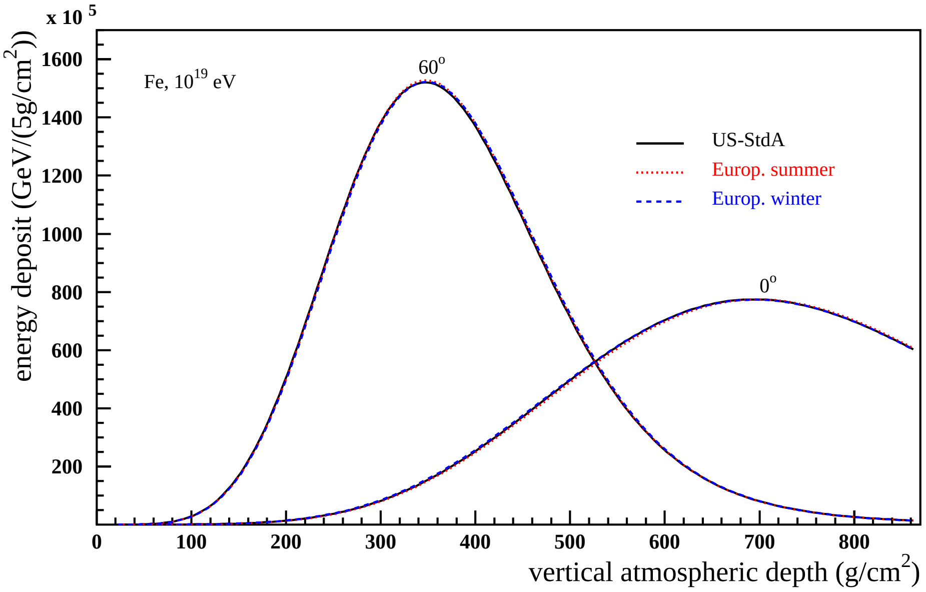

Figure 3.4: Longitudinal shower development of the energy deposit for three different atmospheres. Inclined showers reach their maximum higher in the atmosphere than vertical, both shown as a function of vertical atmospheric depth. Therefore the amount of energy deposit is larger for inclined showers, because they traverse more matter per each vertical 5 g/cm^2.

In Figures 3.6 and 3.7, the corresponding relative differences are plotted. The variations due to changing seasons are small, less than 2%. Around the shower maxima and deeper towards the ground, the fluctuations due to different atmospheres are even < 1%. Higher up in the atmosphere, the vertical showers show larger fluctuations than the inclined because they are at an earlier development stage. The comparison between vertical and 60° inclined EAS in one atmosphere are also less than 2%.

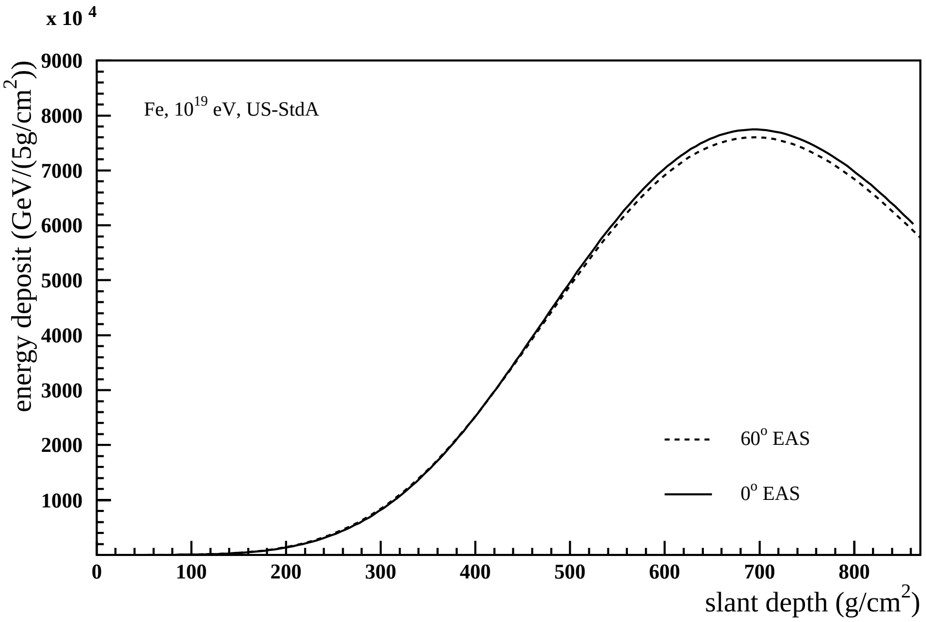

Figure 3.5: Longitudinal shower development for the energy deposit in the US-StdA for a vertical and 60° inclined shower. Both showers are plotted vs. slant depth.

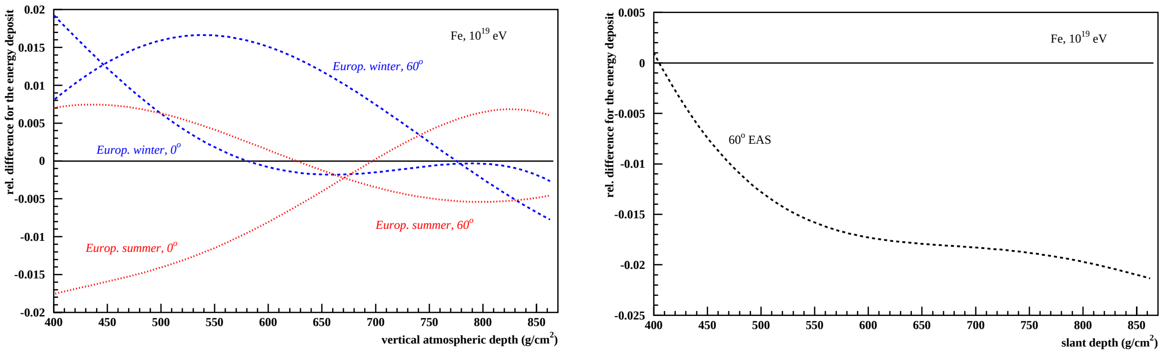

Figure 3.6: Relative differences for the energy deposit simulated in European summer and winter atmospheres for Fe-induced, 0° and 60° inclination according to the corresponding US-StdA.

Figure 3.7: Relative difference for the energy deposit simulated in the US-StdA of the 60° inclined shower vs. slant depth to the same shower with vertical incidence.

These results fit to the introduced image of the EAS development. The decisive factor is the amount of traversed matter, given as the slant depth. This value is independent of different density distributions in air induced by the seasons or different paths in case of slant incidence. Only small influences caused by atmospheric variation can be found due to a changed ratio of decay and interacting probabilities. For simulating which process will happen, the mean free paths are extracted from the atmospheric depth, thus converting X to geometrical heights h which is not independent of the density distribution. Concluding for further simulations, it can be stated that simulations of EAS in the US-StdA is sufficient. The atmospheric dependences can be inserted at subsequent steps.

3.2 Transformation from Vertical Atmospheric Depth to Geometrical Height

The Auger fluorescence telescopes detect the longitudinal shower development within a fixed field of view. The visible height range depends on the distance of the shower to the telescope and is given for several values in Fig. 3.8.

To estimate the geometrical features of EAS images, the simulated shower profiles have to be transformed from a description based on vertical atmospheric depth to geometrical height. The relation between these two was already shown in Chap. 2.2. Applying the transformation to the longitudinal energy deposit profiles, the influence of different atmospheres becomes obvious. The first set of plots (Figs. 3.9 and 3.10) are given for iron induced, 10^{19} eV, showers with vertical incidence. The shower profiles are distorted, mostly in the range between 4 and 10 km. This confirms the expectation that the largest difference between the atmospheric profiles of summer and winter occurs at those heights (compare Fig. 2.5). The position of the shower maximum, which indicates the type of the primary particle, is only slightly affected. For this vertical case, the maximum is reached in average at 694.3 g/cm^2 which is 3.260 km a.s.l. in the US-StdA. The same atmospheric depth corresponds to 3.327 km (+67 m to the US-StdA) in the summer and at 3.099 km (-161 m to the US-StdA) in the winter atmosphere. Detecting such a shower with the Auger fluorescence telescope, the pixel resolution has to be taken into account. Each pixel has a field of view of 1.5° which can be assumed as a very conservative estimate for the resolution. This resolution is only given by the detector geometry. No time information of the PMT pulses is taken into account for this rough estimation on the resolution. The closest distance at which the shower maximum of $\approx$ 700 g/cm^2 can be detected is 5.28 km. The pixel, which has that maximum in its field of view, covers a height range of 190 m. The vertical difference in the shower maximum between

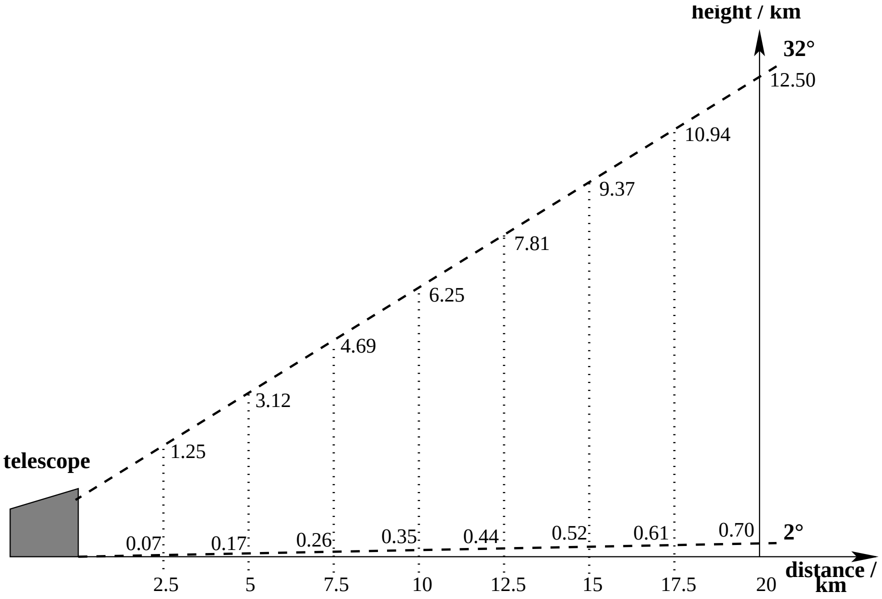

Figure 3.8: Telescope field of view from 2° up to 32° above horizon.

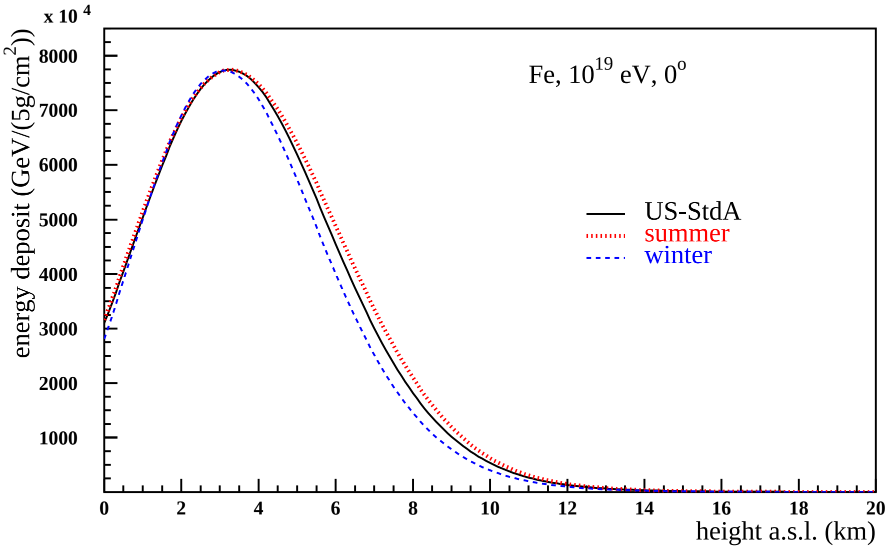

Figure 3.9: Longitudinal development of the energy deposit vs. height in km for Fe-induced, vertical showers.

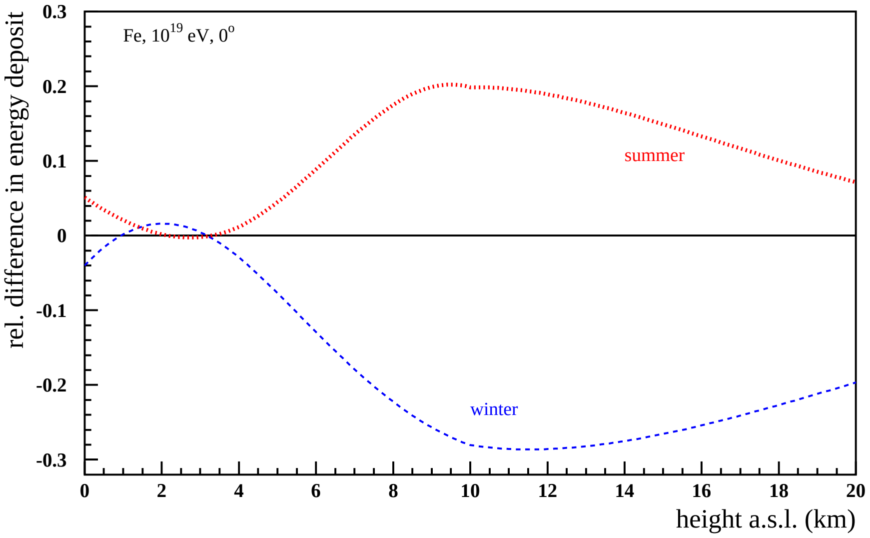

Figure 3.10: Relative differences of the energy deposits between the summer / winter atmosphere and the US-StdA for Fe-induced, vertical showers.

summer and winter amounts to 228 m. Thus, the "same" maximum will be detected during summer with a different pixel than during winter. For larger distances, the height range covered by one pixel is of course larger, at 12.5 km distance it is already 350 m for the pixel viewing at heights around 3.3 km. Therefore, the shift of the shower maximum can hardly be detected by the Auger fluorescence telescopes for vertical, iron induced showers with 10^{19} eV because all possible maxima fall into the same pixel. However for that distance, the part of

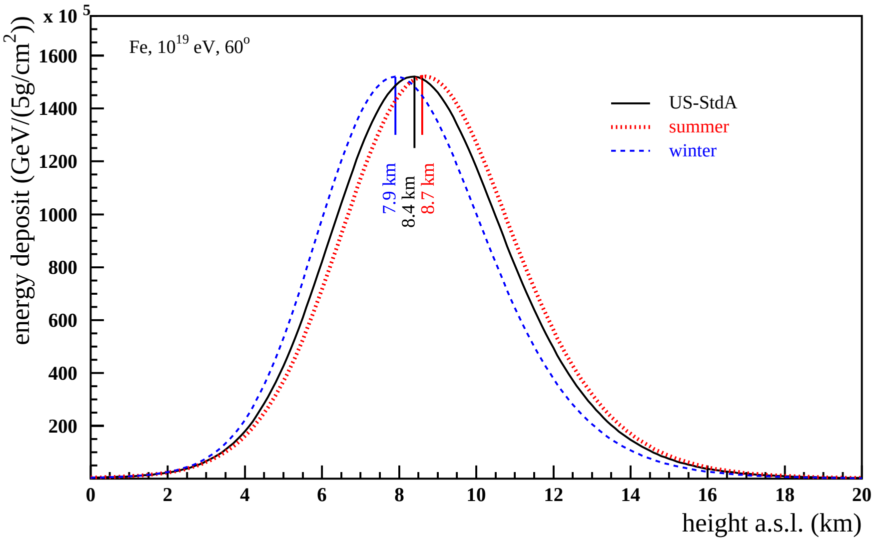

Figure 3.11: Longitudinal development of the energy deposit vs. height in km for Fe-induced, 60° inclined showers.

the EAS closer to the ground can be observed. In summer, the intensity would be increased compared to the US-StdA. At 7 km a.s.l., the energy deposit is enlarged by 12%. During winter, the situation is turned around and at 7 km height, there is a deficit of 16% in the energy deposit compared to US-StdA.

Inclined showers reach their maximum higher in the atmosphere. Choosing 60° as the incoming angle, the shower maximum is reached in average at 347.0 g/cm^2 for Fe-induced, 10^{19} eV EAS (Fig. 3.4). The EAS transformed to geometrical heights is shown in Fig. 3.11 for the three atmospheres. The shower maximum is situated at 8.361 km a.s.l. in the US-StdA which happens to be the region of largest atmospheric effects. The same EAS observed in winter reached the maximum at 7.915 km, 446 m deeper than in the US-StdA. In summer, the development starts earlier and the maximum is at 8.666 km a.s.l. (+305 m to the US-StdA). This shift of the shower maximum position can clearly be detected by the Auger fluorescence telescopes, even so the EAS only can be "seen" for distances larger than 13.4 km. The height resolution for the corresponding pixel at that distance amounts to 480 m, much smaller than the maximum position shift between summer and winter of 751 m. Thus, the same event will be detected by different pixels as the case may be summer or winter. Even at a distance of 20 km, the effect can be observed as the resolution for pixels viewing at heights around 8.4 km is 611 m.

For such inclined showers, also the distortion of the energy deposit profiles is important, see Fig. 3.12. Below the shower maximum, the energy deposit in winter is increased up to 26% at 4.5 km a.s.l. The summer condition shows the opposite behaviour with -14% energy deposit at around 5 km. The EAS energy is derived by integrating over the visible part of the longitudinal shower profile. Thus, distorted profiles could lead to incorrect primary energy estimations while ignoring the atmospheric influences.

In Figs. 3.13 and 3.14, it is pointed out that the shower profiles in different atmospheres are not only shifted parallel according to their maximum position. The left panel exhibits

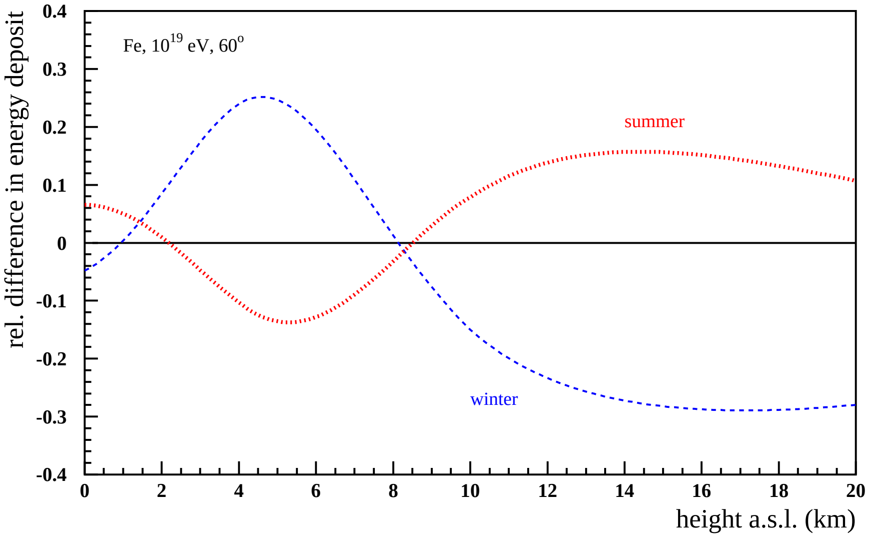

Figure 3.12: Relative differences of the energy deposits between the summer / winter atmosphere and the US-StdA for Fe-induced, 60° inclined showers.

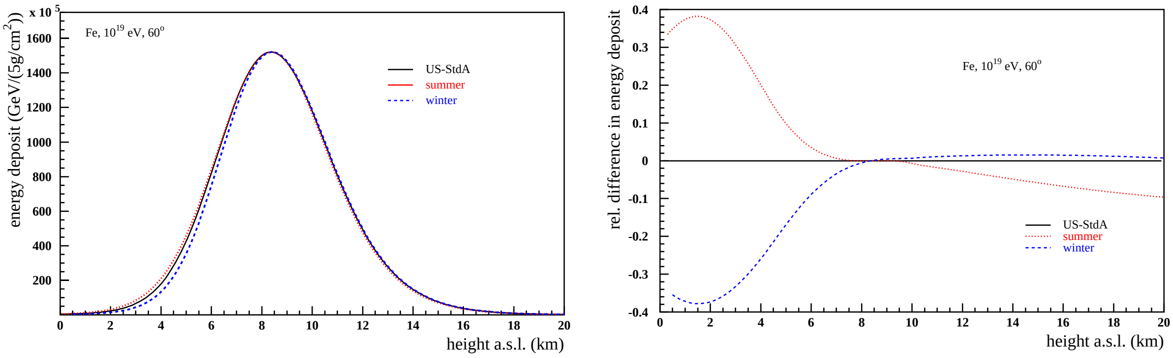

Figure 3.13: The longitudinal shower profiles of Fig. 3.11 are shifted parallel such that all maxima are at the same position namely the position of the maximum in the US-StdA.

Figure 3.14: Relative differences for the shifted profiles. The energy deposits at the maxima are nearly the same, therefore the shifted curves hardly show any difference around 8.4 km.

the longitudinal shower profiles of Fig. 3.11 shifted parallel such as all maxima are at the maximum position of the US-StdA. Higher in the atmosphere, before the maximum, the showers differ not as much as they do deeper in the atmosphere. The right panel gives the corresponding relative differences. During summer, the EAS develops slower than in the US-StdA at altitudes below 8 km and during winter faster.

The transformation from atmospheric depth to geometrical height reveals large dependences on the atmospheric conditions. The distortions of shower profiles lead to shifts of the EAS maximum position which can clearly be detected by the Auger fluorescence telescopes for inclined events. Also incorrect primary energy estimates are likely.

3.3 Fluorescence Light

The atmospheric fluorescence light induced by EAS is mainly emitted by nitrogen molecules in the wavelength region between 300 and 400 nm. The angular distribution of the emission is isotropic.

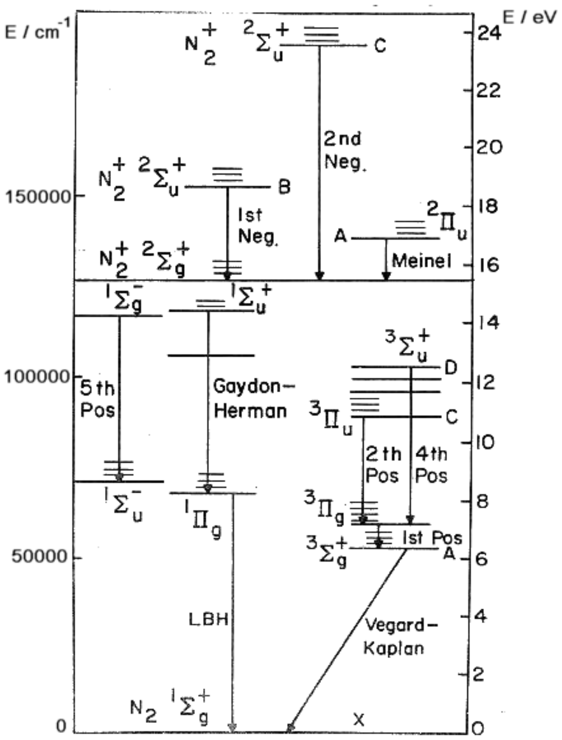

Figure 3.15: Term scheme of N_2 for the second positive (2P) and first negative (1N) system. [Bunner 1967]

It is generally assumed that the fluorescence yield is proportional to the energy deposit of a shower [Kakimoto et al. 1996]. However, a common way for calculating the emitted light using simulated air showers is the application of the particle number in each step of the shower [Song et al. 2000]. In the following, the theoretical background of nitrogen fluorescence in air is presented and also the calculation for EAS based on the energy deposit of the EAS.

3.3.1 Theory of Fluorescence Light Emission

The N_2 fluorescence is an electronic band spectrum caused by transitions between rotational levels of different vibrational levels of an electronic state and the rotational and vibrational levels of another electronic state [Haken & Wolf 1998]. For both, absorption and emission, the *Franck-Condon principle*[3] is taken for granted. The term scheme or energy level diagram for the important systems of N_2 can be seen in Fig. 3.15. For the excitations, three processes can be discriminated:

- direct excitation: The energy deposited in air excites the nitrogen molecules proportional to an energy dependent cross section $\sigma_\nu(E)$ with ν indicating the excitation level. This process mainly acts on the N_2^+ 1N system

$$N_2 + e \rightarrow N_2^{+*} + e + e. \tag{3.4}$$

- via ionisation: High energetic particles of the EAS ionise N_2 producing several lower energetic secondary electrons, called *delta electrons.* These e^- are able to excite also

---

[3] The transition takes place so rapidly in comparison to the vibrational motion that the position and velocity of the nuclei are hardly changed, the internuclear separation stays constant [Herzberg 1950].

the N_2 2P system with a resultant spin change

$$N_2 + e(\uparrow) \rightarrow N_2^*(^3\Pi_u) + e(\downarrow). \tag{3.5}$$

However, the 2P system also can be excited by cascading from higher levels

$$N_2^+ + e \rightarrow N_2^*(^3\Pi_u). \tag{3.6}$$

- via *Auger electrons*: Since high energetic particles of the EAS have about the same probability of interacting with any atomic electron, a certain number of ionisations will release K-electrons which leads to the emission of Auger electrons. These are on their part again able to excite the N_2 molecules.

With the knowledge of the energy dependent excitation, the contribution to the energy deposit according to the initial kinetic energy distribution in an air shower has been studied elsewhere [Risse & Heck 2002]. Only 10% of the energy deposit stems from particles with energies less than 0.1 MeV, as shown in Fig 3.16. Particles with energies between 0.1 and 10 MeV contribute 35%, between 10 and 100 MeV also 35%, and between 100 and 1000 MeV 17%. The remaining 3% are associated with particles of energy above 1000 MeV. Depending on their initial energy, the particles produce secondary electrons with various low energies. These can on the one hand excite the N_2 but on the other hand they may suffer an *attachment process*: if, on their way from the production site to the N_2 molecules, the secondary electrons encounter a strong electronegative pollutant (oxygen or water vapour), they are attached to this pollutants

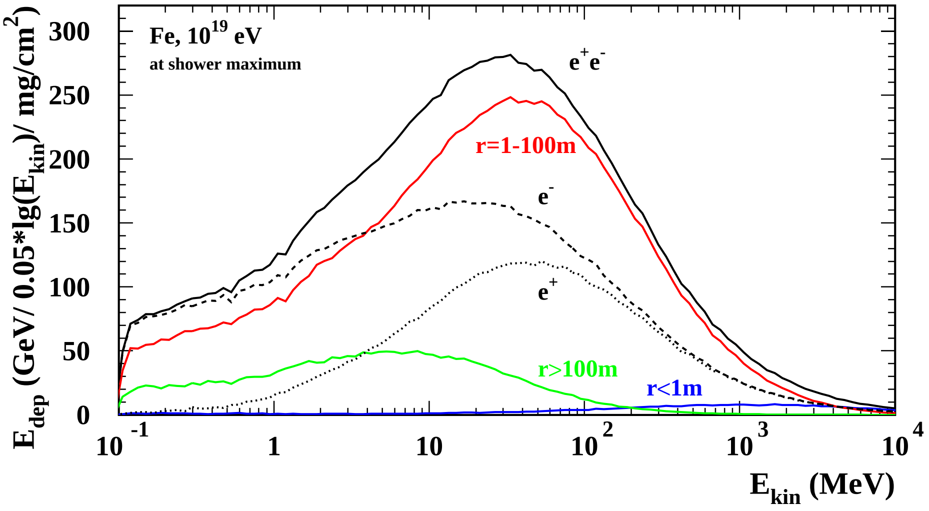

Figure 3.16: Contribution to E_{dep} in the next vertical 1 mg/cm^2 as a function of the initial particle energy. Simulations for primary iron, 10^{19} eV, at shower maximum. The sum $e^\pm$ and their individual distributions are shown. Additionally, the total contribution has been divided in three different distance ranges from the shower axis as indicated. The choice of a very thin layer ensures a small relative energy loss of the penetrating particle [Risse & Heck 2002].

and cannot excite the N_2 molecules anymore [Lebrun 2002]. This process is not quantified in this work.

During the de-excitation also some processes can occur which follow non radiative channels, e.g. collisional[4] and internal[5] quenching. Thus, the quantum efficiency of fluorescence is defined as

$$\frac{\text{rate of de-excitation by radiation}}{\text{total rate of de-excitation}} = \frac{(\tau_0/\tau_\nu)}{1+(\tau_0/\tau_c)} \text{ photons per excitation.} \tag{3.7}$$

The *mean life times* according to the excited states are τ_ν (radiation to any lower state), τ_c (collisional quenching), and τ_i (internal quenching). For simplification, the life time τ_0 was introduced by the relation

$$\frac{1}{\tau_0} = \frac{1}{\tau_\nu} + \frac{1}{\tau_i}. \tag{3.8}$$

The mean life time with respect to collisional quenching is derived from the theory of molecular motion:

$$\tau_c = \frac{1}{\sqrt{2}\cdot\rho_n\cdot\sigma_{Nx}\cdot\overline{v}} = \sqrt{\frac{\pi M_m}{kT}}\cdot\frac{1}{4\rho_n\cdot\sigma_{Nx}}, \tag{3.9}$$

with $\overline{v}$ = mean molecular velocity = $\sqrt{\frac{8kT}{\pi M_m}}$, ρ_n = particle number density, σ_{Nx} = collisional cross section between nitrogen and a further molecule (nitrogen or oxygen), T = temperature, k = Boltzmann constant, and M_m = molecular mass. Now the **fluorescence efficiency** can be defined as

$$\begin{aligned} \varepsilon_\lambda(p,T) &= \frac{\varepsilon_\lambda(p\to 0)}{1+(p/p'_\nu(T))} && (3.10)\\ &= \frac{\text{radiated energy in the form of fluorescence photons}}{\text{energy deposit in the observed medium}} = \frac{n\cdot E_\gamma}{E_{dep}}, && (3.11)\end{aligned}$$

with $\varepsilon_\lambda(p\to 0)$ = fluorescence efficiency for every transition at wavelength λ without collisional quenching, n = number of photons, and $p/p'_\nu = \tau_{0,\nu}/\tau_{c,\nu}$. The pressure p is of the observed medium (e.g. air), p'_ν is a reference pressure, $\tau_{0,\nu}$, and $\tau_{c,\nu}$ are the mean lives for special excitation level ν.

At this stage of the calculation, the first important influence of the atmospheric conditions on the fluorescence light can be recognised. The efficiency is pressure dependent and, by the non-radiative de-excitation via collisions, a further temperature dependence is obtained. Now air is presumed to be a two-component gas with 79% N_2 and 21% O_2, omitting the changing parts of water vapour[6] and the existence of argon[7]. This expands the given relation between p and p'_ν to

$$\frac{p}{p'_\nu} = \tau_{0,\nu}\cdot\left(\frac{1}{\tau_{NN,\nu}(\sigma_{NN,\nu})} + \frac{1}{\tau_{NO,\nu}(\sigma_{NO,\nu})}\right), \tag{3.12}$$

---

[4] De-excitation by impacts with further molecules [Bunner 1967].

[5] Any process by which an isolated molecule can accomplish a downward electronic transition without radiation [Bunner 1967].

[6] Being another contributor to collisional quenching, thus reducing the fluorescence efficiency.

[7] On the one hand: a further candidate for quenching; on the other hand: enhancement of efficiency due to new excitation reaction: $e + Ar \to Ar^*$ followed by $Ar^* + N_2 \to Ar + N_2^*(3\Pi_u)$; in air efficiency enhancement $< 1\%$ [Bunner 1967].

where $\tau_{NN,\nu}$ and $\tau_{NO,\nu}$ are now the explicit terms for the collisional quenching time τ_c:

$$\Leftrightarrow \frac{p}{p'_\nu} = \frac{\tau_{0,\nu} \cdot \rho_{air}(p,T) \cdot N_A}{0.79 \cdot M_{m,N} + 0.21 \cdot M_{m,O}} \cdot \sqrt{\frac{kTN_A}{\pi}} \cdot \left(4 \cdot 0.79 \cdot \sigma_{NN,\nu}\sqrt{\frac{1}{M_{m,N}}} + 2 \cdot 0.21 \cdot \sigma_{NO,\nu}\sqrt{2(\frac{1}{M_{m,N}} + \frac{1}{M_{m,O}})}\right), \tag{3.13}$$

with Avogadro's number N_A, the molecular weights for nitrogen $M_{m,N}$ and oxygen $M_{m,O}$, and the cross sections for collisional de-excitation for nitrogen-nitrogen $\sigma_{NN,\nu}$ and nitrogen-oxygen $\sigma_{NO,\nu}$. The number for the deactivation can be extracted from Table 3.1. By following the introduced way and applying the US-StdA, the fluorescence efficiency is calculated. The obtained values are compared with two elder calculations including measurements in Table 3.2. The numbers obtained for this calculation are a little bit larger than the results from [Bunner 1967]. However, the data given in [Davidson & O'Neil 1964] even exceed all others. Rewriting the fluorescence efficiency as

Table 3.1: Deactivation constants for air in the lower atmosphere, T ≈ 300 K. [Bunner 1967]

	σ_{NO} in m^2	σ_{NN} in m^2	τ_0 in 10^{-8} s
1N $\nu = 0$	13×10^{-19}	4.37×10^{-19}	6.58
2P $\nu = 0$	2.1×10^{-19}	1.0×10^{-20}	4.45
$\nu = 1$	5.0×10^{-19} [a]	3.5×10^{-20}	4.93
$\nu = 2$	7.0×10^{-19} [a]	8.8×10^{-20}	4.45
$\nu = 3$	8.0×10^{-19} [a]	1.2×10^{-19}	6.65

[a] This value is determined by the given results of [Bunner 1967] and not given in his original publication.

$$\frac{n}{E_{dep}}\left[\frac{\text{photons}}{\text{MeV}}\right] = \varepsilon_\lambda(p,T) \cdot \frac{\lambda}{hc}, \tag{3.14}$$

with λ = wavelength, c = speed of light, and h = Planck's constant, the number of emitted photons can be compared, see Figure 3.17. Adding up the values between 300 and 400 nm, the sum of all 19 contributing wavelengths for Bunner is 14.6 photons/MeV and for this work it is 18.0 photons/MeV. For a comparison with the value of Davidson & O'Neil, only the numbers between 328.5 and 400 nm are taken into account: Bunner = 13.0 photons/MeV, Davidson & O'Neil = 17.0 photons/MeV, this work = 16.3 photons/MeV. The uncertainty within the elder measurements is large, in the order of 10%. Therefore it can be stated, that the introduced way of calculating the fluorescence efficiency fits to the measurements and it offers a possibility of including several atmospheric conditions.

In the following, the atmospheric effects on the emission of fluorescence light is studied using the previous calculations and the US-StdA. The height dependence of the fluorescence efficiency is expected to be different for each band system especially for the N_2^+ 1N $\widehat{=}$ 391.4 nm (Fig. 3.18). With increasing altitude, the efficiency becomes larger due to lower rates of collisional quenching. This increase is largest for the 391.4 nm line. At sea level its contribution to the total spectrum amounts to 8.6%, at 20 km a.s.l. it is already 10.7%, and at

Table 3.2: Predictions for cosmic ray fluorescence efficiencies at sea level in the US-StdA. Comparison of calculations including atmospheric models with two further publications. Davidson & O'Neil measured only above 320 nm.

			Fluorescence Efficiency $\epsilon_\lambda(p,T)$		
Wavelength λ (nm)	**Band**	$\epsilon_\lambda(p \to 0)$[a] %	Bunner $\times 10^{-4}\%$	Davidson & O'Neil $\times 10^{-4}\%$	this work $\times 10^{-4}\%$
311.7	2P (3-2)	.005	0.16	-	0.17
313.6	2P (2-1)	.029	1.74	-	1.80
315.9	2P (1-0)	.050	4.3	-	4.60
328.5	2P (3-3)	.0154	0.5	0.64	0.53
330.9	2P (2-2)	.002	0.12	-[b]	0.12
333.9	2P (1-1)	.0041	0.35	-[b]	0.38
337.1	2P (0-0)	.082	15.9	21.00	21.00
346.9	2P (3-4)	.0063	0.21	0.26	0.22
350.0(1)[c]	2P (2-3)	.004	0.24	0.22	0.25
353.7	2P (1-2)	.029	2.48	3.20	2.70
357.7	2P (0-1)	.0615	11.9	15.00	16.00
367.2	2P (3-5)	.0046	0.15	0.19	0.16
371.1	2P (2-4)	.010	0.60	0.76	0.62
375.6	2P (1-3)	.0271	2.31	3.00	2.50
380.5	2P (0-2)	.0213	4.12	5.20	5.50
389.4	2P (3-6)	.003	0.10	-[b]	0.10
391.4	1N (0-0)	.33	4.33	7.00	4.90
394.3	2P (2-5)	.0064	0.38	0.49	0.40
399.8	2P (1-4)	.016	1.36	1.80	1.50

[a] Fluorescence efficiency of a band at λ_i without collisional quenching = $\frac{\text{eV of optical output}}{\text{eV deposited}}$. Based on these values, the following numbers of Bunner and also for this work have been determined.

[b] This transition has not been measured.

[c] In the work of Davidson & O'Neil, the wavelength for this transition is given with 350.1 nm.

30 km a.s.l. 16.8%. However regarding EAS, the rate of emitted photons per metre traversed matter of the EAS is the observed variable. Introducing the energy deposit of an EAS or in the first step of a certain particle, the **fluorescence yield** is

$$Fl.\ Yield_\lambda \;=\; \varepsilon_\lambda(p,T)\cdot\frac{\lambda}{hc}\cdot\frac{dE}{dX}\cdot\rho_{air}\;\left[\frac{\text{photons}}{\text{m}}\right]. \tag{3.15}$$

The fluorescence yield is proportional to the local energy deposit $\frac{dE}{dX}$. Another atmosphere dependent parameter is given with the air density ρ_{air}, by which the number of excitable nitrogen molecules and quenching partners is ascertained. For instance, a 1.4 MeV, minimal ionising electron as exciting particle is chosen. The local fluorescence yield is determined assuming that this particle deposits 1.668 MeV/(g/cm^2) in air. The fluorescence yield profile for different atmospheres is shown in Fig. 3.19. Up to $\approx$ 10 km, the fluorescence yield increases according to the increasing fluorescence efficiency and the decrease of the air density only bates the effect. Higher in the atmosphere, the reduction of nitrogen molecules dominates

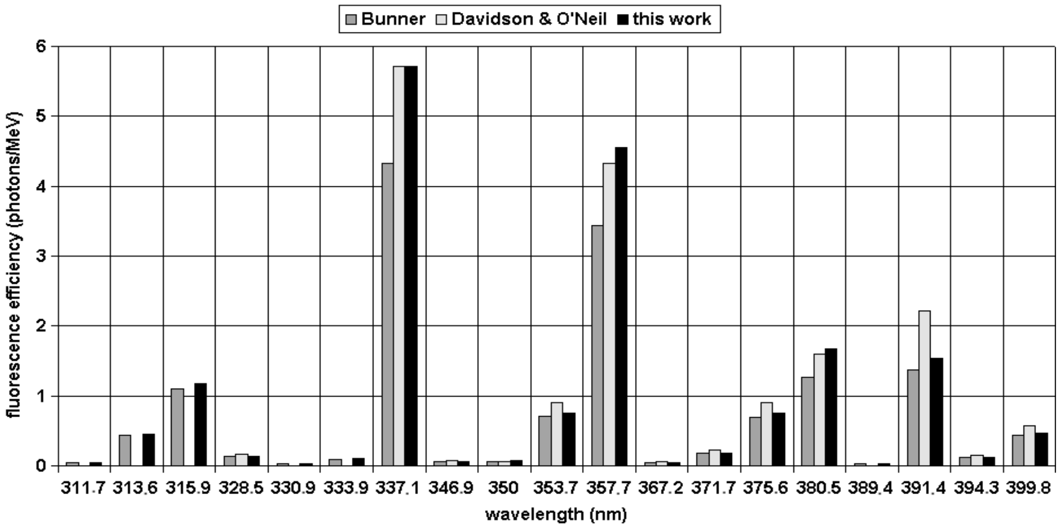

Figure 3.17: Fluorescence efficiency for 19 wavelengths in the US-StdA at sea level.

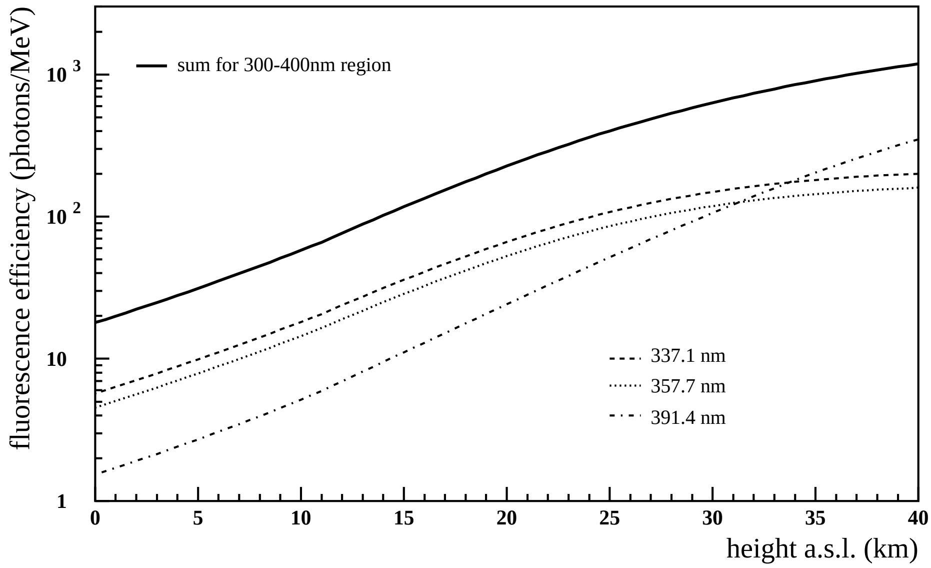

Figure 3.18: Fluorescence efficiency profile for the three main wavelengths in the US-StdA.

the increasing efficiency and the resulting fluorescence yield diminishes. The characteristics in different atmospheres is quite similar among each other, however below 10 km a.s.l. lower temperatures in winter entail larger fluorescence yield and vice versa in summer. The enhancement of the yield in the standard winter atmosphere is about 3.5% at sea level and the reduction in summer nearly 2.5% near ground. The relative differences scale somewhat down for higher altitudes, nevertheless at 8 km a.s.l., the position of the shower maximum for 60° inclined shower with 10^{19} eV, the effect remains to +2.2% in winter and -1.7% in summer. Thus, an additional shift of the shower maximum position according to the fluorescence yield is expected for EAS developing in different atmospheres.

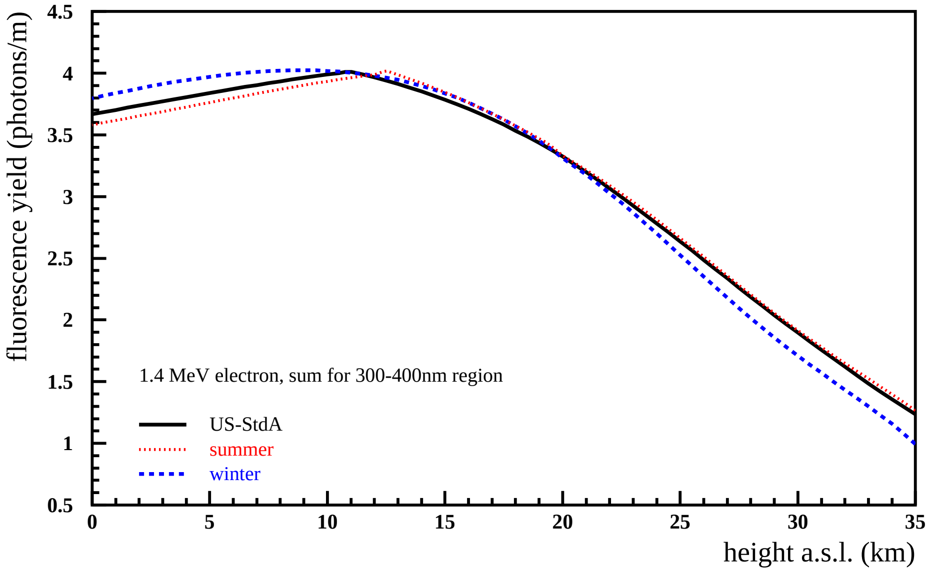

Figure 3.19: Fluorescence yield profile for a 1.4 MeV electron with vertical incidence in three atmospheres.

3.3.2 Excitation by Extensive Air Showers

For the discussion of the fluorescence light emission of EAS, again the average of 100 iron induced showers with 10^{19} eV primary energy is selected. As a first approach, the vertical incidence is regarded, Fig. 3.20. These showers reach their maximum at around 3 km a.s.l. implying a quite large effect on the fluorescence light emission. This expectation is derived from the knowledge obtained by calculations for a 1.4 MeV electron (Fig 3.19). The EAS in the US-StdA is brightest at 3.317 km a.s.l. which corresponds to a shift of 57 m towards higher altitudes with regard to the maximum for the energy deposit of this shower (see Chap. 3.2). The additional maximum shift for the summer case is even 71 m higher up (maximum at 3.398 km) and in winter 46 m (maximum at 3.145 km). Thus, the optical vertical difference in the maximum position between summer and winter has been enlarged from 228 m in terms of energy deposit to 253 m in terms of fluorescence yield. For the closest distance at which the shower maximum can be detected by the Auger telescopes, this elongation is still separated into two pixels. The second effect of the atmosphere dependent fluorescence production is the different amount of emitted photons. Despite the same amount of energy deposit at the shower maximum for all 3 atmospheric cases, the winter shower emits 3.6% more photons and the summer shower 2.1% less according to the US-StdA shower at their maximum positions. The relative differences of the summer / winter EAS to the US-StdA EAS are shown in Fig. 3.21. Around the maximum position, the changed amount of emitted photons is in the order of 5%. At $\approx$ 4.5 km a.s.l., the curves for the fluorescence yield intersect and higher in the atmosphere, the winter EAS emits less photons and the summer EAS more than the EAS in the US-StdA. A relative difference of 20% is reached at 8 km a.s.l. This relative difference is a superposition of the energy deposit and the fluorescence yield profiles. However, these signals only can be detected with the Auger telescopes for air showers being about 13 km away from the station.

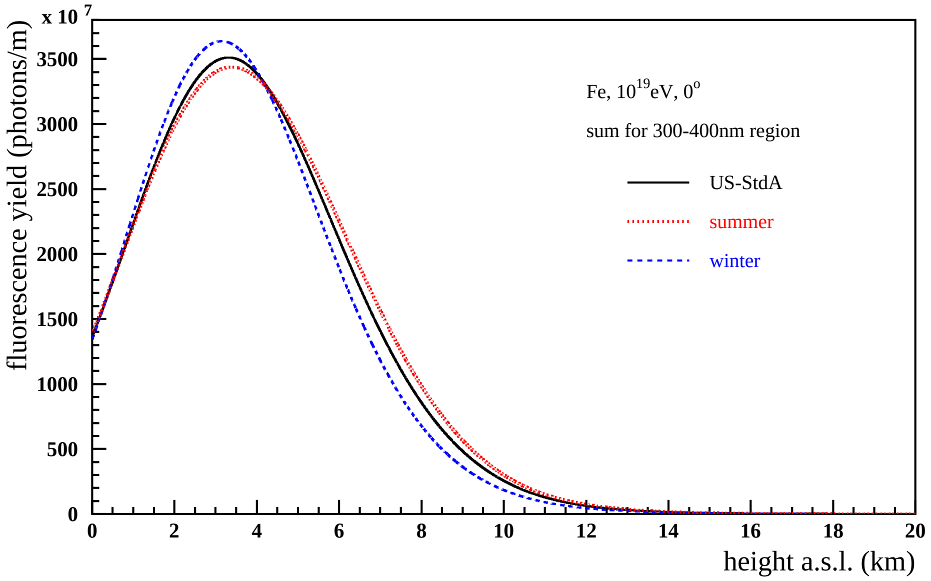

Figure 3.20: Fluorescence yield vs. height for a Fe-induced, 10^{19} eV, vertical shower traversed through three different atmospheric models.

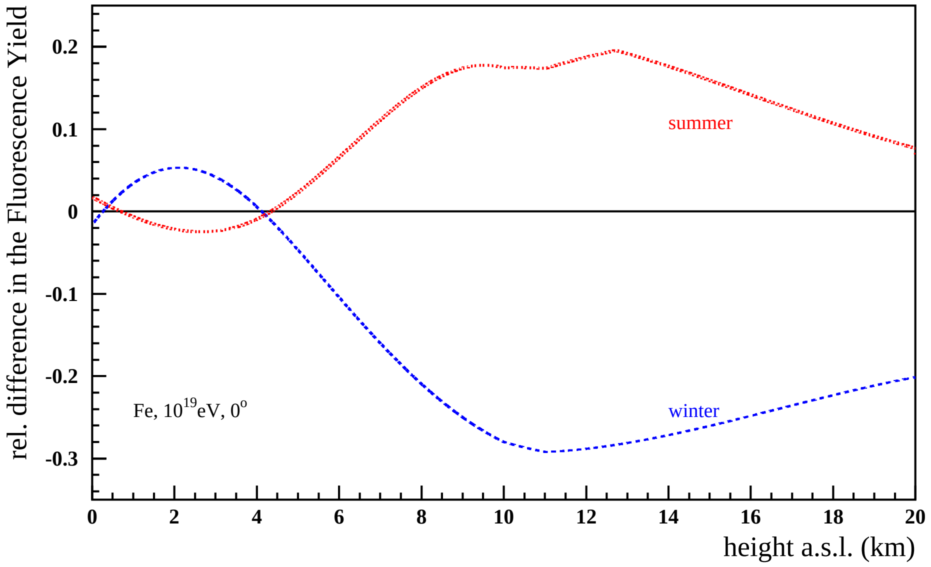

Figure 3.21: Relative difference of the fluorescence yield from summer / winter Fe-induced, 10^{19} eV, vertical shower to the EAS in the US-StdA.

Like in the discussion of the longitudinal energy deposit profiles, it is glanced at 60° inclined showers. The transformation of atmospheric depth to geometrical height entails large seasonal variations of the showers but at their maximum position around 8 km a.s.l., the fluorescence yield differs not so much between the seasons. The fluorescence emission of a Fe-induced EAS with 10^{19} eV and 60° inclination results in the curves of Fig. 3.22. The

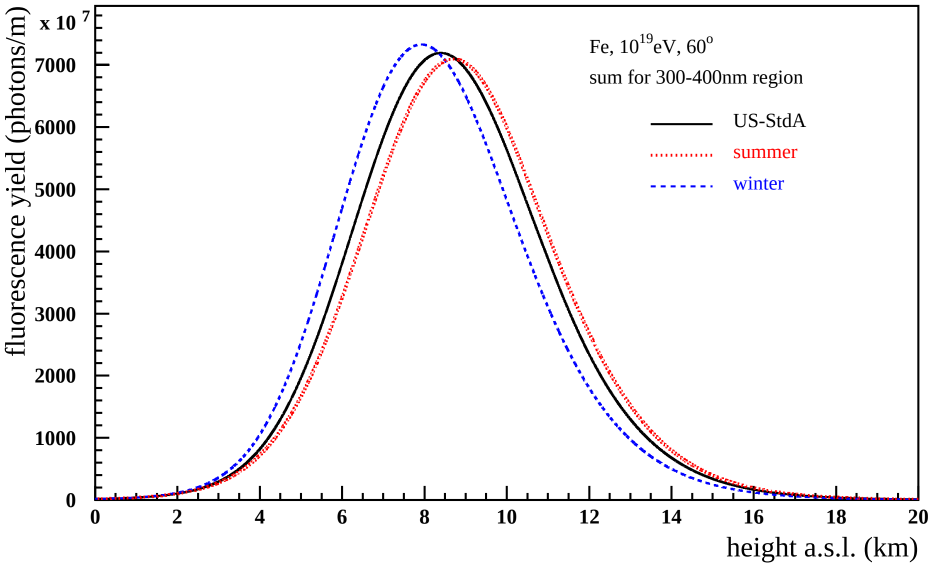

Figure 3.22: Fluorescence yield vs. height for a Fe-induced, 10^{19} eV, 60° shower traversed through three different atmospheric models.

shift of the shower maximum position is enlarged from 751 m for the energy deposit between summer and winter to 783 m for the fluorescence yield of that showers. The maximum for the EAS in the US-StdA has moved 35 m higher up in the atmosphere, for the EAS in summer 40 m, and in winter only 8 m. Also the amount of emitted photons at shower maximum is consistent. The relative differences are -1.4% in the summer case and +1.9% in winter. However, large seasonal variations for inclined showers appear at lower altitudes, Fig. 3.23. The most extreme relative differences (energy deposit plus fluorescence yield) amount to 30% more fluorescence photons for EAS in winter at 5 km a.s.l. and 15% less photons in summer at the same altitude.

To stress the extent of the shift of the shower maximum position, proton and iron induced showers can be compared. Applying the fluorescence technique, the type of the primary particle of the EAS is determined by the position of the shower maximum for a given primary energy. As already discussed in Chap. 3.1, iron induced showers develop faster and consequently reach their maximum higher up in the atmosphere. The resulting fluorescence yield profiles for p- and Fe-induced showers, both in the US-StdA, are given in Fig. 3.24. The positions of the maxima are clearly separated by 783 m vertical height. Therefore, it is expected to identify the type of the primary particle by the position of the shower maximum. However ignoring the atmosphere dependences, a misinterpretation of the type is very likely. Exemplarily a proton induced EAS developing in summer conditions and an iron induced EAS in winter conditions are compared, Fig. 3.25. The deeper penetrating proton shower develops earlier in summer conditions than in US-StdA. A shift of the maximum position of 317 m higher up in the atmosphere can be seen. The fast developing iron shower penetrates deeper in winter conditions and here a shift of 469 m towards ground happens. The two showers are hardly distinguishable, the maxima are just separated by 3 m and the iron shower reaches in this case its maximum even deeper in the atmosphere than the proton shower.

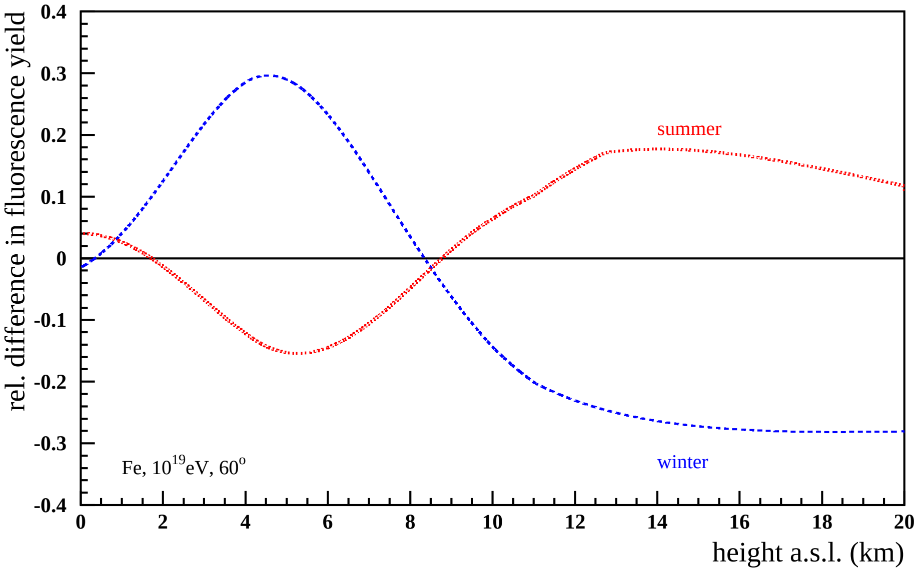

Figure 3.23: Relative difference of the fluorescence yield from summer / winter Fe-induced, 10^{19} eV, 60° shower to the EAS in the US-StdA.

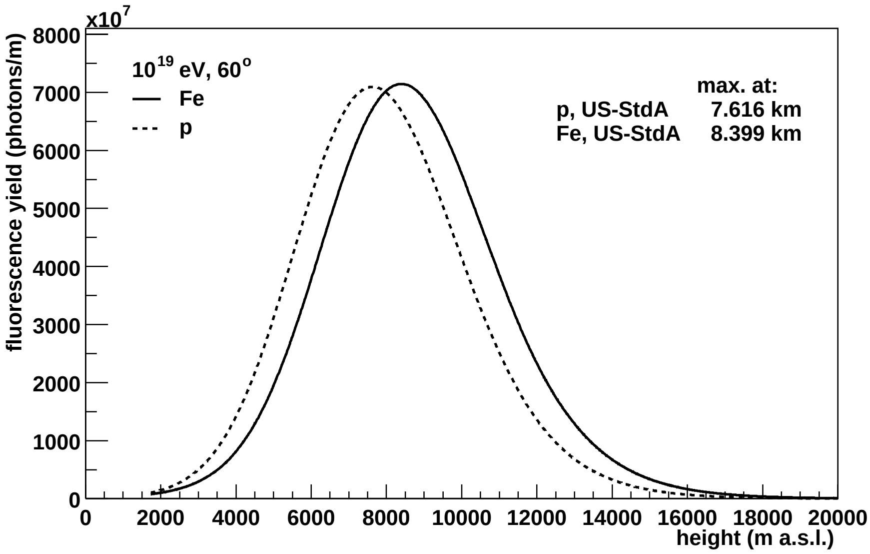

Figure 3.24: Fluorescence yield profiles for p- and Fe-induced EAS in US-StdA with 10^{19} eV and 60° inclination. The fluorescence yield is the sum of all emitted photons between 300 and 400 nm.

The shower profiles for the emitted fluorescence photons show a sensitivity on seasonal variation of atmospheric profiles. The extent of this effect is a superposition of the atmospheric variation of energy deposit profiles and different fluorescence emission during a year. Mainly, the energy deposit vs. geometrical height is affected and the changing emission contributes

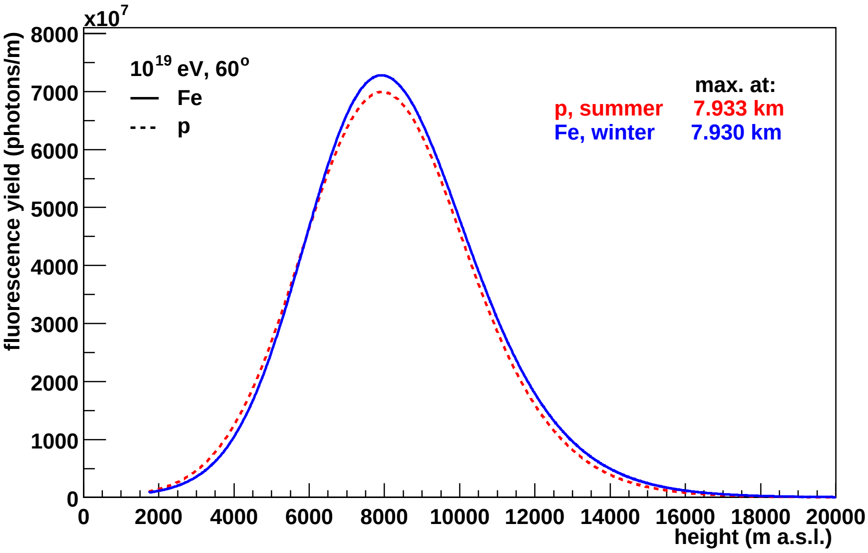

Figure 3.25: Fluorescence yield profiles for p-induced EAS in summer and Fe-induced EAS in winter both with 10^{19} eV and 60° inclination. The fluorescence yield is the sum of all emitted photons between 300 and 400 nm.

less than 5% to the total effect. Therefore, the shower reconstruction processes or simulations have to take into account the resulting emission curves of an EAS for determining the position of the shower maximum correctly as well as the amount of energy deposited in air. The interpretation of the energy is critical for those EAS from which only a small part of the longitudinal development has been observed. E.g. assuming an inclined EAS in winter visible between 3 and 6 km a.s.l., the use of the US-StdA instead of winter conditions leads to a large overestimation of the reconstructed energy.

3.4 Transmission of Fluorescence Light

While the emitted light traverses through the atmosphere towards the telescope, it suffers absorption and scattering caused by different components of the air. In the following, some aspects are discussed separately because it is not sufficient to treat the total transmission at once.

An important aspect is the background of Cherenkov photons which are also emitted by an EAS traversing the atmosphere (see Chap. 3.5). The Cherenkov emission is strongly peaked into forward direction in contrast to the isotropically emitted fluorescence light. Therefore, the different scattering processes have to be investigated separately. One scattering process is due to air molecules (Chap. 3.4.1) and the other due to aerosols. The aerosol scattering, called Mie scattering, can hardly be described analytically. The content of aerosols in air is strongly fluctuating in terms of aerosol type and size as well as density. Thus, the aerosol scattering will be measured in dependence of its angular distribution (phase function) at the Auger experiment site several times a night. However, for analysing the obtained data one has to know the contribution of the Rayleigh scattering very well which can be determined correctly. The Mie scattering is most important for the subtraction of the Cherenkov background and is not discussed here in detail. The calculation of the Rayleigh scattering is applied to the fluorescence light but the theory is also valid for Cherenkov light.

3.4.1 Rayleigh Scattering

The Rayleigh scattering is due to the molecules in air assuming that the scattering centres are much smaller than the wavelength of the incoming light (rec. [Haferkorn 2003], [Bolle 1982]). Using this simplification, the particles may be considered to be placed in a homogeneous electric field $\mathbf{E}_0$ of the incoming unpolarised light. The induced dipole moment can be written as [Van de Hulst 1957]

$$\mathbf{p} = \alpha \cdot \mathbf{E}_0, \tag{3.16}$$

with α being the polarisability of the particle. The scattered electric field for that dipole is given at large distances r as

$$\mathbf{E}_0 = \frac{1}{c^2}\frac{1}{r}\frac{\partial \mathbf{p}}{\partial t}\sin(\beta), \tag{3.17}$$

with β = angle between scattered dipole moment and direction of observation. The resulting intensity of the scattered light is

$$I = \frac{I_0}{r^2} \cdot \alpha^2 \left(\frac{2\pi}{\lambda}\right)^4 \cdot \frac{1+\cos^2(\Theta)}{2} \tag{3.18}$$

$$\Leftrightarrow I(\cos(\Theta)) = \frac{I_0}{r^2} \cdot \alpha^2 \left(\frac{128\pi^5}{3\lambda^4}\right) \cdot \frac{P(\Theta)}{4\pi} \tag{3.19}$$

and the Rayleigh scattering phase function is defined as

$$P(\cos(\Theta)) = \frac{3}{4}(1+\cos^2(\Theta)) \tag{3.20}$$

$$\Rightarrow I(\cos(\Theta)) = \frac{I_0}{r^2}\sigma_R \frac{P(\Theta)}{4\pi}. \tag{3.21}$$

Thus, the scattering cross section for a single molecule is

$$\sigma_R = \alpha^2 \frac{128\pi^5}{3\lambda^4}. \tag{3.22}$$

For the polarisability α, the *Lorentz-Lorenz equation* is applied [Lide 2000]

$$\alpha(\lambda) = \frac{3}{4\pi N}\left[\frac{n^2(\lambda)-1}{n^2(\lambda)+2}\right], \tag{3.23}$$

by which the wavelength dependent refractive index of air is introduced. The optical depth δ_R concerning the Rayleigh scattering can be calculated by

$$\delta_R = \int \sigma_R \cdot N ds, \tag{3.24}$$

with N = particle number density of the medium and ds = path length [Bolle 1982]. The transmission coefficient τ_R can be concluded:

$$\begin{aligned} \tau_R &= \exp(-\delta_R) && (3.25)\\ &= \exp(-\int \frac{24\pi^3 \cdot (n^2-1)^2}{\lambda^4 \cdot N \cdot (n^2+2)^2} \cdot F_{air} \cdot ds). && (3.26) \end{aligned}$$

The *King factor* F_{air} is a correction term which takes into account the anisotropy of air molecules (rec. [Bodhaine et al. 1999], [Bucholtz 1995])

$$F_{air} = \frac{6+3\rho_D}{6-7\rho_D}, \tag{3.27}$$

with ρ_D = depolarisation factor.

For the application of the formulas to the medium air, a suggested approach is to treat the components of air separately [Owens 1967], [Bodhaine et al. 1999]. The discrimination is done in three parts:

1. dry air without CO_2, index: *air*
2. CO_2 contribution, index: CO_2
3. water vapour, index: *vapour*.

The empirical formulas for the refractive index of these components are

$$\begin{aligned} (n_{air}-1) \cdot 10^8 &= 8059.20 + \frac{2480588}{132.274-\lambda^{-2}} + \frac{17452.9}{39.32957-\lambda^{-2}} && (3.28)\\ (n_{\mathrm{CO_2}}-1) \cdot 10^8 &= 22822.1 + 117.8 \cdot \lambda^{-2} + \frac{2406030}{130-\lambda^{-2}} + \frac{15997}{38.9-\lambda^{-2}} && (3.29)\\ (n_{vapour}-1) \cdot 10^8 &= 295.235 + 2.6422 \cdot \lambda^{-2} - 0.03238 \cdot \lambda^{-4} + 0.004028 \cdot \lambda^{-6}. && (3.30) \end{aligned}$$

Furthermore, the refractive index is dependent on temperature and pressure inducing a dependence on atmospheric profiles [Edlén 1966], [Lide 2000]

$$(n-1)_{Tp} = (n-1)_s \cdot \frac{p \cdot [1+p(61.3-T) \cdot 10^{-10}]}{96095.4 \cdot (1+0.003661 \cdot T)} . \tag{3.31}$$

The index Tp indicates the expression for the temperature and pressure dependence, s= sea level, p must be in Pa, and T in °C. The King factor of air can also be combined of several components

$$F_{air} = \frac{78.084 \cdot F(\mathrm{N_2}) + 20.946 \cdot F(\mathrm{O_2}) + 0.934 \cdot F(\mathrm{Ar}) + C_{\mathrm{CO_2}} \cdot F(\mathrm{CO_2})}{78.084 + 20.946 + 0.934 + C_{\mathrm{CO_2}}}. \tag{3.32}$$

Nowadays, the CO_2 contribution is ≈ 360 ppmv = 0.036%. The formulas for the depolarisation F are also again wavelength dependent except for $F(\mathrm{Ar})$ and $F(\mathrm{CO_2})$

$$\begin{aligned} F(\mathrm{N_2}) &= 1.034 + 3.17 \cdot 10^{-4} \cdot \lambda^{-2} && (3.33)\\ F(\mathrm{O_2}) &= 1.096 + 1.385 \cdot 10^{-3} \cdot \lambda^{-2} + 1.448 \cdot 10^{-4} \cdot \lambda^{-4} && (3.34)\\ F(\mathrm{Ar}) &= 1.00 && (3.35)\\ F(\mathrm{CO_2}) &= 1.15 . && (3.36) \end{aligned}$$

Applying these equations to each of the 19 emitted wavelengths of the fluorescence light, the transmission due to Rayleigh scattering can be obtained in a spectral resolution. In order to perform the calculations, a geometry for the light emitting EAS has to be chosen. Exemplarily, a fluorescence detector station is situated at 1700 m a.s.l. which is a realistic condition for the Auger observatory. The EAS passes parallel to the detector front in a distance of 15 km to reduce geometric induced effects. The exemplary geometry is visualised in Fig. 3.26. The EAS enters the atmosphere with a zenith angle of 30° in a manner that the shower is observable in the whole field of view of a single telescope. The transmission coefficient τ_R is plotted vs. the elevation angle of the telescope α. Fig. 3.27 shows the values for the given conditions for the three main wavelengths of the fluorescence light. The shorter wavelengths suffer more scattering processes during the passage because of the factor $1/\lambda^4$ in equation (3.26). Also the light traversing mostly in the lower part of the atmosphere is strongly reduced. The variation of the transmission for different atmospheric profiles is obvious. The relative differences are given in Fig. 3.28. In summer, the atmospheric density is lower near ground than in the US-StdA because of warm air rising up. This entails less scattering centres and therefore a better transmission. In winter, the situation is reversed.

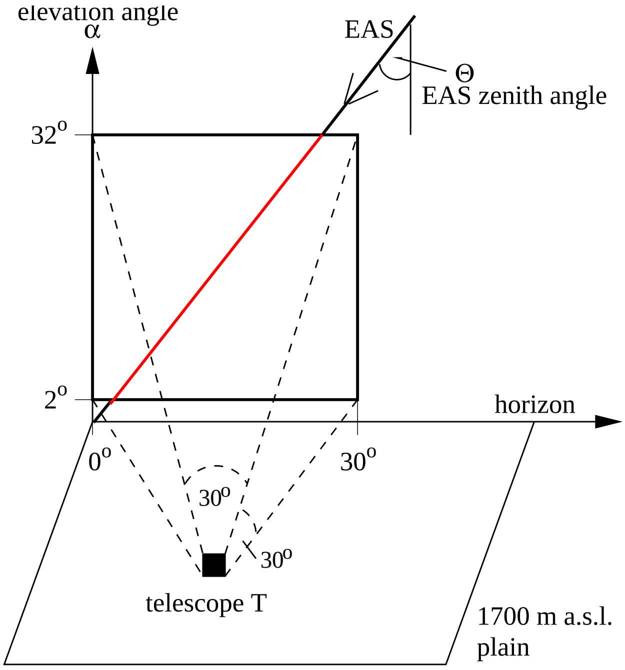

Figure 3.26: Exemplary geometry for calculating the transmission due to Rayleigh scattering.

However using the Rayleigh transmission for correcting further calculations, more sophisticated determinations are possible. Usually, the values of T, p, and ρ are known at ground. Then the transmission coefficient can be extracted based on atmospheric profiles shifted according to the ground values. In the case shown below (Figs. 3.29, 3.30), the summer and winter profiles are shifted so that the values at ground are the same as for the US-StdA but the gradients of the profiles are unmodified. The large differences between summer / winter and US-StdA in Fig. 3.28 could be reduced strongly. Only small variations within 1% are left induced by the slightly different gradients.

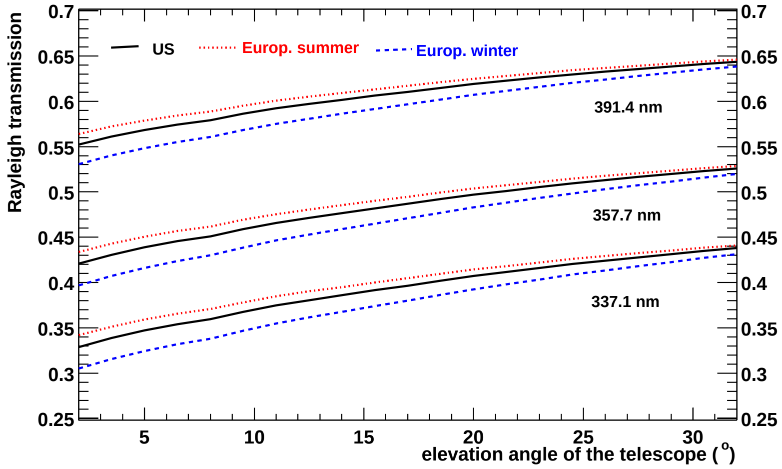

Figure 3.27: Transmission due to Rayleigh scattering for the conditions given in the text. The calculations are performed in the US-StdA, European summer and winter.

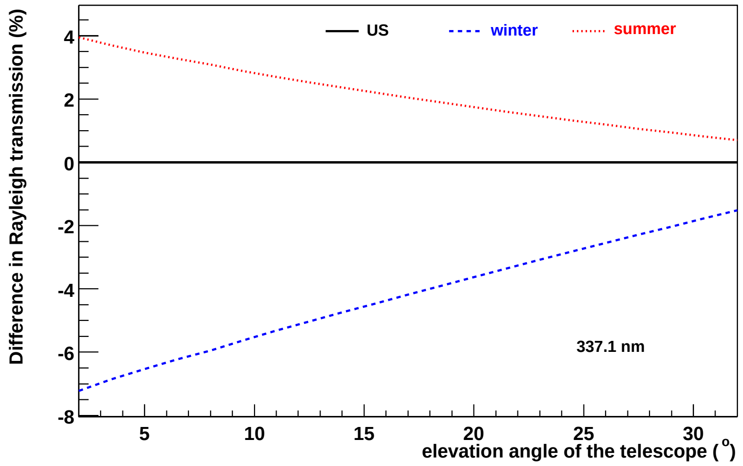

Figure 3.28: Percent difference in transmission due to Rayleigh scattering of European summer / winter to the US-StdA, for the 337.1 nm wavelength.

The atmospheric influence on the transmission due to Rayleigh scattering is quite large. For the European summer and winter conditions differences to the US-StdA can occur in the order of several percent. These numbers are larger for shorter wavelengths and also for light traversing mostly through the lower part of the atmosphere. Nevertheless, a relative correction of the transmission coefficient can be achieved. Assuming unknown atmospheric profiles e.g. in summer or winter, one can use the profile for the US-StdA. The profile is shifted according to the ground values of the real atmospheric conditions and the variations due to the seasons are reduced to a sufficient accuracy.

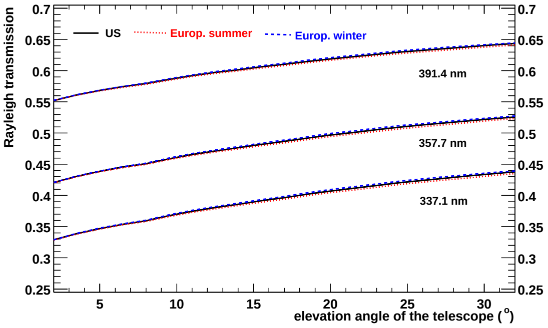

Figure 3.29: Transmission due to Rayleigh scattering with shifted summer / winter profiles according to the conditions at ground in the US-StdA.

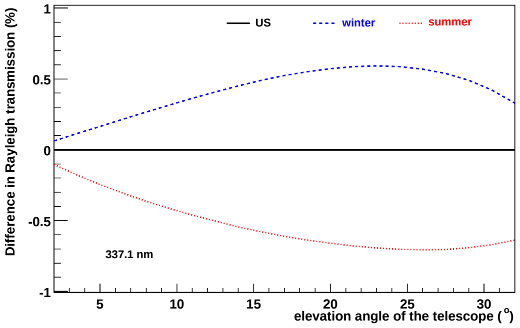

Figure 3.30: Percent difference in the transmission due to Rayleigh scattering of the shifted European summer / winter profiles to the US-StdA, for 337.1 nm.

3.4.2 Ozone Absorption

The ozone concentration in the atmosphere is largest in the stratosphere just below 30 km a.s.l. (Fig. 2.1) with $\approx$ 5.5 ppmv. For lower altitudes, the concentration decreases fast, at 12 km a.s.l. there is only 1 ppmv left. The decrease continues towards ground and the lowest ozone concentration is between 7 and 0 km with only 0.04 ppmv (Table 2.1). These conditions are not stable but vary with changing seasons and degree of industrialisation at a given location.

The ozone acts as an absorber of light. The main absorption spectrum ranges between 230 and 300 nm, the *Harley band*. For the fluorescence light emitted by the EAS, the adjacent wavelength region towards longer wavelengths is more important. The *Huggins band* reaches up to nearly 350 nm. The absorption cross sections σ_O for this band are plotted in Fig. 3.31. A strong decrease of the cross section can be seen which indicates less significance of ozone for the fluorescence detection above $\approx$ 330 nm. Not only a wavelength dependence of the cross section is stated but also a temperature dependence. The function has been parameterised in wavelength intervals:

$$\sigma_O(T) = a_i + b_i \cdot (T - 230) + c_i \cdot (t - 230)^2 \ . \tag{3.37}$$

With respect to the emission wavelengths of the fluorescence light, only five intervals have been taken into account, see Table 3.3.

The calculation of the transmission coefficient due to ozone absorption τ_O is similar to the case for Rayleigh scattering.

$$\begin{aligned} \tau_O &= 1 - \exp(\delta_O) & (3.38) \\ &= 1 - \exp(-\int \sigma_O(T) \cdot cv(h) \cdot \rho(h) \cdot ds), & (3.39) \end{aligned}$$

with $cv(h)$ = mixing ratio of ozone in air, $\rho(h)$ = air density, and ds = path length of the transmitting light. First calculations confirm that the ozone only disturbs the transmission of light below 330 nm significantly. The arising question is, how important this effect is for the Auger experiment and if we have to measure the local ozone concentration profiles

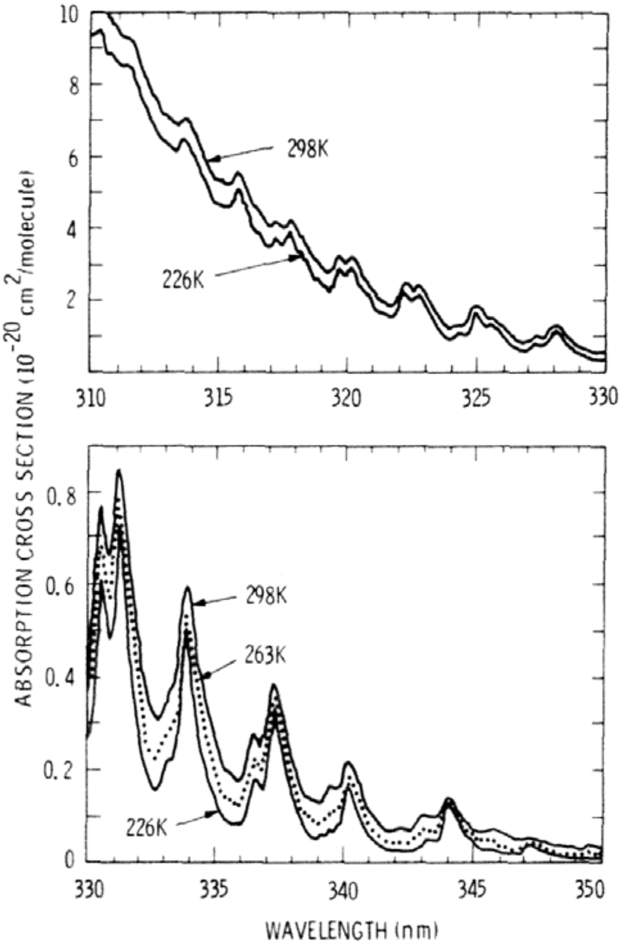

Figure 3.31: Ozone absorption cross sections in the region 310 - 350 nm, the Huggins band, for different temperatures [Molina & Molina 1986].

Table 3.3: Parameters for the ozone absorption cross section as a function of temperature (equation 3.37). T has to be in Kelvin and the resulting σ_O is in units of 10^{-20} cm^2/molecule [Molina & Molina 1986].

Wavelength Range in nm	a_i	b_i	c_i
307.692 - 312.5	10.459	$-2.8831 \cdot 10^{-2}$	$1.3909 \cdot 10^{-4}$
312.5 - 317.5	5.4715	$-2.0092 \cdot 10^{-2}$	$9.887 \cdot 10^{-5}$
327.5 - 332.5	0.69373	$-2.9792 \cdot 10^{-3}$	$3.1038 \cdot 10^{-6}$
332.5 - 337.5	0.32091	$-1.9502 \cdot 10^{-3}$	$5.6456 \cdot 10^{-6}$
342.5 - 347.5	$7.578 \cdot 10^{-2}$	$-5.7359 \cdot 10^{-4}$	$1.6055 \cdot 10^{-6}$

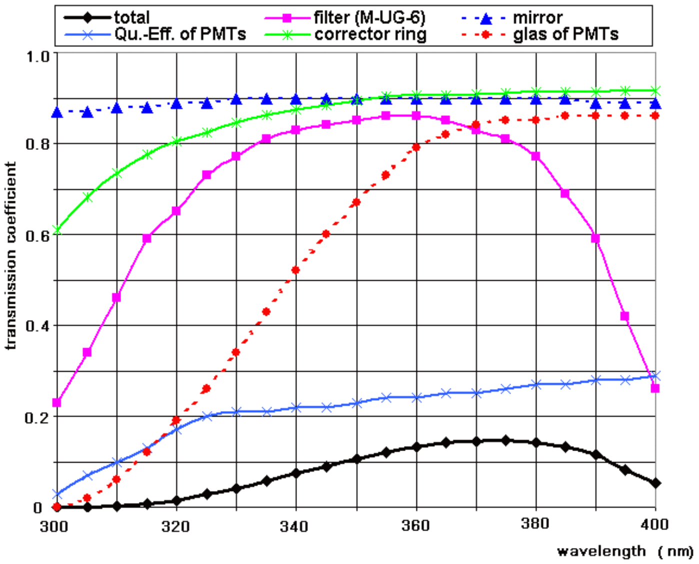

Figure 3.32: Transmission through all fluorescence detector components in dependence of wavelength, folded with PMT quantum efficiency (Courtesy of R. Gumbsheimer).

in Malargüe, Argentina. To answer, the detector transmission, which efficiency is small for shorter wavelengths, has to be inspected (Fig. 3.32). A reducing factor of the system is the quantum efficiency of the photomultipliers. Especially below 320 nm, also the transmission of the photomultiplier glass is low. Combining the detector transmission with the transmission due to ozone absorption, the minor importance of the ozone concentration in the atmosphere becomes obvious (Fig. 3.33). The ozone absorption is calculated for light with vertical inci-

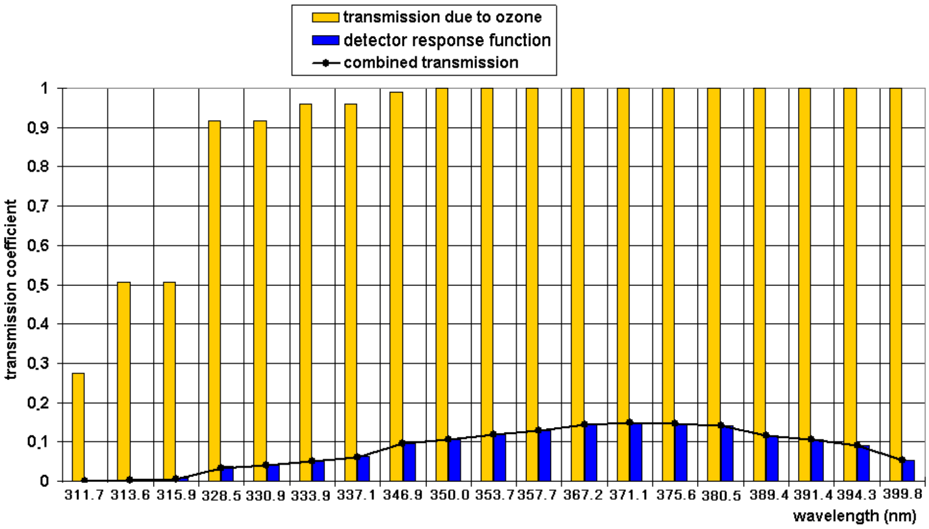

Figure 3.33: Combined transmission of the detector response function and the transmission due to ozone absorption. For the wavelengths suffering ozone absorption, the detector transmission is so small that this effect dominates.

dence directly hitting the detector. The site of emission is assumed to be at 20 km a.s.l. For shorter paths of transmission, the ozone absorption is of course reduced.

It can be concluded that the ozone absorption needs not to be considered for further calculations concerning fluorescence observations. The ozone absorbs light only below 330 nm in a significant way but within this wavelength range the poor transmission properties of the fluorescence detector dominate.

Also the absorption by NO_2 needs not to be taken into account. For the important wavelength region, the cross sections are very similar to those of ozone, in the order of 2 - 3×10^{-19} cm^2/molecule [Davidson et al. 1988]. However, the NO_2 concentration in the entire troposphere is as low as the ozone concentration near ground. Like the ozone absorption below 7 km a.s.l., the absorption due to NO_2 is negligible.

3.5 Cherenkov Background

A lot of particles within the air shower have velocities larger than the speed of light in air, $v > \frac{c}{n}$. This is the precondition for emitting Cherenkov light. The emission angle $\Theta_{\check{C}}$ is defined by

$$\cos(\Theta_{\check{C}}) = \frac{1}{n \cdot \beta}, \tag{3.40}$$

with n being the refractive index of air and $\beta = v/c$. Usually, the resulting Cherenkov cone is peaked strongly into forward direction. Only rare EAS directly pointing at the Auger fluorescence telescope would contaminate the measurement with direct Cherenkov light which is also emitted in the near UV spectrum. Due to the underlying angular distribution of charged particles in an EAS, the effective Cherenkov cone of the Cherenkov light produced by the EAS is enlarged. Fig. 3.34 reflects the angular emission distribution of Cherenkov light compared with fluorescence light at several depths. For larger atmospheric depth, tantamount to lower altitudes, the Cherenkov light is dominating up to 20° to the shower axis. Even up to 35° to the shower axis, the Cherenkov contamination is in the order of 10%. Therefore, the Cherenkov background must be known very well since rejecting all critical events would lead to a large reduction of the fluorescence observation efficiency.

A recently performed analytical description of longitudinal Cherenkov profiles for EAS enables to include different atmospheric models [Nerling et al. 2003]. The Cherenkov emission for a single relativistic electron can be calculated by

$$\left.\frac{dN_{\check{C}}}{dX}\right|_e = \frac{2\pi\alpha}{\rho_{air}} \int_{\lambda_1}^{\lambda_2} \left(1 - \frac{1}{n^2\beta^2}\right) \frac{d\lambda}{\lambda^2} \tag{3.41}$$

$$\overset{(n=1+\delta)}{\approx} \frac{2\pi\alpha}{\rho_{air}} \left(2\delta - \frac{m^2c^4}{E^2}\right) \int_{\lambda_1}^{\lambda_2} \frac{d\lambda}{\lambda^2} \ . \tag{3.42}$$

α is the *fine structure constant*, m the mass of the electron, λ the wavelength of the emitted Cherenkov photons, and E the energy of the electron. Applying this equation to an air shower, the particle and energy distribution must be inserted. The EAS emits a number of Cherenkov photons per traversed slant depth dX:

$$\left.\frac{dN_{\check{C}}}{dX}\right|_{EAS} (X) = \int_{E_t}^{\infty} N_e(X) \cdot \left.\frac{dN_{\check{C}}}{dX}\right|_e \cdot f(X,E) \cdot dE, \tag{3.43}$$

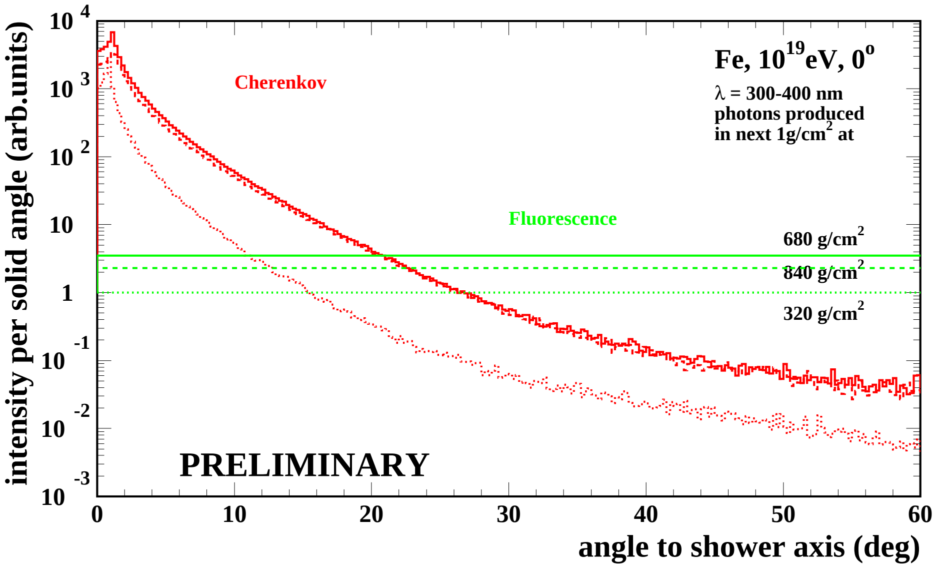

Figure 3.34: Comparison of emission angles for Cherenkov and fluorescence light vs. angle to the shower axis. At lower altitudes, the fluorescence light becomes dominating for angles larger than 20° to the shower axis [Perrone & Risse 2002].

$N_e(X)$ is the number of electrons at depth X calculated by the Gaisser-Hillas formula and $f(X,E)$ is the energy distribution of the electrons. The threshold energy E_t is the lowest energy above which a particle emits Cherenkov light. This value and also the $\delta = n - 1$ is atmosphere dependent via the refractive index of air n. A simulation of Cherenkov profiles in different atmospheric conditions can be seen in Fig. 3.35. The example is given for a proton

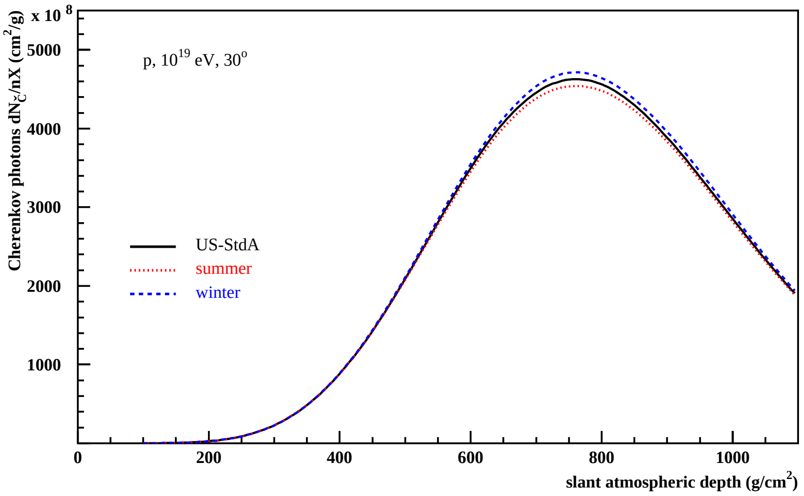

Figure 3.35: Longitudinal profile of emitted Cherenkov photons (λ = 300 - 400 nm) in the next g/cm^2 in slant depth. The abscissa is also in slant depth [Engel 2003].

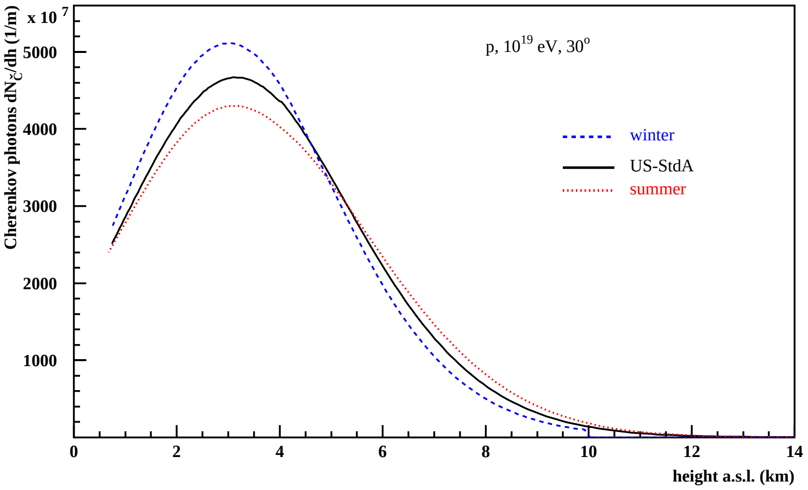

Figure 3.36: Longitudinal profile of emitted Cherenkov photons in the next vertical metre. The abscissa represents height in km [Engel 2003].

induced shower with 10^{19} eV and 30° zenith angle and the Cherenkov photons are calculated in the wavelength range between 300 and 400 nm. A small suppression of Cherenkov emission occurs in summer compared to the US-StdA and in winter more Cherenkov photons are emitted. Both phenomena are in the order of 2%. Converting this photon profiles into emitted photons per next vertical metre vs. height, the graphs in Fig. 3.36 are obtained. The additional influence of the atmospheric depth profiles strengthens the differences between the atmospheric models. During winter, most Cherenkov photons are emitted at 3.05 km for the exemplary EAS and the amount is higher by 9.5% compared to the US-StdA at its maximum at 3.13 km. During summer, the maximum is nearly at the same position as in US-StdA, 3.10 km, however the amount of emitted Cherenkov photons is reduced by 7.6%.

Comparable to the emission of fluorescence photons, the atmospheric effect induced by temperature and pressure in the first case and by the refractive index in the second case is small, well below 5%. However, the distribution of atmospheric density resulting in the atmospheric depth profile, is decisive.

Chapter 4

Measurements in Argentina

The evidence of various atmospheric dependences on the development and detection of EAS using the fluorescence technique demands detailed measurements of the atmospheric conditions at the location of the Auger experiment. The discussions in Chap. 3 have revealed that not only atmospheric data at ground are needed but complete profiles. Since Malargüe is in a rural area, no meteorologic stations performing radio soundings exist nearby. Consequently, the measurements had to be performed which was done within this work.

The aim of the measurements was to obtain the atmospheric profiles at the experiment site in Argentina. How much do they deviate from the conditions described in the US-StdA, mostly applied in EAS simulations and reconstructions, and from the conditions measured in Germany, starting point of this investigation?

One of the subsequent measurement goals was to figure out the stability of weather conditions during each season. How much is the development and detection of EAS affected by moving front systems? Resulting in the question: How often have the radio soundings to be performed? Another goal was to measure the stability during a night. Are the observed EAS data biased by the temperature development during one day?

4.1 Experimental Methods

For including the atmospheric dependences correctly in the reconstruction and simulation processes, at least the profiles of temperature and pressure are needed. A common technique, often applied by meteorologists, are radio soundings. Small, mostly full automatic radiosondes are launched with helium filled balloons. We have adopted this technique by using radiosondes of type DFM-97 with GPS option and a receiver groundstation GK-90C produced by *Dr. Graw Messgeräte* [Graw]. The system provides more information than the minimum requirements. Additionally to the temperature and pressure profiles, the humidity, wind speed and direction, and the GPS position are transmitted from the radiosonde to the groundstation. The accuracy of the data is very good, for details see Table 4.1. The transmitting frequency is selectable between 402 - 406 MHz, in steps of 20 kHz. The deviation of the frequencies is smaller than 5 kHz and the transmission range is at least 250 km.

On average, the data are stored every 3 - 4 seconds, but at least every 8 seconds. This ensures values in height steps between 3 m and 50 m, with an average step size of $\approx$ 20 m.

Data Type	Error	Resolution	Useful Range	Measurable Range
temperature	$< 0.2°$C	0.1°C	-80°C to +44°	-90°C to +80°
humidity	$< 5\%$	1%	not specified	0% to 105%
pressure	< 0.5 hPa < 1.0 hPa	0.1 hPa 0.1 hPa	5 hPa to 200 hPa 200 hPa to 1080 hPa	2 hPa to 1100 hPa

Table 4.1: Accuracies of the radio sounding system [Graw].

The balloon rate of climb depends strongly on pressure and wind conditions as well as the balloon filling pressure ranging between 100 m/min and 500 m/min with an average of roughly 200 m/min. The upper limit of the measurements is given by the height of balloon burst.

Five measurement campaigns have been performed in Argentina covering each season. The winter was observed twice in order to enlarge the statistics and to test possible unstable conditions during a year caused by the ENSO effect (Chap. 2.3). Details of all campaigns can be found in Appendix C. In total, 52 balloon ascents could be accomplished successfully. The main emphasis was placed on night measurements since the Auger fluorescence telescope only can observe EAS at clear nights with less than 50% illuminated moon.

During the first set of measurements in August 2002, small balloons were used. These already burst at heights around 17 km a.s.l. The position of the groundstation, equal to the starting place of the radiosonde, was varied in order to figure out the optimal position for covering entirely the surface array (Fig. 4.1). Most balloons were driven by the typical west wind, therefore it was decided to launch all radiosondes in the future from the fluorescence building Coihueco at the western boundary of the array.

In the second term, still the small balloons were used. The starting point was fixed at Coihueco and nearly all paths of the balloons crossed the array. However, the spring was marked by strong winds blowing the radiosondes far away, partly more than 100 km.

During the third campaign, in early 2003, the radiosondes were launched with larger balloons. Most of them could reach altitudes of 24 km a.s.l. The wind conditions during this summer period were very interesting. Below ≈ 20 km a.s.l., the typical west wind was dominating but above that height, the wind strength broke down. The balloon stopped its lateral motion but was still rising. Around 1 km higher up, the balloon was caught from an east drift and came back. This can be seen in Fig. 4.2, several balloon paths cross the array towards East, then looping around and flying back towards West.

In the Argentine autumn, April / May 2003, the wind was as strong as in the spring before. The first days of measurements were signed by northwest wind and then it turned to a more southwest wind. Also in this term, the radiosondes were launched with large balloons reaching higher altitudes.

The fifth campaign took place in July / August 2003 being early winter. The windspeeds were quite moderate, but the directions often changed ranging from south wind via the more typical west wind to northnorthwest wind, see Fig. C.38 in Appendix C.5. However, the obtained data differ remarkable from the winter data measured in 2002. During this term, they resemble more spring data.

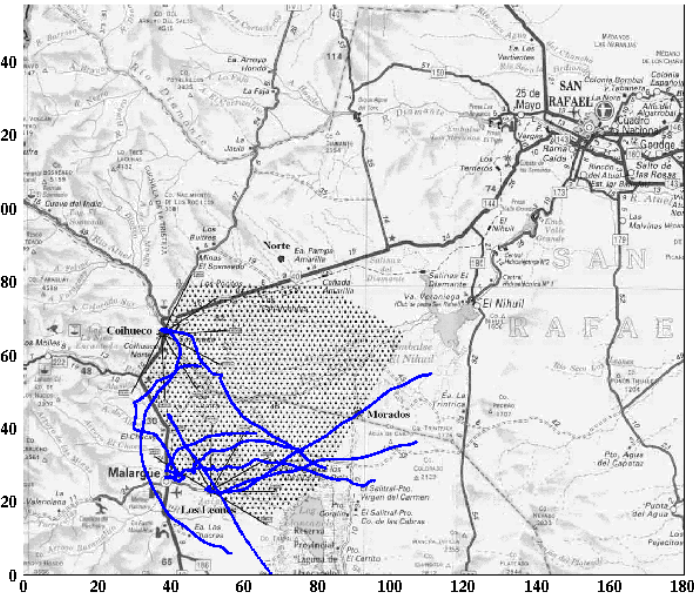

Figure 4.1: Balloon paths of all launches in August 2002 from different starting positions. In total nine launches were performed. A kilometre scale is indicated at the frame.

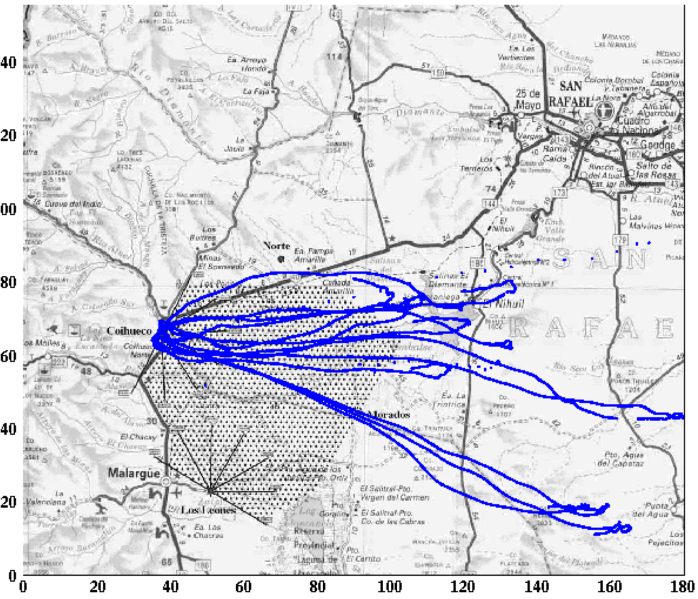

Figure 4.2: Balloon paths of all launches in January / February 2003 from the fluorescence detector building Coihueco. In total 15 launches were performed. A kilometre scale is indicated at the frame.

4.2 Data Obtained and Derived Models

Mainly, the data for temperature, pressure, and humidity in dependence of height are obtained. Based on these data, the density and atmospheric depth as a function of height can be calculated, see Chapter 2. Firstly, the direct observables are discussed, and secondly, the derived quantities. For this discussion, only average profiles of the measured data are shown. The detailed profiles of all launches are given in Appendix C. With respect to the emphasis on night conditions and the demand of clear sky for the fluorescence observation, only selected launches are used for the fits. The winter data will be distinguished in two types, I and II. Winter type I is marked by lower temperatures and lower pressure. Winter II is very similar to spring conditions. The underlying launches for the averaging are the following:

- winter I: ⟨3⟩, ⟨5⟩, ⟨6⟩, ⟨7⟩, ⟨45⟩, ⟨51⟩, ⟨52⟩
- spring: ⟨10⟩, ⟨11⟩, ⟨13⟩, ⟨14⟩, ⟨16⟩
- summer: ⟨20⟩ - ⟨30⟩, ⟨33⟩
- autumn: ⟨37⟩, ⟨39⟩ - ⟨44⟩
  ascent ⟨35⟩ also fulfils the requirements, however it is left out because it is not representative for that measuring period (compare Fig. C.31)
- winter II: ⟨9⟩, ⟨46⟩ - ⟨50⟩.

The obtained formulas for the fitted profiles are given in Appendix A.4 - A.8. These derived atmospheric models for Argentina are valid up to 25 km a.s.l.

The temperature typically has a constant lapse rate of 6.5 K/km up to ≈ 11 km a.s.l. (in the US-StdA). Realistic profiles in Argentina seem to be quite different, Fig. 4.3. Except for winter I, all temperatures at ground (here around 1.4 km a.s.l.) are higher than in the free atmosphere due to the mountain mass effect. Also the lapse rates are larger. The summer temperatures are characterised by a large lapse rate of ≈ 7.2 K/km, the winter II shows the smallest lapse rate of 6.6 K/km which is almost equal to the one of the US-StdA. The lapse rate for winter I is much larger and exceeds even the summer value with 7.3 K/km. The expected more or less constant temperatures within the tropopause can hardly be found, the lapse rates just decrease. During summer, the temperatures reach a minimum of about -70°C at 17 - 18 km. Autumn and spring also show a minimum with about -60°C at that height. During winter, the temperatures are highest in the tropopause compared to other seasons. An unexpected observation was made during autumn. Several temperature profiles show a thick inversion layer near ground, see Fig C.30. This layer exists at least up to 2.5 km, sometimes however even up to ≈ 3 km a.s.l. The strength of the inversion can be 5 - 7 K but also constant temperatures ranging over 400 m within the layer occur. The inversions are not comprehended in the fitted average profile. The variations of the individual temperature profiles around its seasonal average is about ±5 K, only during spring it is slightly more, ±7 - 8 K. Percental, this means a spread of ±2%, 3% respectively.

The pressure conditions in Argentina are highly fluctuating, Fig. 4.4. Since the decrease is nearly exponential, the differences are hardly visible. Printing the differences of the fitted pressure profiles according to the US-StdA, the large variations become obvious, see

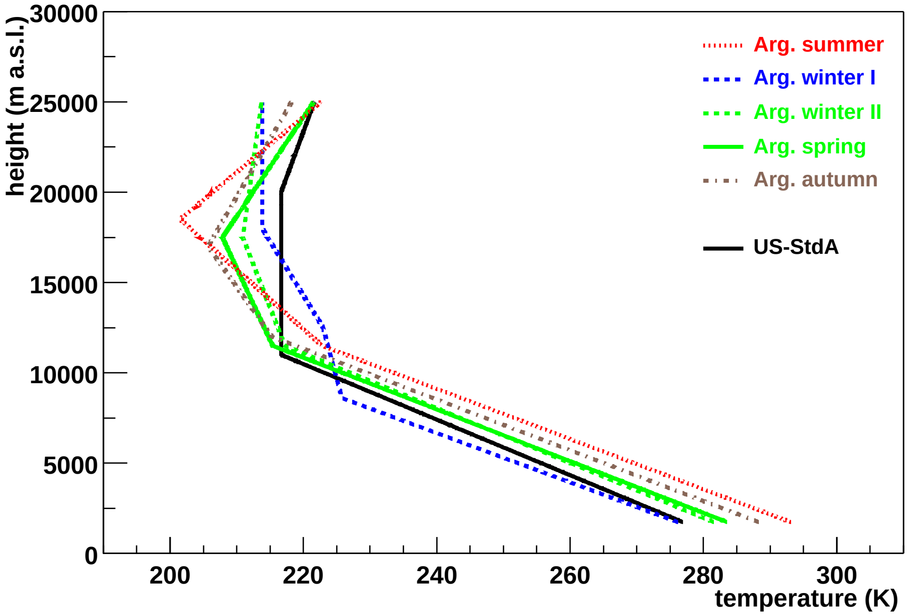

Figure 4.3: Average temperature profiles for Argentina.

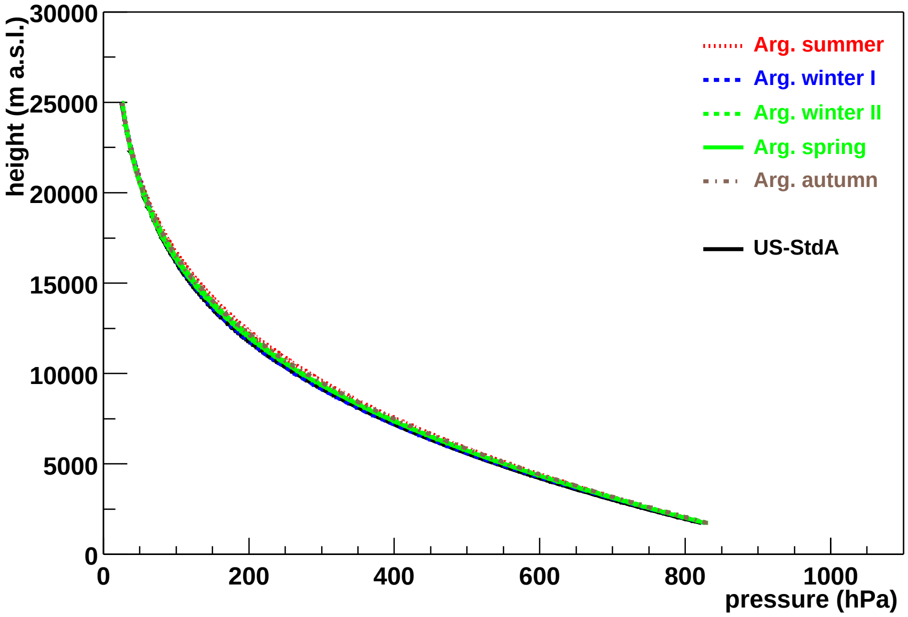

Figure 4.4: Average pressure profiles for Argentina.

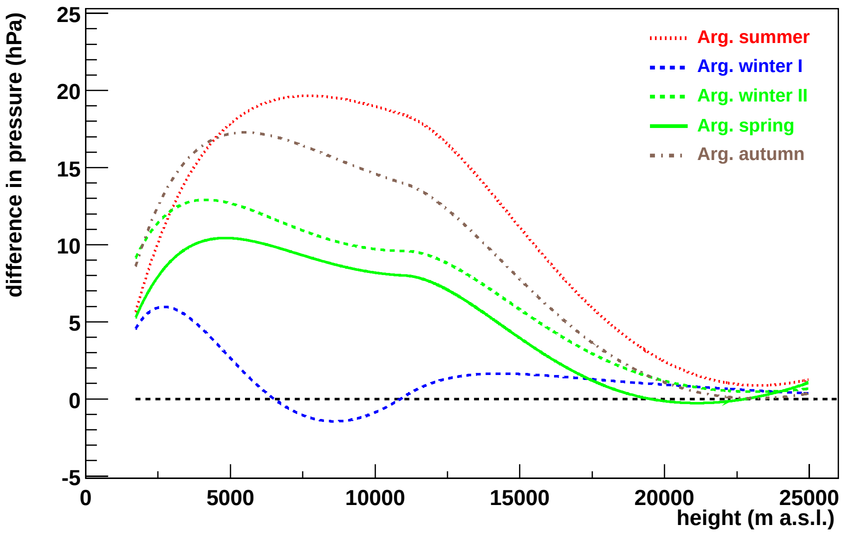

Figure 4.5: Relative differences in the average pressure profiles for Argentina according to the US-StdA.

Fig. 4.5. Most important for the EAS development are the differences at heights between 3 and 9 km a.s.l. During winter I, there appears a small low pressure zone but not very distinct. The milder winter II condition has the same shape like spring even with a little bit higher pressure values. During all other seasons, there is high pressure, very pronounced in summer with $\approx +20$ hPa according to the US-StdA at a large altitude range. The absolute variations of the individual pressure profiles around its seasonal average is uniformly large up to ≈ 10 km a.s.l. and higher in the atmosphere the differences decrease rapidly. For all seasons, the fluctuations are ± 4 - 5 hPa at lower altitudes. However, again during spring the conditions are less stabile with pressure variation of ± 8 hPa at altitudes between 5 and 10 km. The percentage variations are small near ground ($\approx 1\%$) and become larger for higher altitudes (2% in spring and autumn) or stay roughly constant despite decreasing absolute variations because of the nearly exponential pressure decrease. As mentioned above, one atmospheric profile of a clear night is not inserted in the averaging. Ascent $\langle 35 \rangle$ is marked by a drop of ground pressure of 15 hPa compared to the values measured in the nights before and after. Consequently, the entire pressure profile is lower than all others measured during the autumn measurement campaign.

For calculating the air density, also the water vapour could be taken into account (Chapter 2.1). However the effect of lowering the density induced by 100% relative humidity in air is very small, less than 1% of the density for dry air. In Argentina, there is most of the time and at all altitudes less than 40% relative humidity in air. Only small horizontal bands with more water vapour can occur. Therefore, for determining the average density profiles and subsequently the atmospheric depth, the relative humidity is set to zero percent. For determining the individual density and atmospheric depth profiles of each measurement, the data of the relative humidity are included. In the region of balloon data, the height interval $\Delta h = h_2 - h_1$ between two adjacent measurements is sufficiently small, so that the local additional atmospheric depth is deduced from:

$$\Delta X \;=\; \frac{\rho(h_1) \;+\; \rho(h_2)}{2} \cdot (h_2 \;-\; h_1),\text{ where } h_2 \;>\; h_1. \tag{4.1}$$

At the upper end of the measured profile, at the height of balloon burst h_b, it is assumed

$$p(h_b) \;=\; g \cdot \int_{h_b}^{\infty} \rho(h) \cdot dh \;\Leftrightarrow\; X_b \;=\; \frac{p(h_b)}{g(\Phi, h_b)}, \tag{4.2}$$

with $g(\Phi, h_b)$, the acceleration due to gravity, as defined in Chapter 2.1. The resulting atmospheric depth profiles for the seasonal average conditions are plotted in Figure 4.6. Like for the pressure profiles, the differences are hardly to discern. The differences of the Argentine profiles according to the US-StdA (Fig. 4.7) reveal as large variations as for the European conditions. The individual atmospheric depth profiles calculated by the measured temperature and pressure profiles are shown in Appendix C in seasonal groups. During summer, the atmospheric depth is strongly enhanced between 3 and 15 km a.s.l., for about 15 - 20 g/cm^2 compared to the US-StdA. The conditions were very stable during that campaign in January / February 2003. Nevertheless, shifts from measurement to measurement can appear in the range of $\approx$ 8 g/cm^2. This number is valid up to 10 km. Compared to the European summer, the atmospheric depth profile in Argentina is a little bit more enhanced and for a much larger height interval. During winter I, the atmospheric depth is larger below 7 km compared to the US-StdA and between 7 and 11 km a.s.l. it is about 3 g/cm^2 less. This behaviour is similar to the European winter albeit not as distinct. Not represented by this fit are the data of ascent ⟨1⟩. The launch for ⟨1⟩ was performed during daytime, being similar to spring or autumn situations. Ascents ⟨9⟩ was recorded during a night, indicating a strong change for the weather conditions which is affirmed by the minimum and maximum temperatures taken

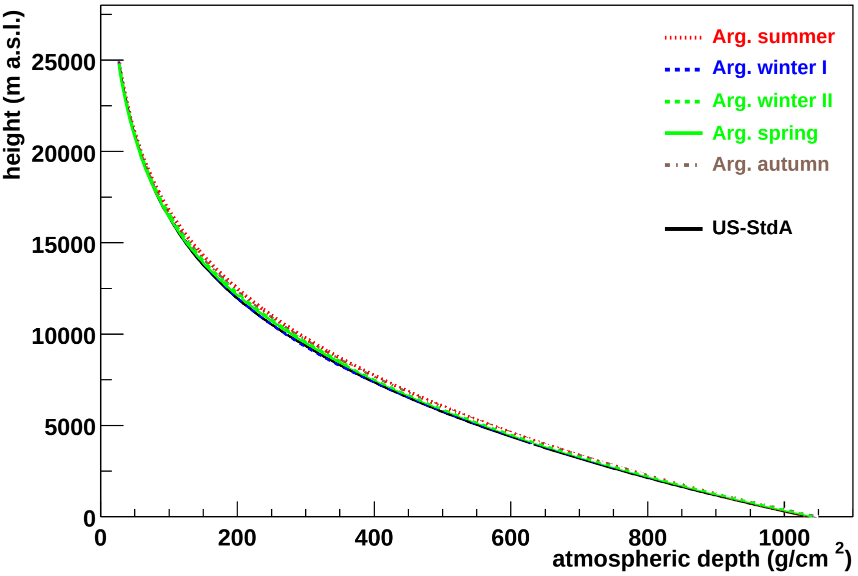

Figure 4.6: Average atmospheric depth profiles for the seasons in Argentina and for the US-StdA.

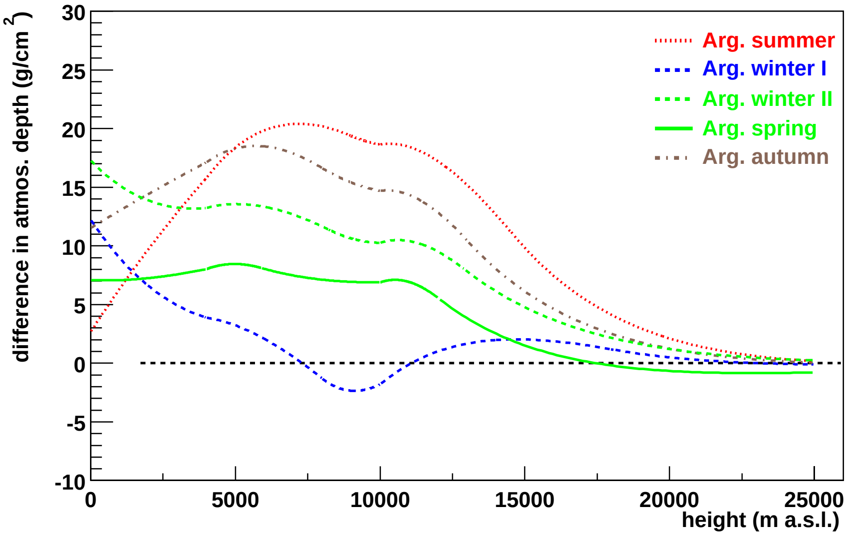

Figure 4.7: Differences in the average atmospheric depth profiles for the seasons in Argentina according to the US-StdA.

at Malargüe airport (see Fig. C.1) and is comprehended by the fit for winter II. Also ascents ⟨2⟩ and ⟨4⟩ were measured during daytime but fitting very well to the obtained average profile for winter I. The average atmospheric depth curves for spring and autumn are between the summer and winter I profiles, both tending towards summer conditions. During spring, the atmospheric depth is constantly enhanced by 7g/cm^2 up to 11 km a.s.l. The fluctuations for the individual profiles are at ground as large as for summer. Higher in the atmosphere, they even become larger, $\approx$ 15 g/cm^2. The sequence of launches ⟨10⟩, ⟨11⟩, ⟨12⟩, and ⟨13⟩ reveals again a change in the weather conditions. Especially ⟨10⟩ seems to be untypical. The conditions during the second winter campaign are similar to spring. The values for atmospheric depth averaged to winter II condition are in-between spring and autumn. An already obvious problem is that the behaviour of the profiles higher up in the atmosphere can not be deduced easily from the data at ground. During autumn and winter II, the atmospheric depth profiles are up to 3 - 5 km most enhanced compared to the US-StdA, even exceeding the summer conditions. Higher in the atmosphere, the autumn atmospheric depth profile is $\approx$ 4 g/cm^2 lower and during winter II, it is 8 g/cm^2 lower than in the Argentine summer. The variations for the individual atmospheric depth profiles in autumn around its seasonal mean are 8 - 10 g/cm^2. For winter II, the variations are also nearly 10 g/cm^2 at ground but increase to 20 g/cm^2 at 7 - 9 km. Ascent ⟨35⟩ is the most diverging profile concerning pressure and subsequently atmospheric depth. This profile enlarges the variation in atmospheric depth at ground to 15 g/cm^2 in autumn.

For using the obtained atmospheric depth profiles in the simulation code CORSIKA, one has to parameterise them, see equation (2.19). This is done for the layer 1 - 4 and layer 5 is adopted as given for the US-StdA, Table B.1. Therefore, the lower limit of layer 1 is set to 0 km a.s.l. and the upper limit of layer 4 is 100 km a.s.l. Having no data above the balloon burst height, one has to assume some atmospheric conditions. Here the pressure profile for the US-StdA is utilised, which is given up to 71 km a.s.l., but shifted according to the last measured pressure value of the data. At 100 km, the atmospheric depth value is fixed to $1.28292 \cdot 10^{-3}$ g/cm^2, according to the Linsley parameterisation for the US-StdA used in CORSIKA. The obtained parameter for the Argentine seasons are given in Tables B.4 - B.8.

Furthermore, a slightly improved parameterisation for the US-StdA is presented. Its calculation conforms to the method applied to the measured data. Based on the temperature and pressure profiles for the US-StdA (A.1), the Linsley parameterisation shows several small deviations. Using the possibility of choosing the layer boundaries freely, a more self-consistent parameterisation can be found. The values are given in Table B.9 and the differences of the Argentine seasonal atmospheric depth profiles according to the new US-StdA parameterisation are shown in Fig. 4.8. It can be seen that the new parameterisation of the US-StdA is about 2 -

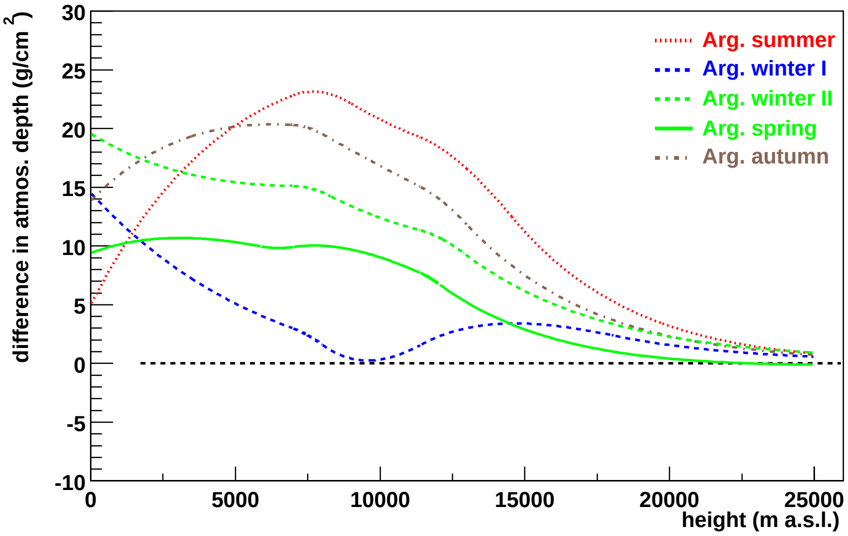

Figure 4.8: Differences in the average atmospheric depth profiles for the seasons in Argentina according to the new parameterisation of the US-StdA.

3 g/cm^2 smaller than the Linsley parameterisation between 1 and 11 km a.s.l. Consequently, all Argentine atmospheres have atmospheric depth values above the new US-StdA.

The set of parameterisations for temperature, pressure, and atmospheric depth profiles for each season are used in the following chapters as the valid atmospheric models for Argentina. However, it has to be stressed that the statistics of the data is still very low. The models obtained are not representative, despite this restriction they are useful tools for estimating the atmospheric influences on the EAS development and detection with more realistic atmospheres than the US-StdA. Anyhow, the aim of this investigation is to emphasise the possible variability due to changing atmospheric conditions. Each undetected temporary weather capriole biases the measured EAS data and has to be taken into account for a proper reconstruction. In this sense, some possible systematic variations of the atmospheric profiles are discussed.

4.3 Variability within the Data

Possible systematic variations can be caused by different locations of the radiosonde launch. This was checked during August 2002, when the balloons were started at 4 different locations nearby the Auger surface array. Another aspect is the daily periodic cycle of the temperature. Details of the effects on the atmospheric depth profiles are separated into day-night changes and variations during one night.

Different Locations

One of the Auger site requirements has been a flat, homogeneous landscape which is met in Argentina at the Pampa Amarilla. The Andes are approximately 80 km away and no local valley conditions affect the atmosphere above the Auger array anymore. This homogeneity is reflected in the measurements. No effects on the atmospheric profiles can be found for radiosonde launches from the fluorescence buildings Los Leones and Coihueco, nor from a place directly in the Pampa at the route to La Junta, a small village near Malargüe. However, launching the balloons from Malargüe city, which was performed in the backyard of a house, can affect the measurement. Especially during winter, a city represents a local heat island. The consequences for the data obtained have been quite small, but the chimney effect of warm rising air could be observed by the balloon path for the lowest 1 - 2 km.

Day-Night Effects

In each season, once the situation appeared that the conditions at night and the following day or vice versa has been measured. During winter, ascent $\langle 4 \rangle$ was measured at daytime and the temperature at ground is typically warmer by ≈ 3 K compared to $\langle 5 \rangle$, measured at the following night. Higher in the atmosphere, the profiles are nearly the same. The pressure is 4 hPa lower at ground at day, but the differences merge at higher altitudes. Consequently, also the atmospheric depth profiles are separated by 4 g/cm^2 at ground. At 7 - 8 km, the day profile is only reduced by 2 g/cm^2 compared to the night profile. During spring, at the 10th of November 2002, shortly after midnight a radio sounding was performed and also in the afternoon. The temperatures at ground differ by 10 K converging above 5 km a.s.l. The pressure values are more or less the same, swinging by 2 hPa around each other. Despite the large temperature difference, the atmospheric depth profiles show analogous behaviours to the pressure profiles, therefore, being approximately the same. Ascents $\langle 31 \rangle$ and $\langle 32 \rangle$ were measured in summer. The temperatures at ground are at the end of that campaign 10 K less than at the beginning. However, almost no differences can be regarded between day and nighttime of one day. The pressure also shows no variations during 24 h resulting in hardly distinguishable atmospheric depth profiles. The day / night measurement during autumn coincide with the extreme pressure situation of $\langle 35 \rangle$, already mentioned above (Chapter 4.2). At that night, the pressure value at ground is 14 hPa less than at the following day or the previous night. The temperature obtained during launch $\langle 36 \rangle$ is about 10 K higher near ground than in the night. This results in quite different atmospheric depth profiles.

Finally, one can say that the difference from day to night are not very large. This is valid for the pressure conditions, mainly determining the atmospheric depth profiles. Consequently, no large differences in the EAS development are expected. Only the temperature curves may differ, which can affect the fluorescence yield. However, one counterexample could be measured during autumn. The pressure was very untypical at that night, which could already be observed at ground. Nevertheless, a correction according to the ground value by 14 hPa, would lead to an overcorrection by 6 hPa at heights around 7.5 km a.s.l.

Variations during Night

Several measurements during one night have only been performed during winter and summer. Usually, one launch is started at late evening, another between midnight and 2 o'clock in the morning, and sometimes a last ascent for the night between four and six o'clock depending on the season, so that the balloon bursts just before sunrise. In August 2002, one night with two and one night with three launches have been done. It can be stated, that the conditions from late evening to shortly after midnight hardly change. Just before sunrise, the temperature at ground is lower due to the radiation of Earth. Another change could be observed higher in the atmosphere. The early morning launch ⟨7⟩ shows a larger temperature inversion between 10 and 13 km a.s.l. than ascents ⟨5⟩ and ⟨6⟩. This inversion is accompanied by higher pressure compared to the conditions earlier during that night, resulting in pressure values very similar to the US-StdA. During summer, in several nights more than one ascent have been done. This campaign confirms that hardly any variations from late evening to shortly after midnight appear. However, the conditions shortly before sunrise may change. On February, 6th, 2003, the temperature at ground was ≈ 8 K lower just before sunrise than during the night. The pressure values at ground are nearly the same but at late evening, the pressure decreases more slowly with increasing altitude compared to just before sunrise. For the resulting atmospheric depth profile, the values at ground are the same during the whole night. At altitudes above 5 km, the values are 2 g/cm^2 less in early morning than during night. In the following night, three launches have been performed. Again, the temperatures are lowest shortly before sunrise. During this night, the pressure is about 2 hPa lower at the midnight launch. These lower values hold up also for higher altitudes. Early in the morning, the situation at ground has returned to the one at late evening. At higher altitudes however, the slightly lower pressure remains. The atmospheric depth profiles behave proportional to the pressure.

The study of variations during a night reveals only small changes for all seasons. The atmospheric depth profiles are very similar to each other. They might only be affected by moving pressure fronts, an effect which is not correlated with the time of day. The temperature decreases near ground towards morning. This hardly distorts the atmospheric depth profiles. A slight increase of fluorescence photon emission is to be expected, however this is partly compensated by a slight decrease in transmission due to Rayleigh scattering.

As a consequence for continuous operation of the Auger Observatory, it can be adhered that actual atmospheric profiles should be measured for important, high energetic EAS events. If e.g. an EAS with $E_0 > 10^{20}$ eV has been observed, the atmospheric profiles should also be obtained during the same night by launching a radiosonde. However, it is sufficient to perform the ascent 2 or 3 hours after the EAS events has been detected. A relevant change for the atmospheric conditions within this time period is unlikely and the reconstruction of that EAS event could be done with higher accuracy than by applying an averaged atmosphere in the reconstruction procedures.

Chapter 5

Observables of the Auger Detectors in the Argentine Atmosphere

5.1 Fluorescence Detector

The important observables for the Auger fluorescence detector have been studied for the US-StdA and European atmospheric models (Chap. 3). The decisive factor turns out to be the conversion from atmospheric depth to geometrical height. Also the emission of fluorescence light suffers atmospheric dependences as well as the transmission due to Rayleigh scattering of that light. The measurements of atmospheric profiles in the Pampa Amarilla have revealed similar seasonal variations to Europe (Chap. 4). Consequently, the observables for the fluorescence detector obtained with Argentine atmospheric models are discussed in the following. As the data for winter II are very similar to spring, only winter I, spring, summer, and autumn data are used for these analyses.

5.1.1 Longitudinal Energy Deposit Profile

With respect to the emission of fluorescence light, the longitudinal development of an air shower is treated in form of the energy deposit. Assuming the same longitudinal development in terms of atmospheric depth, only the transformation to geometrical heights has to be done. The relation between atmospheric depth and geometrical height for Argentine conditions can be seen in Figs. 4.6 and 4.7. Again, the exemplary iron induced shower with 10^{19} eV primary energy and 60° inclination is chosen.

The shower maximum at 347.0 g/cm^2 vertical atmospheric depth corresponds to 8.361 km a.s.l. in the US-StdA, see Fig. 5.1. The larger values for the atmospheric depth in Argentine summer lead to a shift of the position of the shower maximum higher up in the atmosphere by nearly 400 m. The shower develops earlier than in the US-StdA and reaches its maximum already at 8.759 km a.s.l. The opposite case occurs during winter I, however much less distinctly. The atmospheric depth profile for Argentine winter I is closest to the US-StdA compared to other Argentine seasons, therefore also the energy deposit profiles are nearly the same. The EAS in winter I deposits its energy deeper in the atmosphere and the maximum is at 8.323 km a.s.l. The vertical difference of the maximum position between summer and

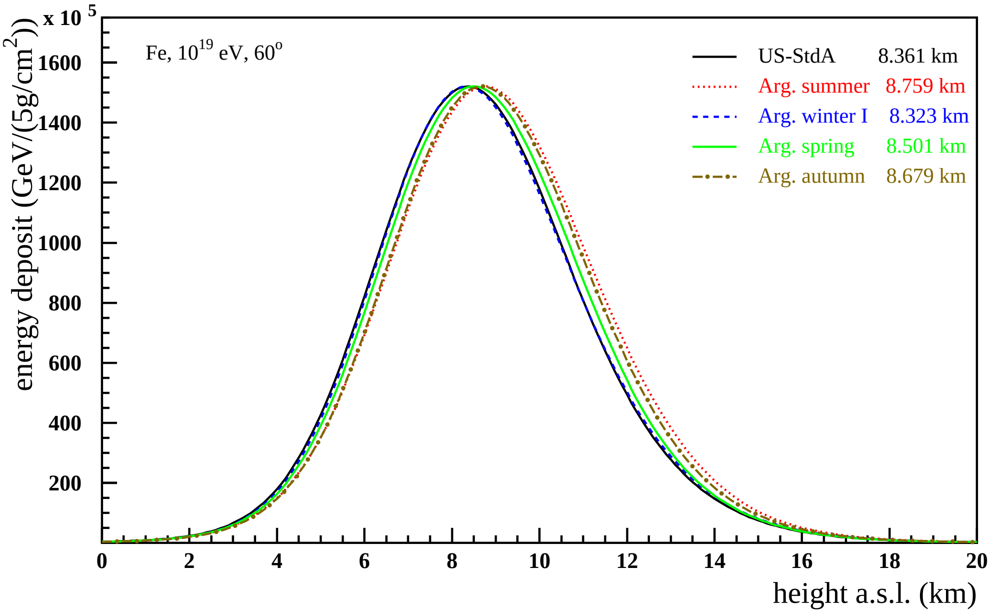

Figure 5.1: Longitudinal development of the energy deposit vs. height in km for an iron induced, 10^{19} eV, 60° inclined shower in Argentine atmospheres.

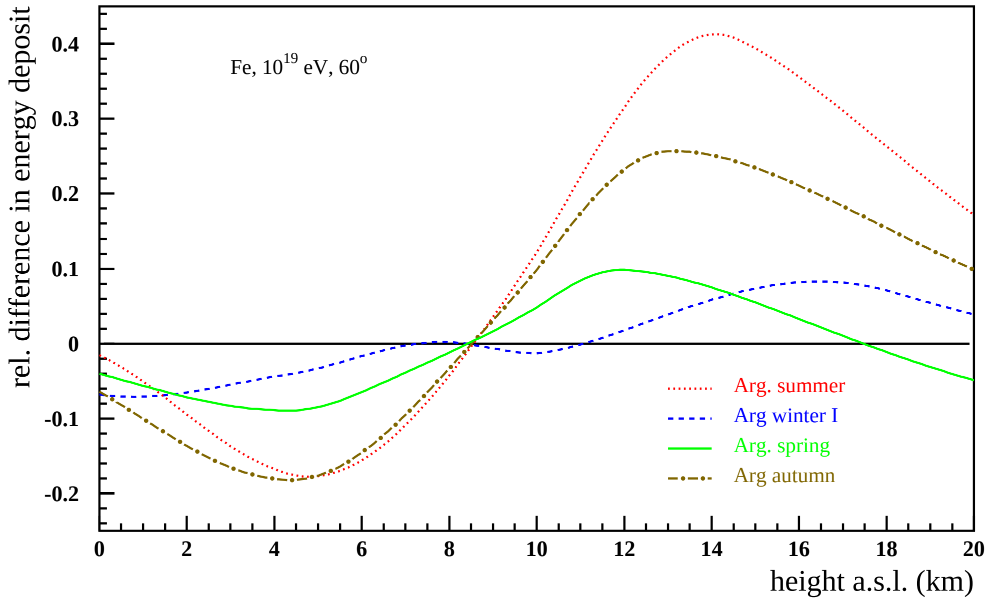

Figure 5.2: Relative differences of the energy deposit between Argentine seasonal atmospheres and the US-StdA for Fe-induced, 10^{19} eV, 60° inclined showers.

winter I conditions amounts to 436 m. Showers developing during spring or autumn lie in between the two extrema. The iron shower in autumn resembles the summer shower. Its maximum is just below the summer maximum, namely at 8.679 km. The EAS in spring reaches its maximum at 8.501 km a.s.l. The relative differences of the energy deposit of EAS in all four Argentine seasons compared to the US-StdA are plotted in Fig. 5.2. Most important for the fluorescence detection technique is the altitude range from ground level up to $\approx$ 12 km a.s.l. The assumption of the same energy deposit profile in terms of atmospheric depth becomes apparent around 8.5 km. The amount of energy deposit at the shower maximum is the same for all cases. Closer towards ground, especially the energy deposit of summer and autumn showers is reduced, strongest at 4 - 5 km with -18%. At ground level of the Auger experiment, 1.4 km a.s.l., the EAS depose equal amounts of energy during winter, spring, and summer.

Trying to identify the type of the primary particle for a large amount of events and not on the event-by-event basis, the standard deviation of the X_{max} value can be used [Risse 2003]. Simulations have shown that the position of the shower maximum with respect to the atmospheric depth is dependent on the hadronic interaction model applied to the Monte Carlo simulation. However, the standard deviation is independent of the interaction model and furthermore, it is significantly smaller for iron induced EAS ($\approx$ 20 g/cm^2) than for proton induced showers ($\approx$ 60 g/cm^2), compare Figure 3.3. Assuming a uniform atmosphere for all events, the value of the standard deviation for X_{max} could reveal the composition of the shower sample. But the different atmospheric conditions itself introduce an additional standard deviation of 10 - 15 g/cm^2 for the shower maximum position while using an averaged atmospheric model all over the year. The expected distribution of X_{max} will be broadened which could be misinterpreted as a lighter composition of the shower sample.

The profiles of the energy deposit of an air shower, observable by the Auger fluorescence telescopes, show large seasonal dependences in Argentina. Despite the same development vs. atmospheric depth, the positions of the shower maximum are shifted significantly and additionally, the profiles are distorted. Mainly during summer and autumn, but also during spring, a large decrease in energy deposit appears.

5.1.2 Emission of Fluorescence Light

As introduced in Chap. 3.3.1, the amount of emitted fluorescence photons by an EAS or a single charged particle is proportional to its energy deposit. For separating the atmospheric influences, in a first step the fluorescence emission induced by a 1.4 MeV electron is shown, Fig. 5.3. The overall shape of the emission profile for all fluorescence photons with wavelengths between 300 and 400 nm is like for European conditions, compare Fig. 3.19. From ground to heights around 10 km, the fluorescence yield increases slowly. Above, the yield decreases disclosing the sensitivity to temperature and pressure variations. During winter I, the lower temperatures compared to the other atmospheric models below 9 km a.s.l. induce a higher fluorescence yield. Up to 17 km, the temperatures are comparative warm leading to a reduced fluorescence yield. During spring, summer, and autumn, the temperatures are higher than in the US-StdA and in winter I, therefore the fluorescence yield is decreased mostly in summer. Above 14 km a.s.l., the very low temperatures during summer result in a very high fluorescence yield. The differences of the fluorescence yield for the Argentine seasons compared to the US-StdA are well below 3%. At Auger level, the increased fluorescence yield during winter I is

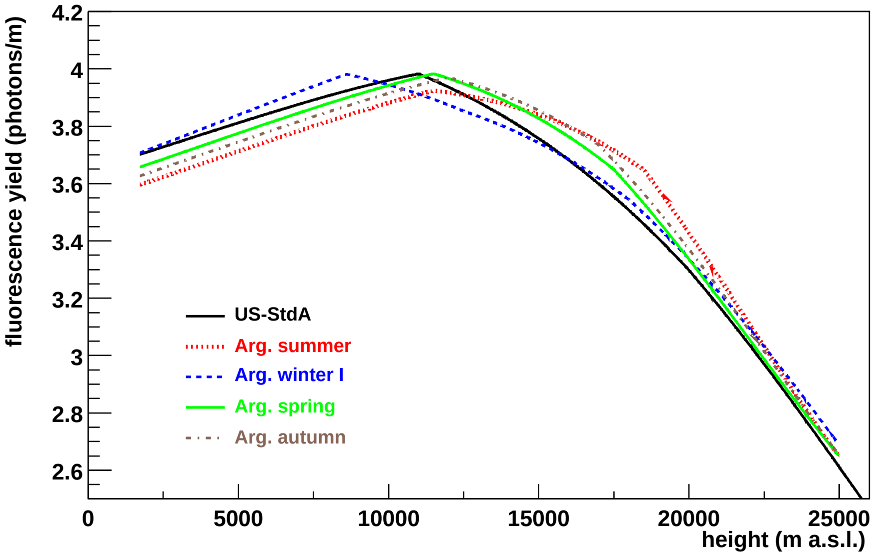

Figure 5.3: Fluorescence yield profile for a 1.4 MeV electron with vertical incidence in Argentine atmospheres. The given yield is a sum of all emitted photons between 300 and 400 nm.

negligible, however the decrease in summer amounts to 2.8%. At ≈ 8 km, the differences of summer and winter I to the US-StdA are in the same size but with opposite signs. In winter I, the fluorescence yield is 1.4% higher than in the US-StdA, and in summer 2.2% lower.

For the fluorescence yield of an EAS, these seasonal variations superpose the seasonal variations of the energy deposit profiles, Fig. 5.4. With respect to the position of the shower maximum, the still increasing fluorescence yield at these heights for all seasons induces an additional shift of the maximum position towards higher altitudes by approximately 45 m. For the winter I conditions, the decrease in the fluorescence yield starts only some hundred metres above the shower maximum position. Therefore, a small descent of the region with a smaller temperature lapse rate would cause a shift of the maximum in fluorescence yield closer to the ground enlarging the difference between summer and winter I. Nevertheless, for the assumed averaged atmospheric conditions, the vertical difference between the visible summer and winter I shower maximum is nearly the same as for the energy deposit, 439 m. The distortion of each shower profile is strengthened by the atmosphere dependent fluorescence emission. In Fig. 5.5, the reduction of the fluorescence yield for e.g. summer and autumn around 4 - 5 km a.s.l. is about 20% compared to the US-StdA. This value is exactly the superposition of the decrease in the energy deposit for the shower and the decrease in fluorescence emission.

Concluding, the emission of fluorescence light suffers some influences of atmospheric variations. The differences between summer and winter I conditions are 3 - 4%. The different profiles for the fluorescence yield lead to an additional shift of the position of the shower maximum compared to the pure shift of the position of the shower maximum concerning the energy deposit due to the conversion to geometrical heights. The reduction of the energy deposit for spring, summer, and autumn in Argentina below 8 km a.s.l. is strengthened by ≈ 2% as a superposition of the energy deposit profile and the fluorescence yield profile.

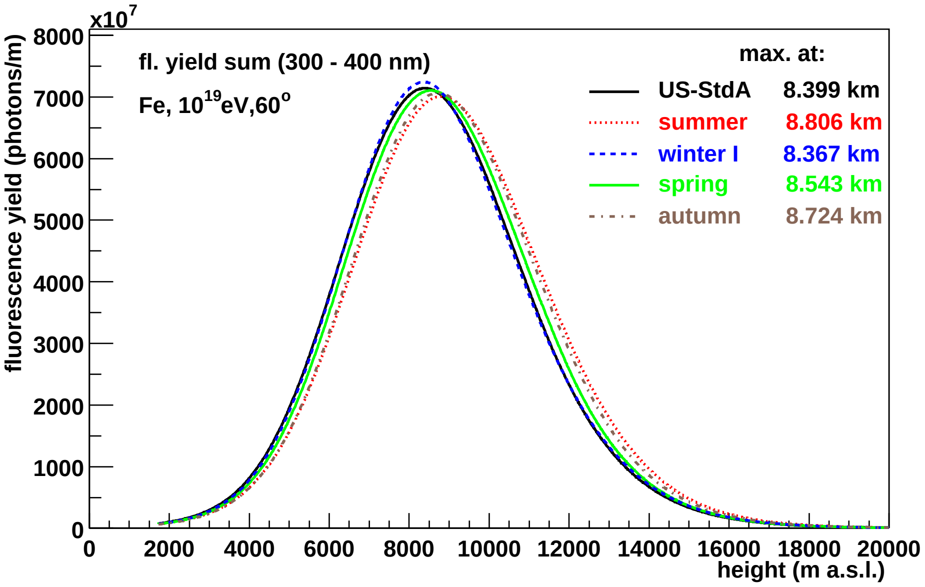

Figure 5.4: Fluorescence yield profile for a iron induced, 10^{19} eV, 60° inclined shower in Argentine atmospheres. The given yield is a sum of all emitted photons between 300 and 400 nm.

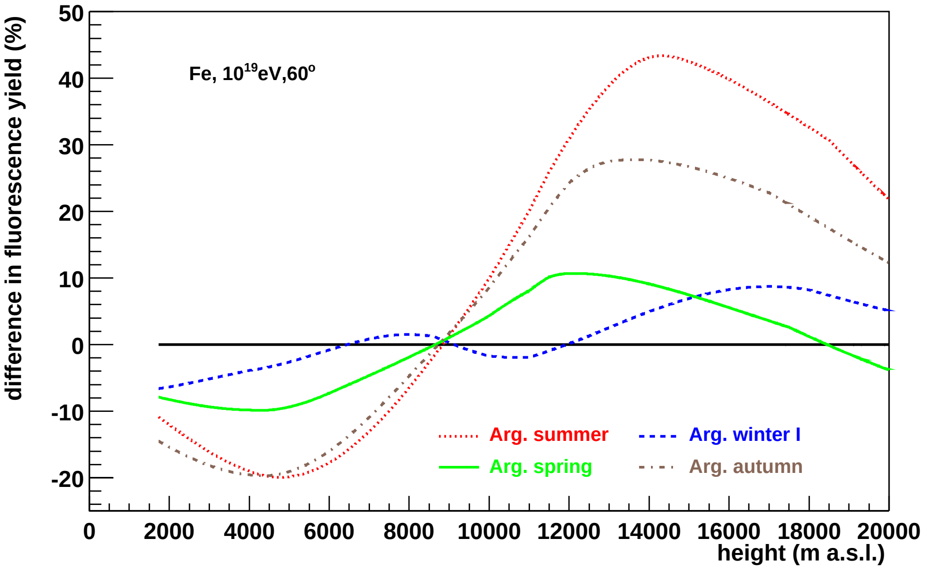

Figure 5.5: Relative differences of the fluorescence yield profile for a iron induced, 10^{19} eV, 60° inclined shower in Argentine atmospheres.

In order to test the extent of the atmosphere dependent distortions of the shower profiles, proton and iron induced showers are compared like in Chap. 3.3.2. The difference between these two shower types is 783 m in vertical height for the US-StdA at shower maximum (Fig. 3.24). Simulating a proton induced shower developing in Argentine summer conditions and an iron induced shower in Argentine winter conditions, both with 10^{19} eV and 60° inclination, the fluorescence yield profiles in Fig. 5.6 are obtained. Even if the effect is weaker than for the extreme European atmospheres, the profiles are quite close to each other in the average Argentine atmospheres. The maxima are only separated by 354 m which cannot be resolved easily by the Auger telescopes assuming the simple resolution introduced in Chap. 3.2.

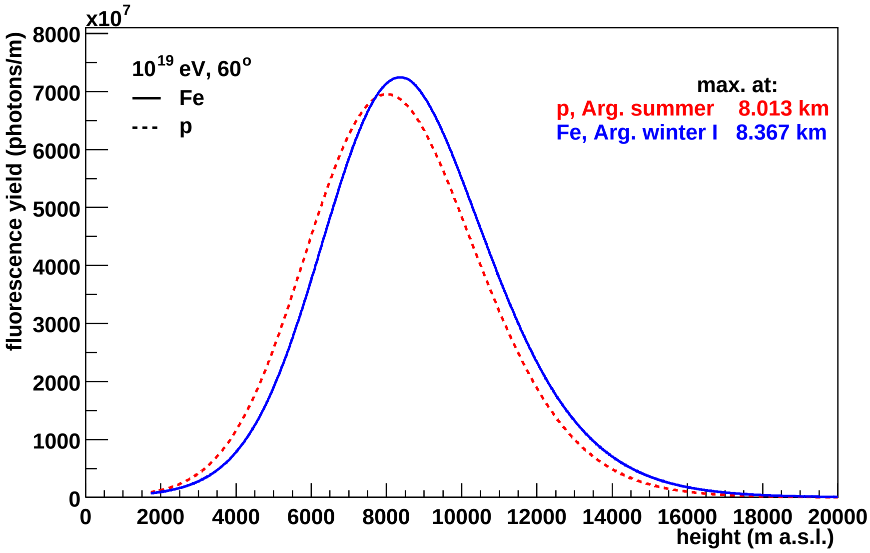

Figure 5.6: Fluorescence yield profiles for p-induced EAS in Argentine summer and F-induced EAS in Argentine winter both with 10^{19} eV and 60° inclination. The fluorescence yield is the sum of all emitted photons between 300 and 400 nm.

5.1.3 Transmission of Fluorescence Light

Underlying the argumentation of Chap. 3.4, only the transmission due to Rayleigh scattering is treated. The geometry as shown Fig. 3.26 is again chosen and the transmission is calculated for the Argentine seasonal atmospheric models. The result is given for the main wavelengths 337.1 nm, 357.7 nm, and 391.4 nm in Fig. 5.7. The overall tendency of higher transmission for longer wavelengths and lower transmission near ground is of course also valid in Argentina. In summer, the transmission coefficient is larger than in European summer and consequently larger than in the US-StdA. Near ground, the value for the 337.1 nm line is enlarged by 5.5% according to US-StdA decreasing with increasing altitude. In Argentine winter I, the transmission is more or less constantly reduced by 1% compared to the US-StdA.

Using the calculations of the transmission due to Rayleigh scattering for e.g. subtracting the Cherenkov background, a correction of the measured profiles can be performed. The profiles are shifted parallel according to the ground values of the US-StdA. The obtained

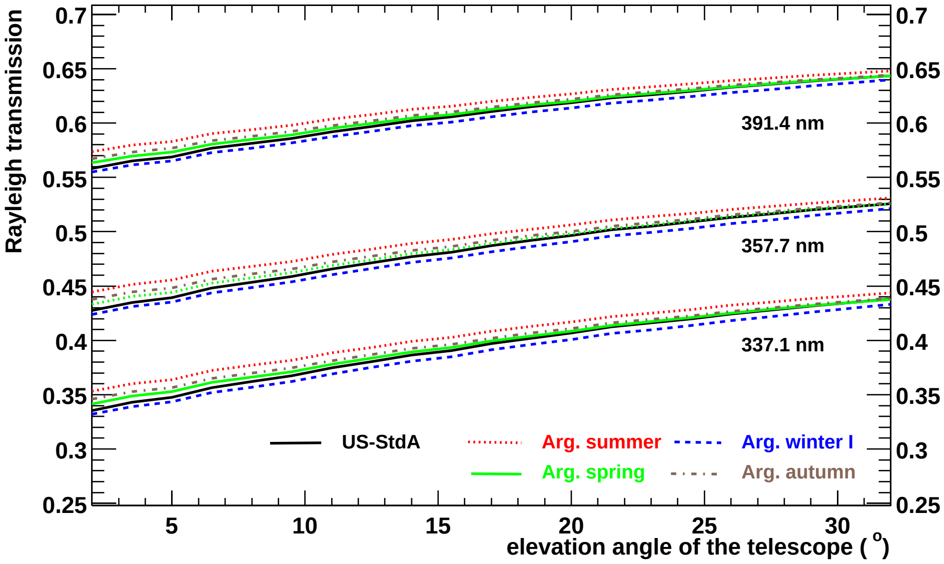

Figure 5.7: Transmission due to Rayleigh scattering for the geometry shown in Fig. 3.26 and for Argentine atmospheres.

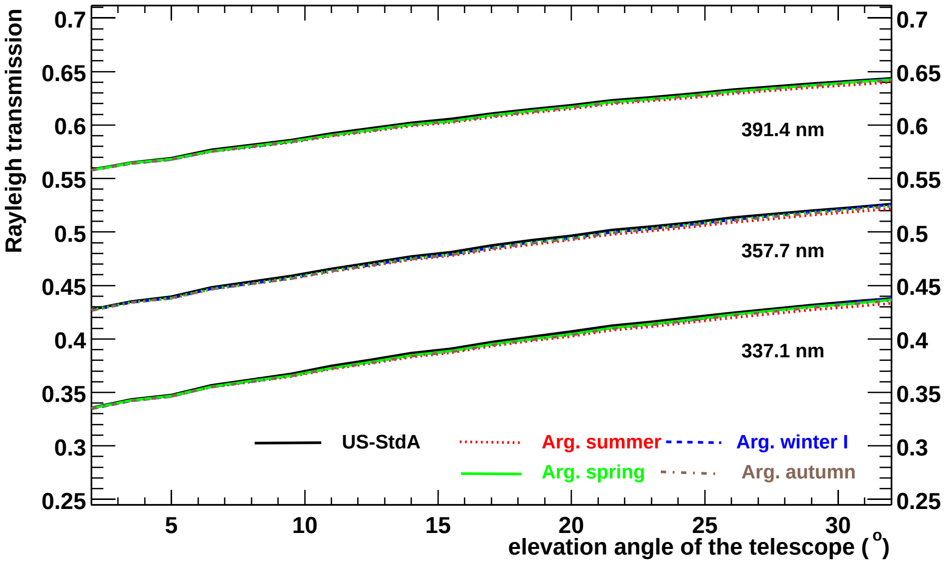

Figure 5.8: Transmission due to Rayleigh scattering with shifted Argentine atmospheric profiles according to the conditions at ground in the US-StdA.

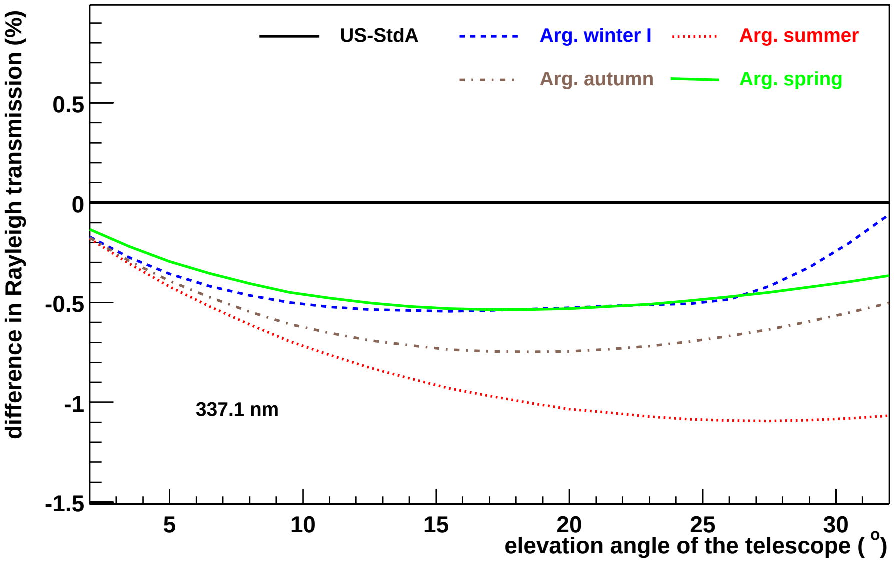

Figure 5.9: Percent difference in the transmission due to Rayleigh scattering of the shifted Argentine atmospheric profiles to the US-StdA, for 337.1 nm.

transmissions are then hardly changed due to atmospheric variations, see Fig. 5.8. The percent differences for the corrected case are plotted in Fig. 5.9 for the 337.1 nm wavelength. In all Argentine seasons, the correction would lead to a small underestimation being largest for summer. Above viewing angles of 20°, the difference is about 1%.

5.1.4 Observed Photon Profile at the Telescope

With the knowledge of all single contributing effects which are atmosphere dependent, a resulting photon profile at the diaphragm of the telescope can be calculated. The iron induced, 10^{19} eV, 60° shower is again chosen with a geometry like the one used for the discussion of the Rayleigh scattering, compare Fig. 3.26. However, it has to be mentioned that the 60° inclined EAS passes two adjacent single telescopes of one telescope station, see Fig. 1.7. The photons at the diaphragm are given for each of the 19 fluorescence wavelengths, but for clarity only two wavelengths, 337.1 nm and 391.4 nm, are plotted in Fig. 5.10. The number of photons emitted at 337.1 nm is more than three times higher than for the 391.4 nm, see Figure 3.17. However, the transmission of these photons is strongly reduced. Therefore, the longer wavelengths become more important. Also clearly visible is the shift of the shower maximum due to different atmospheres. Summer and autumn showers reach their maximum higher in the atmosphere but emit less photons compared to the US-StdA. The similarity of the Argentine winter conditions to the US-StdA are reflected in this Figure, too. The percent differences for the 337.1 nm photons is visualised in Fig. 5.11. The enhanced transmission during summer and autumn causes only some more photons compared to the pure effect of the fluorescence emission which is strongly suppressed during these seasons.

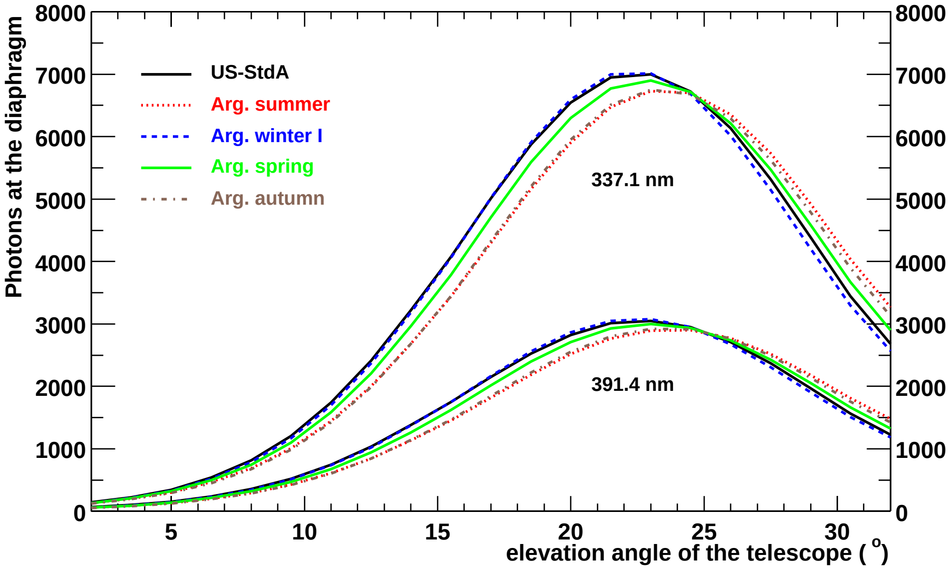

Figure 5.10: Photons at the diaphragm of the Auger telescope vs. elevation angle. The underlying EAS is iron induced, 10^{19} eV with 60° inclination and the geometry of the Rayleigh scattering is chosen, compare Fig. 3.26. Only the wavelength 337.1 nm and 391.4 nm are shown.

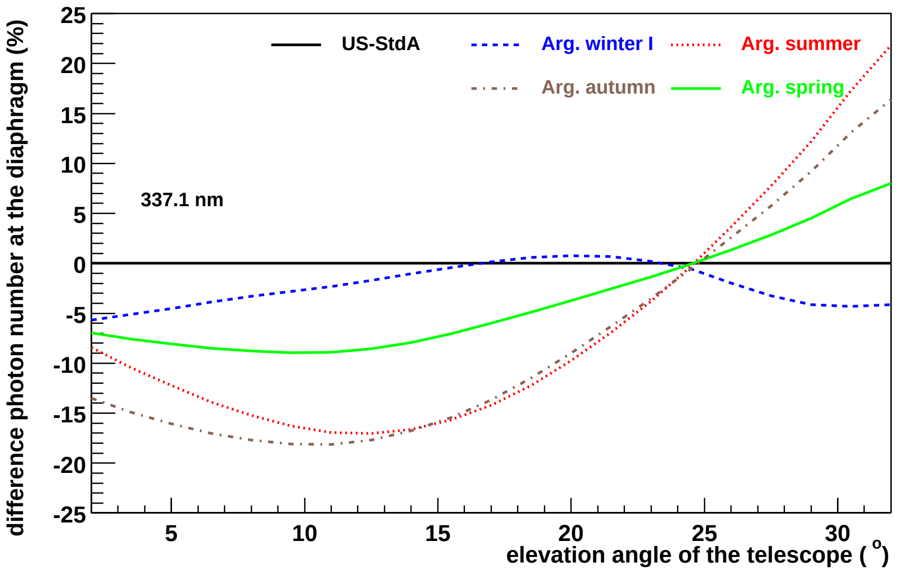

Figure 5.11: Percent difference in the number of photons at the diaphragm for 337.1 nm wavelength.

5.2 Surface Detector

A large advantage of the Auger observatory is its hybrid technique (Chap. 1.3). Water Cherenkov tanks at ground measure the primary energy and the type of the primary particle independently of the fluorescence telescopes. However, these two values are only obtained dependently on each other like for the fluorescence detectors. The important observable is the ratio of $e^+ + e^-$ and $\mu^+ + \mu^-$ changing with shower development and inclination angle of the EAS. Thus, the reconstruction procedures will extract the number of $(e^+ + e^-)$, further on shortly named electrons, and $(\mu^+ + \mu^-)$, further on muons, from the raw data. A rough estimation of atmospheric effects on these observables of the Auger surface detectors is given in the following.

Like for the calculations of the observables for the fluorescence detector, usually the atmospheric conditions of the US-StdA are taken. For estimating the largest atmospheric effects, the Argentine summer and winter I models are chosen. The average Auger surface level is at 1450 m a.s.l., meaning 870 g/cm^2 in US-StdA. The atmospheric depth values for summer and winter I are a little bit higher than for the US-StdA but amongst each other nearly the same, 878 g/cm^2. The shower particle numbers are simulated with CORSIKA. The average longitudinal development stage of 100 Fe-induced, 10^{19} eV showers with vertical incidence is analysed for electrons and muons. No lateral particle distribution is included. For these simulations, the height of first interaction is fixed at 11 g/cm^2 in all three atmospheric models for reducing the intrinsic shower-to-shower fluctuations.

During summer and winter, the surface detectors would record 2 - 2.5% less electrons than expected for the US-StdA. This is coherent with the fact that the atmospheric depth is 8 g/cm^2 higher at ground. The number of electrons is ascertained by the stage of the longitudinal development which is given by the atmospheric depth. Thus for summer and winter in Argentina, the showers have developed further than in the US-StdA at 1450 m resulting in an advanced electron number decrease. However, the electron number can partly be corrected by considering the air pressure at ground. Since pressure and atmospheric depth are roughly proportional, an equal value for the atmospheric depth at ground, the value given in the US-StdA, is assumed in the following. Then the lack of electrons diminishes. At 870 g/cm^2, the number of electrons in the shower is only 0.1% less for the winter atmosphere and 0.3% less for the summer atmosphere compared to the US-StdA. The number of muons depends on the fraction of $\pi^\pm$ and K$^\pm$ mesons decaying higher in the atmosphere, see Chap. 1.2. The probability relation between hadronic interaction and decay of the $\pi^\pm$ and K$^\pm$ mesons is shown in Fig. 5.12 for the US-StdA. Particles with less energy than given by the lines in the plot prefer the decay and contribute to the muonic component of the shower. Also the dependence on atmospheric depth can be seen, induced by the density distribution of air. The different atmospheric depth profiles for Argentine summer and winter I change the decay probability. This might be detected by slightly more (+0.4%) muons in winter and less (-2.1%) muons in summer at 1450 m a.s.l. than in the US-StdA. The summer conditions emerge as higher density above 8 km a.s.l., compare Fig. C.25, and higher atmospheric depth values over the total altitude range. This induces a higher interaction probability of $\pi^\pm$ mesons. During winter, the situation is close to the US-StdA. The number of muons at 1450 m is nearly the same, however during winter slightly increased due to less atmospheric depth between 7 and 11 km. A correction according to the ground value of atmospheric depth could not reduce the total difference between summer and winter of 2.5%. At 870 g/cm^2, there are 0.7% more

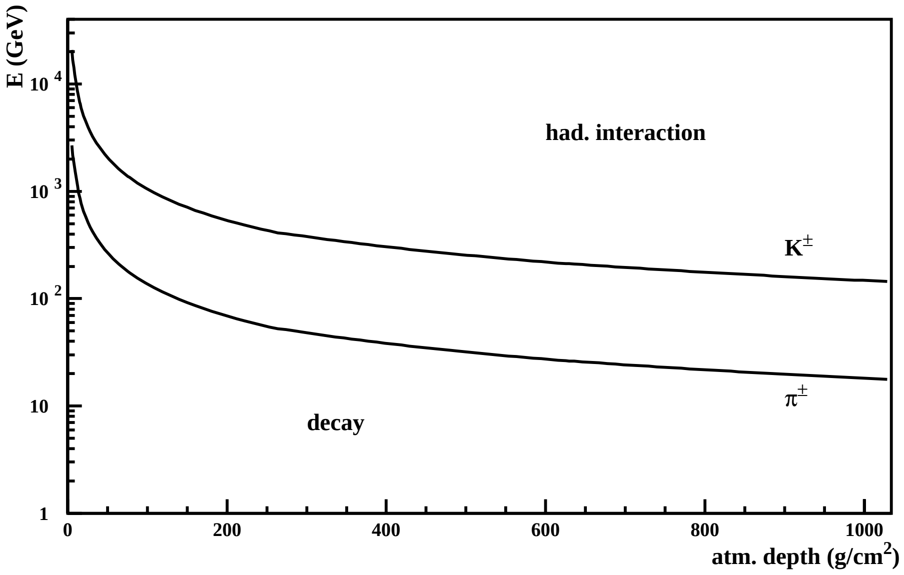

Figure 5.12: The upper line is the energetic boundary between hadronic interaction and decay of K$^\pm$ in the US-StdA. The lower line is the analogue curve for $\pi^\pm$. The K$^\pm$ decay results with $\approx$ 63.5% in $\mu^\pm$ and the $\pi^\pm$ decay results in almost 100% $\mu^\pm$ [Knapp 1997].

muons during winter and 1.8% less muons during summer.

The observed electron to muon ratio at 1450 m a.s.l. would be reduced for both situations, summer and winter, compared to US-StdA. The slightly enhanced muon number and reduced electron number during winter result in a 2.7% smaller ratio. During summer, the number of electrons has decreased already a little bit more but also the number of muons is reduced. This combination leads to a 0.5% smaller electron to muon ratio. A correction to 870 g/cm^2 would not improve the situation as the ratio would be lower by 0.8% during winter and during summer 1.6% higher than in the US-StdA. Therefore, a correction according to the ground value of atmospheric depth could correct the number of electrons sufficiently, however the number of muons depends more on the profile of atmospheric depth.

Another effect on the surface detectors induced by pressure, atmospheric depth conditions respectively, is the trigger efficiency. Higher ground values for these quantities induce an enhanced shower development stage. The influence of the atmospheric details on the trigger efficiency is largest for low energetic showers. These just reach the ground level with a detectable size before dying out. A slightly increased path would make these shower undetectable. Since the Auger experiment is still in its construction phase, a detailed study of the correlation of trigger efficiency and ground pressure is impossible. Nevertheless, this effect has been observed at other ground based experiments like KASCADE. This experiments measures EAS with primary energies in the region of 10^{15} eV [Antoni et al. 2003]. In Fig. 5.13, the anti-correlation between the trigger rate and ground pressure can be seen.

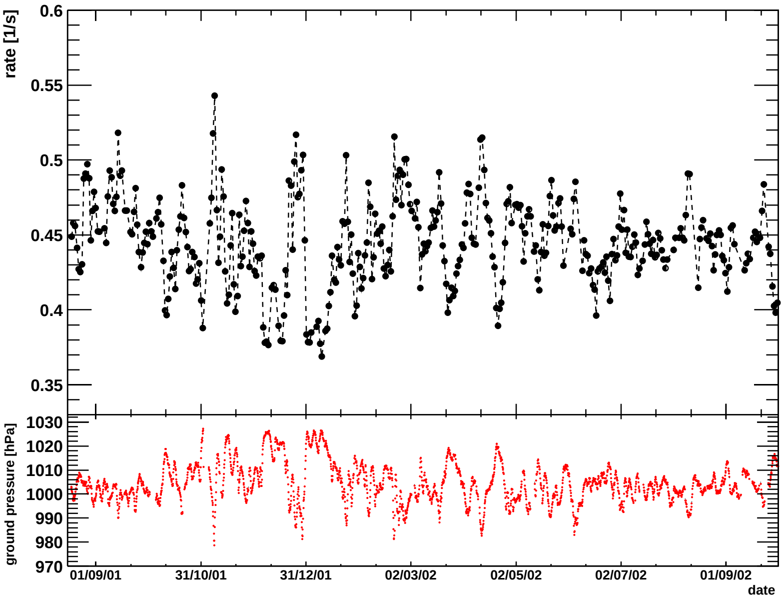

Figure 5.13: Anti-correlation between trigger efficiency and ground pressure for the KASCADE experiment. The upper plot shows the average shower rate versus time for EAS with $N_e > 10^4$. The lower panel displays the pressure at the experiment altitude (110 m a.s.l.) for the same period of time [Antoni et al. 2003].

Chapter 6

Alternative Data Sources for the Argentine Atmosphere

The previous chapters have shown that the model of the US-StdA is inadequate to describe the data measured in the Pampa Amarilla with the precision level required by the Auger experiment. The atmospheric profiles obtained by radio soundings are the exact solution for the application of atmospheric dependences. However, performing these measurements is an exhausting business. Therefore, in this chapter two alternatives are figured out to reduce the necessity of radio soundings. Different sources of atmospheric data are presented which may complement the information obtained by less frequently performed radio soundings.

6.1 Comparison with other Atmospheric Models

Several other models of the Earth's atmosphere exist, more detailed in terms of zonal and annual variations. One of them is the COSPAR[1] ***I****nternational* ***R****eference* ***A****tmosphere 1986* (CIRA 1986). It is given for every 5° latitude in the range 80°N to 80°S and for every month. The provided tables contain data for temperature, pressure, geopotential height, and geometrical height [CIRA 1986]. For the comparison with the measured data, the value for 35°S are selected.

The temperature profiles of the model cover a broad band of variation during a year, Fig. 6.1. At Auger ground level, the values for all month are higher than in the US-StdA decreasing with a slightly larger lapse rate than in the standard atmosphere. At altitudes between 16 and 17 km a.s.l., the temperatures are lowest especially for summer months with $\approx$ -65°C. These conditions represent the measured data above the Pampa Amarilla except for the obtained winter I.

The pressure conditions are outlined by monthly differences according to the US-StdA, see Fig. 6.2. The generally higher pressure values found in Malargüe are reflected by the CIRA model but the large variations measured are not covered entirely. The low pressure zone higher up in the atmosphere observed during winter is not described by the model as well as the strength of the high pressure zone higher up in the atmosphere during summer.

---

[1] Committee on Space Research

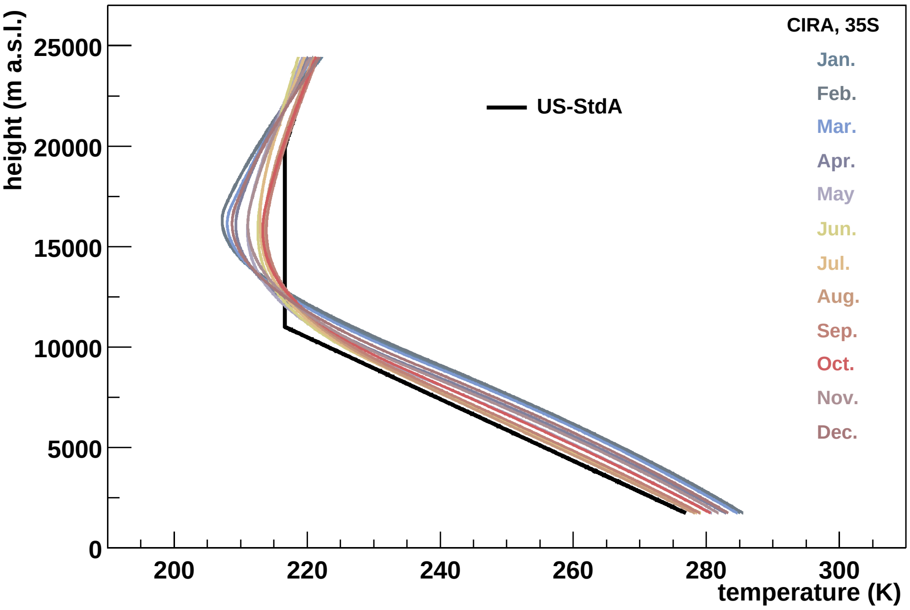

Figure 6.1: Temperature profiles of atmospheric model CIRA 1986 for 35°S and all 12 months.

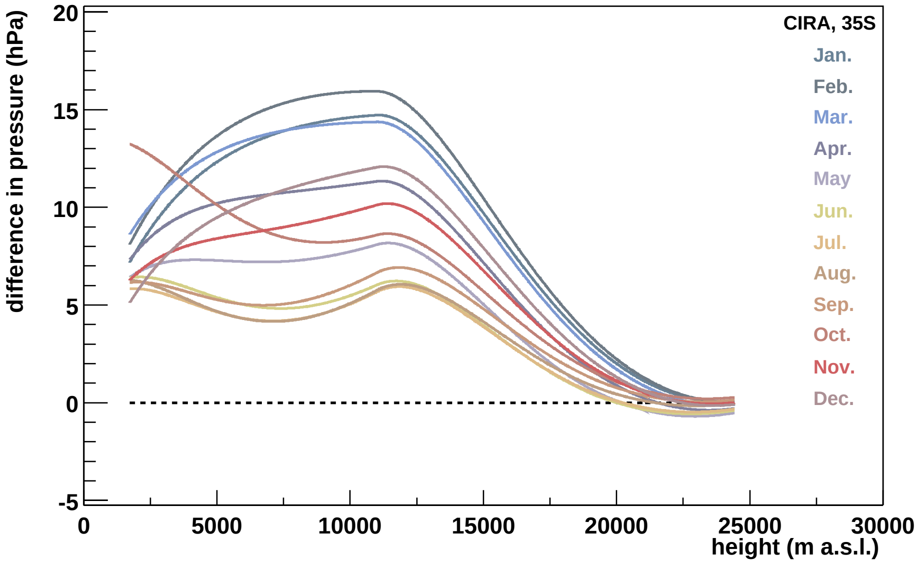

Figure 6.2: Difference in pressure profiles of atmospheric model CIRA 1986 for 35°S and all 12 months according to the US-StdA.

Based on these profiles, the density for each month is calculated as introduced in Chap. 2.1 with no humidity in air. Subsequently, the atmospheric depth profiles are derived. In Fig. 6.3, the differences of these values to the US-StdA are shown. Like for the pressure profiles, the average shape of atmospheric depths of the model are in agreement with Argentine data but not as pronounced. For direct comparison, the months during which the measurements were performed are plotted together with the average Argentine models, Fig. 6.4. The summer months given by the CIRA model describe the measured summer data quite well. Nearly at all altitudes, the CIRA data are < 3 g/cm^2 lower than the measured values. However for all other seasons, the CIRA model cannot reproduce the Argentine conditions. The CIRA winter months are in-between the two measured winter types, not reflecting the real large variations. CIRA winter is nearly identical with Argentine spring. CIRA spring is similar to the two CIRA autumn month. The spring model describes the high pressure conditions measured during November 2002 (compare Fig. C.18), but not the lower pressure situations which lead to the quite flat average curve for measured spring. The CIRA autumn months indicate larger variations during this season like it can be found for the measurements. However, the radiosonde values are on average 3 - 7 g/cm^2 higher than the CIRA values.

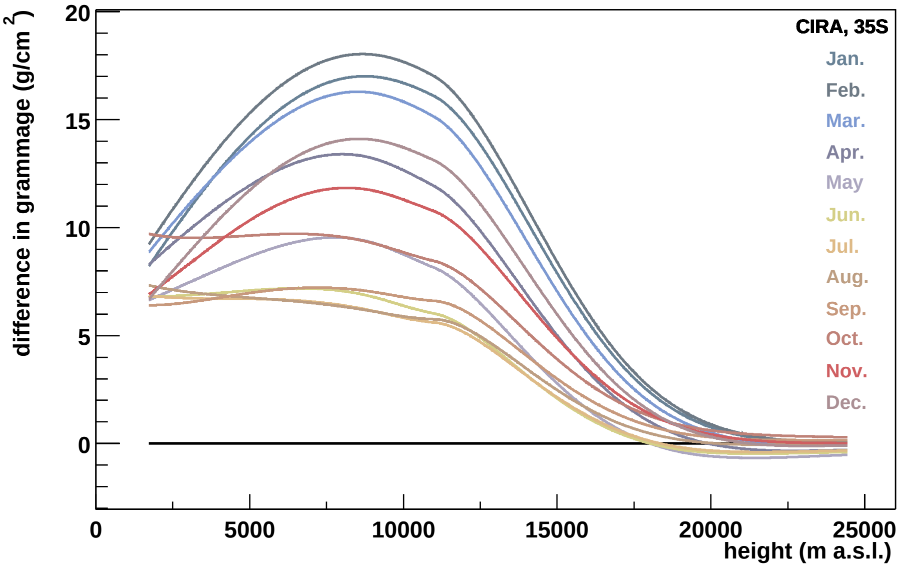

Figure 6.3: Difference in atmospheric depth profiles of atmospheric model CIRA 1986 for 35°S and all 12 months according to the US-StdA.

Concluding, it can be stated that the CIRA monthly models are closer to the data than the US-StdA. Nevertheless, the data measured in the present study cannot be reproduced by the CIRA mean values. For an accurate shower event reconstruction, it is necessary to educe the atmospheric conditions in more detail. For general shower simulations however, the CIRA model might be suitable and only smaller corrections remain to be done.

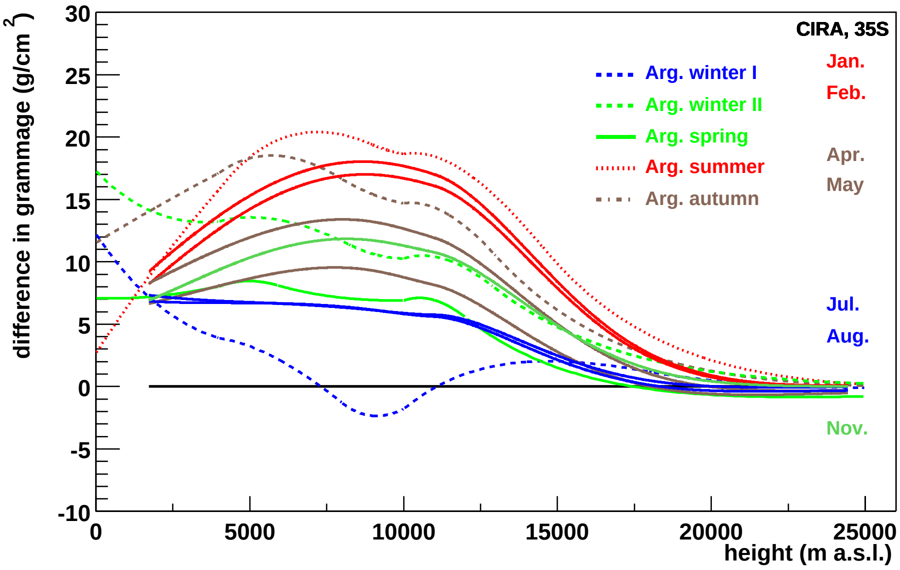

Figure 6.4: Difference in atmospheric depth profiles of atmospheric model CIRA 1986 for 35°S and the months during which the measurements were performed according to the US-StdA. For comparison, also the seasonal averaged profiles for Argentina are plotted.

6.2 Conclusions from Ground-based Weather Stations

For several reasons, the Auger observatory is operating ground-based weather stations. The aim is to record continously temperature and pressure values near the Earth's surface. For an appraisal if these data are sufficient for conclusions on the atmospheric profiles, a weather station located at 1750 m a.s.l. is assumed. This assumption is consistent with the situation at the fluorescence detector building Coihueco.

The most important factor on the air shower development is the atmospheric depth profile, derived from the air density profile. As known from Chapter 2, atmospheric depth is only approximately proportional to pressure. Thus, four different sets of atmospheric depth profiles measured in Argentina are compared. The underlying pressure profiles are not shown explicitly but can be found in Appendix C. Within each set, the same ground pressure values have been obtained by the radio sonde, strictly speaking the value at 1750 m a.s.l. which would be given by the ground-based weather station. The four sets cover each at least two different measurement campaigns. The first set is a comparison of atmospheric depth profiles with ground pressure values of 825.0 ± 0.2 hPa, see Figure 6.5. The second is for ground pressure of 826.0 ± 0.2 hPa (Figure 6.6), the third for 829.0 ± 0.2 hPa (Figure 6.7), and the fourth for 834.5 ± 0.2 hPa (Figure 6.8). The Figures always show the difference of the measured atmospheric depth to the values of the US-StdA. The three atmospheric depth profiles of the first set are measured during Argentine winter, spring, and summer. Each shows a typical behaviour according to its season, compare Figure 4.7. The same ground pressure value is reflected by the same atmospheric depth value at ground. Nevertheless, the shape of the profiles are totally different and at around 8 km a.s.l., the atmospheric depth

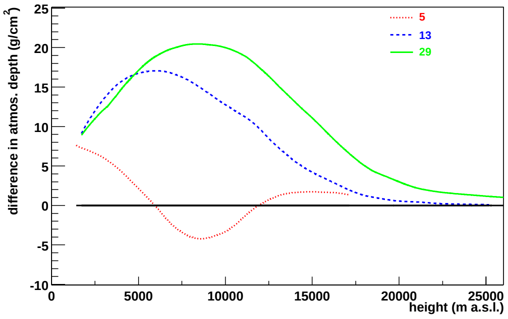

Figure 6.5: Difference of three atmospheric depth profiles, all of them with the same ground pressure value of 825.0 ± 0.2 hPa, to the US-StdA.

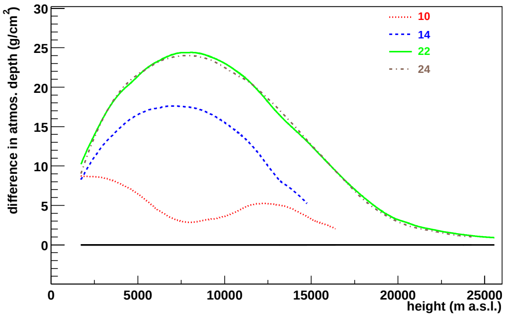

Figure 6.6: Difference of four atmospheric depth profiles, all of them with the same ground pressure value of 826.0 ± 0.2 hPa, to the US-StdA.

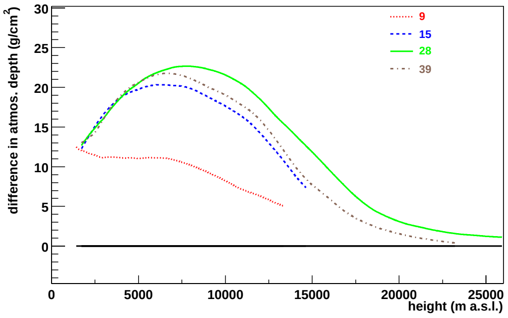

Figure 6.7: Difference of four atmospheric depth profiles, all of them with the same ground pressure value of 829.0 ± 0.2 hPa, to the US-StdA.

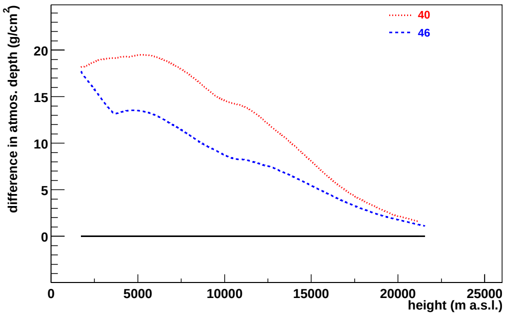

Figure 6.8: Difference of two atmospheric depth profiles, all of them with the same ground pressure value of 834.5 ± 0.2 hPa, to the US-StdA.

differs by 25 g/cm^2 for profile ⟨5⟩ and ⟨29⟩. The second set contains four profiles, two of them are measured during Argentine spring and the others during summer. The two summer profiles, ⟨22⟩ and ⟨24⟩, are typical for summer conditions and are hardly distinguishable from each other. Thus in this case, the same ground pressure value leads to the same atmospheric depth profiles. However, the two spring profiles differ from each other. ⟨10⟩ is a bit more similar to winter I type conditions than to spring and ⟨14⟩ resembles Argentine autumn profiles. The difference appeared during spring amounts to $\approx$ 15 g/cm^2 at around 8 km which is larger than the difference between the two summer profiles and ascent ⟨14⟩ of spring. The third set shows an example, where the same ground pressure values result in nearly the same atmospheric depth profiles independent of the season. Profiles of ascents ⟨15⟩, ⟨28⟩, and ⟨39⟩ are measured during spring, summer, and autumn respectively. The differences are negligible below 5 km a.s.l. and still very small, less than 4 g/cm^2, at higher altitudes. Only profiles ⟨9⟩, obtained during winter, is different. The fourth set contains two profiles with high ground pressure values of 834.5 hPa. The data are recorded during autumn and the second winter campaign. The overall shape of these atmospheric depth profiles is nearly the same, however difference of 6 g/cm^2 occur depending on altitude.

At this stage, no possibility is seen to conclude from ground pressure data on the atmospheric depth profiles. Different seasons do not demand necessarily different atmospheric depth profiles as shown in the third set. Sometimes, the same ground pressure within one season denotes the same atmospheric depth profiles but sometimes not (Figure 6.6). Thus, no regular scheme is spotted.

A further point of investigation is the influence of temperature profiles on the fluorescence yield. For this, data with the same ground temperature, again at 1750 m a.s.l., are compared. The fluorescence yield is exemplarily calculated for a 1.4 MeV electron with vertical incidence, for details see Chapter 3.3.1. Again, the underlying temperature and pressure profiles are not given explicitly but can be found in Appendix C. In total, three sets of data are given with ground temperatures of 3.0 ± 0.5°C, 12.0 ± 0.5°C, and 16.0 ± 0.5°C respectively. The profiles for the first set are measured during both winter campaigns and autumn, see Figure 6.9. The ground temperature is recorded to 3.0°C, however the corresponding pressure data may differ which turned out to be not very important. The difference in fluorescence yield to the values for the US-StdA given in percent are not very large but worth mentioning. The fluorescence profile calculated with the data of ascent ⟨5⟩ is quite different to the other winter profiles ⟨49⟩ and ⟨51⟩, obtained approximately one year later. The largest difference occurs at 6 km a.s.l. between ⟨5⟩ and ⟨49⟩ with 4% in the fluorescence yield. The second set, shown in Figure 6.10, is based on data of spring, summer, and autumn. The overall shape of the fluorescence yield profiles is nearly the same, the differences are in the order of 1%. The third

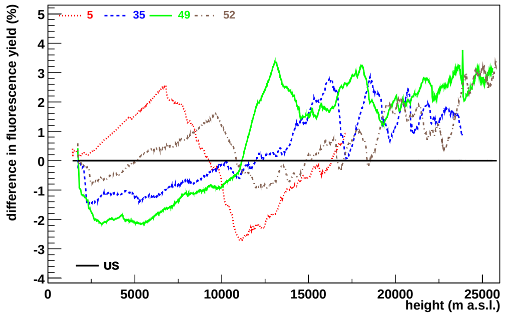

Figure 6.9: Difference of fluorescence yield profiles, all of them with the same ground temperature value of 3.0 ± 0.5°C, to the US-StdA.

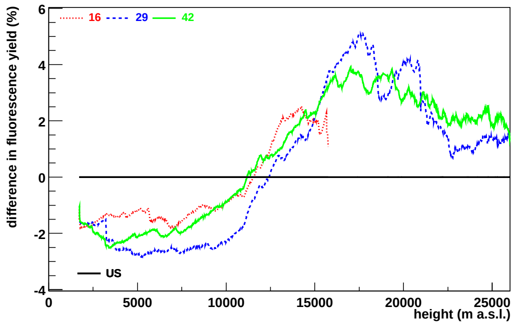

Figure 6.10: Difference of fluorescence yield profiles, all of them with the same ground temperature value of 12.0 ± 0.5°C, to the US-StdA.

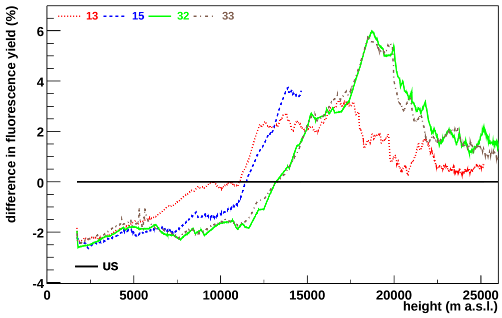

Figure 6.11: Difference of fluorescence yield profiles, all of them with the same ground temperature value of 16.0 ± 0.5°C, to the US-StdA.

set is marked by ground temperature values of 16.0°C. The data are each a couple of spring, ⟨13⟩ and ⟨15⟩, and summer, ⟨32⟩ and ⟨33⟩, given in Figure 6.11. Up to 6 km a.s.l., the fluorescence yield shows no variation by the individual profiles. However higher in the atmosphere, the fluorescence yield of ⟨13⟩ changes mostly and differs by 2% compared to the summer curves.

Thus, like for the atmospheric depth behaviour based on equal ground pressure, the fluorescence yield profile is not predictable by the ground temperature value. However, the fluctuations are not as large as for the atmospheric depth. All profiles have a main fluorescence yield shape in common, except for ⟨5⟩. Having a closer look to the exact values of temperature and fluorescence yield, it can be extracted that an increase of roughly 5°C results in a decrease in fluorescence yield of approximately 1% and vice versa for reversed signs.

For the following analysis, a second, higher located weather station is assumed, perhaps build on the top of a nearby mountain. Its altitude is chosen to 2500 m a.s.l. The question is if there exists a combination of data from both weather stations adopted for concluding to the correct atmospheric depth profiles as measured by the radio sondes. A further restriction is imposed since only profiles obtained during nights are taken into account. For these pressure profiles, the gradient of decrease between these two altitudes is calculated by

$$\frac{dp}{dh} = \frac{p_{2500} - p_{1750}}{0.75\ \mathrm{km}}. \tag{6.1}$$

The values are between 91.2 hPa/km and 100.0 hPa/km. Smaller values of pressure decrease are correlated with summer conditions, thus high pressure zones at higher altitudes. Larger values indicate conditions like in Argentine spring or winter I. The boundaries between the different behaviours are weak and a safe approximation can only be done for the border areas. A pressure decrease gradient between the two given heights of the weather stations of $\geq$ 98.0 hPa/km indicates a winter I or spring type condition for the atmospheric depth profile. In Figure 6.12 the difference in the atmospheric depth to the US-StdA is plotted for the seven candidates fulfilling the required condition. All of these profiles have in common that the difference to the US-StdA is at around 8 km a.s.l. 10 g/cm^2 smaller than at ground. The second safe indicator for a prediction of the atmospheric depth profile is a pressure decrease gradient of $\leq$ 94.0 hPa/km. The contemplable 13 candidates of all measured profiles are shown in Figure 6.13, again as the difference in atmospheric depth according to the US-StdA. These profiles represent the Argentine summer conditions and at 7 - 8 km a.s.l., the difference to the US-StdA is about 10 g/cm^2 larger than at ground.

A second weather station at higher altitudes may help to reduce the necessity of radio soundings. However for a safe prediction of atmospheric profiles based on the data of ground-based weather stations, more detailed analyses of combined information have to be done. The first rough test presented shows a possibility using pressure values but an implication of temperature data may advance the result since the application of the pressure decrease gradient leads to predictions for the atmospheric depth profiles of only 38.5% of all launches performed during one year. A further information, which could be consulted, is the Southern Oscillation Index, see Chapter 2.3. This value may help to identify the spacious weather situation. It is possible, that the remarkable difference between the two performed winter campaigns is reflected by the SOI, compare Figure 2.12. Especially for the field of ENSO effects on the weather conditions above the Auger array, long term studies remain to be done.

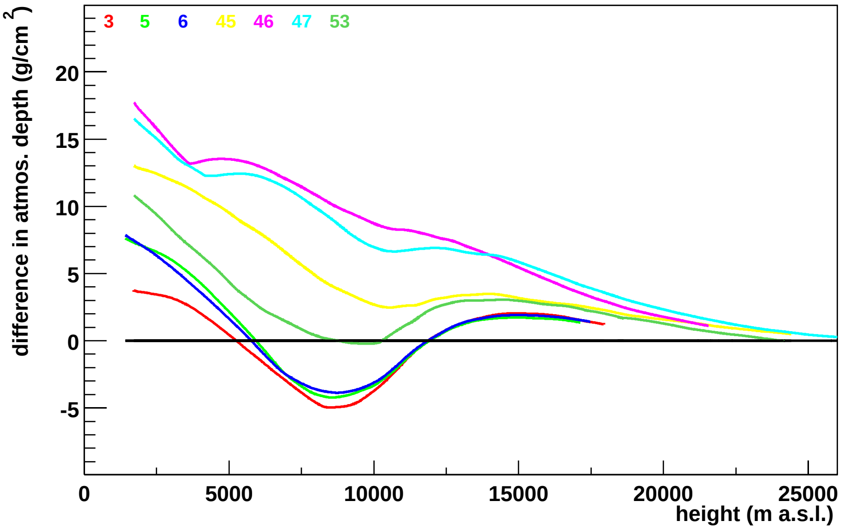

Figure 6.12: Difference in atmospheric depth for all measured profiles with a pressure decrease gradient $\geq$ 98.0 hPa/km.

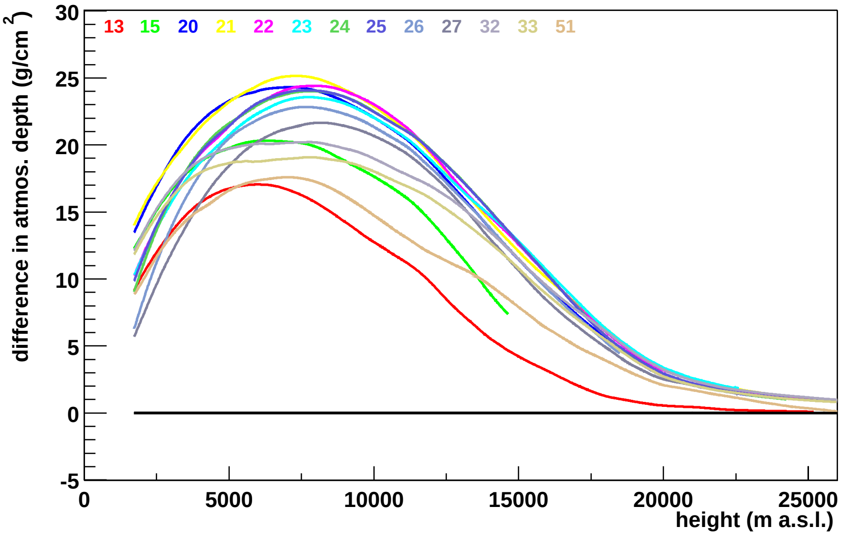

Figure 6.13: Difference in atmospheric depth for all measured profiles with a pressure decrease gradient $\leq$ 94.0 hPa/km.

Chapter 7

Summary & Outlook

Within this thesis, the atmospheric influences on the development of extensive air showers (EAS) induced by ultrahigh energy cosmic rays have been examined. The work was accomplished within the Pierre Auger Observatory. Consequently, also the variations of the observables of the Auger detector components, fluorescence and surface detectors, have been studied for changing atmospheric conditions mainly due to seasons. For this, the possible effects have been quantified first of all on the basis of the US standard atmosphere 1976 (US-StdA) usually applied in the data analyses and two extreme atmospheric models for summer and winter conditions in south Germany. Having revealed the significant influences of the atmosphere, measurements in Argentina for acquiring atmospheric profiles have been performed. Afterwards, the obtained Argentine atmospheres have been applied to the calculations of air shower development and their observables by the Auger Observatory.

The crucial role of the atmosphere is caused by its various influences on different parts of the experiment. The air showers develop in the atmosphere, thus it provides as a calorimeter. Induced by ionisation processes, fluorescence light is emitted. The atmosphere represents at this point a scintillator medium. Finally, the different atmospheric conditions affect the transmission of the light from the site of emission towards the telescopes. For studying these influences in detail, emphases have been placed on the seasonal variability of the atmosphere and on the height dependent variation of the state variables of the atmosphere. For obtaining the relevant atmospheric profiles, the meteorological technique of radio soundings has been applied. Within this thesis, automatic radiosondes have been launched on helium filled balloons above the Pampa Amarilla, Argentina. They reached altitudes of 20 - 25 km a.s.l. and in height steps of about 20 m data were stored. The first measurement campaign has been performed during winter and the places of launch have been varied. Four further campaigns followed whereby the last campaign took place in the ensuing winter. The receiver ground-station was installed permanently at the fluorescence detector building *Coihueco* during the second campaign. In total, 52 launched have been performed successfully. The prominent attributes of the seasons, the variations during seasons, and also night-to-night fluctuations have been fixed. Five seasonal average atmospheric models have been worked out, extremely different winter conditions demanded two winter models. These Argentine atmospheres are from now on available in the air shower simulation program CORSIKA.

From the physical point of view, the amount of traversed matter is most relevant for the air shower development. Thus, EAS are described by means of atmospheric depth in air shower simulation programs and reconstruction procedures. However, the fluorescence detector setup emphasises the geometrical point of view. The fluorescence telescopes observe the longitudinal shower development in dark nights with a fixed field of view. The air shower description can no longer be done in terms of atmospheric depth but in terms of geometrical height. The transformation of these two quantities into each other is based on air density profiles. Since the air density is determined by air pressure and temperature, seasonal variations are obvious. With respect to the US-StdA, the largest differences in atmospheric depth for summer and winter occur between 4 and 10 km a.s.l. The optical observation of EAS is made by detecting the fluorescence light with telescopes. The particles in the EAS excite nitrogen molecules in the atmosphere via ionisation and part of the de-excitation happens by emission of fluorescence light. The fluorescence efficiency depends on air temperature and pressure, consequently showing a height dependent, temporal varying profile. The subsequent fluorescence yield is proportional to the local energy deposit of the EAS and the air density profile. This induces a further small distortion. The shower profiles, detectable in the fluorescence data, deviate slightly from the EAS profiles by charged particles or energy deposit. The last point of atmospheric influence results from the fact that the atmosphere also serves as light propagation medium. On its passage from emission towards the telescopes of the Auger experiment, the light suffers absorption and scattering. The scattering can be separated into two parts, one is due to scattering on air molecules, Rayleigh scattering, and the other due to scattering on aerosols, Mie scattering. The Rayleigh scattering is exactly calculable, whereas the Mie scattering fluctuates for different sizes and shapes of aerosols. Thus, the Mie scattering will be measured within the Auger project several times a night. The Rayleigh scattering depends on air temperature, pressure, and density inducing an altitude dependent and seasonal variation. The aspect of light absorption is negligible for the observed wavelength region of 300 - 400 nm since contemplable absorbers like ozone or NO_2 have only low concentrations in the lower atmosphere and not sufficiently high cross sections in this wavelength region.

For EAS induced by ultrahigh energy cosmic rays with an incidence angle of $> 30°$, the range of the shower maximum position coincides with the height interval of largest seasonal variation for the atmospheric depth. This is the region of substantial interest because the type of the primary particle of EAS is derived from the position of the shower maximum while using the fluorescence technique. The total, visible shift of the position of the shower maximum due to summer and winter conditions is approximately as large as the shift of the maximum induced by proton showers instead of iron showers for example.

In the following, the results of the measurements in Argentina are summarised and these data have been applied to the calculations of air shower development and their observation with the Auger detectors. Putting an emphasis on atmospheric depth profiles, it can be stated that the largest variation between averaged summer and winter in Argentina also occurs at altitudes between 5 and 10 km a.s.l., however being not as pronounced as for chosen German conditions. The differences between summer and winter in Argentina are around the position of the shower maxima in the order of 20 - 30 g/cm^2. The colder winter type is very similar to the US-StdA while the Argentine summer exceeds the conditions in German summer. Also Argentine autumn is quite different to the US-StdA which leads to strongly distorted air shower profiles in the lower atmosphere (0 - 7 km a.s.l.). This is very important for the EAS energy reconstruction. The atmosphere dependent fluorescence yield varies the visible EAS profiles in comparison to the energy deposit profile slightly. Higher air temperatures result in reduced fluorescence yield, a temperature increase of +5°C connotes 1% less fluorescence photons. Thus, in combination with the deficit in energy deposit in the lower atmosphere during summer and autumn, the EAS energy would be systematically underestimated during these seasons while applying the US-StdA within the reconstruction procedures. The shift of the shower maximum position could feign a heavier composition of the incoming cosmic rays during summer. The variation of the Rayleigh transmission during seasons is quite small. The atmospheric effects on the observables of the surface detectors of the Auger Observatory have been studied only briefly. The trigger efficiency is expected to be corrected by the ground pressure. However the influence on the electron to muon ratio can not simply be corrected by the parameters measured at ground. The muon number is affected by the longitudinal shower development, thus differences in the electron to muon ratio due to seasonal variation are expected in the order of several percent.

Introducing seasonal average atmospheric models, the variability and the therefore implied uncertainties in the simulation and reconstruction can be reduced especially for the atmospheric depth. Within each season, the differences in the atmospheric depth at the position of the shower maxima remain to 10 g/cm^2. This is a clear improvement compared to the US-StdA, however uncertainties still exist. Thus, further radio soundings are necessary in future.

Though, continuous measurements of atmospheric profiles induce large financial and manned effort. Therefore, possibilities for reducing the necessity of frequent radio soundings have been studied. For this, further atmospheric models have been tested. The most promising one is a model providing atmospheric profiles every 5° in latitude and every month. A comparison with the measured data leads to the conclusion that the general behaviour of the atmosphere in Argentina can be described by this model much better than by the US-StdA. However on a monthly basis, inconsistencies still exist. Another possibility is to use ground based weather stations with continuous data taking. This could be a suitable complement for less frequent radio soundings (three or four nights per dark period of a month) if at least two weather stations at two different altitudes (e.g. 1750 and 2500 m a.s.l.) are installed. First indicating parameters have been figured out but more detailed studies remain to be done. Especially within this respect, possible effects due to the El Niño Southern Oscillation (ENSO) have been viewed. However, this topic might also help in terms of providing detailed atmospheric information in a spacious scale since this is a field of high priority in climatology. Long-term observations have to reveal if the Argentine atmospheric models worked out in this thesis are representative and how large the variations are due to real ENSO events.

A next step is the flexible implementation of varying atmospheric profiles in the reconstruction procedures mainly for the Auger fluorescence detector as well as the implementation of the Argentine model atmospheres. The effects on the EAS energy reconstruction have to be quantified which seems to be very important particularly for those EAS of which only a small part of the longitudinal development has been observed by the fluorescence telescopes. For EAS simulation programs it could furthermore be reasonable to implement one averaged Argentine models apart from the already existing seasonal parameterisations.

However for important, high energetic EAS events, e.g. EAS with $E_0 > 10^{20}$ eV, it seems to be necessary that the atmospheric profiles have to be measured during the same night. It is sufficient to perform the launch of the radiosonde 2 or 3 hours later, but the high degree of accuracy in the reconstruction obtained by these additional information should not missed.

A further point of investigation has to be the expressiveness of atmospheric ground parameter. Operating ground-based weather stations provides continuous data and is much more comfortable than performing radio soundings during nights. First studies have shown that two stations at two different altitudes could help to reduce the necessity of radio soundings. A quantifying analysis on the remaining variability of the atmospheric profiles has still to be done. The first indicating variable for atmospheric depth profiles derived from ground-based pressure values leads to a prediction on the shape of the atmospheric depth profile. However, this variable only fits for nearly 40% of all the launches performed during one year. Another possibility is to combine existing atmospheric models like CIRA 1986 with the data obtained by the radio soundings. This could also be a way for achieving quite realistic atmospheric models, e.g. on a monthly basis.

Appendix A

Formulas for Standard Atmospheres

A.1 US-StdA

For calculations h must be put in unit m.

<u>0 - 11 km:</u>

$$T(\mathrm{K}) = 288.15 - 0.0065 \cdot h \tag{A.1}$$

$$p(\mathrm{hPa}) = 1013.272684 \cdot (1.0 - 2.255771988 \cdot 10^{-5} \cdot h)^{5.255876} \tag{A.2}$$

$$\rho(\mathrm{kg/m^3}) = 1.22467 \cdot (1.0 - 2.255771988 \cdot 10^{-5} \cdot h)^{4.255876} \tag{A.3}$$

<u>11 - 20 km:</u>

$$T(\mathrm{K}) = 216.65 \tag{A.4}$$

$$p(\mathrm{hPa}) = 226.3256 \cdot \exp(1.734547727 - 1.576872006 \cdot 10^{-4} \cdot h) \tag{A.5}$$

$$\rho(\mathrm{kg/m^3}) = 0.3638204069 \cdot \exp(1.734547727 - 1.576872006 \cdot 10^{-4} \cdot h) \tag{A.6}$$

<u>20 - 32 km:</u>

$$T(\mathrm{K}) = 196.65 + 0.001 \cdot h \tag{A.7}$$

$$p(\mathrm{hPa}) = 1013.272684 \cdot (0.988626 + 0.5027336647 \cdot 10^{-5} \cdot h)^{-34.16319} \tag{A.8}$$

$$\rho(\mathrm{kg/m^3}) = 1.224671151 \cdot (0.978261 + 0.4974625134 \cdot 10^{-5} \cdot h)^{-35.16319} \tag{A.9}$$

<u>32 - 47 km:</u>

$$T(\mathrm{K}) = 139.05 + 0.0028 \cdot h \tag{A.10}$$

$$p(\mathrm{hPa}) = 1013.272684 \cdot (0.898309 + 1.808891012 \cdot 10^{-5} \cdot h)^{-12.20144} \tag{A.11}$$

$$\rho(\mathrm{kg/m^3}) = 1.224671151 \cdot (0.857003 + 1.725713329 \cdot 10^{-5} \cdot h)^{-13.20144} \tag{A.12}$$

<u>47 - 51 km:</u>

$$T(\mathrm{K}) = 270.6500742 \tag{A.13}$$

$$p(\mathrm{hPa}) = 110.9087749 \cdot \exp(5.932594645 - 1.262249883 \cdot 10^{-4} \cdot h) \tag{A.14}$$

$$\rho(\mathrm{kg/m^3}) = 0.001427146032 \cdot \exp(5.932594645 - 1.262249883 \cdot 10^{-4} \cdot h) \tag{A.15}$$

51 - 71 km:

$$T(\mathrm{K}) = 413.4500105 - 0.002799996493 \cdot h \tag{A.16}$$

$$p(\mathrm{hPa}) = 1013.272684 \cdot (0.838263 - 0.5676959685 \cdot 10^{-5} \cdot h)^{12.20114} \tag{A.17}$$

$$\rho(\mathrm{kg/m^3}) = 1.224671151 \cdot (0.79899 - 0.5410980646 \cdot 10^{-5} \cdot h)^{11.20114} \tag{A.18}$$

A.2 European summer

For calculations h must be put in unit m.

0 - 11 km:

$$T(\mathrm{K}) = 302.0237894 - 0.00714454889 \cdot h \tag{A.19}$$

$$\begin{aligned} p(\mathrm{hPa}) &= 1011.651649 - 0.114178254 \cdot h + 0.505036457 \cdot 10^{-5} \cdot h^2 \\ &\quad -0.948519838 \cdot 10^{-10} \cdot h^3 \end{aligned} \tag{A.20}$$

$$\rho(\mathrm{kg/m^3}) = 2.896 \cdot \frac{1011.651649 - 0.114178254 \cdot h + 0.505036457 \cdot 10^{-5} \cdot h^2 - 0.948519838 \cdot 10^{-10} \cdot h^3}{2511.179817 - 0.05940342319 \cdot h} \tag{A.21}$$

11 - 12.724 km:

$$T(\mathrm{K}) = 302.0237894 - 0.00714454889 \cdot h \tag{A.22}$$

$$\begin{aligned} p(\mathrm{hPa}) &= 1054.415556 - 0.1192343998 \cdot h + 0.489389176 \cdot 10^{-5} \cdot h^2 \\ &\quad -0.712603376 \cdot 10^{-10} \cdot h^3 \end{aligned} \tag{A.23}$$

$$\rho(\mathrm{kg/m^3}) = 2.896 \cdot \frac{1054.415556 - 0.1192343998 \cdot h + 0.489389176 \cdot 10^{-5} \cdot h^2 - 0.712603376 \cdot 10^{-10} \cdot h^3}{2511.179817 - 0.05940342319 \cdot h} \tag{A.24}$$

12.724 - 20 km:

$$T(\mathrm{K}) = 201.3748154 + 7.658647 \cdot 10^{-4} \cdot h \tag{A.25}$$

$$\begin{aligned} p(\mathrm{hPa}) &= 1054.415556 - 0.1192343998 \cdot h + 0.489389176 \cdot 10^{-5} \cdot h^2 \\ &\quad -0.712603376 \cdot 10^{-10} \cdot h^3 \end{aligned} \tag{A.26}$$

$$\rho(\mathrm{kg/m^3}) = 2.896 \cdot \frac{1054.415556 - 0.1192343998 \cdot h + 0.489389176 \cdot 10^{-5} \cdot h^2 - 0.712603376 \cdot 10^{-10} \cdot h^3}{1674.332916 + 0.006367789707 \cdot h} \tag{A.27}$$

20 - 35 km:

$$\begin{aligned} T(\mathrm{K}) &= 179.2557608 + 0.00384280733 \cdot h - 0.1468413652 \cdot 10^{-6} \cdot h^2 \\ &\quad +0.2571584941 \cdot 10^{-11} \cdot h^3 \end{aligned} \tag{A.28}$$

$$\begin{aligned} p(\mathrm{hPa}) &= 500.3627886 - 0.04069189531 \cdot h + 0.1144781831 \cdot 10^{-5} \cdot h^2 \\ &\quad -0.1101926725 \cdot 10^{-10} \cdot h^3 \end{aligned} \tag{A.29}$$

$$\rho(\mathrm{kg/m^3}) = 2.896 \cdot \frac{500.3627886 - 0.04069189531 \cdot h + 0.1144781831 \cdot 10^{-5} \cdot h^2 - 0.1101926725 \cdot 10^{-10} \cdot h^3}{1490.423816 + 0.03195105997 \cdot h - 0.1220913999 \cdot 10^{-5} \cdot h^2 + 0.2138146871 \cdot 10^{-10} \cdot h^3} \tag{A.30}$$

A.3 European winter

For calculations h must be put in unit m.

<u>0 - 11 km:</u>

$$T(\mathrm{K}) = 269.5470817 - 0.00714596976 \cdot h + 0.1999036281 \cdot 10^{-6} \cdot h^2 \tag{A.31}$$

$$p(\mathrm{hPa}) = 1022.913383 - 0.1288058047 \cdot h + 0.62479976 \cdot 10^{-5} \cdot h^2 - 0.114947958 \cdot 10^{-9} \cdot h^3 \tag{A.32}$$

$$\rho(\mathrm{kg/m^3}) = 2.896 \cdot \tag{A.33}$$

$$\frac{1022.913383 - 0.1288058047 \cdot h + 0.62479976 \cdot 10^{-5} \cdot h^2 - 0.114947958 \cdot 10^{-9} \cdot h^3}{2241.151906 - 0.05941523703 \cdot h - 0.1662100715 \cdot 10^{-5} \cdot h^2}$$

<u>11 -20 km:</u>

$$T(\mathrm{K}) = 269.5470817 - 0.00714596976 \cdot h + 0.1999036281 \cdot 10^{-6} \cdot h^2 \tag{A.34}$$

$$p(\mathrm{hPa}) = 889.6568501 - 0.09838580521 \cdot h + 0.392968395 \cdot 10^{-5} \cdot h^2 - 0.557567304 \cdot 10^{-10} \cdot h^3 \tag{A.35}$$

$$\rho(\mathrm{kg/m^3}) = 2.896 \cdot \tag{A.36}$$

$$\frac{889.6568501 - 0.09838580521 \cdot h + 0.392968395 \cdot 10^{-5} \cdot h^2 - 0.557567304 \cdot 10^{-10} \cdot h^3}{2241.151906 - 0.05941523703 \cdot h - 0.1662100715 \cdot 10^{-5} \cdot h^2}$$

<u>20 - 35 km:</u>

$$T(\mathrm{K}) = 269.5470817 - 0.00714596976 \cdot h + 0.1999036281 \cdot 10^{-6} \cdot h^2 \tag{A.37}$$

$$p(\mathrm{hPa}) = 483.2118004 - 0.04118594969 \cdot h + 0.1214012445 \cdot 10^{-5} \cdot h^2 - 0.1223043465 \cdot 10^{-10} \cdot h^3 \tag{A.38}$$

$$\rho(\mathrm{kg/m^3}) = 2.896 \cdot \tag{A.39}$$

$$\frac{483.2118004 - 0.04118594969 \cdot h + 0.1214012445 \cdot 10^{-5} \cdot h^2 - 0.1223043465 \cdot 10^{-10} \cdot h^3}{2241.151906 - 0.05941523703 \cdot h - 0.1662100715 \cdot 10^{-5} \cdot h^2}$$

A.4 Argentine winter, type I

For calculations h must be put in unit m.

<u>0 - 8.6 km:</u> [1]

$$T(\mathrm{K}) = 288.874 - 0.00733746 \cdot h \tag{A.40}$$

$$p(\mathrm{hPa}) = (1002.85 + 0.0778668 \cdot h - 2.10941 \cdot 10^{-6} \cdot h^2 + 4.8057 \cdot 10^{-11} \cdot h^3) \cdot \exp(-1.815298 \cdot 10^{-4} \cdot h) \tag{A.41}$$

$$\rho(\mathrm{kg/m^3}) = 2.896 \cdot \exp(-1.815298 \cdot 10^{-4} \cdot h) \cdot \frac{1002.85 + 0.0778668 \cdot h - 2.10941 \cdot 10^{-6} \cdot h^2 + 4.8057 \cdot 10^{-11} \cdot h^3}{8.31451 \cdot (288.874 - 0.00733746 \cdot h)} \tag{A.42}$$

<u>8.6 - 12.5 km:</u>

$$T(\mathrm{K}) = 231.974 - 0.000721185 \cdot h \tag{A.43}$$

$$p(\mathrm{hPa}) = (1002.85 + 0.0778668 \cdot h - 2.10941 \cdot 10^{-6} \cdot h^2 + 4.8057 \cdot 10^{-11} \cdot h^3) \cdot \exp(-1.815298 \cdot 10^{-4} \cdot h) \tag{A.44}$$

$$\rho(\mathrm{kg/m^3}) = 2.896 \cdot \exp(-1.815298 \cdot 10^{-4} \cdot h) \cdot \frac{1002.85 + 0.0778668 \cdot h - 2.10941 \cdot 10^{-6} \cdot h^2 + 4.8057 \cdot 10^{-11} \cdot h^3}{8.31451 \cdot (231.974 - 0.000721185 \cdot h)} \tag{A.45}$$

<u>12.5 - 18 km:</u>

$$T(\mathrm{K}) = 243.717 - 0.00166067 \cdot h \tag{A.46}$$

$$p(\mathrm{hPa}) = (1002.85 + 0.0778668 \cdot h - 2.10941 \cdot 10^{-6} \cdot h^2 + 4.8057 \cdot 10^{-11} \cdot h^3) \cdot \exp(-1.815298 \cdot 10^{-4} \cdot h) \tag{A.47}$$

$$\rho(\mathrm{kg/m^3}) = 2.896 \cdot \exp(-1.815298 \cdot 10^{-4} \cdot h) \cdot \frac{1002.85 + 0.0778668 \cdot h - 2.10941 \cdot 10^{-6} \cdot h^2 + 4.8057 \cdot 10^{-11} \cdot h^3}{8.31451 \cdot (243.717 - 0.00166067 \cdot h)} \tag{A.48}$$

<u>18 - 25 km:</u>

$$T(\mathrm{K}) = 213.825 \tag{A.49}$$

$$p(\mathrm{hPa}) = (1002.85 + 0.0778668 \cdot h - 2.10941 \cdot 10^{-6} \cdot h^2 + 4.8057 \cdot 10^{-11} \cdot h^3) \cdot \exp(-1.815298 \cdot 10^{-4} \cdot h) \tag{A.50}$$

$$\rho(\mathrm{kg/m^3}) = 2.896 \cdot \exp(-1.815298 \cdot 10^{-4} \cdot h) \cdot \frac{1002.85 + 0.0778668 \cdot h - 2.10941 \cdot 10^{-6} \cdot h^2 + 4.8057 \cdot 10^{-11} \cdot h^3}{8.31451 \cdot 213.825} \tag{A.51}$$

---

[1] Since the data on which these fits rely on are measured at altitude above ≈ 1700 m a.s.l., the parameterisations should not be overstrained for height below roughly 1500 m a.s.l. Especially the pressure formulas, mainly for winter, show quite low values towards ground which must not be taken for granted. Subsequently, also the density formulas might underestimate the real conditions below 1500 m a.s.l.

A.5 Argentine winter, type II

For calculations h must be put in unit m.

<u>0 - 11.5 km:</u> [1]

$$\begin{aligned}
T(\mathrm{K}) &= 292.955 - 0.00658613 \cdot h && \text{(A.52)}\\
p(\mathrm{hPa}) &= (1010.55 + 0.00944127 \cdot h - 2.78278 \cdot 10^{-6} \cdot h^2 + 6.28386 \cdot 10^{-11} \cdot h^3)\\
&\quad \cdot \exp(-1.177247 \cdot 10^{-4} \cdot h) && \text{(A.53)}\\
\rho(\mathrm{kg/m^3}) &= 2.896 \cdot \exp(-1.177247 \cdot 10^{-4} \cdot h) \cdot && \text{(A.54)}
\end{aligned}$$

$$\frac{1010.55 + 0.00944127 \cdot h - 2.78278 \cdot 10^{-6} \cdot h^2 + 6.28386 \cdot 10^{-11} \cdot h^3}{8.31451 \cdot (292.955 - 0.00658613 \cdot h)}$$

<u>11.5 - 17.5 km:</u>

$$\begin{aligned}
T(\mathrm{K}) &= 229.277 - 0.00104889 \cdot h && \text{(A.55)}\\
p(\mathrm{hPa}) &= (1010.55 + 0.00944127 \cdot h - 2.78278 \cdot 10^{-6} \cdot h^2 + 6.28386 \cdot 10^{-11} \cdot h^3)\\
&\quad \cdot \exp(-1.177247 \cdot 10^{-4} \cdot h) && \text{(A.56)}\\
\rho(\mathrm{kg/m^3}) &= 2.896 \cdot \exp(-1.177247 \cdot 10^{-4} \cdot h) \cdot && \text{(A.57)}
\end{aligned}$$

$$\frac{1010.55 + 0.00944127 \cdot h - 2.78278 \cdot 10^{-6} \cdot h^2 + 6.28386 \cdot 10^{-11} \cdot h^3}{8.31451 \cdot (229.277 - 0.00104889 \cdot h)}$$

<u>17.5 - 25 km:</u>

$$\begin{aligned}
T(\mathrm{K}) &= 204.383 + 0.000373608 \cdot h && \text{(A.58)}\\
p(\mathrm{hPa}) &= (1010.55 + 0.00944127 \cdot h - 2.78278 \cdot 10^{-6} \cdot h^2 + 6.28386 \cdot 10^{-11} \cdot h^3)\\
&\quad \cdot \exp(-1.177247 \cdot 10^{-4} \cdot h) && \text{(A.59)}\\
\rho(\mathrm{kg/m^3}) &= 2.896 \cdot \exp(-1.177247 \cdot 10^{-4} \cdot h) \cdot && \text{(A.60)}
\end{aligned}$$

$$\frac{1010.55 + 0.00944127 \cdot h - 2.78278 \cdot 10^{-6} \cdot h^2 + 6.28386 \cdot 10^{-11} \cdot h^3}{8.31451 \cdot (204.383 + 0.000373608 \cdot h)}$$

A.6 Argentine spring

For calculations h must be put in unit m.

<u>0 - 11.5 km:</u> [1]

$$\begin{aligned}
T(\mathrm{K}) &= 295.638 - 0.00697773 \cdot h && \text{(A.61)}\\
p(\mathrm{hPa}) &= (1006.28 - 0.00235474 \cdot h - 2.5759 \cdot 10^{-6} \cdot h^2 + 6.64777 \cdot 10^{-11} \cdot h^3)\\
&\quad \cdot \exp(-1.066242 \cdot 10^{-4} \cdot h) && \text{(A.62)}\\
\rho(\mathrm{kg/m^3}) &= 2.896 \cdot \exp(-1.066242 \cdot 10^{-4} \cdot h) \cdot && \text{(A.63)}
\end{aligned}$$

$$\frac{1006.28 - 0.00235474 \cdot h - 2.5759 \cdot 10^{-6} \cdot h^2 + 6.64777 \cdot 10^{-11} \cdot h^3}{8.31451 \cdot (295.638 - 0.00697773 \cdot h)}$$

11.5 - 17.5 km:

$$\begin{aligned} T(\mathrm{K}) &= 229.839 - 0.00125607 \cdot h && \text{(A.64)} \\ p(\mathrm{hPa}) &= (1006.28 - 0.00235474 \cdot h - 2.5759 \cdot 10^{-6} \cdot h^2 + 6.64777 \cdot 10^{-11} \cdot h^3) \\ &\quad \cdot \exp(-1.066242 \cdot 10^{-4} \cdot h) && \text{(A.65)} \\ \rho(\mathrm{kg/m^3}) &= 2.896 \cdot \exp(-1.066242 \cdot 10^{-4} \cdot h) \cdot && \text{(A.66)} \end{aligned}$$

$$\frac{1006.28 - 0.00235474 \cdot h - 2.5759 \cdot 10^{-6} \cdot h^2 + 6.64777 \cdot 10^{-11} \cdot h^3}{8.31451 \cdot (229.839 - 0.00125607 \cdot h)}$$

17.5 - 25 km:

$$\begin{aligned} T(\mathrm{K}) &= 175.929 + 0.0018245 \cdot h && \text{(A.67)} \\ p(\mathrm{hPa}) &= (1006.28 - 0.00235474 \cdot h - 2.5759 \cdot 10^{-6} \cdot h^2 + 6.64777 \cdot 10^{-11} \cdot h^3) \\ &\quad \cdot \exp(-1.066242 \cdot 10^{-4} \cdot h) && \text{(A.68)} \\ \rho(\mathrm{kg/m^3}) &= 2.896 \cdot \exp(-1.066242 \cdot 10^{-4} \cdot h) \cdot && \text{(A.69)} \end{aligned}$$

$$\frac{1006.28 - 0.00235474 \cdot h - 2.5759 \cdot 10^{-6} \cdot h^2 + 6.64777 \cdot 10^{-11} \cdot h^3}{8.31451 \cdot (175.929 + 0.0018245 \cdot h)}$$

A.7 Argentine summer

For calculations h must be put in unit m.

0 - 11.5 km: [1]

$$\begin{aligned} T(\mathrm{K}) &= 305.577 - 0.00719682 \cdot h && \text{(A.70)} \\ p(\mathrm{hPa}) &= (1003.17 - 0.0172454 \cdot h - 1.81458 \cdot 10^{-6} \cdot h^2 + 5.22625 \cdot 10^{-11} \cdot h^3) \\ &\quad \cdot \exp(-9.6620 \cdot 10^{-5} \cdot h) && \text{(A.71)} \\ \rho(\mathrm{kg/m^3}) &= 2.896 \cdot \exp(-9.6620 \cdot 10^{-5} \cdot h) \cdot && \text{(A.72)} \end{aligned}$$

$$\frac{1003.17 - 0.0172454 \cdot h - 1.81458 \cdot 10^{-6} \cdot h^2 + 5.22625 \cdot 10^{-11} \cdot h^3}{8.31451 \cdot (305.577 - 0.00719682 \cdot h)}$$

11.5 - 18.5 km:

$$\begin{aligned} T(\mathrm{K}) &= 257.831 - 0.00304497 \cdot h && \text{(A.73)} \\ p(\mathrm{hPa}) &= (1003.17 - 0.0172454 \cdot h - 1.81458 \cdot 10^{-6} \cdot h^2 + 5.22625 \cdot 10^{-11} \cdot h^3) \\ &\quad \cdot \exp(-9.6620 \cdot 10^{-5} \cdot h) && \text{(A.74)} \\ \rho(\mathrm{kg/m^3}) &= 2.896 \cdot \exp(-9.6620 \cdot 10^{-5} \cdot h) \cdot && \text{(A.75)} \end{aligned}$$

$$\frac{1003.17 - 0.0172454 \cdot h - 1.81458 \cdot 10^{-6} \cdot h^2 + 5.22625 \cdot 10^{-11} \cdot h^3}{8.31451 \cdot (257.831 - 0.00304497 \cdot h)}$$

18.5 - 25 km:

$$T(\mathrm{K}) = 141.145 + 0.003262232 \cdot h \tag{A.76}$$

$$\begin{aligned} p(\mathrm{hPa}) = {} & (1003.17 - 0.0172454 \cdot h - 1.81458 \cdot 10^{-6} \cdot h^2 + 5.22625 \cdot 10^{-11} \cdot h^3) \\ & \cdot \exp(-9.6620 \cdot 10^{-5} \cdot h) \end{aligned} \tag{A.77}$$

$$\rho(\mathrm{kg/m^3}) = 2.896 \cdot \exp(-9.6620 \cdot 10^{-5} \cdot h) \cdot \frac{1003.17 - 0.0172454 \cdot h - 1.81458 \cdot 10^{-6} \cdot h^2 + 5.22625 \cdot 10^{-11} \cdot h^3}{8.31451 \cdot (141.145 + 0.003262232 \cdot h)} \tag{A.78}$$

A.8 Argentine autumn

For calculations h must be put in unit m.

0 - 12 km: [1]

$$T(\mathrm{K}) = 300.614 - 0.00711149 \cdot h \tag{A.79}$$

$$\begin{aligned} p(\mathrm{hPa}) = {} & (1005.49 + 0.00111054 \cdot h - 2.65891 \cdot 10^{-6} \cdot h^2 + 6.39959 \cdot 10^{-11} \cdot h^3) \\ & \cdot \exp(-1.071743 \cdot 10^{-4} \cdot h) \end{aligned} \tag{A.80}$$

$$\rho(\mathrm{kg/m^3}) = 2.896 \cdot \exp(-1.071743 \cdot 10^{-4} \cdot h) \cdot \frac{1005.49 + 0.00111054 \cdot h - 2.65891 \cdot 10^{-6} \cdot h^2 + 6.39959 \cdot 10^{-11} \cdot h^3}{8.31451 \cdot (300.614 - 0.00711149 \cdot h)} \tag{A.81}$$

12 - 17 km:

$$T(\mathrm{K}) = 238.255 - 0.00191483 \cdot h \tag{A.82}$$

$$\begin{aligned} p(\mathrm{hPa}) = {} & (1005.49 + 0.00111054 \cdot h - 2.65891 \cdot 10^{-6} \cdot h^2 + 6.39959 \cdot 10^{-11} \cdot h^3) \\ & \cdot \exp(-1.071743 \cdot 10^{-4} \cdot h) \end{aligned} \tag{A.83}$$

$$\rho(\mathrm{kg/m^3}) = 2.896 \cdot \exp(-1.071743 \cdot 10^{-4} \cdot h) \cdot \frac{1005.49 + 0.00111054 \cdot h - 2.65891 \cdot 10^{-6} \cdot h^2 + 6.39959 \cdot 10^{-11} \cdot h^3}{8.31451 \cdot (238.255 - 0.00191483 \cdot h)} \tag{A.84}$$

17 - 25 km:

$$T(\mathrm{K}) = 179.081 + 0.00156597 \cdot h \tag{A.85}$$

$$\begin{aligned} p(\mathrm{hPa}) = {} & (1005.49 + 0.00111054 \cdot h - 2.65891 \cdot 10^{-6} \cdot h^2 + 6.39959 \cdot 10^{-11} \cdot h^3) \\ & \cdot \exp(-1.071743 \cdot 10^{-4} \cdot h) \end{aligned} \tag{A.86}$$

$$\rho(\mathrm{kg/m^3}) = 2.896 \cdot \exp(-1.071743 \cdot 10^{-4} \cdot h) \cdot \frac{1005.49 + 0.00111054 \cdot h - 2.65891 \cdot 10^{-6} \cdot h^2 + 6.39959 \cdot 10^{-11} \cdot h^3}{8.31451 \cdot (179.081 + 0.00156597 \cdot h)} \tag{A.87}$$

Appendix B

Parameterisation of the Atmospheric Depth

Layer i	Altitude h (km)	a_i (g/cm^2)	b_i (g/cm^2)	c_i (cm)
1	0 ... 4	-186.5562	1222.6562	994186.38
2	4 ... 10	-94.919	1144.9069	878153.55
3	10 ... 40	0.61289	1305.5948	636143.04
4	40 ... 100	0.0	540.1778	772170.16
5	> 100	0.01128292	1.	10^9

Table B.1: Parameters of the US-StdA [Heck et al. 1998].

Layer i	Altitude h (km)	a_i (g/cm^2)	b_i (g/cm^2)	c_i (cm)
1	0 ... 4	-195.837264	1240.48	933697.
2	4 ... 10	-50.4128778	1117.85	765229.
3	10 ... 40	0.345594007	1210.9	636790.
4	40 ... 100	$5.46207 \cdot 10^{-4}$	608.2128	733793.8
5	> 100	0.01128292	1.	10^9

Table B.2: Parameters of the AT223 atmosphere (February 23, 1993) [Heck et al. 1998].

Layer i	Altitude h (km)	a_i (g/cm^2)	b_i (g/cm^2)	c_i (cm)
1	0 ... 4	-77.875723	1103.3362	932077.
2	4 ... 10	-214.96818	1226.5761	1109960.
3	10 ... 40	0.3721868	1382.6933	630217.
4	40 ... 100	$5.5309816 \cdot 10^{-4}$	685.6073	726901.3
5	> 100	0.01128292	1.	10^9

Table B.3: Parameters of the AT822 atmosphere (August 22, 1993) [Heck et al. 1998].

For CORSIKA versions 5.8 (release August 1998) and higher, it is possible to read in external atmospheric models. This option enables not only the change of the parameters but also the variable selection of the boundaries for the four lowest layers.

Layer i	Altitude h (km)	a_i (g/cm^2)	b_i (g/cm^2)	c_i (cm)
1	0 ... 8	-150.247839	1198.5972	945766.30
2	8 ... 18.1	-6.66194377	1198.8796	681780.12
3	18.1 ... 34.5	0.94880452	1419.4152	620224.52
4	34.5 ... 100	$4.8966557223 \cdot 10^{-4}$	730.6380	728157.92
5	> 100	0.01128292	1.	10^9

Table B.4: Parameters of the average Argentine winter I atmosphere.

Layer i	Altitude h (km)	a_i (g/cm^2)	b_i (g/cm^2)	c_i (cm)
1	0 ... 8.3	-126.110950	1179.5010	939228.66
2	8.3 ... 12.9	-47.6124452	1172.4883	787969.34
3	12.9 ... 34	1.00758296	1437.4911	620008.53
4	34 ... 100	$5.1046180899 \cdot 10^{-4}$	761.3281	724585.33
5	> 100	0.01128292	1.	10^9

Table B.5: Parameters of the average Argentine winter II atmosphere.

Layer i	Altitude h (km)	a_i (g/cm^2)	b_i (g/cm^2)	c_i (cm)
1	0 ... 5.9	-159.683519	1202.8804	977139.52
2	5.9 ... 12	-79.5570480	1148.6275	858087.01
3	12 ... 34.5	0.98914795	1432.0312	614451.60
4	34.5 ... 100	$4.87191289 \cdot 10^{-4}$	696.42788	730875.73
5	> 100	0.01128292	1.	10^9

Table B.6: Parameters of the average Argentine spring atmosphere.

Layer i	Altitude h (km)	a_i (g/cm^2)	b_i (g/cm^2)	c_i (cm)
1	0 ... 9	-136.562242	1175.3347	986169.72
2	9 ... 14.6	-44.2165390	1180.3694	793171.45
3	14.6 ... 33	1.37778789	1614.5404	600120.97
4	33 ... 100	$5.06583365 \cdot 10^{-4}$	755.56438	725247.87
5	> 100	0.01128292	1.	10^9

Table B.7: Parameters of the average Argentine summer atmosphere.

Layer i	Altitude h (km)	a_i (g/cm^2)	b_i (g/cm^2)	c_i (cm)
1	0 ... 8	-149.305029	1196.9290	985241.10
2	8 ... 13	-59.771936	1173.2537	819245.00
3	13 ... 33.5	1.17357181	1502.1837	611220.86
4	33.5 ... 100	$5.03287179 \cdot 10^{-4}$	750.89705	725797.06
5	> 100	0.01128292	1.	10^9

Table B.8: Parameters of the average Argentine autumn atmosphere.

Layer i	Altitude h (km)	a_i (g/cm^2)	b_i (g/cm^2)	c_i (cm)
1	0 ... 7	-149.801663	1183.6071	954248.34
2	7 ... 11.4	-57.932486	1143.0425	800005.34
3	11.4 ... 37	0.63631894	1322.9748	629568.93
4	37 ... 100	$4.35453690 \cdot 10^{-4}$	655.67307	737521.77
5	> 100	0.01128292	1.	10^9

Table B.9: Parameters of the US-StdA obtained with the method applied in this work.

Appendix C

Details of all Data Obtained

C.1 Measurement campaign August 2002

- 9 launches
- all ascents with small (100 g) balloons
- 3 launches in the daytime, 6 launches in the nighttime
- on August 20th, 2002, 3 launches per night
- on August 21st, 2002, 2 launches per night

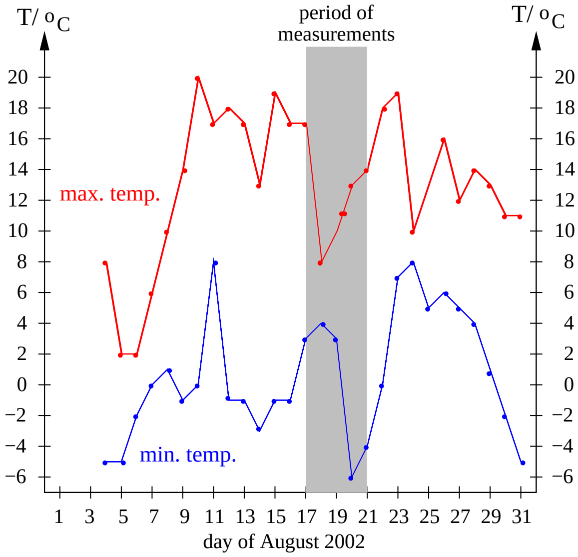

Figure C.1: Minimum and maximum temperatures measured at Malargüe airport, 1425 m a.s.l., 35.3°S, 69.35°W.

Ascent No.	**Date** (dd.mm.yyyy)	**Time** (hh:mm:ss)	**Location of Ground Station**	**Height of Ground Station** in m a.s.l.	**Maximum of reached Altitude** in m a.s.l.	**Moon < 50%**
1	17.08.2002	19:14:43	route to La Junta	1446	17263	no
2	18.08.2002	17:14:45	FD Coihueco	1709	17269	no
3	19.08.2002	06:46:40	FD Coihueco	1709	17930	no
4	19.08.2002	19:39:06	Malargüe	1420	20113	no
5	20.08.2002	00:41:04	Malargüe	1420	17101	no
6	20.08.2002	03:53:05	Malargüe	1420	17422	no
7	20.08.2002	09:19:39	Malargüe	1420	16918	no
8	21.08.2002	01:23:40	FD Los Leones	1450	14669	no
9	21.08.2002	03:54:30	FD Los Leones	1450	13332	no

Table C.1: Measurement campaign August 2002. The dates and times are given in UTC, the altitudes are geopotential heights; FD = fluorescence detector building.

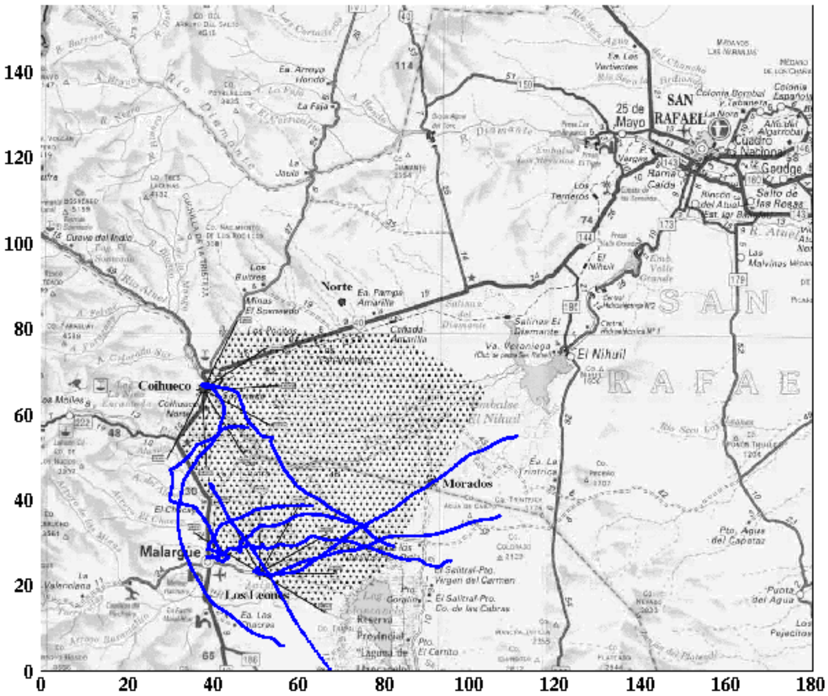

Figure C.2: Balloon paths of all launches in August 2002 from different starting positions. In total nine launches were performed. A kilometre scale is indicated at the frame.

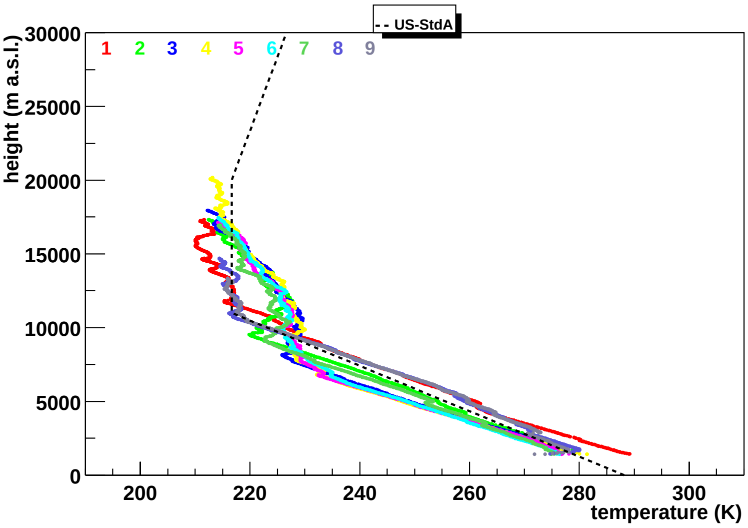

Figure C.3: All temperature profiles measured during August 2002, near Malargüe, Argentina.

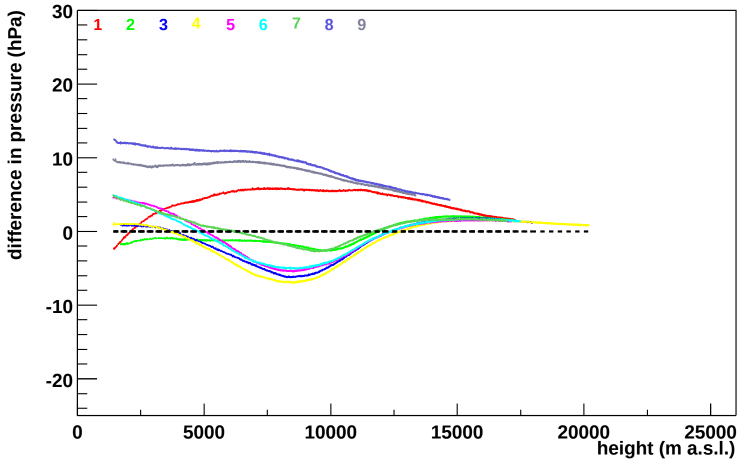

Figure C.4: Difference in all pressure profiles according to the US-StdA measured during August 2002, near Malargüe, Argentina.

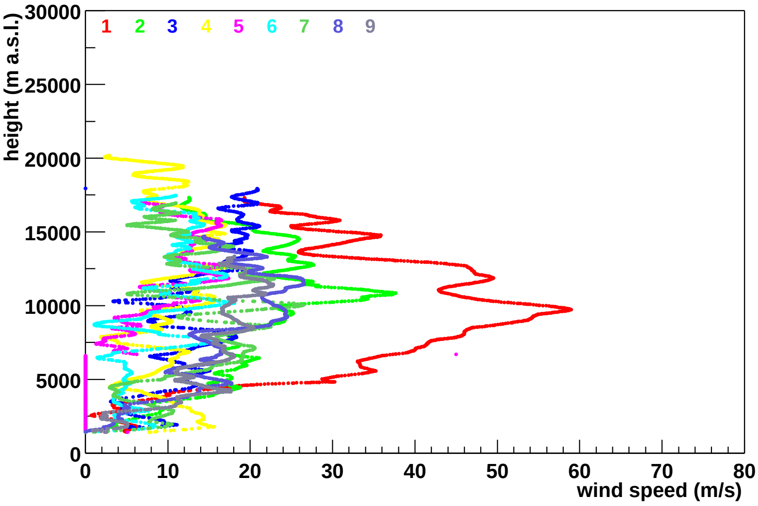

Figure C.5: All windspeed profiles measured during August 2002, near Malargüe, Argentina.

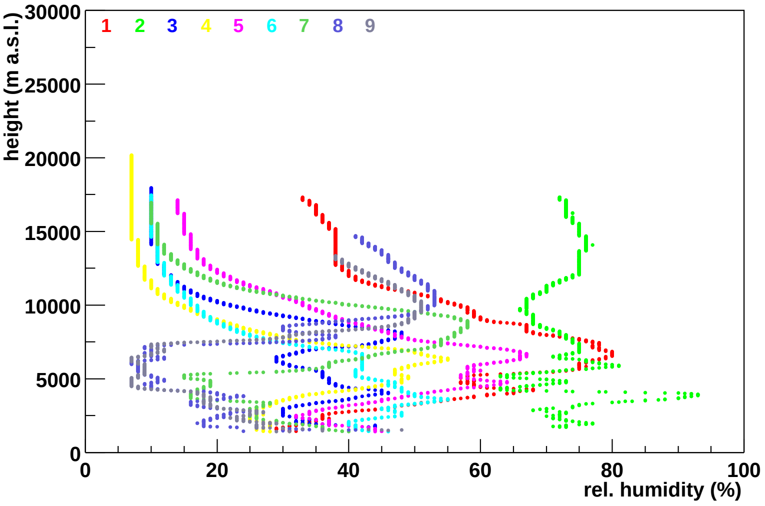

Figure C.6: All relative humidity profiles measured during August 2002, near Malargüe, Argentina.

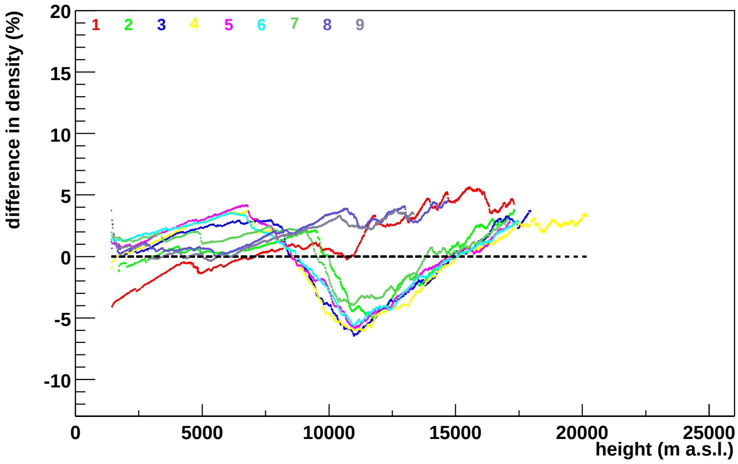

Figure C.7: Percent difference in all density profiles according to the US-StdA measured during August 2002, near Malargüe, Argentina.

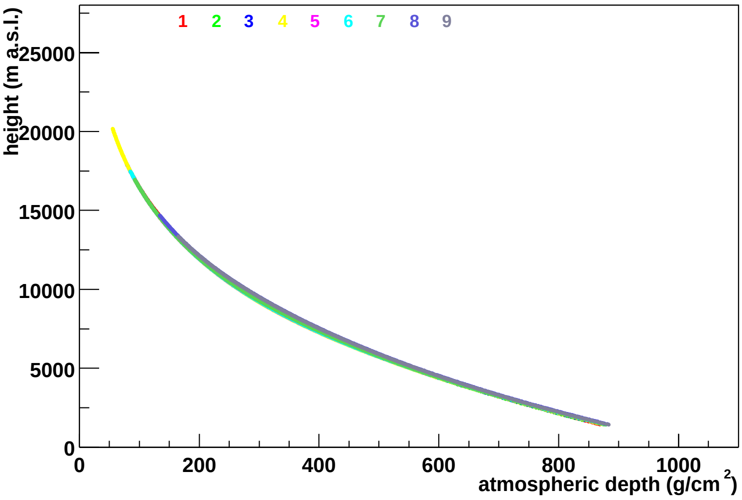

Figure C.8: All atmospheric depth profiles measured during August 2002, near Malargüe, Argentina.

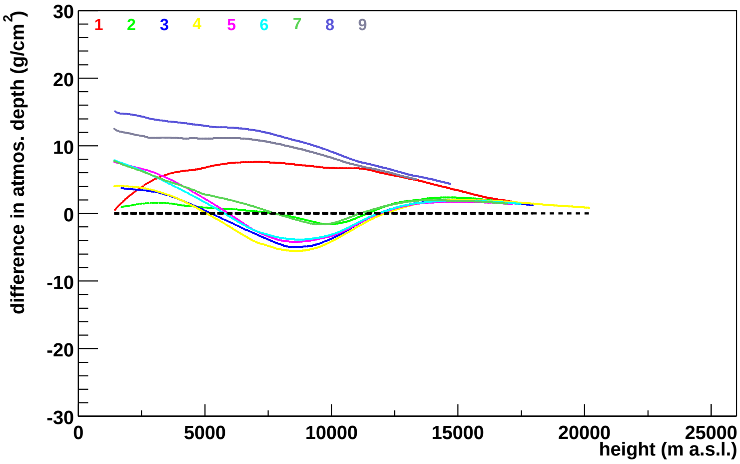

Figure C.9: Difference in all atmospheric depth profiles according to the US-StdA measured during August 2002, near Malargüe, Argentina.

C.2 Measurement campaign November 2002

- 9 launches
- all ascents with small (100 g) balloons, except for ascent number ⟨13⟩ → testing new balloons with 200 g
- 2 launches in the daytime, 7 launches in the nighttime

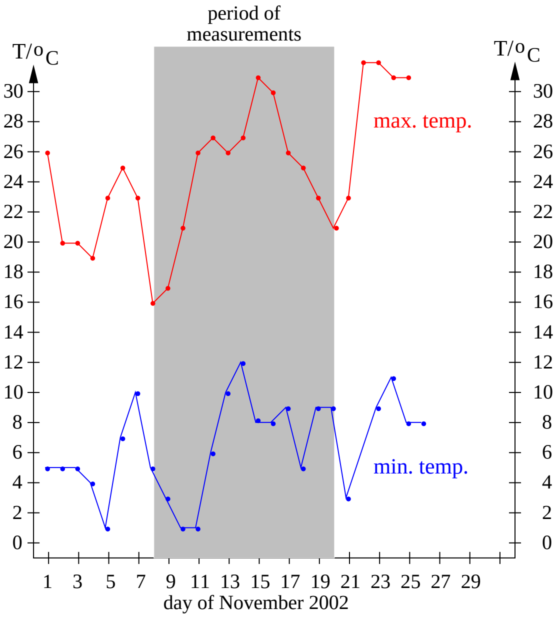

Figure C.10: Minimum and maximum temperatures measured at Malargüe airport, 1425 m a.s.l., 35.3°S, 69.35°W.

Ascent No.	**Date** (dd.mm.yyyy)	**Time** (hh:mm:ss)	**Location of Ground Station**	**Height of Ground Station** in m a.s.l.	**Maximum of reached Altitude** in m a.s.l.	**Moon < 50%**
10	09.11.2002	02:02:22	FD Coihueco	1700	16385	yes
11	10.11.2002	03:46:08	FD Coihueco	1730	14918	yes
12	10.11.2002	17:54:11	FD Coihueco	1730	18935	yes
13	13.11.2002	02:04:42	FD Coihueco	1725	25078	yes
14	14.11.2002	02:22:43	FD Coihueco	1725	14729	no
15	15.11.2002	02:35:09	FD Coihueco	1725	14597	no
16	18.11.2002	03:04:19	FD Coihueco	1725	15736	no
17	19.11.2002	02:30:42	FD Coihueco	1725	18937	no
18	20.11.2002	13:36:42	FD Coihueco	1725	16914	no

Table C.2: Measurement campaign November 2002. The dates and times are given in UTC, the altitudes are geopotential heights; FD = fluorescence detector building.

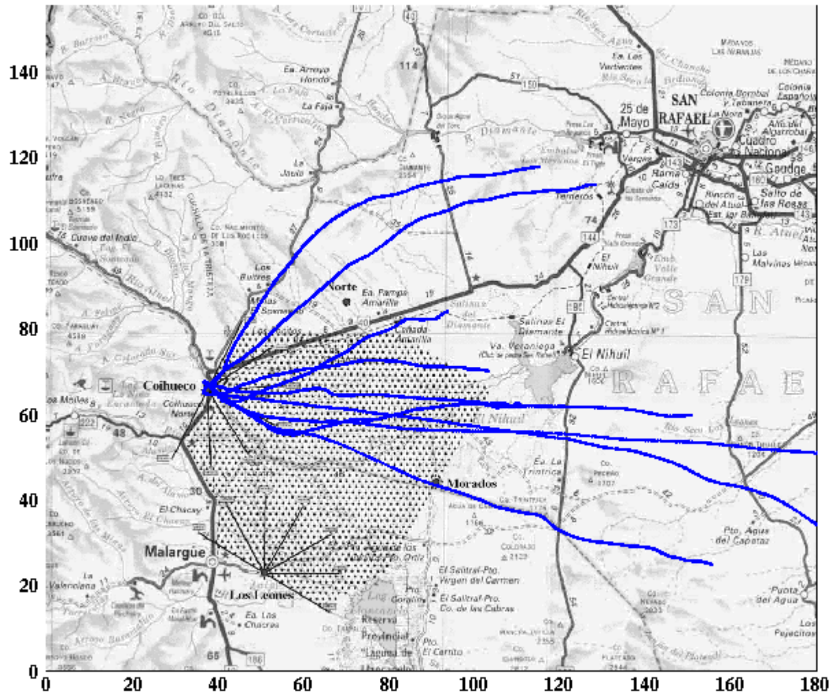

Figure C.11: Balloon paths of all launches in November 2002 from the fluorescence detector building Coihueco. In total nine launches were performed. A kilometre scale is indicated at the frame.

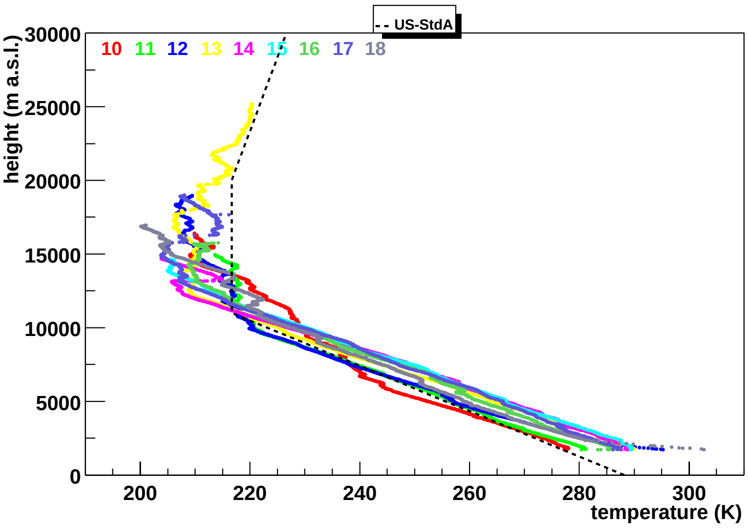

Figure C.12: All temperature profiles measured during November 2002, near Malargüe, Argentina.

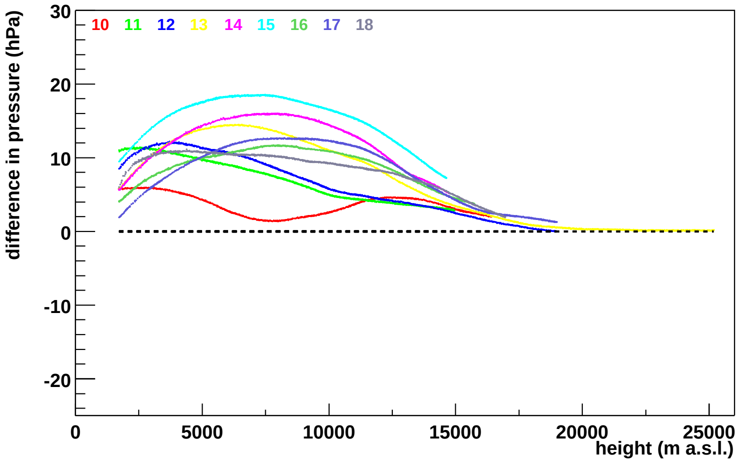

Figure C.13: Difference in all pressure profiles according to the US-StdA measured during November 2002, near Malargüe, Argentina.

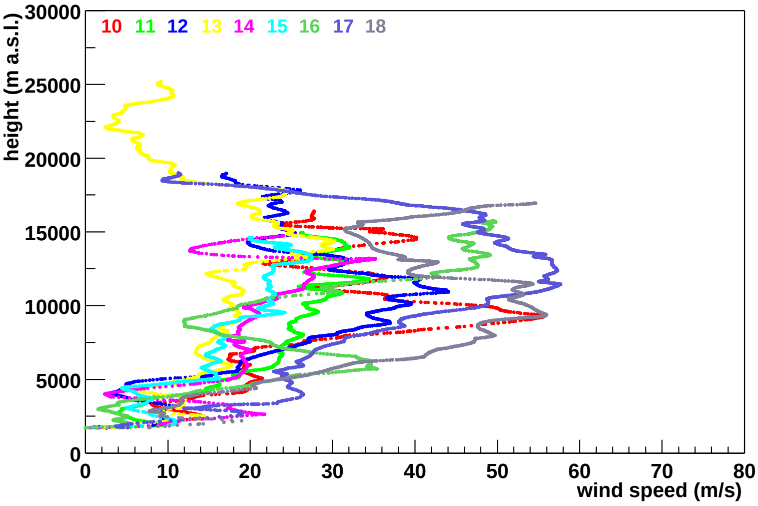

Figure C.14: All wind-speed profiles measured during November 2002, near Malargüe, Argentina.

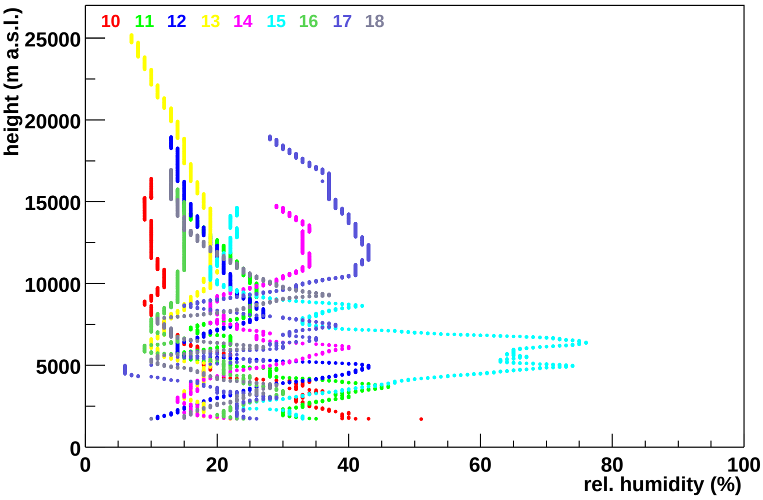

Figure C.15: All relative humidity profiles measured during November 2002, near Malargüe, Argentina.

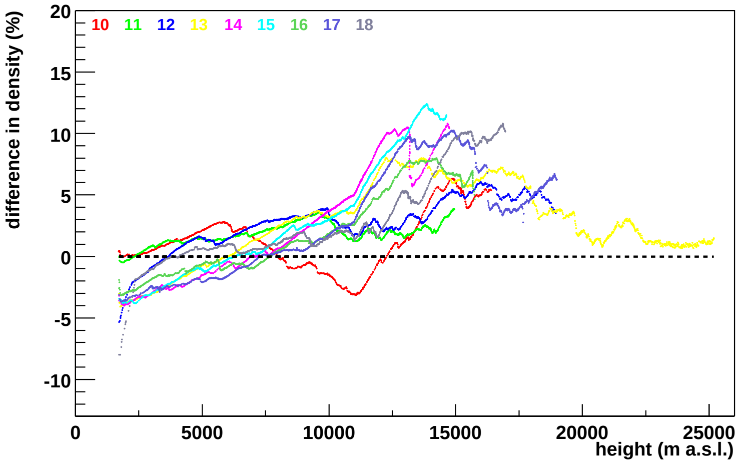

Figure C.16: Percent difference in all density profiles according to the US-StdA measured during November 2002, near Malargüe, Argentina.

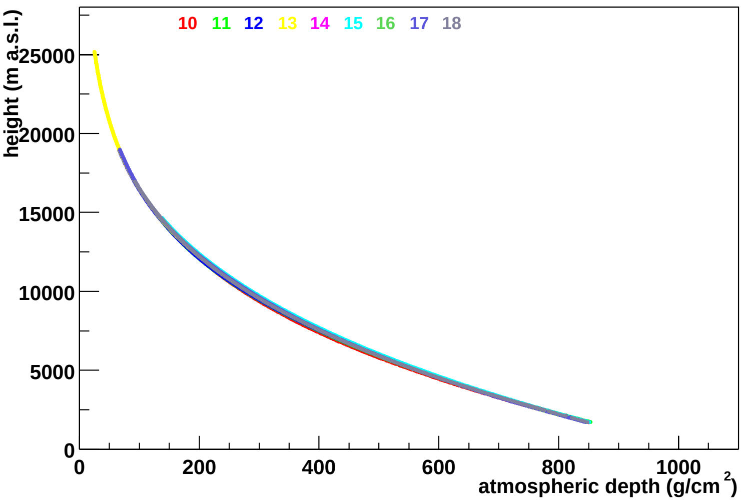

Figure C.17: All atmospheric depth profiles measured during November 2002, near Malargüe, Argentina.

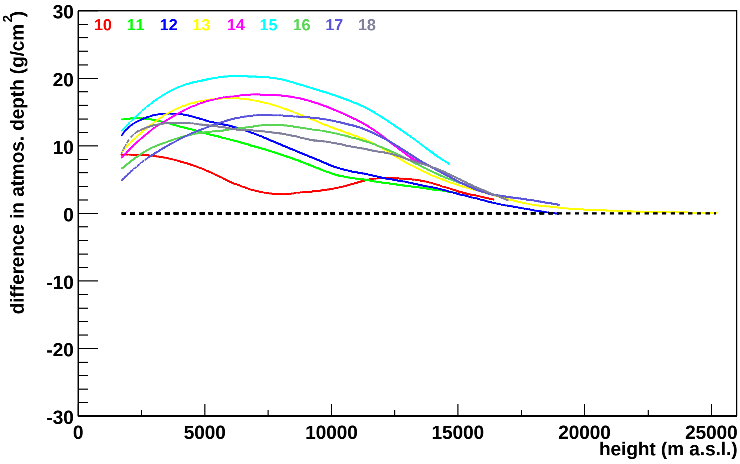

Figure C.18: Difference in all atmospheric depth profiles according to the US-StdA measured during November 2002, near Malargüe, Argentina.

C.3 Measurement campaign January / February 2003

- 15 launches
- only number ⟨19⟩ was launched on a small balloon, all others were accomplished with new 200 g balloons for reaching higher altitudes
- 2 ascents in the daytime, 13 in the nighttime
- on February, 3rd, 4th, 5th, 6th, and 12th of 2003, 2 launches per night
- on February, 7th 2003, 3 launches per night
- very stabile conditions over a long period of time

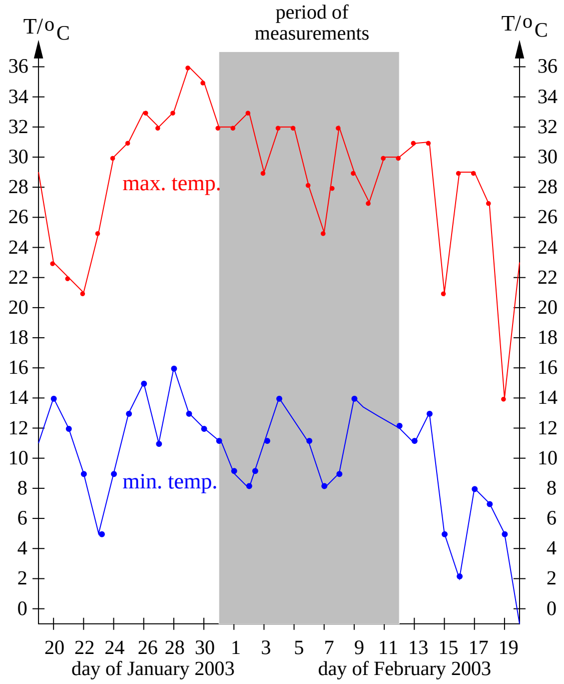

Figure C.19: Minimum and maximum temperatures measured at Malargüe airport, 1425 m a.s.l., 35.3°S, 69.35°W.

Ascent No.	**Date** (dd.mm.yyyy)	**Time** (hh:mm:ss)	**Location of Ground Station**	**Height of Ground Station** in m a.s.l.	**Maximum of reached Altitude** in m a.s.l.	**Moon** **$< 50\%$**
19	31.01.2003	19:17:58	FD Coihueco	1725	17894	no
20	03.02.2003	01:46:49	FD Coihueco	1725	23131	yes
21	03.02.2003	03:58:47	FD Coihueco	1725	26203	yes
22	04.02.2003	02:29:23	FD Coihueco	1725	22743	yes
23	04.02.2003	05:13:43	FD Coihueco	1725	20828	yes
24	05.02.2003	02:43:50	FD Coihueco	1725	22440	yes
25	05.02.2003	04:57:10	FD Coihueco	1725	22640	yes
26	06.02.2003	01:07:47	FD Coihueco	1725	18440	yes
27	06.02.2003	07:25:14	FD Coihueco	1725	26055	yes
28	07.02.2003	02:22:39	FD Coihueco	1725	25846	yes
29	07.02.2003	04:54:18	FD Coihueco	1725	25982	yes
30	07.02.2003	07:13:09	FD Coihueco	1725	25674	yes
31	11.02.2003	13:55:33	FD Coihueco	1725	24050	no
32	12.02.2003	04:38:55	FD Coihueco	1725	26093	no
33	12.02.2003	06:49:38	FD Coihueco	1725	25866	no

Table C.3: Measurement campaign January / February 2003. The dates and times are given in UTC, the altitudes are geopotential heights; FD = fluorescence detector building.

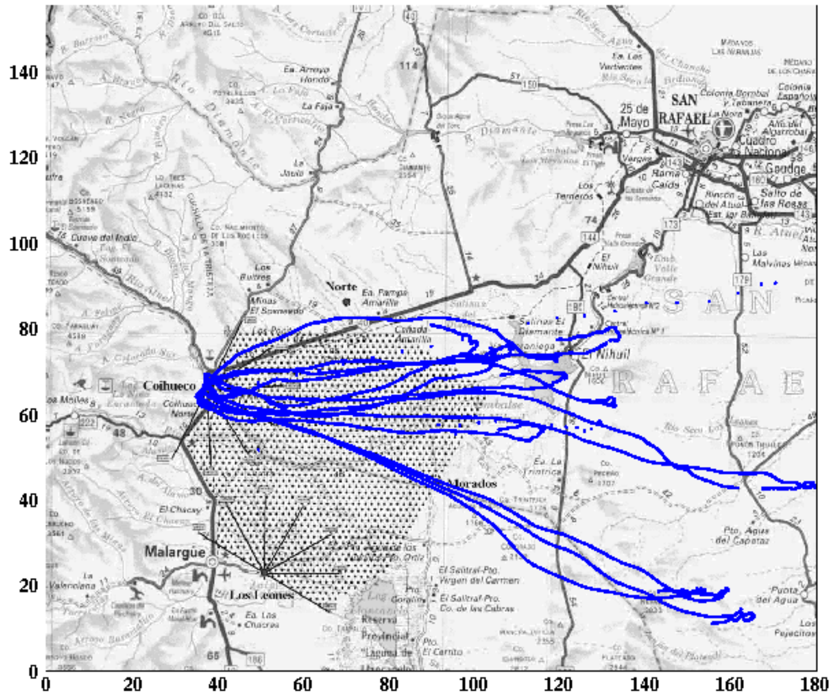

Figure C.20: Balloon paths of all launches in January / February 2003 from the fluorescence detector building Coihueco. In total 15 launches were performed. A kilometre scale is indicated at the frame.

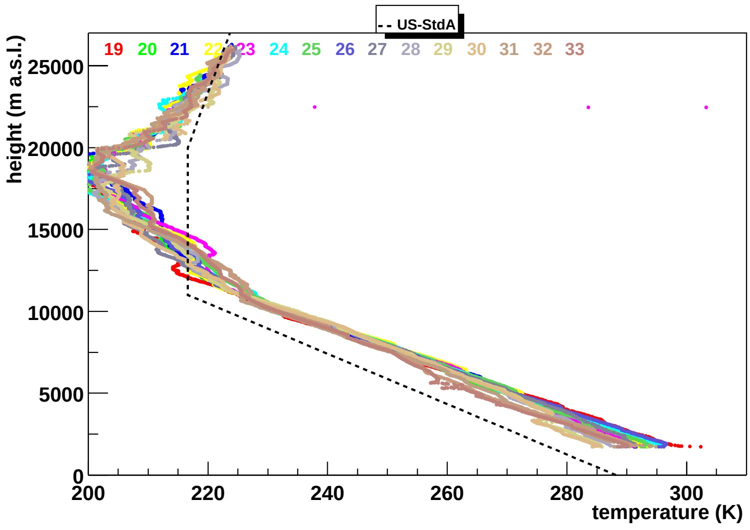

Figure C.21: All temperature profiles measured during January / February 2003, near Malargüe, Argentina.

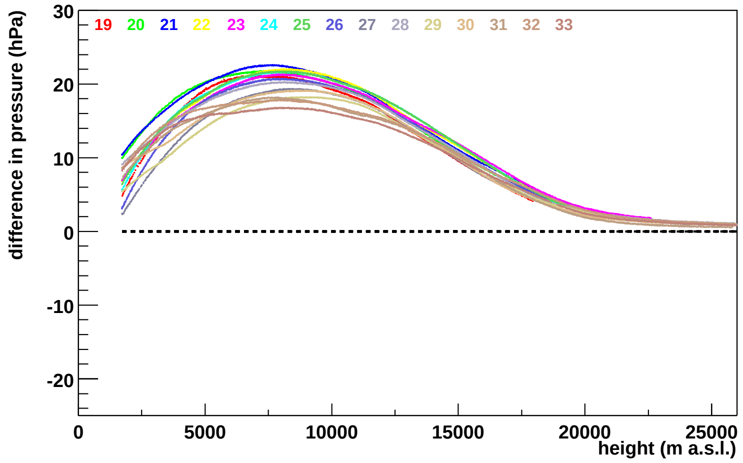

Figure C.22: Difference in all pressure profiles according to the US-StdA measured during January / February 2003, near Malargüe, Argentina.

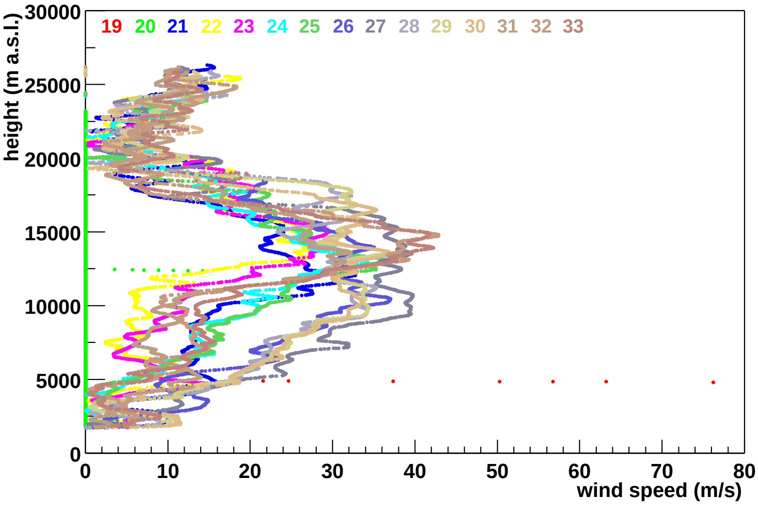

Figure C.23: All wind-speed profiles measured during January / February 2003, near Malargüe, Argentina.

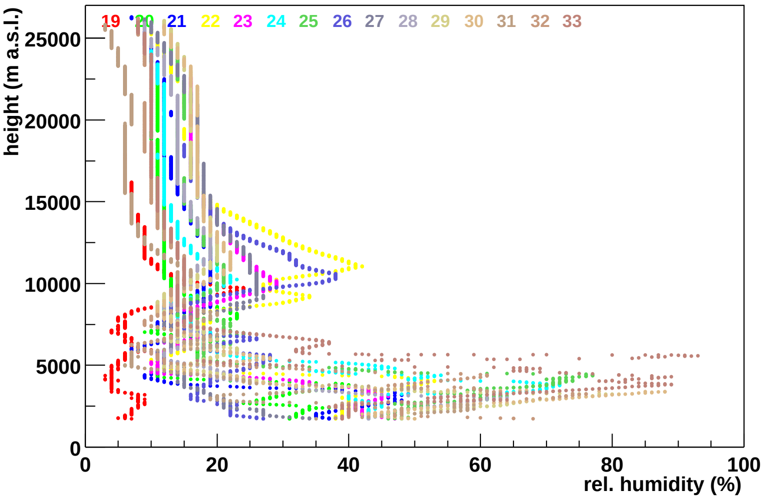

Figure C.24: All relative humidity profiles measured during January / February 2003, near Malargüe, Argentina.

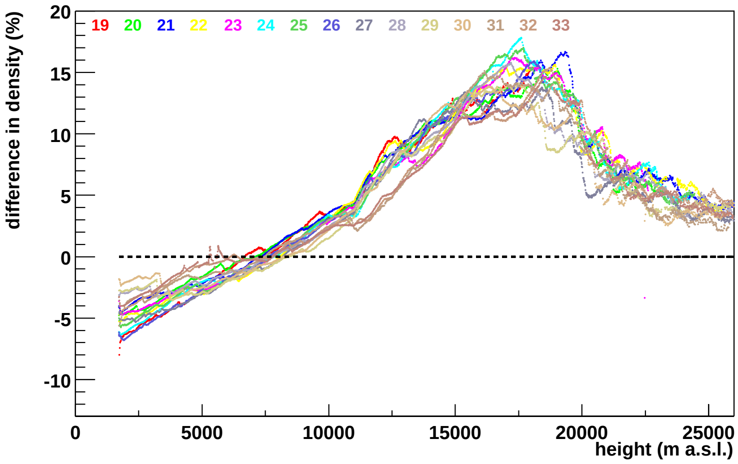

Figure C.25: Percent difference in all density profiles according to the US-StdA measured during January / February 2003, near Malargüe, Argentina.

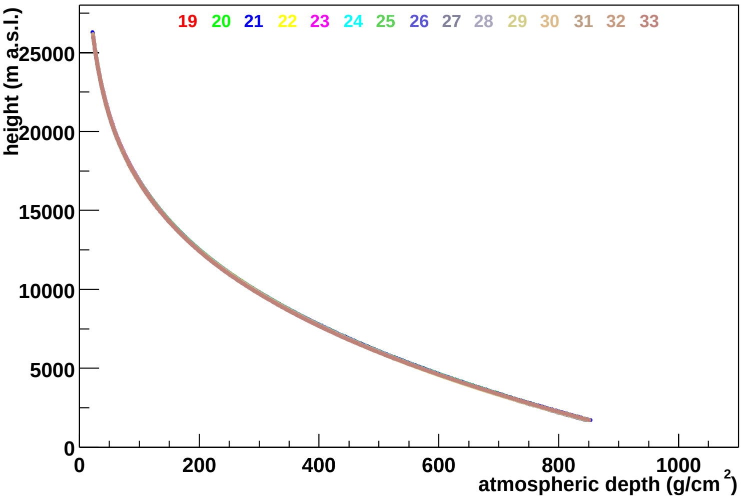

Figure C.26: All atmospheric depth profiles measured during January / February 2003, near Malargüe, Argentina.

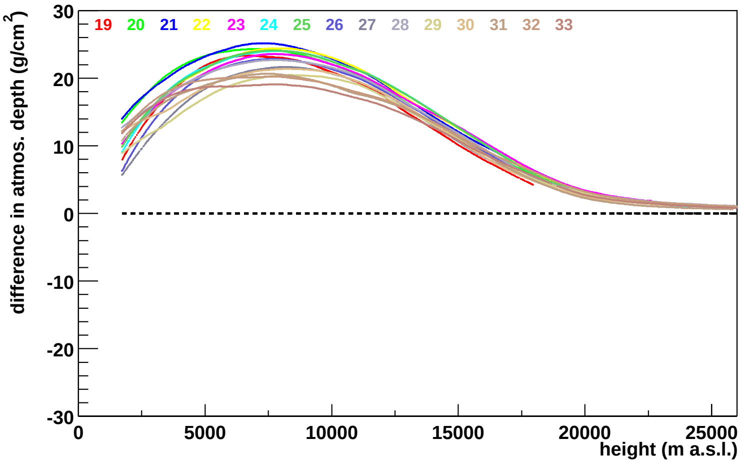

Figure C.27: Difference in all atmospheric depth profiles according to the US-StdA measured during January / February 2003, near Malargüe, Argentina.

C.4 Measurement campaign April / May 2003

- 11 launches
- all ascents with large (200 g) balloons
- 3 launches in the daytime, 8 in the nighttime
- on May, 7th 2003, 2 launches per night

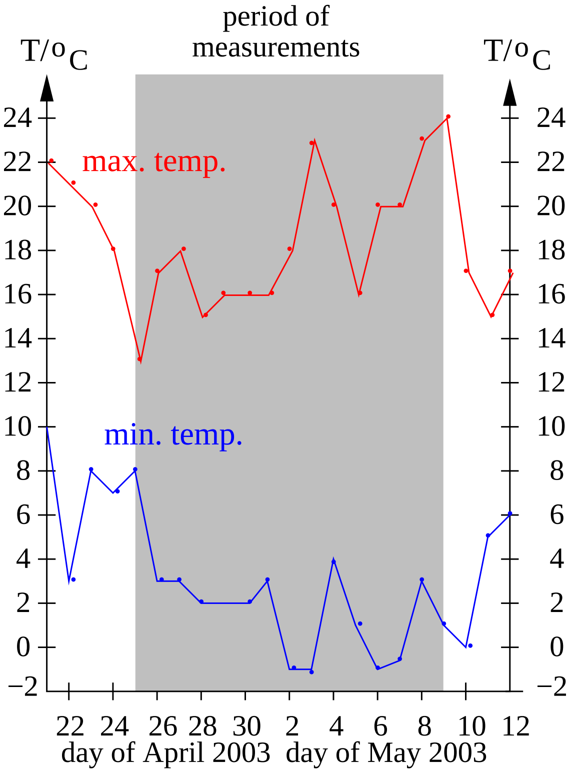

Figure C.28: Minimum and maximum temperatures measured at Malargüe airport, 1425 m a.s.l., 35.3°S, 69.35°W.

Ascent No.	**Date** (dd.mm.yyyy)	**Time** (hh:mm:ss)	**Location of Ground Station**	**Height of Ground Station** in m a.s.l.	**Maximum of reached Altitude** in m a.s.l.	**Moon < 50%**
34	25.04.2003	16:34:22	FD Coihueco	1709	23990	no
35	26.04.2003	02:51:28	FD Coihueco	1734	23784	yes
36	26.04.2003	20:18:24	FD Coihueco	1725	24899	yes
37	28.04.2003	01:34:49	FD Coihueco	1725	24255	yes
38	01.05.2003	18:41:43	FD Coihueco	1725	17646	yes
39	03.05.2003	01:09:15	FD Coihueco	1725	23160	yes
40	05.05.2003	02:15:55	FD Coihueco	1725	21134	yes
41	06.05.2003	02:08:16	FD Coihueco	1725	26855	yes
42	07.05.2003	01:36:21	FD Coihueco	1725	27457	yes
43	07.05.2003	04:33:11	FD Coihueco	1725	22869	yes
44	09.05.2003	03:49:45	FD Coihueco	1725	19930	yes

Table C.4: Measurement campaign April / May 2003. The dates and times are given in UTC, the altitudes are geopotential heights; FD = fluorescence detector building.

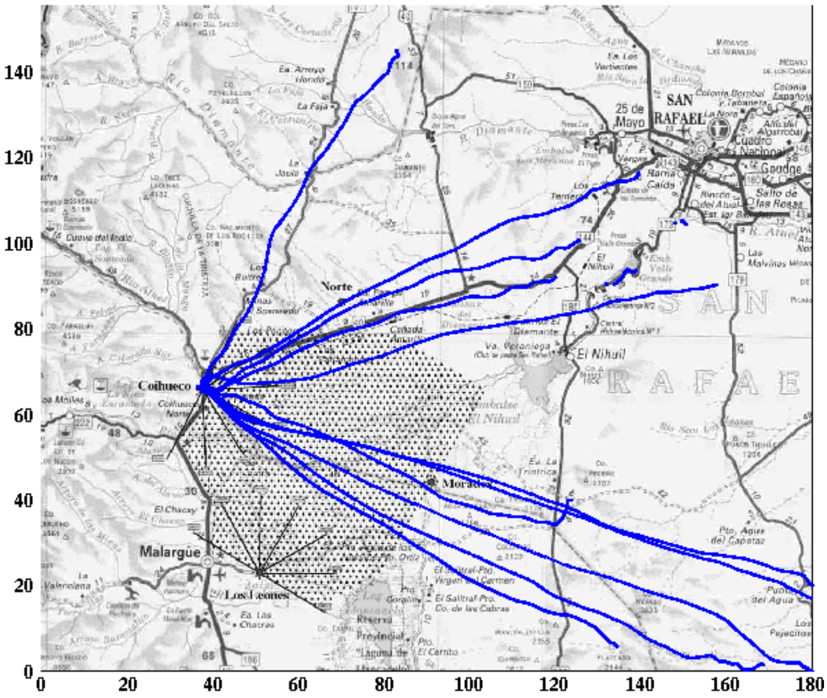

Figure C.29: Balloon paths of all launches in April / May 2003 from the fluorescence detector building Coihueco. In total eleven launches were performed. A kilometre scale is indicated at the frame.

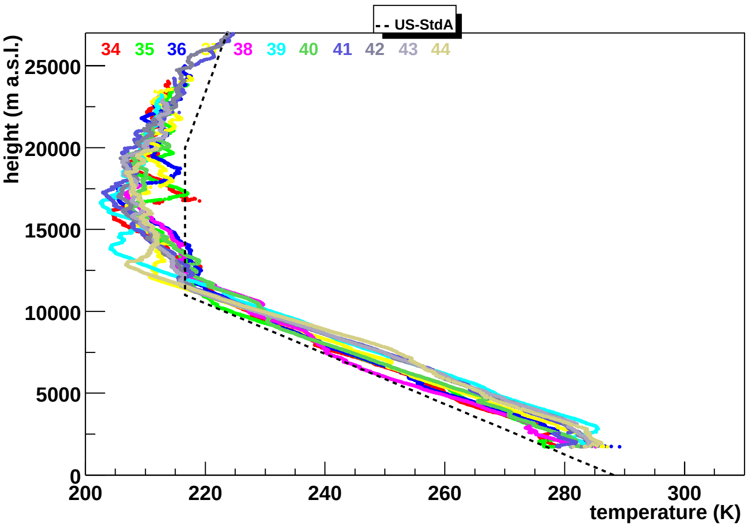

Figure C.30: All temperature profiles measured during April / May 2003, near Malargüe, Argentina.

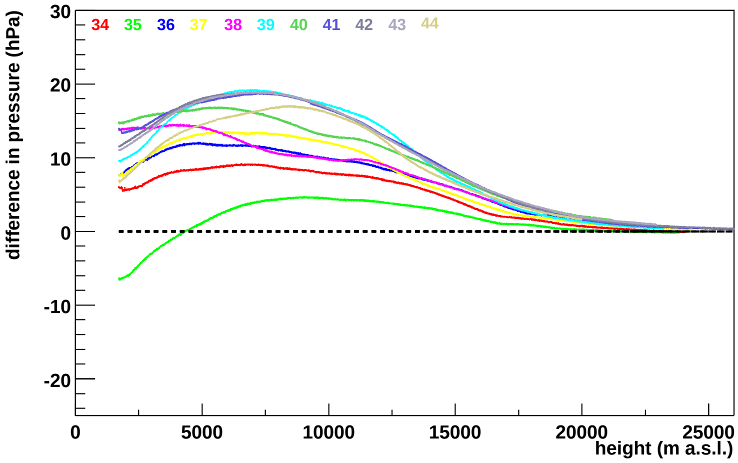

Figure C.31: Difference in all pressure profiles according to the US-StdA measured during April / May 2003, near Malargüe, Argentina.

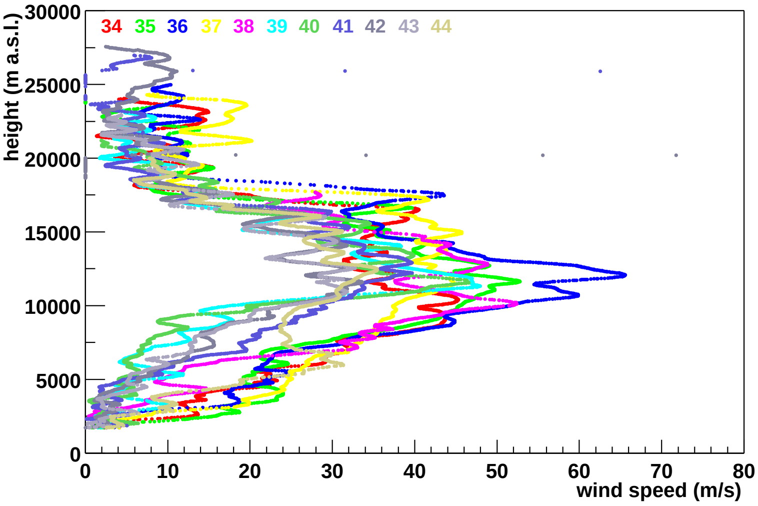

Figure C.32: All wind-speed profiles measured during April / May 2003, near Malargüe, Argentina.

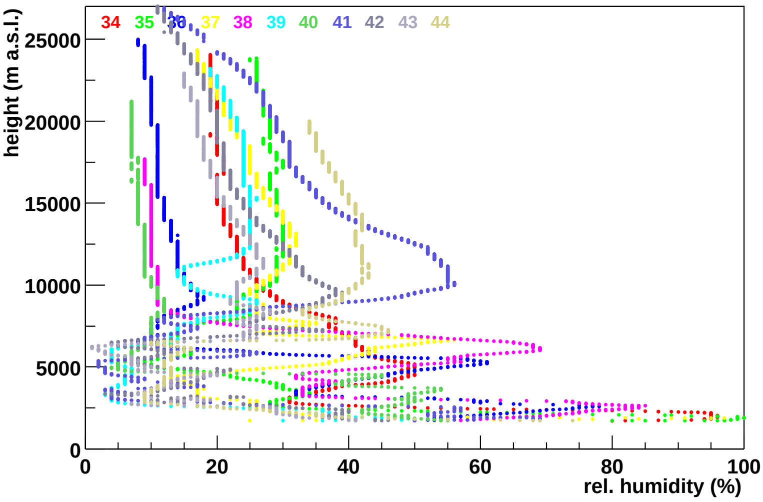

Figure C.33: All relative humidity profiles measured during April / May 2003, near Malargüe, Argentina.

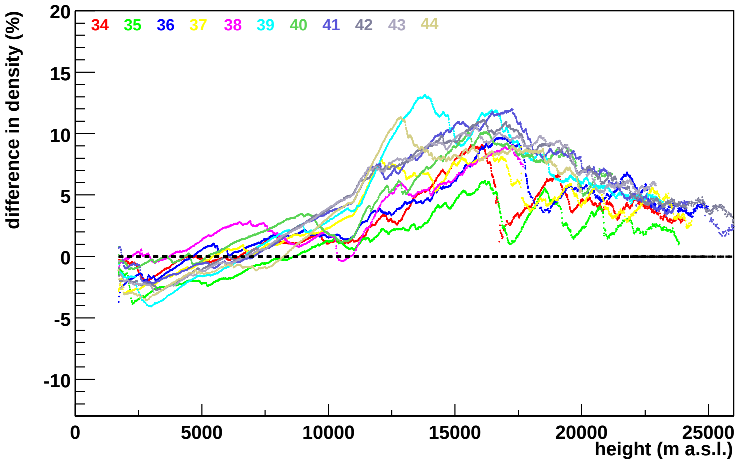

Figure C.34: Percent difference in all density profiles according to the US-StdA measured during April / May 2003, near Malargüe, Argentina.

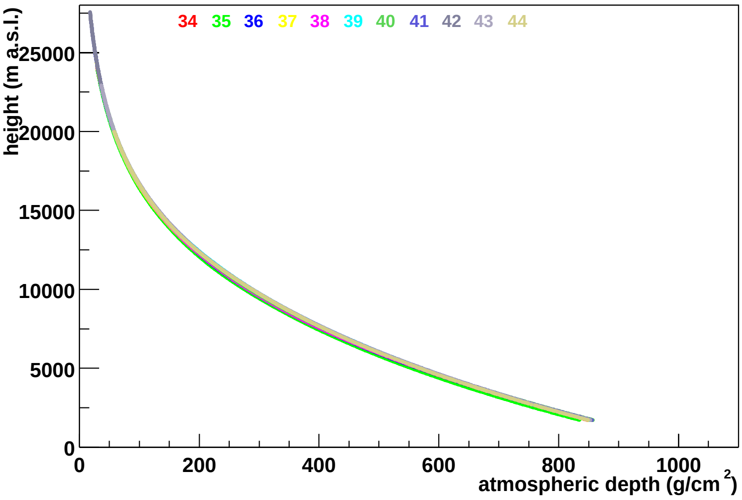

Figure C.35: All atmospheric depth profiles measured during April / May 2003, near Malargüe, Argentina.

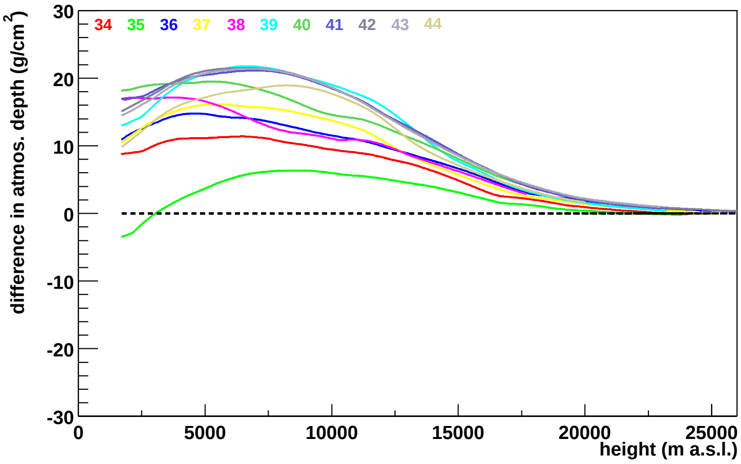

Figure C.36: Difference in all atmospheric depth profiles according to the US-StdA measured during April / May 2003, near Malargüe, Argentina.

C.5 Measurement campaign July / August 2003

- 8 launches
- all ascents with large (200 g) balloons
- all launches in the nighttime

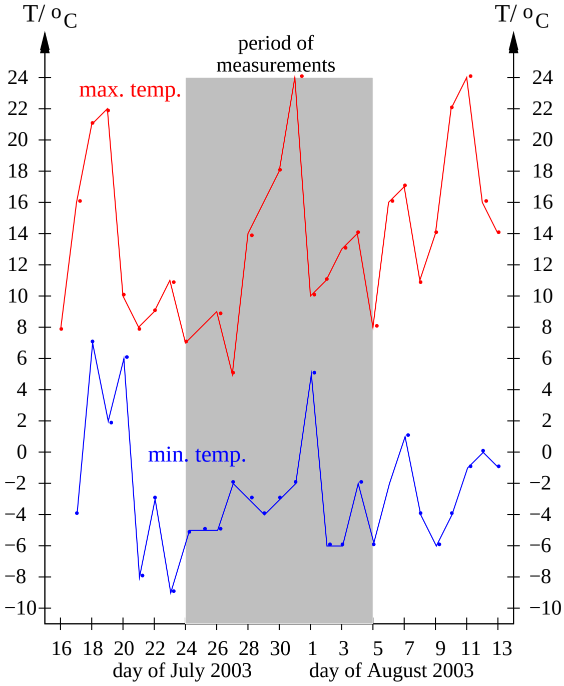

Figure C.37: Minimum and maximum temperatures measured at Malargüe airport, 1425 m a.s.l., 35.3°S, 69.35°W.

Ascent No.	**Date** (dd.mm.yyyy)	**Time** (hh:mm:ss)	**Location of Ground Station**	**Height of Ground Station** in m a.s.l.	**Maximum of reached Altitude** in m a.s.l.	**Moon** $< 50\%$
45	24.07.2003	03:51:52	FD Coihueco	1725	24331	yes
46	26.07.2003	02:31:32	FD Coihueco	1725	21514	yes
47	27.07.2003	02:48:31	FD Coihueco	1725	26775	yes
48	29.07.2003	04:18:13	FD Coihueco	1725	26019	yes
49	30.07.2003	02:49:39	FD Coihueco	1725	25490	yes
50	31.07.2003	05:18:19	FD Coihueco	1725	26048	yes
51	04.08.2003	03:06:50	FD Coihueco	1725	25730	yes
52	05.08.2003	03:53:56	FD Coihueco	1725	24078	yes

Table C.5: Measurement campaign July / August 2003. The dates and times are given in UTC, the altitudes are geopotential heights; FD = fluorescence detector building.

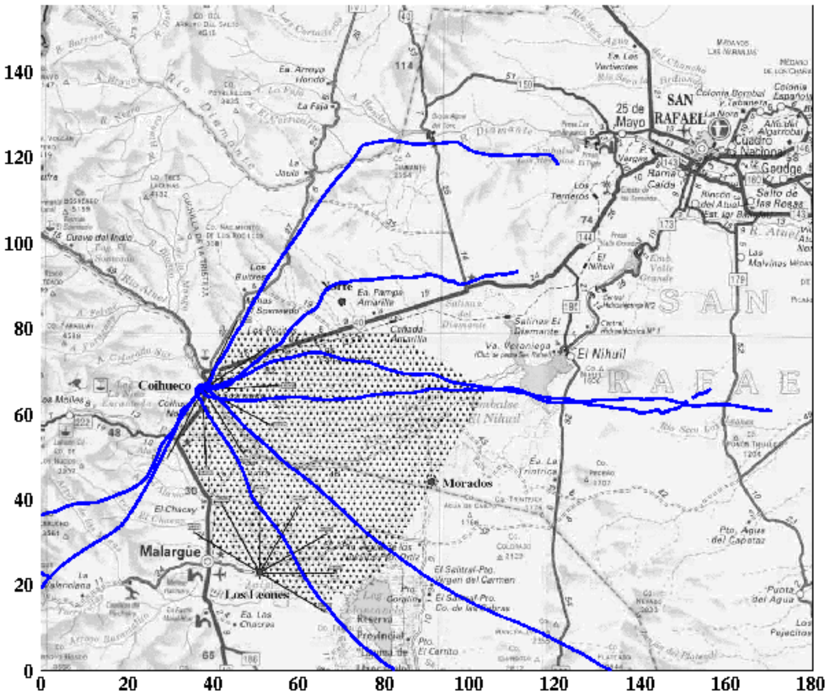

Figure C.38: Balloon paths of all launches in July / August 2003 from the fluorescence detector building Coihueco. In total eight launches were performed. A kilometre scale is indicated at the frame.

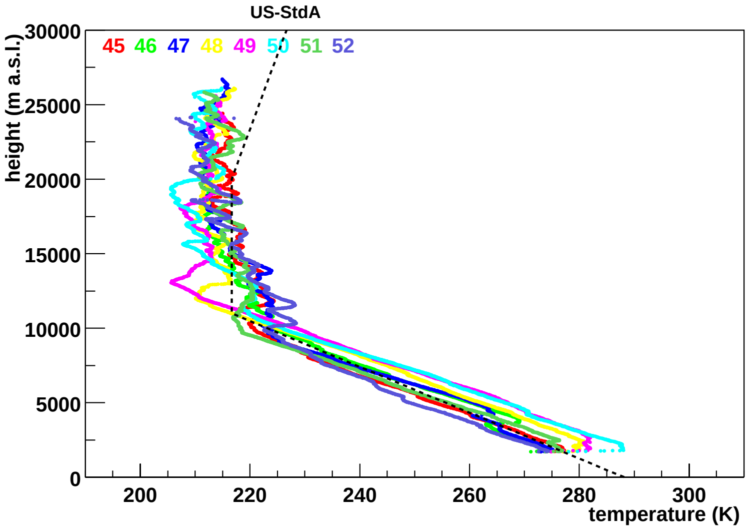

Figure C.39: All temperature profiles measured during July / August 2003, near Malargüe, Argentina.

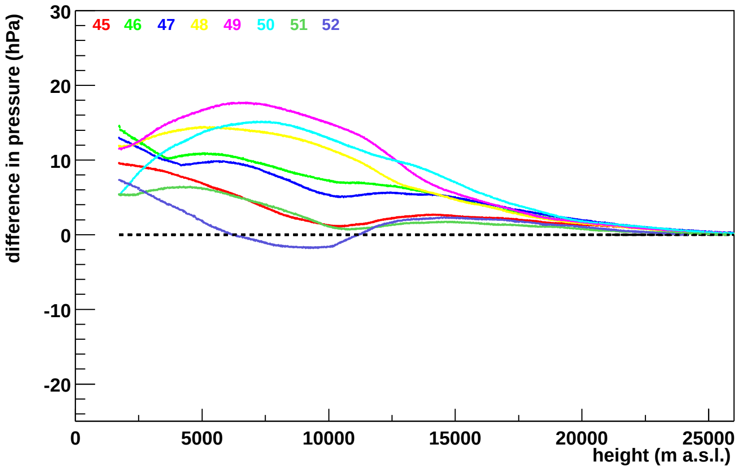

Figure C.40: Difference in all pressure profiles according to the US-StdA measured during July / August 2003, near Malargüe, Argentina.

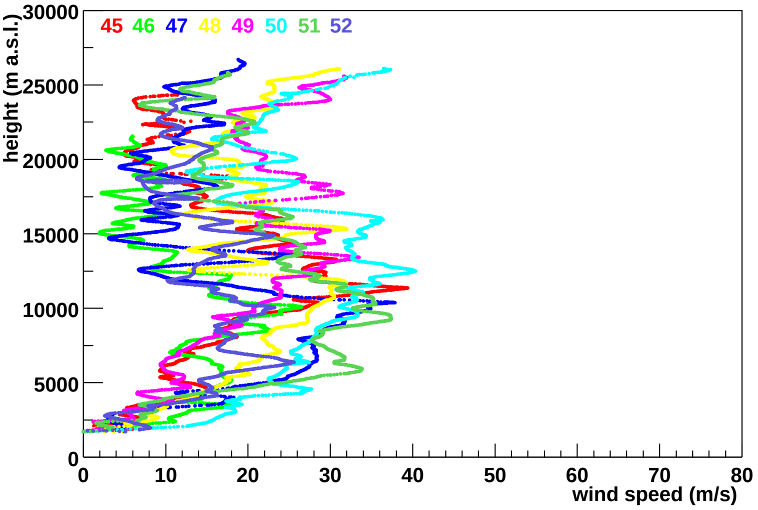

Figure C.41: All wind-speed profiles measured during July / August 2003, near Malargüe, Argentina.

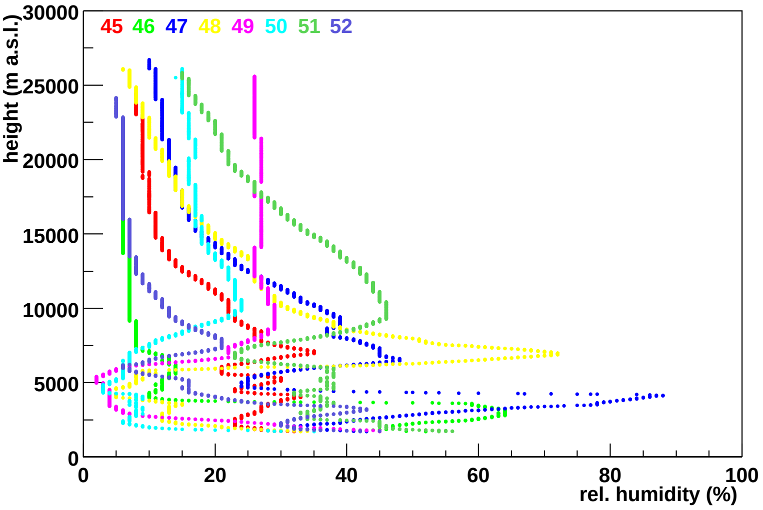

Figure C.42: All relative humidity profiles measured during July / August 2003, near Malargüe, Argentina.

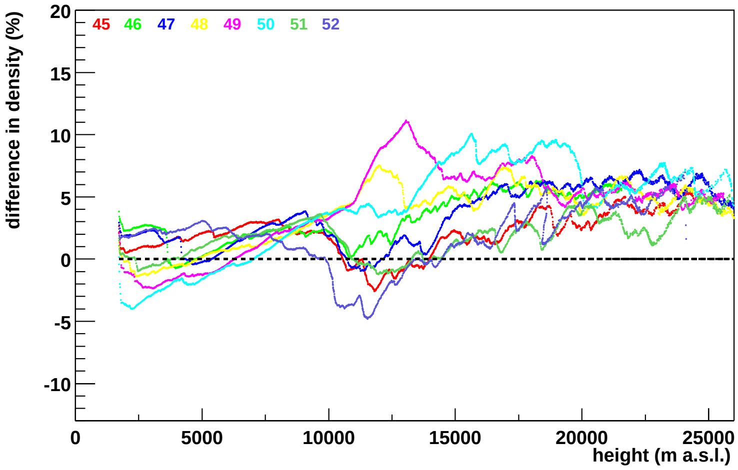

Figure C.43: Percent difference in all density profiles according to the US-StdA measured during July / August 2003, near Malargüe, Argentina.

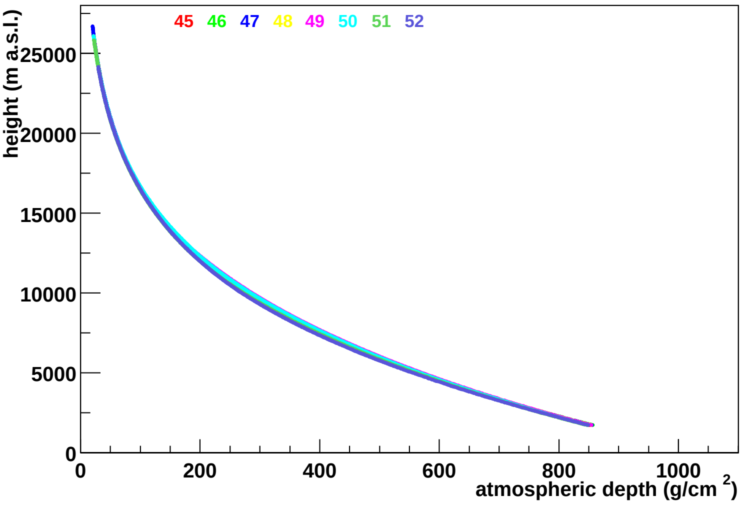

Figure C.44: All atmospheric depth profiles measured during July / August 2003, near Malargüe, Argentina.

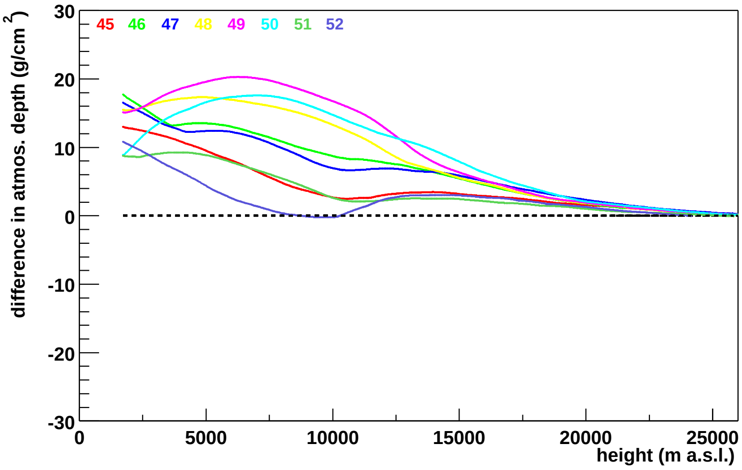

Figure C.45: Difference in all atmospheric depth profiles according to the US-StdA measured during July / August 2003, near Malargüe, Argentina.

List of Figures

Bibliography

[Ahrens 1994] C. D. Ahrens, Meteorology Today, West Publishing Company, Minneapolis / St. Paul, (1994)

[Allkofer 1975] O. C. Allkofer, Introduction to Cosmic Radiation, Verlag Karl Thiemig, München, (1975)

[Antoni et al. 2002] T. Antoni et al., KASCADE-Collaboration, Astropart. Phys. 16, 373, (2002)

[Antoni et al. 2003] T. Antoni et al., KASCADE-Collaboration, Nucl. Instr. and Meth. in Phys. Res. A, Vol. 513, Issue 3, 429, (2003)

[Auger-DR 1997] Auger Collaboration, Pierre Auger Project Design Report, (1997)
http://www.auger.org/admin/DesignReport/index.html

[Auger-TDR 2002] Auger Collaboration, Technical Design Report, (2002)
http://tdpc01.fnal.gov/auger/org/tdr/index.html

[Ave et al. 2001] M. Ave et al. for The Pierre Auger Observatory Collaboration, Proc. 27th Int. Cosmic Ray Conf., Hamburg (Germany), Vol. 2, 707, (2001)

[Baldenhofer 2001] K. Baldenhofer (ed.), Das ENSO-Phänomen, Projekt des Bildungszentrums Markdorf, Version 2.0, (2001)
http://www.enso.info/enso.html

[Bertou et al. 2000] X. Bertou, M. Boratav, A. Letessier-Selvon, Int. J. Mod. Phys. A, Vol. 15, No. 15, 2181, (2000)

[Bhattacharjee & Sigl 2000] P. Bhattacharjee, G. Sigl, Phys. Rep. 327, 109, (2000)

[Biermann & Schlüter 1953] L. Biermann, A. Schlüter, Die Herkunft der kosmischen Strahlung. Zeitliche Schwankungen, In: Vorträge über kosmische Strahlung (ed. W. Heisenberg), Springer Verlag, (1953)

[Blümer 2003] J. Blümer for The Pierre Auger Observatory Collaboration, J. Phys. G: Nucl. Part. Phys. 29, 867, (2003) [Bodhaine et al. 1999] B. A. Bodhaine et al., J. Atmos. Ocean. Tech., Vol. 16, 1854, (1999)

[Boeker & van Grondelle 1997] E. Boeker, R. van Grondelle, Physik und Umwelt, Vieweg Verlag, Braunschweig / Wiesbaden, (1997)

[Bolle 1982] H.-J. Bolle, Radiation and Energy Transport in the Earth Atmosphere System, In: The Handbook of Environmental Chemistry (ed. O. Hutzinger), Vol. 1, Part B, Springer Verlag, Berlin, (1982)

[Bucholtz 1995] A. Bucholtz, Appl. Opt., Vol. 34, No. 15, 2765, (1995)

[Bunner 1967] A. N. Bunner, Cosmic Ray Detection by Atmospheric Fluorescence, PhD thesis, Cornell University, Ithaca, NY, USA, (1967)

[CIRA 1986] National Space Science Data Center (NSSDC), http://nssdc.gsfc.nasa.gov/space/model/atmos/cospar1.html

[Cronin 1992] J. W. Cronin, Nucl. Phys. B (Proc. Suppl.) 28B, 213, (1992)

[Davidson & O'Neil 1964] G. Davidson, R. O'Neil, J. Chem. Phys. 41, No. 12, 3946, (1964)

[Davidson et al. 1988] J. A. Davidson et al., J. Geophys. Res., Vol. 93, No. D6, 7105, (1988)

[Dova 2001] M. T. Dova for The Pierre Auger Observatory Collaboration, Proc. 27th Int. Cosmic Ray Conf., Hamburg (Germany), Vol. 2, 699, (2001)

[DWD] http://www.dwd.de

[DWD 1987] Leitfäden für die Ausbildung im Deutschen Wetterdienst (DWD), Nr. 1: Allgemeine Meteorologie, Selbstverlag des DWD, Offenbach am Main, (1987)

[Edlén 1966] B. Edlén, Metrologia, Vol. 2, No. 2, 12, (1966)

[Endlicher et al. 1988/89] W. Endlicher, K. A. Habbe, H. Pinzner, Zum El Niño - Southern Oscillation - Ereignis 1983 und seine Auswirkungen im peruanischen Küstengebiet, In: Mitteilungen der Fränkischen Geographischen Gesellschaft, Band 35 / 36, Selbstverlag der Fränkischen Geographischen Gesellschaft (ed. E. Wirth), (1988/89)

[Engel 2003] R. Engel, private communication, (2003)

[Escobar et al. 2001] C. O. Escobar et al. for The Pierre Auger Observatory Collaboration, Proc. 27th Int. Cosmic Ray Conf., Hamburg (Germany), Vol. 2, 749, (2001)

[Friedlander 1989]	M. W. FRIEDLANDER, Cosmic Rays, Harvard University Press, Cambridge, (1989)
[Gaisser 1990]	T. K. GAISSER, Cosmic Rays and Particle Physics, Cambridge University Press, Cambridge, (1990)
[Gaisser 1997]	T. K. GAISSER, Proc. of the Mexican School on Nuclear Astrophysics (edd. J. G. HIRSCH, D. PAGE), Guanajuato (Mexico), 245, (1997)
[Gaisser & Hillas 1977]	T. K. GAISSER, A. M. HILLAS, Proc. 15th Int. Cosmic Ray Conf., Plovdiv (Bulgaria), Vol. 8, 353, (1977)
[Graw]	DR. GRAW MESSGERÄTE GmbH & CO., Nürnberg, www.graw.de
[Greisen 1965]	K. GREISEN, Proc. 9th Int. Cosmic Ray Conf., London (UK), Vol. 2, 609, (1965)
[Greisen 1966]	K. GREISEN, Phys. Rev. Lett., Vol. 16, 748, (1966)
[Haferkorn 2003]	H. HAFERKORN, Optik, WILEY-VCH Verlag, Weinheim, (2003)
[Hagiwara et al. 2002]	K. HAGIWARA et al., PARTICLE DATA GROUP, Phys. Rev. D, Vol. 66, No. 1-I, 182, (2002)
[Haken & Wolf 1998]	H. HAKEN, H. C. WOLF, Molekülphysik und Quantenchemie, Springer Verlag, Berlin, (1998)
[Heck et al. 1998]	D. HECK et al., CORSIKA: A Monte Carlo Code to Simulate Extensive Air Showers, Report FZKA 6019, Forschungszentrum Karlsruhe, (1998)
[Herzberg 1950]	G. HERZBERG, Molecular Spectra and Molecular Structure: I. Spectra of Diatomic Molecules, D. van Nostrand Company, Inc., New York, (1950)
[Hillas 1984]	A. M. HILLAS, Ann. Rev. of Astr. and Astrophys. 22, 425, (1984)
[Kakimoto et al. 1996]	F. KAKIMOTO et al., Nucl. Instr. and Meth. in Phys. Res. A 372, 527, (1996)
[Kalmykov et al. 1997]	N. N. KALMYKOV, S. S. OSTAPCHENKO, A. I. PAVLOV, Nucl. Phys. B (Proc. Suppl.) 52B, 17, (1997)
[Khristiansen et al. 1980]	G. B. KHRISTIANSEN, G. KULIKOV, J. FOMIN, Cosmic Rays of Superhigh Energies, Verlag Karl Thiemig, München, (1980)

[Knapp 1997] J. Knapp, Vergleich hadronischer Wechselwirkungsmodelle zur Simulation ausgedehnter Luftschauer der kosmischen Strahlung, Report FZKA 5970, Forschungszentrum Karlsruhe, (1997)

[Knapp & Heck] J. Knapp, D. Heck, Extensive Air Shower Simulation with CORSIKA: A User's Guide, Report KfK 5196B, Kernforschungszentrum Karlsruhe, (1993); Auger technical note GAP-1998-012, (1998);
for an up-to-date version see http://www-ik.fzk.de/~heck/corsika/usersguide/corsika_tech.html

[Kobal 2001] M. Kobal for The Pierre Auger Observatory Collaboration, Astropart. Phys. 15, 259, (2001)

[Kraus 2000] H. Kraus, Die Atmosphäre der Erde, Vieweg Verlag, Braunschweig / Wiesbaden, (2000) OR Springer Verlag, Berlin, (2001)

[Lebrun 2002] D. Lebrun, private communication, (2002)

[Lide 2000] D. R. Lide (ed.), CRC-Handbook of Chemistry and Physics, 81th edition, CRC Press, Florida / Boca Raton, 10-160 and 10-220, (2000/2001)

[Malberg 2002] H. Malberg, Meteorologie und Klimatologie, Springer Verlag, Berlin, (2002)

[Molina & Molina 1986] L. T. Molina, M. J. Molina, J. Geophys. Res., Vol. 91, No. D13, 14501, (1986)

[Müller 1987] M. J. Müller, Handbuch ausgewählter Klimastationen der Erde, In: Forschungsstelle Bodenerosion der Universität Trier, Mertesdorf (Ruwertal) (ed. G. Richter), (1987)

[Nagano & Watson 2000] M. Nagano, A. A. Watson, Rev. Mod. Phys., Vol. 72, No. 3, 689, (2000)

[Nelson et al. 1985] W. R. Nelson, H, Hirayama, D. W. O. Rogers, The EGS4 Code System, Report SLAC 265, Stanford Linear Accelerator Center, (1985)

[Nerling et al. 2003] F. Nerling et al., Proc. 28th Int. Cosmic Ray Conf., Tsukuba (Japan), Vol. 2, 611, (2003)

[NSSDC] National Space Science Data Center (NSSDC), http://nssdc.gsfc.nasa.gov/space/model/atmos/us_standard.html

[Olinto 1999] A. V. Olinto, Proc. of the Int. Summer School on Experimental Physics of Gravitational Waves, Urbono (Italy) (1999); astro-ph/0003013

[Owens 1967]	J. C. OWENS, Appl. Opt., Vol. 16, No. 1, 51, (1967)
[Perrone & Risse 2002]	L. PERRONE, M. RISSE, Auger technical note GAP-2002-060, (2002); http://www.auger.org/admin/GAP_Notes/GAP2002/gap2002_060.pdf
[Ptuskin 2001]	V. S. PTUSKIN, Cosmic Ray Origin: General Overview, In: Astrophysical Sources of High Energy Particles and Radiation (edd. M. M. SHAPIRO, et al.), NATO Science Series II, Vol. 44, 251, (2001)
[Queensland 2003]	THE CROWN IN RIGHT OF THE STATE QUEENSLAND, The Long Paddock - Climate Management Information for Rural Australia, http://www.longpaddock.qld.gov.au/SeasonalClimateOutlook/SouthernOscillationIndex/SOIGraph/index.html, (2003)
[Risse & Heck 2002]	M. RISSE, D. HECK, Auger technical note GAP-2002-043, (2002); http://www.auger.org/admin/GAP_Notes/GAP2002/gap2002_043.pdf
[Risse 2003]	M. RISSE, private communication, (2003)
[Roedel 1992]	W. ROEDEL, Physik unserer Umwelt: Die Atmosphäre, Springer Verlag, Berlin, (1992)
[Schwerdtfeger 1976]	W. SCHWERDTFEGER (ed.), Climates of Central and South America, In: World Survey of Climatology (ed. H. E. LANDSBERG), Vol. 12, Elsevier Science Publishing Company, Amsterdam, (1976)
[Sokolsky 1989]	P. SOKOLSKY, Frontiers in Physics: Introduction to Ultrahigh Energy Cosmic Ray Physics, Addison-Wesley Publishing Company, California / Redwood City, (1989)
[Sommers 2001]	P. SOMMERS, Rapporteur talk 27th Int. Cosmic Ray Conf., Hamburg (Germany), 170, (2001)
[Song et al. 2000]	C. Song et al., Astropart. Phys. 14, 7, (2000)
[Stull 1995]	R. B. STULL, Meteorology Today For Scientists and Engineers - A Technical Companion Book to [Ahrens 1994], West Publishing Company, Minneapolis / St. Paul(1995)
[Ulrich et al. 1997]	H. ULRICH, Untersuchung atmosphärischer Einflüsse auf die Entwicklung ausgedehnter Luftschauer anhand von Simulationsrechnungen, Diploma thesis, University of Karlsruhe, (1997) (unpublished) OR H. ULRICH, K. H. KAMPERT, H. O. KLAGES, Auger technical note GAP-98-043, (1998);

http://www.auger.org/admin/GAP_Notes/GAP1998/GAP_98_043.ps.gz

[US-StdA 1976] National Aeronautics and Space Administration (NASA), U.S. Standard Atmosphere 1976, NASA-TM-X-74335, (1976)

[Van de Hulst 1957] H. C. Van de Hulst, Light Scattering by Small Paricles, John Wiley & Sons, New York, (1957)

[Visconti 2001] G. Visconti, Fundamentals of Physics and Chemistry of the Atmosphere, Springer Verlag, Berlin, (2001)

[Waldenmaier 2001] T. Waldenmaier, Untersuchung der Abbildungseigenschaften eines Schmidt-Teleskopes für das Pierre-Auger-Projekt, Diploma thesis, University of Karlsruhe, (2001) (unpublished)

[Weischet 1977] W. Weischet, Einführung in die Allgemeine Klimatologie, B. G. Teubner, Stuttgart, (1977)

[Zatsepin & Kuz'min 1966] G. T. Zatsepin, V. A. Kuz'min, Sov. Phys. JETP Lett. (Engl. Transl.), Vol. 4, 78, (1966)